



Organic and eco-friendly corrosion inhibitors for sweet and sour conditions (Investigation of corrosion inhibition mechanisms using experimental and molecular modelling)

Gupta, Shivangi

Publication date:
2022

Document Version
Publisher's PDF, also known as Version of record

[Link back to DTU Orbit](#)

Citation (APA):
Gupta, S. (2022). *Organic and eco-friendly corrosion inhibitors for sweet and sour conditions (Investigation of corrosion inhibition mechanisms using experimental and molecular modelling)*. Technical University of Denmark.

General rights

Copyright and moral rights for the publications made accessible in the public portal are retained by the authors and/or other copyright owners and it is a condition of accessing publications that users recognise and abide by the legal requirements associated with these rights.

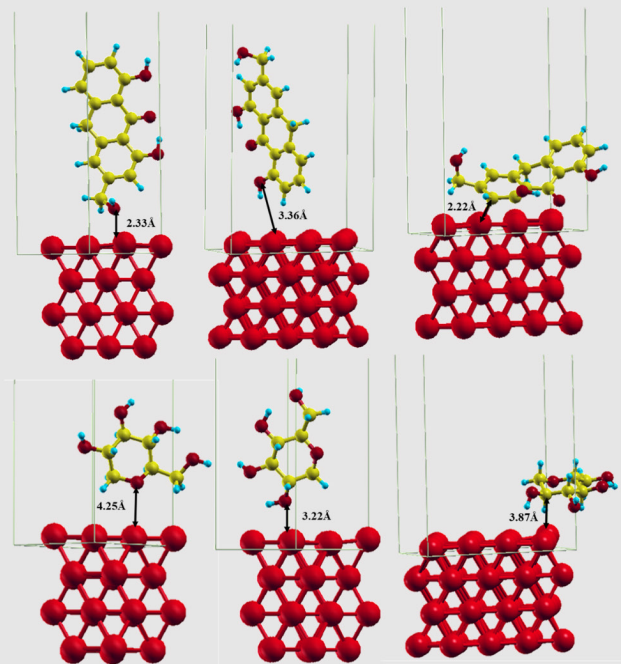
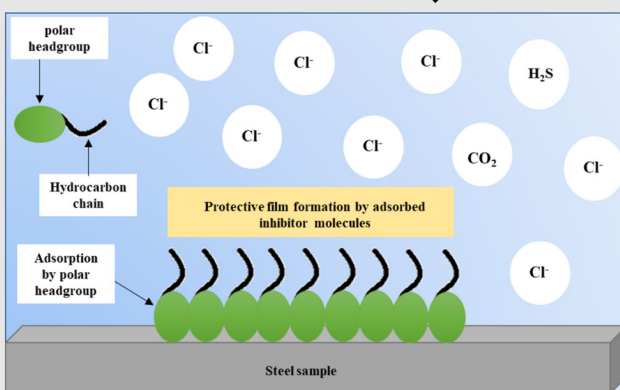
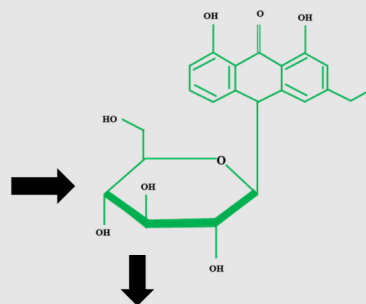
- Users may download and print one copy of any publication from the public portal for the purpose of private study or research.
- You may not further distribute the material or use it for any profit-making activity or commercial gain
- You may freely distribute the URL identifying the publication in the public portal

If you believe that this document breaches copyright please contact us providing details, and we will remove access to the work immediately and investigate your claim.

Organic and eco-friendly corrosion inhibitors for sweet and sour conditions

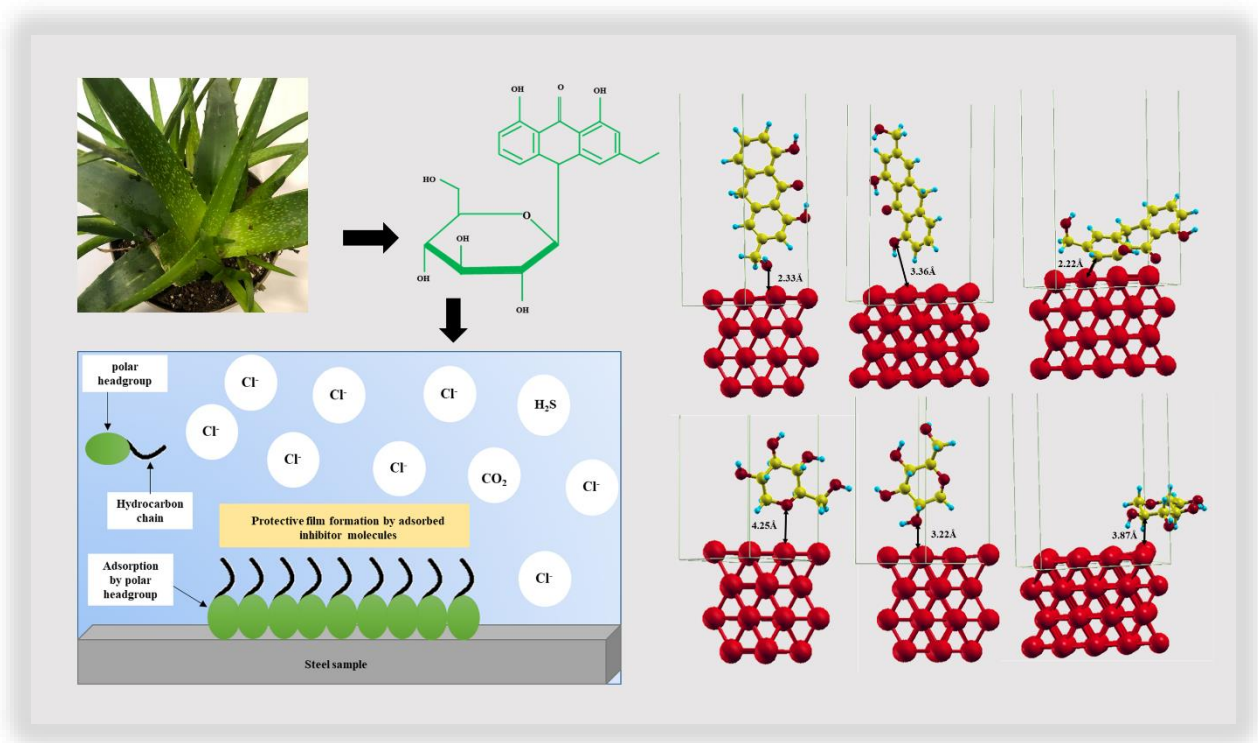
(Investigation of corrosion inhibition mechanisms using experimental and molecular modelling)

Shivangi Gupta



Organic and eco-friendly corrosion inhibitors for sweet and sour conditions

(Investigation of corrosion inhibition mechanisms using experimental and molecular modelling)



Shivangi Gupta

Ph.D. Thesis

Department of Mechanical Engineering

Technical University of Denmark

January 2022



Title of the thesis:

**Organic and eco-friendly corrosion inhibitors for sweet and sour conditions
(Investigation of corrosion inhibition mechanisms using experimental and
molecular modelling)**

Ph.D. student:

Shivangi Gupta

Email: Shig@mek.dtu.dk

Email: Shivangi.gupta645@gmail.com

Supervisors:

Prof. Rajan Ambat

Assoc. Prof. Martin Andersson

Section for Materials and Surface Engineering

Department of Mechanical Engineering

Technical University of Denmark (DTU)

Produktionstorvet, Building 425

2800 Kgs. Lyngby, Denmark



**“Know how to solve every problem that has
ever been solved”**

~ Richard Feynman ~

Preface

This dissertation is submitted in partial fulfilment of the requirements for obtaining the degree of Ph.D. at the Technical University of Denmark (DTU). The project was funded by Danish Hydrocarbon Research and Technology Centre (DHRTC) and carried out at the Technical University of Denmark (DTU), Department of Mechanical Engineering, Section of Materials and Surface Engineering (MTU) during the period from 1st September, 2018 until 15th January 2022. This project was supervised by Prof. Rajan Ambat, Technical University of Denmark, Department of Mechanical Engineering. As part of the Ph.D. project, molecular modelling studies were done in collaboration with Chemical Engineering Department at Technical University of Denmark. The molecular modelling was carried out under the supervision of Assoc. Prof. Martin Andersson.

Shivangi Gupta

Kogens Lyngby, 15th January 2022

Abstract

Corrosion is an issue in oil and gas industry leading to major economic losses. This thesis investigated efficacy of amines, imidazolines and aloe vera in corrosion inhibition of 1 Cr steel in CO₂ or H₂S environment. Different electrochemical techniques such as Linear Polarization Resistance (LPR), Electrochemical Impedance Spectroscopy (EIS), Potentiodynamic Sweep were used throughout this research work to follow the corrosion process. To investigate the morphologies and cross sections of the corrosion products and scales, Scanning Electron Microscopy (SEM) and Energy Dispersive X-Ray Spectroscopy (EDS) were used. In order to examine phase analysis of corrosion products, X-ray Diffraction (XRD) was used. For the chemical analysis, Fourier Transform Infrared Spectroscopy (FTIR) and X-ray Photoelectron Spectroscopy (XPS) were used. In addition, molecular modelling were used to investigate the molecular mechanisms (adsorption energy) underlying the corrosion inhibition of different inhibitor molecules. Amines, imidazolines, and aloe vera were found to be effective in corrosion inhibition of 1 Cr steel. The inhibition properties depended on different factors such as concentration of the inhibitor, pH, temperature and presence of H₂S. In pure CO₂ environment, iron carbonate (FeCO₃) is the main corrosion product at higher temperatures, which may or may not be protective against corrosion. Among the tested amines, Ethanolamine had the best corrosion inhibition efficiency. Addition of amines before FeCO₃ formation delayed the formation of FeCO₃. Among imidazolines, 2-PI had better corrosion inhibition efficiency due to the presence of the phenyl group, which provides additional site for bonding with the Fe surface facilitating its adsorption. The aloe vera led to substantially higher efficiency when used in higher concentrations (8000 ppm). In the presence of H₂S, iron sulfide (FeS) is the corrosion product, which can offer corrosion prevention; however, higher concentration of H₂S can lead to localized corrosion. Higher concentrations of H₂S also lowered the effectiveness of aloe vera. Addition of other organic molecules such as mono ethylene glycol led to greater corrosion inhibition of the inhibitors used in this thesis likely due to binding to active sites of the steel surface. The molecular modelling results confirmed the binding of the molecules to the active sites on the Fe surface explaining their corrosion inhibition mechanisms. Molecular modelling-based calculation of adsorption energy was found to be associated with the corrosion inhibition efficiency of the molecules in this thesis. Molecular modelling can therefore be a useful tool for screening inhibitor molecules and identifying those with potentially good corrosion inhibition properties.

Dansk Resume

Korrosion er problemstilling af olie- og gasindustrien, som giver store økonomiske tab. Denne afhandling undersøgte virkningsgraden af aminer, imidaxonliner og aloe vera som korrosionshæmmere for 1 Cr stål i et CO₂ eller H₂S miljø. Forskellige elektrokemiske teknikker så som Linear Polarization Resistance (LPR), Electrochemical Impedance Spectroscopy (EIS), Potentiodynamic Sweep blev anvendt gennem hele dette forskningsarbejde for at følge korrosionsprocessen. Scanning Electron Microscopy (SEM) og Energy Dispersive X-ray Spectroscopy (EDS) blev anvendt til at undersøge morfologien og tværsnittene af korrosionsprodukterne og det korroderede lag. Henholdsvis, X-ray diffraction (XRD), Fourier Transform Infrared Spectroscopy (FTIR) og X-ray Photoelectron Spectroscopy (XPS) blev anvendt til at undersøge fase- og kemiske kompositioner. Derudover, blev molekylær modellering anvendt til at undersøge de underliggende molekulære mekanismer (adsorptionsenergi) af forskellige inhibitormolekyler, som hæmmer korrosion. Aminer, imidaxonliner og miljøvenlig, grøn aloe vera viste sig at være effektive til korrosionshæmning af 1 Cr stål og deres inhibitionsegenskaber afhang af forskellige faktorer så som koncentration af inhibitoren, pH, temperatur og tilstedeværelsen af H₂S. I et rent CO₂ miljø er jernkarbonat (FeCO₃) det primære korrosionsprodukt ved højere temperaturer, som måske eller måske ikke er beskyttende mod korrosion. Blandt de testede aminer havde ethanolamin den bedste virkningsgrad af korrosionsinhibition. Tilføjelsen af aminer før formationen af FeCO₃ forsinkede formationen af FeCO₃. Blandt imidazoliner havde 2-PI bedre virkningsgrad af korrosionsinhibition grundet tilstedeværelsen af en phenylgruppe, hvilket giver yderligere lokationer for binding med jernoverfladen, som faciliterer dens adsorption. Aloe vera gav en substantielt højere virkningsgrad, når det blev anvendt i høje koncentrationer (8000 ppm). Ved tilstedeværelse af H₂S dannes jernsulfid (FeS) som korrosionsprodukt, hvilket kan yde korrosionsbeskyttelse, men høje koncentrationer af H₂S kan lede til stedvis korrosion. Højere koncentrationer af H₂S sænkede også effektiviteten af aloe vera. Tilføjelsen af andre organiske molekyler så som ethylenglykol gav den højeste korrosionsinhibition af de inhibitors anvendt i denne afhandling, sandsynligvis på grund af binding til aktive lokationer på ståloverfladen. Resultaterne af molekylær modellering bekræftede bindingen af molekylerne til de aktive lokationer på jernoverfladen, hvilket forklarer mekanismerne for deres korrosionsinhibition. Beregning af adsorptionsenergi baseret på molekylær modellering viste sig at være relateret til virkningsgraden af korrosionsinhibition af molekylerne i denne afhandling. Molekylær modellering kan derfor være et nyttigt værktøj til at screene inhibitormolekyler og identificere de molekyler med potentielt gode egenskaber som korrosionsinhibitorer.

Acknowledgments

Firstly, I would like to express my deepest gratitude to Prof. Rajan Ambat for believing in my potential and mentoring me throughout this project. Thank you for your time and valuable advice as those have helped me tremendously in my professional development and led to success of my thesis projects. I am also thankful to my co-supervisor Assoc. Prof. Martin Andersson who helped me develop skills in molecular modelling. Your one-to-one sessions and prompt feedback on my work helped me to implement molecular modelling to my Ph.D. work.

Thanks to Danish Hydrocarbon Research & Technology Centre (DHRTC) and their team members - Kitt Anita Ravnkilde and Yanina Dragomilova Ivanova for the financial and technical support.

I am grateful to Peter Westermann for always helping in acquiring chemicals, lab equipment and in his assistance in developing the H₂S laboratory. I am grateful to Lars Pedersen for preparing the steel samples for the corrosion experiments. Special thanks to Flemming Bjerg Grumsen and Niklas Brinckman for assisting me during XRD training and sample preparation for analysis.

I am very thankful to Dr. Rouhollah Yazdi for providing constructive feedback on my PhD work and to motivate me to develop manuscripts in time. I will remember support from my colleagues - Kapil Kumar Gupta and Riccardo Rizzo who were always available for healthy discussion on corrosion science and clearing my technical doubts.

I want to thank all my colleagues in the section of Materials and Surface Engineering, especially Dr. Saber Haratain for helping me with XRD analysis and Cecilie for translating my PhD abstract to Danish.

I am indebted to my parents who, despite of being miles away, have always supported me in their best way. Lastly, a special thanks to my husband Tarun for his endless patience and standing by me through thick and thin. You are my strength and being with you motivated me to finish my Ph.D. on time.

List of abbreviations

API	American Petroleum Institute
MIC	Microbiologically Influenced Corrosion
UDC	Under Deposit Corrosion
SCC	Stress Corrosion Cracking
DFT	Density Functional Theory
EIS	Electrochemical Impedance Spectroscopy
OCP	Open Circuit Potential
LPR	Linear Polarization Resistance
Cdl	Double Layer Capacitance
Cfc	Capacitance of the Film
Rct	Charge Transfer Resistance
Rpr	Pore Resistance
Rs	Solution Resistance
EDS	Energy-Dispersive X-ray Spectroscopy
SEM	Scanning Electron Microscope
XRD	X-Ray Diffraction
XPS	X-ray Photoelectron Spectroscopy
FTIR	Fourier Transform Infrared Spectroscopy
Z	Impedance
Ω	Ohm
2-PI	2-Phenyl-2-Imidazoline
2-MI	2-Methyl-2- Imidazoline
MEG	Mono Ethylene Glycol

List of publications

The following articles constitute a part of this thesis:

Shivangi Gupta, Kapil Kumar Gupta, Martin Andersson, Rouhollah Yazdi, Rajan Ambat, Electrochemical and molecular modelling studies of CO₂ corrosion inhibition characteristics of alkanolamine molecules for the protection of 1Cr steel, Corrosion Science 195 (2022) 10999. doi.org/10.1016/j.corsci.2021.109999.

Shivangi Gupta, Martin Andersson, Rajan Ambat, Electrochemical and molecular modelling studies of corrosion inhibition characteristics of Imidazolines on 1Cr steel under sweet conditions, submitted to Electrochimica Acta, 2022.

Shivangi Gupta, Martin Andersson, Rouhollah Yazdi, Rajan Ambat, CO₂ corrosion inhibition capability of an eco-friendly inhibitor containing green aloe vera plant extract on 1Cr steel: experimental and molecular modelling studies, submitted to Corrosion Science 2022.

Shivangi Gupta, Martin Andersson, Rouhollah Yazdi, Rajan Ambat, Corrosion inhibition properties of eco-friendly green inhibitors containing aloe vera plant extract on 1 Cr steel under H₂S conditions with CO₂, manuscript form to be submitted.

The Ph.D. student has authored and co-authored the following articles during the course of the Ph.D. work but do not constitute a part of this thesis:

S. Gupta, K. K. Gupta, M. Rogowska, R. Ambat, Investigation of corrosion inhibition mechanisms on mild carbon steel in Sweet conditions, Eurocorr 2019.

R. Rizzo, **S. Gupta**, M. Rogowska, R. Ambat, Corrosion of carbon steel under CO₂ conditions: effect of CaCO₃ precipitation on the stability of the FeCO₃ protective layer, Corros. Sci. (2019) 108214. doi:10.1016/j.corsci.2019.108214.

R. Rizzo, **S. Gupta**, R. Ambat, Experimental evaluation of the behaviour of L80 and L80-13Cr in different produced waters in CO₂-H₂S atmosphere, Eurocorr 2018.

R. Rizzo, **S. Gupta**, M. Rogowska, R. Ambat, Effect of CaCO₃ precipitation on the corrosion resistance of pseudo-passivated mild carbon steel, Eurocorr 2019.

Table of Contents

1. Introduction.....	15
1.1. Corrosion in oil and gas industry and corrosion inhibition.....	15
1.2. Scope of the thesis.....	16
1.3. Structure of the thesis.....	18
2. Literature review.....	21
2.1. Corrosion issues in oil and gas production tubings.....	21
2.2. Forms of corrosion in oil and gas production operations.....	21
2.3. Literature review on CO ₂ corrosion (sweet corrosion).....	27
2.3.1. Factors affecting formation of iron carbonate formation.....	30
2.4. Literature review on H ₂ S corrosion (sour corrosion).....	33
2.4.1. Factors affecting formation of iron sulfide.....	35
2.5. Corrosion control techniques for oil and gas production tubings.....	37
2.6. Inhibitor application methods.....	38
2.6.1. Continuous treatment.....	39
2.6.2. Batch treatment.....	39
2.6.3. Squeeze treatment.....	39
2.7. Corrosion inhibition mechanisms.....	40
2.8. Corrosion inhibition using inhibitors.....	40
2.8.1. Amine based inhibitor.....	41
2.8.2. Imidazoline based inhibitor.....	42
2.8.3. Green inhibitors.....	43
2.9. Molecular modelling using density functional theory (DFT).....	44
2.9.1. Introduction.....	44
2.9.2. Theoretical background.....	45
2.9.3. Materials and methods for calculations.....	46
2.10. Summary.....	48
3. Materials and methods.....	61
3.1. Material and specimen preparation.....	61

3.2. Electrochemical corrosion testing.....	62
3.2.1. Electrochemical glass cell setup.....	62
3.2.2. Electrolyte preparation.....	62
3.3. Types of inhibitors investigated.....	63
3.4. Electrochemical techniques.....	63
3.4.1. Linear Polarization Resistance and inhibitor efficiency.....	64
3.4.2. Electrochemical Impedance Spectroscopy (EIS).....	64
3.4.3. Potentiodynamic Sweep.....	65
3.5. Surface characterization and phase analysis.....	65
3.5.1. Scanning Electron Microscopy (SEM).....	65
3.5.2. X-ray Diffraction.....	65
3.5.3. X-ray Photoelectron Spectroscopy.....	66
4. Summary of the experimental chapters.....	69
5. Paper I: Electrochemical and molecular modelling studies of CO ₂ corrosion inhibition characteristics of alkanolamine molecules for the protection of 1Cr steel.....	75
6. Paper II: Electrochemical and molecular modelling studies of corrosion inhibition characteristics of Imidazolines on 1Cr steel under sweet conditions and annexure to the investigation of corrosion inhibition effects of 2-Phenyl-2-Imidazoline on 1Cr steel with CO ₂ : Effect of H ₂ S.....	93
7. Paper II: Annexure to the investigation of corrosion inhibition effects of 2-Phenyl-2-Imidazoline on 1Cr steel with CO ₂ : Effect of H ₂ S.....	119
8. Paper III: CO ₂ corrosion inhibition capability of an eco-friendly inhibitor containing green aloe vera plant extract on 1Cr steel: experimental and molecular modelling studies.....	129
9. Paper IV: Corrosion inhibition properties of eco-friendly green inhibitors containing aloe vera plant extract on 1 Cr steel under H ₂ S conditions with CO ₂	159
10. Overall discussion.....	183
10.1. Molecular modelling for screening inhibitor molecules.....	183
10.2. Inhibition studies using organic amines and Imidazoline.....	183
10.3. Eco-friendly green inhibitor.....	184
11. Overall conclusions.....	187
12. Future work.....	189

1. Introduction

1.1. Corrosion in oil and gas industry and corrosion inhibition

Oil and gas industry is a significant contributor to the economy of many nations. In Denmark, oil and gas is mainly produced from the North Sea since 1972, which has contributed significantly to the economy. The economic impact of the oil and gas industry is reflected from the exorbitant value from 1963-2014, which has been over DKK 1000 billion [1]. The oil and gas production value for recent years have been over DKK 40 billion/year [1]. Due to such high production, the Denmark has been a net exporter of oil and gas since 1997. The onshore and offshore facilities are also a major source of employment opportunities for Danish residents [1]. Due to its socioeconomic contributions, the oil and gas industry has an important role in Denmark and many other countries.

Corrosion in oil and gas industry poses serious threats to safety and causes economic burden on the industry. Corrosion and its products can account for 25% of the operational safety incidents (pipeline, production tubing explosion), 8.5% increase in capital expenditure and 11.5% increase in the lifting costs [2]. At a national level, annual corrosion cost in upstream oil and gas industry is estimated at around 1.3 billion USD and about 33% of this expense (~463 million USD) is associated with downhole corrosion and material challenges [3,4]. Clean oil production is also most important for reducing environmental impact, and therefore for sustainable oil production.

The problem of corrosion is accentuated by multiple factors – use of low carbon steel, extreme environmental conditions such as high temperature and pressure, and gases like CO₂ and H₂S that are highly corrosive in presence of water. Low carbon steel is most preferred due to its low cost and structural stability; however, it is conducive to corrosion especially in extreme conditions. In the presence of water, CO₂ and H₂S forms corrosion products such as FeCO₃ and FeS, which leads to deposition of scales on the steel surface. The corroded steel loses its structural integrity in different forms (pitting, pores, erosion, etc.), which can lead to its accidental failure. When this metal failure is unexpected and undetected, this can lead to accidents, production shutdown, and requires frequent inspections and repair. This adds substantially to the oil production costs.

Due to the significant challenges imposed by the corrosion, various mitigation techniques are used in the oil and gas industry. These techniques can be broadly categorized into 3 categories [5]:

- Corrosion Resistant Alloys
- Internal Lining/Cladding, and
- Chemical Treatments (corrosion inhibitors)

The use of corrosion inhibitors is the most preferred methods because of its low cost, ease, and the ability to prevent corrosion from inside of the production tubings. Inhibitors can be easily injected into the production tubings as shown in Fig.1.1. These inhibitors get adsorbed on the metal surface (physisorption and chemisorption), forms a protective film, and protects the underlying metal from corrosion. The commonly used corrosion inhibitors include amines and imidazolines that have been used on different metals and in different environments. Lastly, the

use of commercially synthesized corrosion inhibitors poses a risk of environmental degradation. As a result, there is a growing interest in environmentally friendly “green inhibitors”. The green inhibitors utilize naturally occurring compounds (e.g. aloe vera, banana peel, ginger extract, etc.) that have corrosion inhibition properties as many of these natural extracts have molecules with hetero atoms providing lone pair of electrons for chemical bonding to the metal surface. The mechanism of action of commercially available and green inhibitors is thought to result from heteroatoms O, N, P and S that bind to the metal surface and helps in adsorption of the inhibitor. In order to use the corrosion inhibitors effectively, the inhibitor must also be compatible with the metal surface and the expected environment conditions. Especially for oil & gas, effect of inhibitor on oil and water separation is an important factor, which depends on the partition coefficient.

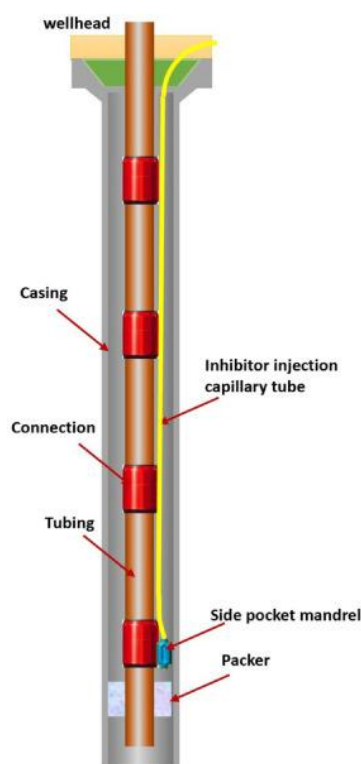


Figure 1.1. Schematic showing injection of inhibitor through the capillary tube [5].

1.2. Scope of the thesis

Although, many inhibitor chemistries are used commercially in form of organic molecules, there is still lack of understanding of the characteristics of corrosion inhibitor molecules, their adsorption to the metal surface, and corrosion inhibition properties. Firstly, there is a limited understanding on the exact inhibition properties of molecules such as amines, imidazolines etc. on the corrosion inhibition of L-80 1Cr steel in CO_2 and H_2S . In addition, the relationship between the corrosion inhibition properties and adsorption of the inhibitor molecules to the metal surface needs to be studied. Also it is not clear how the adsorption of the inhibitors to the metal surface and scale formation change the inhibition behaviour. This is an important aspect in connection with the use of inhibitor in actual practice and its consumption. In addition, adsorption is a critical mechanism for the inhibitors to work on metal surface for corrosion inhibition. Studying the adsorption properties will help in understanding the mechanisms with which these inhibitors get adsorbed on the steel surface and cause corrosion prevention. Also, effect on inhibitors on environment is a serious concern today when using commercially

available inhibitors leading to an increased demand for making oil production more environmental friendly and sustainable. Therefore, there is a need to investigate corrosion inhibition properties of environmentally friendly “green” inhibitors that offer alternative ways for corrosion prevention while offsetting the toxicity caused by commercially available inhibitors. Testing the corrosion inhibition properties of the inhibitors and identifying the underlying mechanisms is the first step towards their application in the oil and gas industry.

The overall purpose of this thesis was to combine experimental and molecular modelling techniques to investigate the corrosion inhibition properties and underlying adsorption mechanisms of inhibitor molecules. The first part of this thesis focuses on commonly used molecules (amines and imidazoline) on L-81 1Cr in CO₂ and H₂S environments, while the second part deals with corrosion inhibition properties and adsorption mechanisms of eco-friendly green inhibitor aloe vera. Various experimental techniques and molecular modelling were employed for the investigations.

This thesis has been structured into 4 studies to answer the following questions:

Objective – I: Electrochemical and molecular modelling studies of CO₂ corrosion inhibition characteristics of alkanolamine molecules for the protection of 1Cr steel.

- The effect of amine-based organic corrosion inhibitors on bare 1Cr steel at different temperatures using a combination of experimental and molecular modelling.
- Effect of amines on the pre-and post-formed FeCO₃ scale using electrochemical techniques as well as molecular modelling.
- Understanding of inhibitor injection frequency in order to elucidate the role of the application method in corrosion mitigation.

Objective - II: Electrochemical and molecular modelling studies of corrosion inhibition characteristics of Imidazoline based inhibitors on 1Cr steel in sweet conditions and annexure to the investigation of corrosion inhibition effects of 2-Phenyl-2-Imidazoline on 1Cr steel with CO₂: Effect of H₂S.

- Influence of different pendant groups attached to imidazoline on corrosion inhibition of steel using molecular modelling and experimental study.
- Effect of ethylene glycol addition on the enhancement of inhibition efficiency and related mechanisms.
- Impact of repeated doses of imidazoline to understand if the effects of degrading inhibitors can be lowered with subsequent doses.
- Effect of 2-Phenyl-2-Imidazoline on corrosion inhibition of 1Cr steel in presence of H₂S.

Objective - III: CO₂ corrosion inhibition capability of an eco-friendly inhibitor containing green aloe vera plant extract on 1Cr steel: experimental and molecular modelling studies.

- New approach for corrosion inhibition using ecofriendly green inhibitor (aloe vera) over commercial inhibitors at 40 °C.
- Effect of aloe vera extract concentration in combination with MEG to study the synergistic effect on 1 Cr steel surface at 40 °C.
- Impact of injection frequency of aloe vera on corrosion inhibition with time.

Objective - IV: Corrosion inhibition properties of eco-friendly green inhibitors containing aloe vera plant extract on 1Cr steel under H₂S conditions with CO₂.

- H₂S concentration effect on corrosion inhibition of 1Cr steel in 1% NaCl solution with and without aloe vera extract as green inhibitor and understanding of its surface morphology.
- Study the synergistic effect of addition of MEG with aloe vera extract in H₂S environment.

1.3. Structure of the thesis

The thesis is organized in 12 sections, which is shown with the help of flow chart in Fig.1.3. Chapter 1 gives the comprehensive introduction about corrosion issues in oil and gas production tubings and its inhibition together with objective of this thesis. Chapter 2 contains detailed literature review related to the topic and the prior information on CO₂ and H₂S corrosion. This chapter also includes, corrosion mitigation using different types of inhibitors and its corrosion mechanism. In addition, this chapter also gives a detailed information about adsorption studies using DFT molecular modelling. Further, chapter 3 includes material, electrochemical and characterization techniques used in this thesis. Later, chapter 4 presents summary of all experimental work and their connection with each other. The experimental work is further divided into separate chapters (5-9) under two categories - first category is “Studies on organic molecules as inhibitors” and second is “Eco-friendly green inhibitor chemistries”. Chapter 5 presents the effect of alkanolamines on corrosion inhibition of L-80 1 Cr steel in CO₂ environment with the help of electrochemical and molecular modelling studies. In addition, the effect of alkanolamines on iron carbonate scale formation was also studied. In chapter 6, the effect of different types of imidazoline inhibitor alone and in mixture with ethylene glycol was reported. Chapter 7 is annexure to chapter 6 where corrosion inhibition effects of 2-Phenyl-2-Imidazoline on 1Cr steel under H₂S conditions with CO₂ are discussed. Chapter 8 shows the new approach for corrosion inhibition of L-80 1 Cr steel in CO₂ environment using eco-friendly green inhibitor (aloe vera). In addition, the synergistic effect of MEG in combination with aloe vera extract was studied. In last experimental chapter 9, the effect of aloe vera alone and in combination with MEG at different concentration of H₂S of was studied. The latter three chapters (10-12) of this thesis include all-inclusive discussion, overall conclusion and future work respectively.

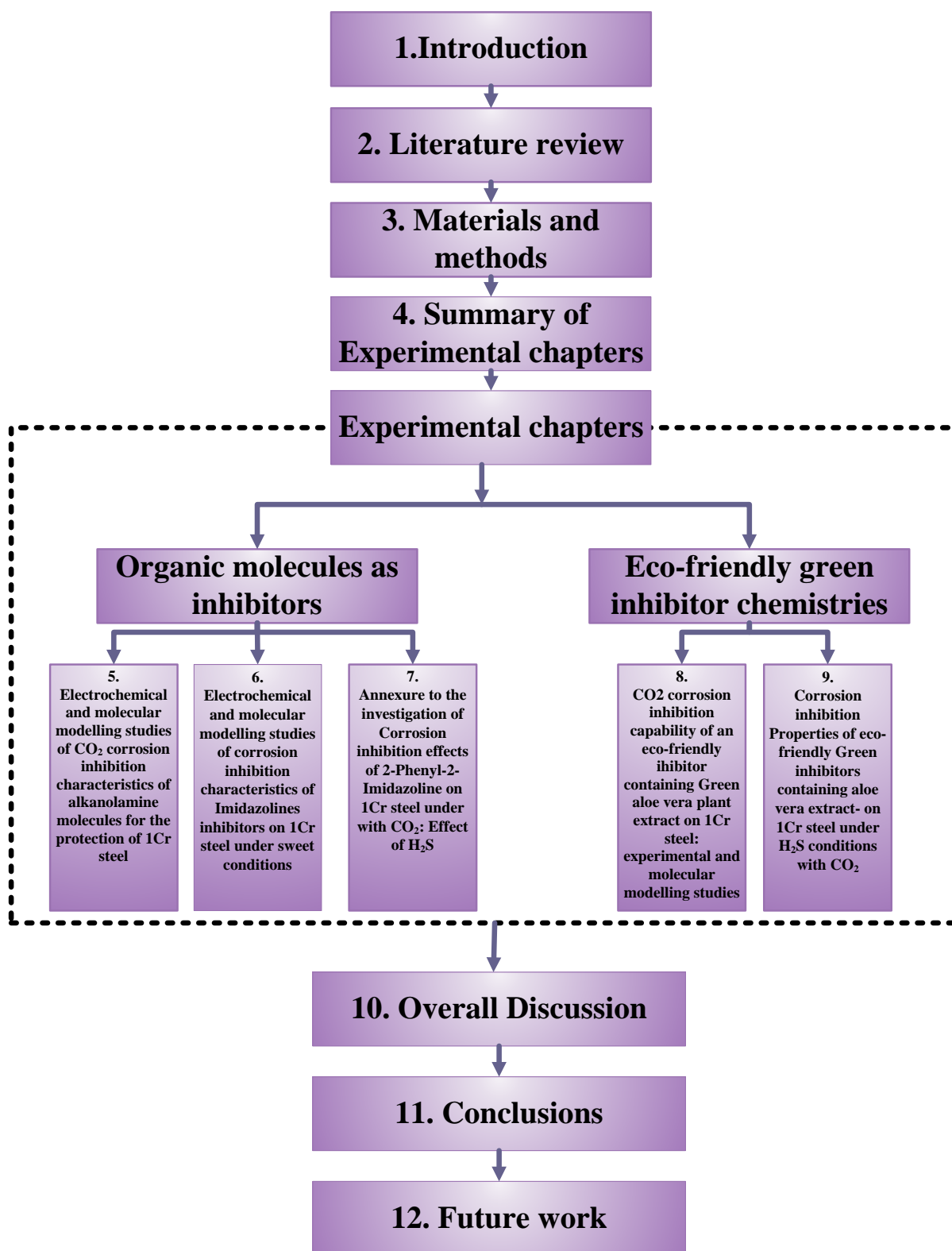


Figure 1.2. Flow chart representing the structure of the Ph.D. Thesis.



2. Literature review

2.1. Corrosion issues in oil and gas production tubings

The oil and gas industry can be viewed to have three major domains - upstream, midstream, and downstream. The upstream deals with exploration, localization, and production of crude oil and natural gas from onshore (underground) and offshore (underwater) fields. The midstream sector consists of transportation, processing, storage, and wholesale marketing of crude or refined petroleum products. The downstream sector includes refining of crude oil in refineries, generation of various petroleum products (lubricants, fertilizers, antifreeze, etc.) in petrochemical plants, and their distribution [1]. Corrosion is prevalent in all streams of oil and gas industry, is detrimental to the safety, and leads to huge expenditure.

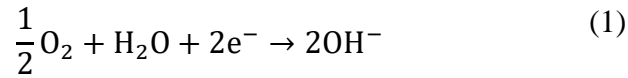
Carbon steel, due to its cost effectiveness, is the most commonly used material for oil and gas tubing. Production tubing are able to withstand operational and extreme load conditions during production as long as the production standards are met. The American Petroleum Institute (API) have published Specifications, Recommended Practices, and Bulletins (API-5CT) for steel tubing that meet the standards to be used in the oil and gas industry [2]. According to these specifications, steel grades are standardized according to the manufacturing processes, chemical content, and heat treatments, and therefore have different mechanical properties. Some of the common types of steel that are used in the oil and gas industry are Type 1Cr, 9Cr and 13Cr. Amongst these, the Type 1Cr is the most commonly used due to its lower price. The Type 1Cr steel type offers resistance to Sulfide Stress Cracking (SSC), but may suffer from uniform corrosion [3]. It is not uncommon for oil and gas tubing to be functional without any corrosion control measures for several decades as long as the environment conditions are not extreme [4]. However, in most cases due to extreme conditions imposed by the environment in oil and gas tubing, corrosion is a very serious concern impacting the operational cost. The bottom-hole temperature and pressure can rise to very high levels adding to the extreme environmental conditions. For example, the bottom-hole temperature can reach to values higher than 200 °C (~390 °F), and the pressure can rise to over 90Mpa (~13000 psi) [4]. In addition, there can be gases like CO₂ and H₂S that can accelerate the corrosion process. Lastly, water from chemical reactions and natural sources creates an environment favoring the corrosion processes [4].

2.2. Forms of corrosion in oil and gas production Operations

Corrosion in oil and gas especially for production tubing occurs usually under sweet (CO₂ corrosion) or under sour condition (H₂S). Depending on the deaeration efficiency related to different treatment, sometime oxygen related corrosion can also occur. Among the type of corrosion caused by these environments together with involved tubing alloys include uniform, or general, galvanic or two-metal, crevice, pitting, intergranular, erosion, stress, acid, under-deposit, and microbiologically influenced corrosion (MIC). Common factor for the above mentioned types of corrosion is the presence of an aqueous medium, which comes in contact with the metal surface. Corrosion under CO₂ and H₂S conditions and corrosion mechanisms are pertinent to this thesis work, therefore discussed in detail. However, a short description of other types of corrosion is provided prior to this.

1. Oxygen Corrosion

Oxygen can contribute significantly during the cathodic reaction during electrochemical process of corrosion. Due to its strong oxidative properties, it can lead to fast reduction as per the following equation [4]:



The oxygen can be introduced through drilling, leaking pump seals, casing and process vents, commonly leading to drill pipe corrosion. The presence of oxygen accelerates and substantiates the corrosive effects of CO₂ and H₂S adding to the challenge of corrosion prevention.

2. Uniform Corrosion

Uniform corrosion is a form of corrosion where the surface is removed almost evenly. The partial reactions (metal dissolution and oxygen reduction or other cathodic reactions depending on the environment) are distributed over the surface, leading to more or less homogenous dissolution of the metal and uniform formation of corrosion products (e.g. red rust on carbon steel). Uniform corrosion takes place on unprotected carbon steel (in oil and gas production when tubing is not exposed to inhibitors) under production conditions. In reality, purely homogenous corrosion attack is unlikely to take place [5], although overall it can be called as uniform corrosion.

3. Galvanic or Two-Metal Corrosion

A potential difference between the two metals when they are connected with a conductive electrolyte medium leads to a flow of current. Similarly, if two different metals (i.e. with different redox potential) are exposed to corrosive environment or solution (electrolyte), there is a flow of electron between these two metals, which can lead to corrosion. The corrosive properties of the involved metals have an influence of the Galvanic corrosion [6]. The metal with more negative potential (see Fig. 2.1) will exhibit a greater extent of galvanic corrosion. Whereas, the metal with less negative potential will demonstrate lesser corrosion than that observed when it is not in contact with the other metal. This behavior is likely because the less resistant metal becomes anodic, whereas the more resistant metal turns cathodic and the cathodic surface shown little to no corrosion. For example: in oil and gas industry galvanic corrosion usually occur in carbon steel coupled with brass or high nickel alloy as completion tools [7].

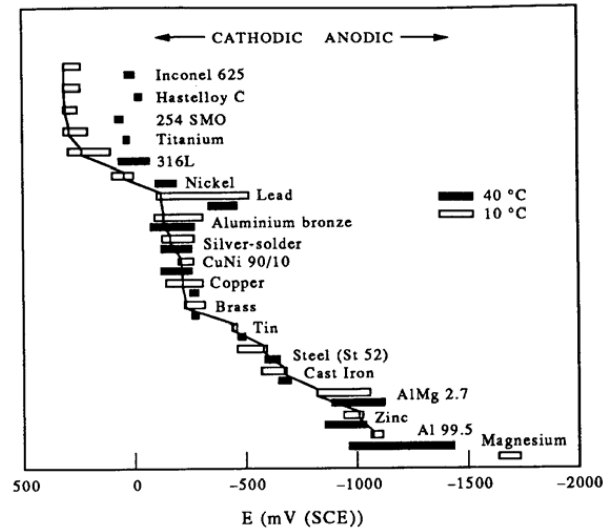


Figure 2.1. Galvanic series of different materials in seawater at 10°C and 40°C [8].

4. Crevice Corrosion

It is a form of localized corrosion typically seen within the gaps/fissures/cracks and other shielded areas on metal surfaces when exposed to a corrosive environment. This type of corrosion can occur at the contact surfaces between metal and another metal or non-metal, for example, gaskets, couplings, and joints. In this type of corrosion, the metal contact surface is exposed to small volumes of conductive solution that remains stagnant due to holes, gasket surfaces, lap joints, surface deposits, and crevices under bolt and rivet heads [6]. For example, in the oil and gas industry this type of corrosion is seen in threads of tubing (see Fig. 2.2). Another area that is vulnerable to crevice corrosion is the area between the pipe and its supports (see Fig. 2.3).



Figure 2.2. Selective attack on the internal surface at the thread juncture of the tubing and the tubing box [6].



Figure 2.3. Crevice corrosion between pipe bottom and pipe support [6].

5. Pitting

Pitting is another localized form of corrosion that can be highly destructive and deceptive. The rate of corrosion for this type can be 10-100 times that of uniform corrosion. It can lead to multiple pits or holes in the metal, which can be deceptive causing sudden and unexpected failures. These pits can be small or large, in various shapes, highly localized and isolated, or connected to each other (Fig. 2.4). Like many other forms of corrosion, the rate of pitting is influenced by several factors including diffusion, temperature, and conductivity, type of ions, pH value, and electrochemical potential [6].



Figure 2.4. Deep, round, and elongated pits at the internal surface of tubing [9].

6. Erosion corrosion

Erosion–corrosion occurs due to the relative motion between the metal and the environmental solution that is in contact with the metal causing mechanical wear leading to increase in corrosion. There is also the removal of the protective corrosion film. There can be visible grooves, gullies, waves, rounded holes, and valleys [9]. The patterns are typically directional, such as horseshoe or bullet marks or beach marks. An example of erosion–corrosion is shown in Fig. 2.5.



Figure 2.5. Changeover 3 in. \times 6 in. diameter, gas producer with 4.5% CO₂, erosion–corrosion damage on the 3 in. side [9].

7. Stress-Corrosion Cracking (SCC)

Stress-corrosion cracking (SCC) is caused by a tensile stress in the presence of a corrosive environment. The failure seen by a combination of the tensile stress and the corrosive environment would not occur in the absence of either. The failure is directly related to the amount of stress on the material such that higher stress leading to quicker cracks. The stresses can be residual (cold working, welding, surface treatment such as grinding, etc.) or applied (hydrostatic, vapor pressure of contents, bending, etc.). The failure from SCC may not necessarily results from the corrosion-related damage itself, but the pits may act as stress concentrators leading to initiation of metal cracking [6].

The most common type of SCC is sulfide stress cracking or sulfide stress corrosion cracking (SSCC), which is a commonly observed cracking mechanisms in the oil and gas industry (see Fig. 2.6). This type of cracking occurs in the presence of H₂S with a partial pressure > 0.05 psi and water. Also, the corroding material is typically under tensile stress (residual or applied) [6].



Figure 2.6. SCC attack on a pipeline section [10].

8. Under-Deposit Corrosion (UDC)

This is another common form of localized corrosion that causes failures in oil and gas operations. There is no single mechanism that explains this type of corrosion; however, the corrosion develops around or beneath the deposits (sand, elemental sulfur, wax, or corrosion products like iron carbonate) seen on the metal surface [11]. The UDC is typically a secondary form of reaction that follows a uniform or general corrosion. Although secondary to the other

forms, UDC is difficult to predict and cause extensive damages. At certain localized sites there can be deposition of chemicals (e.g. chloride) in higher quantity than that seen in the environment, which leads to UDC. Fig. 2.7 shows a simplified sequence of UDC leading to metal failure.

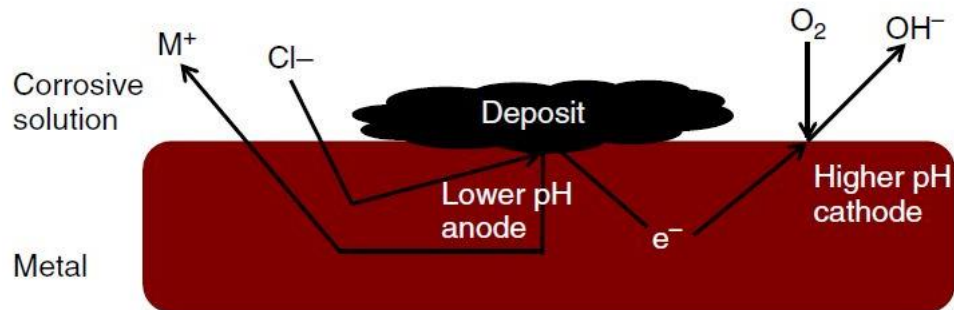


Figure 2.7. Schematics of under-deposit corrosion [9].

9. Microbiologically Induced Corrosion (MIC)

As the name suggests, this type of corrosion is induced by the bacteria that may be present in the corroding environment. The bacteria are capable of producing waste products like CO_2 , H_2S , and organic acids that adds to the toxicity of the solution leading to corrosion of the metal surface in contact with the solution [12]. In an environment conducive to bacterial growth, the microbes can form colonies exaggerating the corrosive effects (see Fig. 2.8). Different species of microbes have reported to be involved in corrosion, such as *Bacillus*, *Pseudomonas*, *Micrococcus*, *Mycobacterium*, *Clostridium*, and *Escherichia* [6,13–15]. This type of corrosion appears as black slimy waste material on the metal surface and as pitting of the pipe wall underneath these deposits.

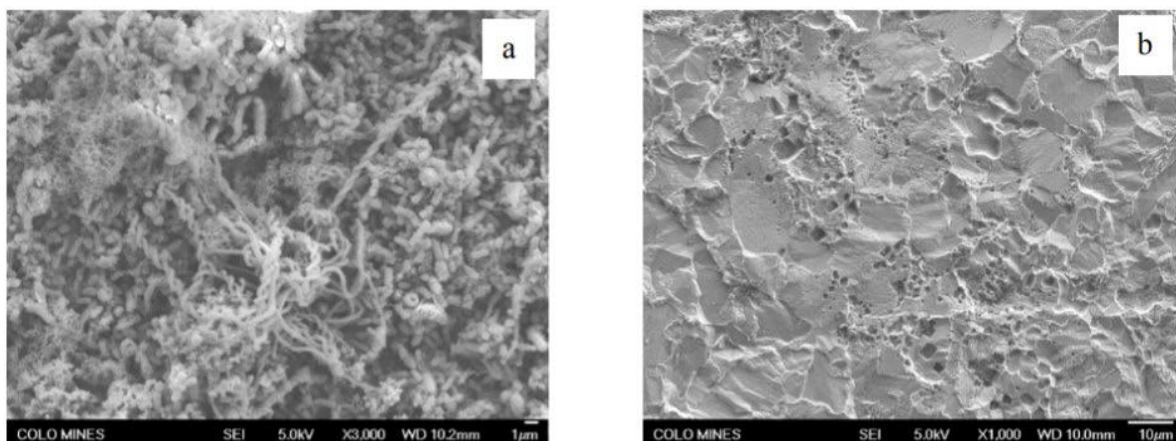


Figure 2.8. FE-SEM images (a): biofilm produced by a SRB and (b): resultant pitting of the API 5L X52 line pipe steel [16].

2.3. Literature review on CO₂ corrosion (sweet corrosion)

Carbon dioxide itself is a weak acid. However, it hydrates to form carbonic acid (H₂CO₃) and creates an acidic environment. The carbonic acid promotes an electrochemical reaction between the aqueous phase and the steel, leading to iron dissolution (see electrochemical reactions section) [17–21]. There is a formation of corrosion product i.e. iron carbonate (siderite, FeCO₃) scale on the steel surface due to its reaction with the carbonic acid depending on the temperature conditions, partial pressure of CO₂, and iron concentration. The CO₂ corrosion involves electrochemical, chemical and mass transport processes that take place on the corroding surface [22]. The current understanding of the equilibrium reactions and electrochemical processes involved in the CO₂ corrosion are discussed below:

Chemical equilibrium reactions

The following equation shows chemical equilibria related to dissolved CO₂ with corresponding equilibrium constant [23–27]. The dissolution of CO₂ in water is shown in Eq. (2). The dissolved CO₂ reacts with the water molecules and yields carbonic acid, H₂CO₃, as shown Eq. (3) [28]. The carbonic acid is a diprotic weak acid, which dissociates in two steps. In the first part of the dissociation, there is a release of bicarbonate (HCO₃⁻) and hydrogen ions (H⁺), Eq. (4) [17,28]. In the second step, the HCO₃⁻ dissociates further to release more H⁺ and carbonate (CO₃²⁻), see Eq. (5). The chemical equilibria reactions for CO₂ dissolution in pure water including water dissociation, Eq. (6) are given below [29]:

Dissolution of CO₂



Where K_{CO_2} is the proportionality constant, represented by the Henry's constant for ideal gas and solutions.

CO₂ hydration



Carbonic acid dissolution



Bicarbonate anion dissociation



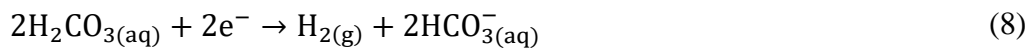
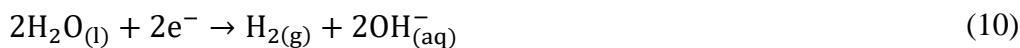
Water dissociation**Electrochemical processes**

In aqueous CO₂, the corrosion of carbon steel is an electrochemical process consisting of anodic and cathodic reactions. The following paragraphs discuss the current understanding of the cathodic and anodic reactions that take place during CO₂ corrosion on steel surface:

Cathodic reactions

There are different cathodic reactions that take place during corrosion and lead to the release of hydrogen gas i.e. “hydrogen evolution” [30–33]. The dissociation of H₂CO₃ is not direct, and takes place at the metal-solution interface. A buffer of H⁺ is created that are then reduced according to Eq. (2.6) [34,35]. These processes are influenced by the pH. For example, direct reduction of H₂CO₃, Eq. (8) contributes to the cathodic reaction at 4 < pH < 6 [36]. Another step involving HCO₃⁻ reduction Eq. (9), may be possible in less acidic conditions where pH > 6 [37]. Water reduction is shown in Eq. (10) and its contribution under typical oil & gas conditions is minimal due to its slower kinetics.

Cathodic electrochemical reactions associated with CO₂ corrosion in pure water are given below [29]:

Hydrogen reduction**Carbonic acid reduction****Bicarbonate reduction****Water reduction****Anodic reactions**

The electrochemical dissolution of iron is the main reaction that characterizes the corrosion of steel. This dominant anodic reaction involves oxidation of Fe to Fe²⁺ ions Eq. (11). The sweet corrosion is completed by this anodic reaction [38–45]. This reaction is also pH dependent.



Siderite ($FeCO_3$) precipitation

The precipitation of $FeCO_3$ is seen when the concentration of Fe^{2+} and CO_3^{2-} generated from the anodic and cathodic reactions exceed the solubility of $FeCO_3$. The thermodynamic equation for the formation of $FeCO_3$ from is shown in the Eq. (12) [20,22]:



The $FeCO_3$ forms a protective layer that can have an effect on the corrosion process. The extent of protection depends on the surface structure of the $FeCO_3$ layer and the rate of its formation. Precipitation depends on the rate of saturation, which especially, governs the saturation ratio or super-saturation Eq. (13) [46]:

$$S = \frac{a_{Fe^{2+}} + a_{CO_3^{2-}}}{K_{sp}} \quad (13)$$

Where, $a_{Fe^{2+}}$ and $a_{CO_3^{2-}}$ are the ferrous and carbonate ion activities (in mol/L) and K_{sp} is the solubility product of $FeCO_3$.

The $FeCO_3$ film formation described above depends on factors that affect the species activity (K_{sp}). For example, supersaturation value is one of such factors. Typically, $FeCO_3$ precipitation can occur at values > 1 ; however, significant precipitation is only seen at higher values of supersaturation [47,48]. Four regions of $FeCO_3$ growth have been identified on the basis of levels of supersaturation as seen in Fig. 2.9 [49].

The *Region 1* is the Dissolution characterized by a saturation level < 1 . Since the saturation level is at the sub-optimal levels, dissolution of crystals may occur leading to no crystal growth. The *Region 2* is Metastable/Seeded growth where the solubility limit is exceeded, but the growth occurs only on seed crystals.

The *Region 3* is the Heterogeneous Nucleation/Growth, nucleation is induced by foreign factors (surface roughness, defects, etc. [50].), which is subsequently followed by crystal growth.

The *Region 4* is the Homogeneous Nucleation/Growth, which takes place when the saturation level goes above and beyond the Region 3. *Region 4* is characterized by spontaneous nucleation and growth [50].

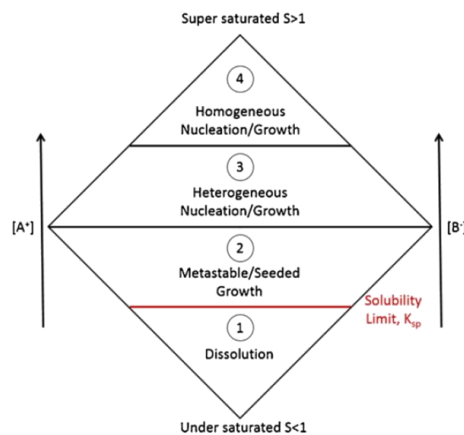


Figure 1.9. Regions of $FeCO_3$ crystal growth adapted from the work of Lasaga [48].

2.3.1. Factors affecting formation of iron carbonate formation

2.3.1.1. The effect of temperature

Experimental and modelling techniques have been utilized to study the effects of temperature on FeCO_3 solubility [51–56]. The overall consensus in the literature is that higher temperatures are conducive to faster FeCO_3 formation increasing the protectiveness, kinetics and adhesion of FeCO_3 film [29]. However, the critical temperature above which a protective FeCO_3 is formed is not clear. In the literature, a range of 50 °C to 70 °C have shown to be critical in formation of a protective FeCO_3 layer [57,58]. Increase in temperature is also thought to relate to supersaturation such that higher temperature leads to lower supersaturation (equation 14)[59]. As a result, at higher temperatures the corrosion layer can be dense and crystalline offering good protection against corrosion. However, at lower temperatures (<40 °C), a non-protective porous Fe_3C network with minimal FeCO_3 precipitation is observed.

Cross-sectional images have been used to study the morphology and protectiveness of the FeCO_3 layer on carbon steel in super-saturated solutions at different temperatures (Fig. 2.10a-c). At 40 °C and $S < 40$ (Fig. 2.10a) a non-protective porous Fe_3C network with minimal FeCO_3 precipitation is observed. At 40 °C and $S > 40$, a loose and low crystalline layer is observed (Fig. 2.10b), which does not offer much protection. At 80 °C and $S < 10$, a dense and protective layer is observed (Fig. 2.10c).

$$\text{Log}(K_{\text{SP}}) = -59.3498 - 0.041377(T_K) - \frac{2.1963}{T_K} + 24.5724 \cdot \text{Log}(T_K) \quad (14)$$

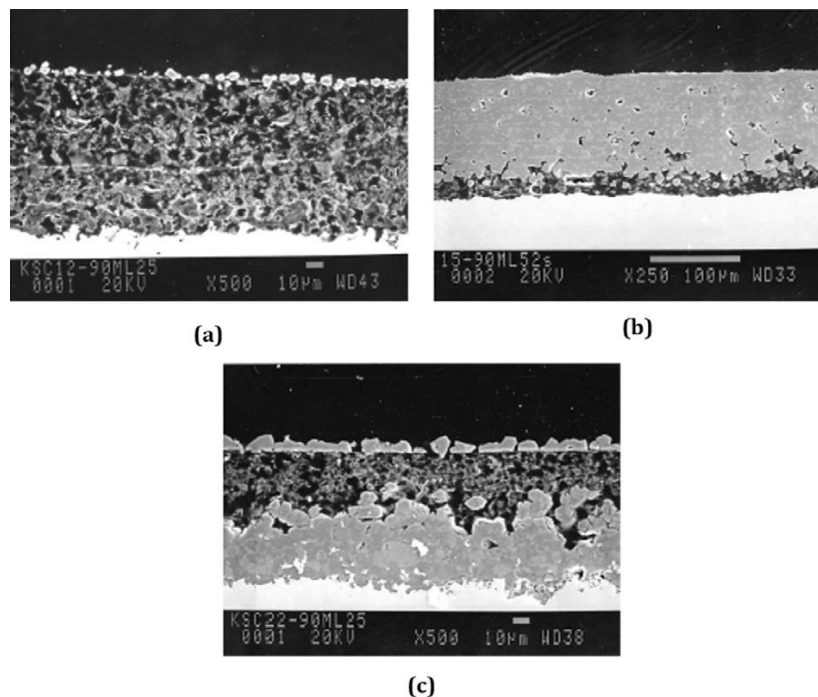


Figure 2.10. Cross sectional view of samples exposed at (a): 40 °C and $S < 40$ in the bulk solution, (b): 40 °C and $S > 40$ in bulk solution and (c): 80 °C and $S < 10$ in bulk solution [22].

2.3.1.2. The effect of pH

The pH of the solution also influences the rate of FeCO_3 precipitation [60–62]. At higher value of pH, the solubility limit of FeCO_3 is decreased requiring lesser concentration of Fe^{2+} ions for formation of FeCO_3 film [29]. At lower pH, there is an increased degradation of the iron, likely due to the presence of higher concentration of H^+ ions. A higher concentration of H^+ ions support the cathodic reactions that were discussed previously, facilitating the corrosion in the presence of CO_2 . A decrease in pH can also contribute towards increased solubility of FeCO_3 , reversing the direction of chemical processes and reversing the carbonate scale precipitation towards increased corrosion [63].

Fig. 2.11 shows an example of the association between the pH levels and the Fe^{2+} in 1 wt.% NaCl solution [22]. The higher values of pH are associated with the lower Fe^{2+} values. This can likely be due to local release of Fe^{2+} and consumption of H^+ ions during the corrosion process [27,64,65]. This results in an increase in supersaturation at the steel surface, with possible FeCO_3 precipitation on the metal surface.

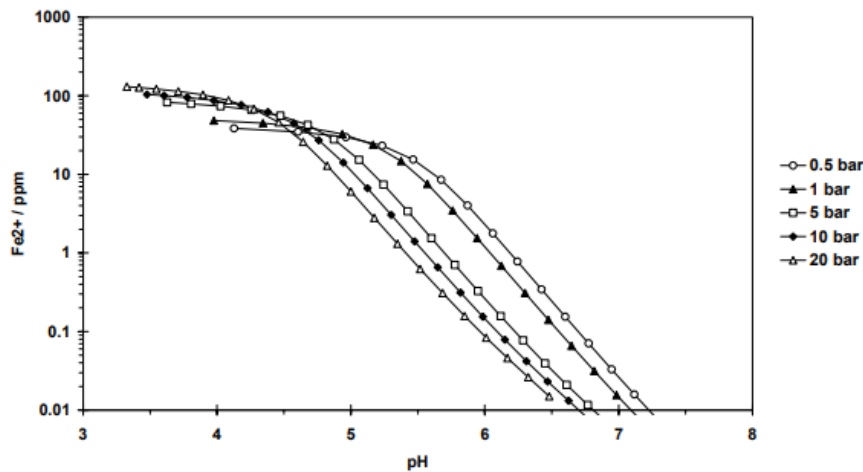


Figure 2.11. Amount of Fe^{2+} required to reach FeCO_3 saturation as function of pH in the brine [22].

The pH plays a significant role in the morphology of iron carbonate film in terms of protectiveness. The protectiveness of iron carbonate layer increases with increase in pH value. The formation of nano-polycrystalline iron carbonate film takes place at $\text{pH} = 3.6$ (see Fig. 2.12a). Whereas, at $\text{pH} = 6.6$ the nano-polycrystalline film is replaced by protective cubic crystal shaped film (see Fig. 2.12b), followed by rhombohedral crystal shaped film at $\text{pH} = 7.5$ as shown in Fig. 2.12c [66].

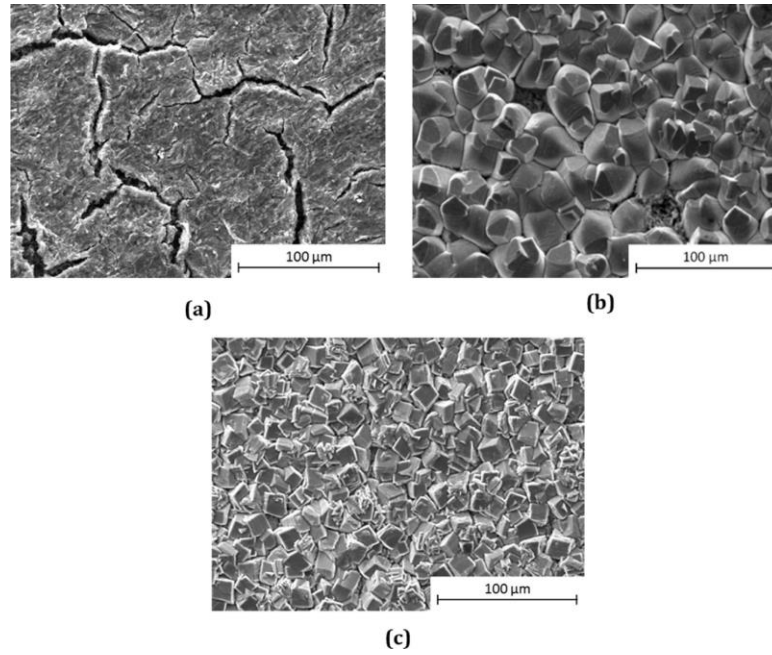


Figure 2.12. SEM images of X65 steel surfaces after exposure to a 3.5 wt.% NaCl solution at a temperature of 50 °C for 168h; (a): starting pH of 3.8 (b): pH 6.6 and (c): pH 7.5 [66].

The role of pH at different temperatures has been studied. Since lower temperatures are not favorable for FeCO₃ formation, pH of at least 6 is needed for formation of a protective FeCO₃ layer [67]. At higher temperatures (>65 °C), most protective layer is formed at pH of 6.5 [68]. These findings from the literature show that the FeCO₃ formation is dependent on the interaction between pH and temperature levels.

2.3.1.3. The effect of CO₂ partial pressure

An increase in partial pressure of CO₂ (pCO₂) has shown to result in higher corrosion rate [69]. The changes in the pH level that are associated with a change in pCO₂ are thought to contribute to changes in the corrosion rate [70,71]. A relationship between CO₂ partial pressure and solution pH was established by De Waard and Milliams [71], on the assumption of Henry's law approximation. According to Henry's law, a higher pCO₂ can lead to a greater solubility of CO₂ in the dissolved form facilitating the formation of H₂CO₃. Hence, the relation; see equation 15 [71].

$$pH = -\frac{1}{2} \log P_{CO_2} + k \quad (15)$$

Where, k incorporates Henry's constant (H) and dissociation constant (K) as $-\frac{1}{2} \log P_{CO_2} + k$.

An increase in corrosion rate can also cause an increase in concentration of Fe²⁺ and CO₃²⁻ ions leading to a supersaturated solution. Over time, depending on the other factors, the supersaturated solution can lead to increase in precipitation and FeCO₃ scale formation, which offers protection against the corrosion. Previous literature has shown that an increase in pCO₂ can accelerate the formation of FeCO₃ scale on carbon steel [72].

Videm et al. [72] in their experiments at 80 °C and pH = 5 reported that film formation on carbon steel occurred much faster when the pCO₂ was increased from 1 bar to 10 bar. However, depending on pH (more acidic condition), despite of accelerated FeCO₃ formation, there can be pitting and localized forms of corrosion [73].

2.4. Literature review on H₂S corrosion (sour corrosion)

Corrosion resulting from the presence of >10 ppm H₂S can be classified as sour corrosion. Sour corrosion is a highly prevalent problem in the oil and gas industry but is relatively an under-studied area. Natural gas, oil, and the water that is produced in the oil wells contains H₂S in the gaseous or dissolved forms. The H₂S produced during the chemical reactions react with the metal surface to form metal sulfides that precipitates over the metal surface.

Corrosion is typically seen when the H₂S partial pressures is above 0.30 kPa [8]. Based on the concentration of H₂S, four regions of corrosion (shown in Fig. 2.13) have been identified - *region 0* (trace H₂S concentration), *region 1* (H₂S slightly higher than the threshold leading to mild sour corrosion), *region 2* (higher H₂S leading to intermediate sour corrosion), and *region 3* (very high H₂S leading to severe sour corrosion with low in-situ pH value) [74,75].

Overall, the H₂S corrosion is affected by the presence of CO₂. The dominant corrosion mechanism i.e. sweet or sour corrosion, is ascertained by the ratio of the partial pressures (p) of the gases. A pCO₂: pH₂S ratio of < 20 causes H₂S dominant corrosion, whereas if the ratio > 500, then CO₂ corrosion is dominant. A ratio between 20 and 500 will lead to a mixed corrosion mechanism (sweet and sour corrosion) [74,75].

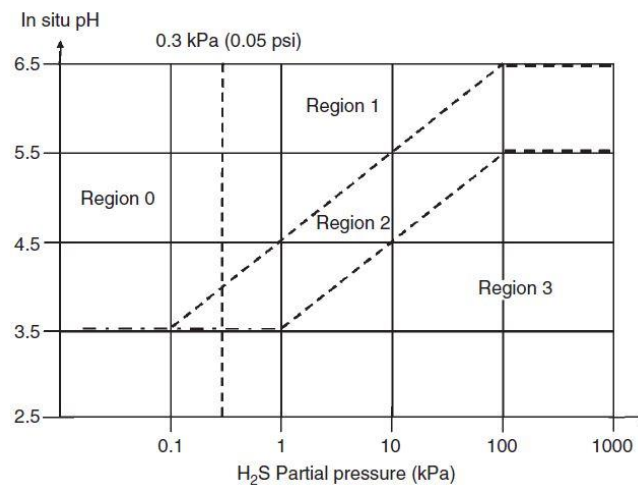


Figure 2.13. NACE MR 0175/ISO 15156 “region of service” for sour conditions [30].

The water chemistry of H₂S helps in understanding the mechanism of H₂S corrosion. The dissolution of H₂S in water leads to a vapor-liquid equilibrium as shown below [76–79]:



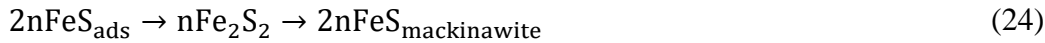
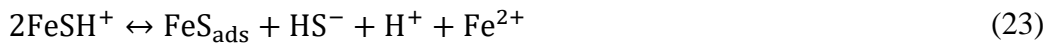
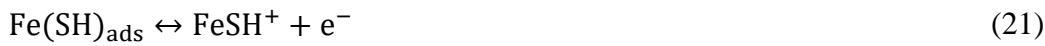
The dissolved H₂S then dissociates into bisulfide and sulfide in two steps:





Where $K_{\text{H}_2\text{S}}$ and K_i ($i=1, 2$) represented the solubility constants and ionization constants, respectively.

On the anodic site, carbon steel oxidation takes place according to the following reactions [76,80–82]:



Where $\text{FeSH}_{\text{ads}}^-$ and $\text{Fe}(\text{SH})_{\text{ads}}$ are adsorbed mesophases and FeS_{ads} is the adsorbed amorphous FeS. The hydrolysis of $\text{FeSH}_{\text{ads}}^-$ mesophase promotes the formation of Fe^{2+} .

There are a series of depolarization processes involving H_2S , H_2S^- and H^+ in the corresponding cathodic reactions (see below equations 25-27). There is reduction of the H^+ ions that are produced by the ionization of H_2S to H_2 [78]:



The overall H_2S corrosion reaction for Fe in aqueous medium is therefore given as:



The H_2S corrosion leads to formation of iron sulfide that is formed from the reaction between the steel surface and H_2S [83,84]. The formation of the iron sulfide on the metal surface controls the rate of corrosion. Upon introduction of small concentration of H_2S , a slower rate of corrosion is observed. Over time, this layer of corrosion product continues to grow until a critical level of thickness is reached. Following this, the corrosion product layer cracks due to the development of internal stresses [85]. As a result, more corrosive species such as H_2S or H^+ enter into the now porous iron sulfide layer, further corroding the metal.

There are different forms of iron sulfide that can be formed during H_2S corrosion such as mackinawite, pyrrhotite, greigite, marcasite, and pyrite. At low H_2S concentration,

mackinawite is typically the first iron sulfide corrosion product [86]. Mackinawite is a sulfur deficient iron, which is thermodynamically less stable as compared to other iron sulfide forms, such as pyrrhotite [87]. The pyrrhotite is a form of iron sulfide that is formed in lower concentration of iron with a composition range from Fe_7S_8 to FeS (which is called troilite) [88,89]. Smythite is another form of iron sulfide that is morphologically and structurally similar to Pyrrhotite and Troilite (hexagonal pyrrhotite [86]), but is even more deficient in iron. Smythite is also strongly ferromagnetic [90]. Smythite can be converted to pyrrhotite at high temperatures [86]. Mackinawite, upon reaction with sulfur can also convert to greigite, pyrite, and marcasite [86]. Greigite (Fe_3S_4) is isostructural with magnetite (Fe_3O_4) and has been identified as a corrosion product of steel in the presence of H_2S [86].

Pyrite is commonly found in corrosion products where sulfur is present in the environment. Pyrite has a cubic structure and is the most common iron sulfide because of its stable structure. Marcasite (FeS_2) is also called “white iron pyrite” as it has the same formula as Pyrite. The Marcasite structure is not very stable, so it tends to undergo transformations to other phases. Irrespective of the form, iron sulfide layer formation in the presence of H_2S decreases the corrosion rate.

In the H_2S environment, the iron sulfide layers can get partially removed leading to localized (pitting) corrosion. These regions with partially or fully removed iron sulfide layer forms active anodic and cathodic sites for localized corrosion. This localized and pitting corrosion is an understudied area concerning the oil and gas industry.

2.4.1. Factors affecting formation of iron sulfide

There are several factors which are interdependent and affects the formation of iron sulfide. These factors may include: H_2S concentration, temperature and exposure duration, metal chemistry and surface deposits (i.e. corrosion products, scales, wax, etc.), and fluid chemistry (i.e. water chemistry, pH, water cut, organic acids, phase ratios, oil wettability, etc.). Only few factors (concentration, temperature and pH) are in scope of this thesis work and are discussed further [81]:

2.4.1.1. Effect of H_2S concentration

The concentration of H_2S has a direct effect on the corrosion rate of carbon steel such that a higher concentration leads to a higher level of corrosion. This higher level of corrosion is mediated by enhancement of hydrogen evolution reaction [91]. The first layer of mackinawite film also depends on the concentration of H_2S . For example, the first layer of mackinawite film during sour corrosion is unstable for H_2S concentrations of up to 0.035 mol/l [92,93]. The breakdown of mackinawite film increases the susceptibility of carbon steel to localized and pitting corrosion.

In a $\text{CO}_2/\text{H}_2\text{S}$ coexisting environment, addition of small amount of H_2S leads to a decrease in the corrosion rate of the steel. With further increase in H_2S concentration, the protective film can even become loose and detach from the metal surface due to the higher thickness of the scale, leading to an increase in corrosion rate [94].

2.4.1.2. Effect of temperature and exposure duration

At the initial exposure to the sour environment, the corrosion rate of carbon steel increases with the rise in temperature. The increased corrosion rate with increase in temperature is thought to be mediated by different mechanisms such as decrease in solubility of gases leading to increase in pH, changes in kinetics of film formation, and rate of corrosion processes at metal – brine interface of steel [70,95]. As the exposure time increases, the effect of temperature on the corrosion process are diminished, likely due to formation of iron sulfide layer [85,91,96–98]. This also suggests that the effect of “direct” or “solid state” reactions have a stronger effect than the effect of temperature on the corrosion process. However, higher temperature along with changes in pH can lead to thermodynamic changes causing breakdown in the H₂S film causing initiation and propagation of pits in the metal surface [99–103].

2.4.1.3. Effect of pH

Like CO₂ corrosion, the sour corrosion is affected by the pH of the solution. At a given temperature and H₂S concentration, the corrosion rate generally decreases with an increase in pH [70,95]. This reduction in corrosion rate is likely due to a reduction in the number of the H⁺ ion available for reduction at cathodic sites [70,95]. In the presence of trace amounts of H₂S in CO₂ environment, the solution is under-saturated with FeCO₃ and FeS, as a result the corrosion rate decreases linearly with increase in pH, especially at lower pH (4 - 4.5) values [77]. However, with increase in H₂S concentration, there is formation of FeS on the metal surface, which significantly controls the overall corrosion behavior [77,85,101,102]. Due to the FeS layer, the further corrosion is dependent on the “solid state” or “direct reduction” reaction of H₂S and Fe and there is a reduced effect of solution saturation on the corrosion. For example, a potentiodynamic experiment was conducted at 10% H₂S concentration in H₂S-CO₂ gas mixture (shown in Fig. 2.14). From Fig. 2.14 It can be seen that the limiting current was almost the same at pH of 4 and pH of 5, which means the corrosion reaction has shown to be governed fully by the presence of H₂S gas between pH values of 4 and 5 [104,105]. However, there is a different behavior to the effect of changing the pH in a pure CO₂ corrosion environment. The thermodynamic states of the iron sulfide also depend on the pH level. At neutral pH values (~ 7), thermodynamically more stable form of iron sulfide i.e. mackinawite is formed; however, at lower pH (~4) there is a greater tendency of pyrrhotite formation reducing the stability of the iron sulfide film. By influencing the type of thermodynamic states of iron sulphide, the pH can have an impact on the integrity of the iron sulphide corrosion product layers and may lead to pitting corrosion [101–103].

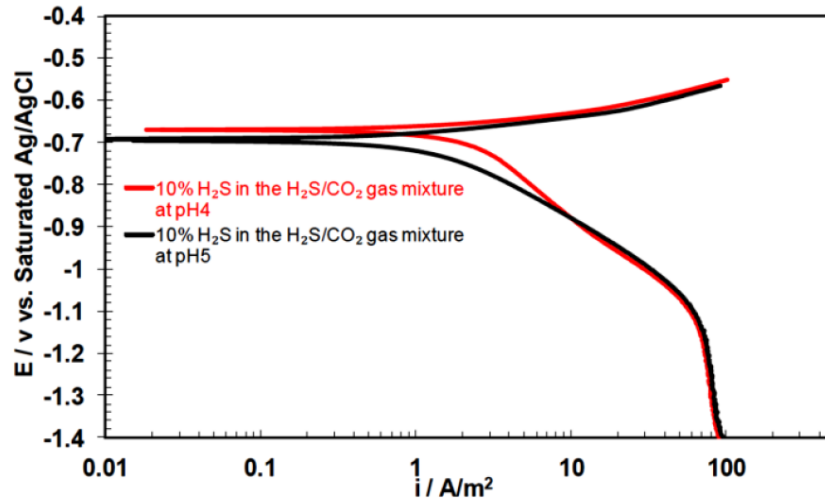


Figure 2.14. Effect of pH on potentiodynamic sweeps of mild steel corrosion in the solution purged with 10% H₂S in the CO₂-H₂S gas mixture at total pressure of 0.1MPa, 30 °C, 1wt% NaCl,1000rpm rotating speed, exposure time < 2 hours [105].

2.5. Corrosion control techniques for oil and gas production tubings

It is not uncommon for oil and gas tubing to be functional without any corrosion control measures for several decades. However, given extreme conditions in the oil wells due to the water and different chemical compounds that result from the chemical reactions, the corrosion becomes frequent and problematic. As a result, the industry has adopted several corrosion mitigation techniques that can be categorized into 3 categories – Corrosion Resistant Alloys, Internal Lining/Cladding, and Chemical Treatments (Fig. 2.15) [4].

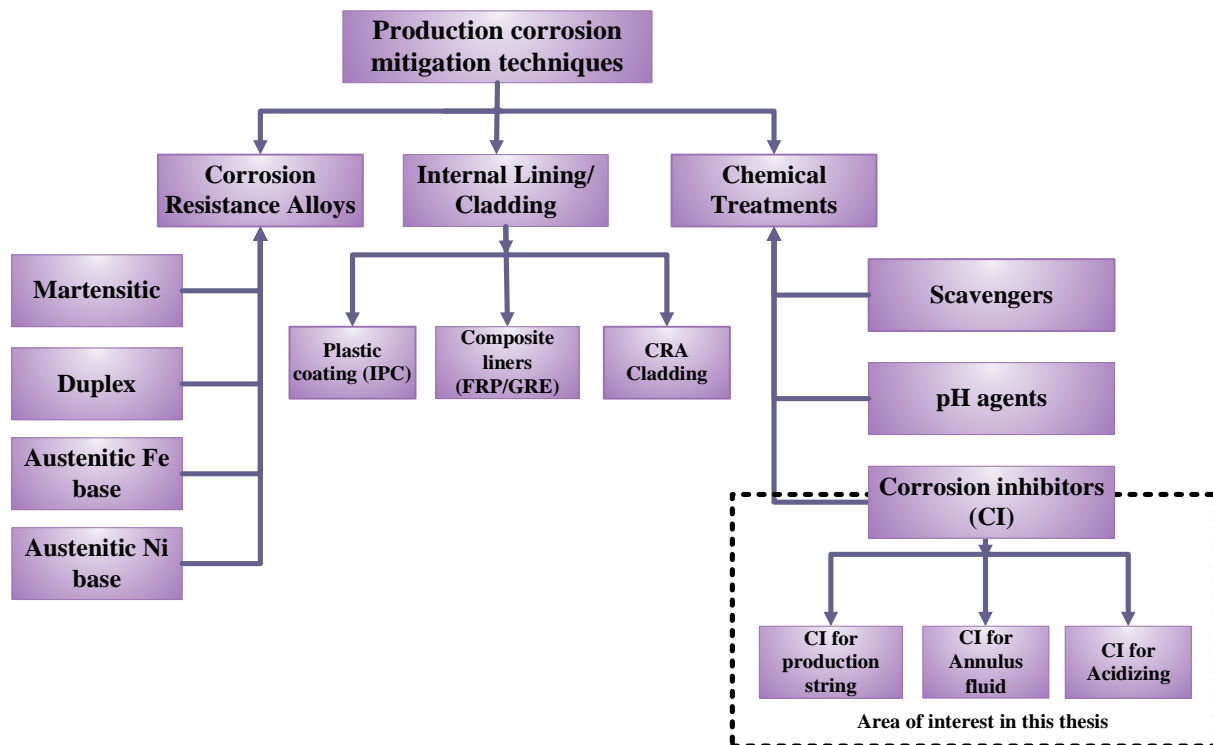


Figure 2.15. Downhole corrosion control techniques [4].

Among the available corrosion resistant alloys, low carbon steel is most commonly used in the oil and gas industry. Although, low carbon steel is preferred due to its low cost and structural integrity, it is susceptible to corrosion during oil and gas production.

Coating is another mitigation technique, but it is mainly used against external corrosion as their application requires routine maintenance [4]. When used on the internal surface of the pipelines, they are prone to damages during the process of welding/joining pipe sections [106]. Further it is very difficult for the coating to withstand the extreme conditions in the production tubing caused by the aqueous and oil phase, flow characteristics, temperature, and pressure together with CO₂ and H₂S conditions.

The use of corrosion inhibitors allows to overcome the limitations of the first two mitigation techniques. Firstly, the inhibitors offer a cheaper alternative than expensive corrosion resistant alloys. Secondly, the inhibitors can be easily injected into the production tube through capillary tubes [107]. Also, inhibitors can offer good corrosion inhibition efficiencies and can be injected frequently without any complications.

2.6. Inhibitor application methods

The application of the inhibitor should take into consideration two important factors - the initial dose, and the subsequent doses and frequency of the inhibitor. The initial dose should be of sufficient concentration to cover the entire exposed surface of the metal. Secondly, the subsequent doses of inhibitor should be able to replace the degrading inhibitor layer and should spontaneously form another layer. Below are some of the commonly used corrosion inhibitor application methods [108,109]:

2.6.1. Continuous treatment

This method is used on production wells, injection wells, pipelines, and flow lines. In this method, corrosion inhibitor is injected continuously, preferably through a small tube that runs in the annulus. Typically, water-soluble inhibitors such as quaternary amines, amine salts, or salted imidazolines are used in this form of treatment. In the process, the injected fluid converts into a sticky material that can eventually clog of the injection valve. This clogging should be avoided, especially in the case solvents have a high boiling point [109]. In addition, if due to slow injection rate, if the inhibitor remains in the annular space for too long, it can cause degradation of the inhibitory material, reduce its efficiency and can clog the valve. Table 2.1 gives the general criteria for selecting the treatment dosage.

Table 2.1. General Criteria for selecting treatment dosage [76].

Corrosion severity	Recommended dosage rate (ppm)*
Mild corrosion	10-15
Moderate corrosion	15-25
Severe corrosion	>25

*These concentrations are based on total produced fluid.

The concentration of inhibitors should be between 25 to 100 ppm [76]. At high temperatures (>150 °C), the organic chemical inhibitors may not condense on the tubing wall until they reach high up on the tubing string, therefore such inhibitors should be avoided in this method. The commonly used water-soluble inhibitors in continuous injection of water containing systems include quaternary amines, amine salts, or salted imidazolines. Alternatively, oil-soluble inhibitors include long-chain primary amines, imidazolines, fatty acids, and phosphate esters [76].

2.6.2. Batch treatment

This treatment is preferred when the continuous injection method cannot be used. Such conditions include gas wells, remote wells without power, and when the corrosion conditions are not severe [76]. This method is preferred for inhibitors that form a stable film. The disadvantage is that there can be corrosion in between the intervals between subsequent injections. In addition, there can be extensive waste of inhibitors when restarting the production. Lastly, if the operating conditions are deteriorating, the method is changed from batch to continuous, or batch along with continuous methods [110].

2.6.3. Squeeze treatment

In this method, pressure is used to pump the inhibitor into the well. The pressure is thought to help with penetration of the oil into the pores of the product formation. The frequency of the injections depend on the inhibitor in use, and nature of the product and the rate of its formation [76]. The squeeze treatment is suitable for wells with different completions. This method can lead to plugging formation, as a result there can be chemical losses leading to premature drop in corrosion inhibitor concentration [76].

2.7. Corrosion inhibition mechanisms

The corrosive inhibitive properties of the inhibitors depend on their adsorption ability on the metal surface. These adsorption results from Physisorption or Chemisorption. The electrostatic attraction resulting between the inhibitor ions and a charged metal surface causes the Physisorption [111,112]. Due to Physisorption, there is a formation of inhibitor film on the metal surface that results from the van der Waals forces [113]. This film is further stabilized by chemisorption [113]. The chemisorption results from the formation of primary bonds between the metal surface and the adsorbed molecules [114].

Once the inhibitor is adsorbed on the metal surface, it can physically limit the penetration of molecules and ions, thus preventing the corrosion. It can also block the active sites of anodic and cathodic sites to participate in corrosion reaction. The physical barrier prevents the penetration of molecules and ions. It also affects the electrochemical reactions by altering the electric double layer formed at the metal/solution interface. The inhibitors typically consist of heteroatoms such as O, N, S, and P, which binds over the metal surface and blocks the active corrosion sites [115]. The adsorption of the inhibitors on the metal surface depends on the bonds formed by these heteroatoms. In addition, the adsorption depends on physiochemical properties of the inhibitor, such as the functional groups, electron density at the donor atoms, p-orbital character, and electronic structure of the molecule [115].

Corrosion inhibitors usually contains surfactants, solvents, intensifiers, amines quaternary, acetylenic alcohols, various nitrogen-containing heterogeneous rings, and impurities [116]. Surfactants are surface-active compounds that help spreading of the corrosion inhibitor inside the acid and solvents to help with the product formulation [117]. The surfactants have excellent wetting for the metal surface [118–120], that provides them with good corrosion resistance properties [121,122]. The solvents are helpful in reducing viscosity and in enhancing the stability of the product. The intensifiers enhance the performance of other acid corrosion inhibitors in creating adequate protection against metal corrosion [123]. Typical acid corrosion inhibitors require intensifiers in extreme environmental conditions such as strong acids, high temperatures, or prolonged contact times. Although, they can accentuate the effects of acid inhibitors, the intensifiers have a high degree of toxicity causing significant environmental concerns [123].

2.8. Corrosion inhibition using inhibitors

The functional groups of commonly used corrosion inhibitors consists of one or more heteroatoms (O, N, S, P). These heteroatoms are responsible for binding the inhibitor on the metal surface. This binding of the inhibitor is crucial as this causes the adsorption of inhibitors on metal surfaces, which is the first stage of corrosion inhibition. Different type of organic/chemical compounds are used in the oil and gas industry as corrosion inhibitors. This thesis will focus on some water-soluble inhibitors that are commonly used in the oil and gas industry.

2.8.1. Amine based inhibitor

Amines are derivatives of ammonia and are commonly used for corrosion inhibition. Their structure contains nitrogen atom with an electron pair. Based on the nature and number of substituents attached to the nitrogen atom, amines can be classified as primary, secondary, and tertiary [76]. Amines are the most utilized inhibitor in the sour corrosion environment [74]. They get adsorbed on the metal surface and are less expensive than other organic inhibitors such as imidazolines and amides [124]. Amine-based inhibitors like dibutylamine and tributylamine can exhibit high corrosion inhibition efficiency, which is likely due to the presence of nitrogen heteroatom, which has high electron density and can act as the adsorption center. Also, amines with good water solubility, such as ethoxylated amines offer better corrosion inhibition [76].

Addition of other chemical compounds such as iodide can also lead to improved corrosion inhibition efficiencies as they have synergistic effects on amines mediated corrosion inhibition. Similarly, higher corrosion inhibition is observed using ethanolamine in the presence of hydrochloric acid. The improved corrosion efficiency in presence of hydrochloric acid can be due to the behavior of -OH group as electron repellent which provides high nitrogen electron density [124].

The corrosion inhibition properties of different amines have been studied on corrosion inhibition on different surfaces and in different environments. Some of these studies have been discussed here. Different amine-based inhibitors, including 2-ethylhexyl amine, aniline, benzylamine, butylamine, ethylamine, isopropylamine, octylamine, and triethanolamine were studied on C15 grade mild steel in 3 wt% NaCl solution. The effectiveness of these amines varied with the temperature and their combination with other compounds. The lowest corrosion rates were obtained for 2-ethylhexyl amine at 25 °C and triethanolamine at 70 °C. Upon addition of KI, the lowest corrosion rate at 25 °C and 70 °C was obtained for butylamine and isopropylamine, respectively. These results show that some inhibitors had synergistic effect with KI in corrosion inhibition. The corrosion inhibition properties of these inhibitors were also associated with the adsorption energy properties of these compounds of the steel surface [125].

In another study different types of amines were studied for their effect of their molecular size on the corrosion inhibition of metal and scale formation. The results showed that with increase in molecular size, the corrosion inhibition efficiencies improved. The amount of surface coverage increases with the molecular size of the inhibitor. The diethylenetriamine, triethylenetetramine, pentaethylenehexamine had corrosion inhibition efficiency values of 75%, 78%, and 92%, respectively [115].

The effects of corrosion inhibition using amine compounds have also been studied on different metal surface and environments, such as aluminium in 3 wt. % NaCl solution, saturated with CO₂. Ethanolamine was added at 20 °C and in different concentrations between 1 mM and 8 mM. The least corrosion rate and the highest inhibition efficiency was observed for 5 mM of ethanolamine. Furthermore, the corrosion inhibition effects of ethanolamine were found to be due to the adsorption mechanism, which varied with the concentration of the inhibitor. The adsorption increased up to the concentration of 5mM and then decreased at higher concentrations [126].

2.8.2. Imidazoline based inhibitor

Another form of commonly used chemical inhibitors are imidazoline-type inhibitor. Imidazolines consists of three parts: a 5-member head ring, a hydrophilic pendant chain, and a long hydrophobic hydrocarbon chain (Fig. 2.16). The two nitrogen atoms of the head ring act as its reactive sites and adsorbs on the metal through the formation of bonds with the metal atoms on the surface. The pendant chain with a hydrophilic active functional group (-R₁) acts as an anchor to the adsorbent surface [127,128]. The long hydrocarbon chain (-R₂ group) can consist of various carbon numbers and is also thought to influence the corrosion inhibition properties of the inhibitor. Imidazoline inhibitors, due to their higher adsorption energy values than the water molecules, have preferential adsorption on the metal surface in aqueous mediums [129].

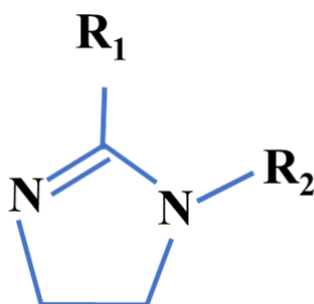


Figure 2.16. Schematic of a general imidazoline-type inhibitor.

The corrosion inhibition mechanisms of imidazolines are complex and may involve physisorption and/or chemisorption. For example, a study investigated the corrosion inhibition properties of three halogen-substituted imidazoline derivatives (1-IM, 2-IM, 3-IM) on mild steel surface in hydrochloric acid solution at 30°C-70°C. The study found limited effect of temperature on the corrosion inhibition performance of these inhibitors, such that at higher temperatures the corrosion inhibition either decreased (1-IM, 3-IM) or changed only slightly (2-IM). Based on these findings, it was suggested that these compounds were mainly physisorbed on the metal surfaces. Another study found a different type of imidazoline inhibitor (2-phenyl-2- imidazoline; 2-PI) to be effective in corrosion inhibition on AA5052 aluminum alloy in 1M HCl solution [130]. The effect of temperature on the corrosion inhibition was also studied on the corrosion inhibition properties of different imidazoline derivatives on the corrosion inhibition of aluminum in acid solutions at various temperatures (30 °C-60 °C) [131]. They found a decrease in inhibition efficiency with a rise in temperature for all the tested imidazoline derivatives suggesting the temperature may play a role at lower temperatures (<80 °C) [129].

Corrosion inhibition characteristics of a combination of 2-undecyl-1-sodium ethanoate-imidazoline salt (2M2) and thiourea (TU) was studied on the corrosion of N80 mild steel in CO₂ saturated 3 wt% NaCl solution at 25 °C, 1 bar and a pH of 4. Increase in 2M2 concentration increased the inhibition efficiency, whereas increase in TU concentration reduced the inhibition efficiency. These results suggest that the concentration of the two mixed compounds needs to be balanced optimally [132].

The corrosion inhibition properties of 2-undecyl-1-ethylamino imidazoline (2UEI) on N80 mild steel in 3% NaCl solutions saturated with CO₂ increases with an increase in 2UEI concentration or the temperature. In addition, the 2UEI shows synergistic effects with the

iodide ions [133]. The addition of iodide ions also improve the corrosion efficiency of amidoimidazoline derivative on API 5L X52 steel in 3 wt% NaCl solution which is saturated in CO₂ [134]. A concentration of 8.1×10^{-5} mol/L of Carboxyamido imidazoline works optimally for corrosion inhibition of X-70 pipeline steel in saltwater saturated with CO₂ at 50°C. Higher concentrations result in desorption from the metal surface leading to lower corrosion inhibition [135].

2.8.3. Green inhibitors

Most of the commercially used inhibitors are synthetic and may have effective corrosion inhibition properties; however, they can lead to toxicity and environmental hazards. As a result, there is growing interest in alternative plant-based inhibitors that are cleaner and do not lead to environmental toxicity. Such environment-friendly inhibitors are commonly called as “green inhibitors”.

Different extracts of natural products (e.g., plant roots, leaves, fruits, flower, etc.) are used as green inhibitors. These extracts have been used in different forms in CO₂ saturated solution in NaCl solution on different steel surfaces [136]. Although used in different concentrations, the results show low (18%) to high (99%) efficiency values. Lower efficiency values (< 30%) were observed for green extracts like *Coptis Chinensis*, *Momordica Charantia*, and Bark Tannin [137–139]. Whereas higher efficiencies (>95%) were observed for extract like *Murraya Koenigii* leave, *Chromolaena Odorata* leaves, *Tridax Procumbent* leave extract [140,141]. The stark differences in the efficiencies of these green inhibitors could be due to differences in the different molecules it contain and structure of these compounds, the concentration levels used in the studies, and other extrinsic factors like test temperatures.

Most studies have used green inhibitors in their pure form; however, few studies have combined the extract from the green inhibitors with other products like ethylene glycol and thiourea. For example, Anise extract (Fig. 2.17) in ethylene glycol in the CO₂ saturated 3wt% NaCl solution on CK 10 steel led to high corrosion efficiency values (83 - 97%) [142]. Similarly, Berberine extract in combination with thiourea in the CO₂ saturated 3wt% NaCl solution on L360 steel led to high corrosion efficiency values (73 - 88%) [143].

There are other natural inhibitors that are tested in the HCl environment and provide a high efficiency. For example, the efficiency of the extract of potato peels (PPE) to reduce the corrosion of mild steel in a 2M HCl solution, can be up to 90% [144]. Similarly, banana peel extract (BPE) can be used for corrosion inhibition of carbon steel in sea water. The main constituent of BPE is bananadine [(3Z,7Z,10Z)-1-oxa-6-azacyclododeca-3,7,10-triene], which in combination with 15 ppm can offer corrosion inhibition efficiency up to 98% [145]. In sulfide-contaminated NaCl solution, ginger extract can be used for steel corrosion inhibition such that the corrosion inhibition increases with the concentration of the extract [146].

The inhibition properties of these compounds result from the presence of heteroatoms (O, N, S, P). Fig. 2.17 shows the presence of the heteroatoms in the Anise molecule. The adsorption of the inhibitor molecules on the carbon steel surface is due to the donor – acceptor interactions. For example, the donors in these structures are π electrons of oxygen atoms and aromatic rings of inhibitors, which interact with the vacant d orbital of the acceptor iron surface atoms [147].

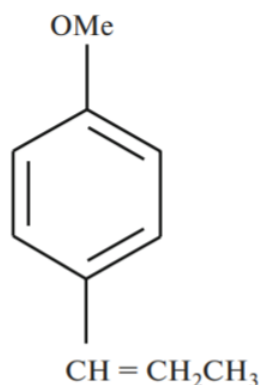


Figure 2.17. The molecular structure of main component in anise extract (transanethol) [142].

Another example is aloe vera, which is a natural product rich in several organic compounds of high molecular weight (tannins, saponins, aloin, aloe emodins) with heteroatom and π centers in their molecular structures [148–150]. Due to their good corrosion inhibition efficiencies and environment-friendly nature, the green inhibitors like aloe vera offer an excellent substitute for the synthetic inhibitors that are currently being used in the oil and gas industry. However, the corrosion inhibition properties are yet to be studied on different metals (e.g. L80-1Cr) that are commonly used in oil and gas industry. Moreover, there is a need to study the mechanisms (e.g. molecular level adsorption energies) to understand the optimal dose and working mechanisms of these inhibitors in different environments.

2.9. Molecular modelling using density functional theory (DFT)

2.9.1. Introduction

Density-functional theory (DFT) is a modelling method based on the principles of computational quantum mechanics. The DFT modelling is used to investigate the electronic structure (or nuclear structure) (principally the ground state) of many-body systems, in particular atoms, molecules, and the condensed phases. The DFT focuses on the electron density function, instead of the many-body wave function. Therefore, it overcomes the problems associated with the full-quantum mechanical computational difficulties [151]. The DFT theory can be used to determine the properties of a many-electron system using functionals, i.e. functions of another function. DFT is becoming a method of choice for condensed-matter physics, computational physics, and computational chemistry [152].

The DFT can be used for modeling of adsorption phenomena on solid surfaces. Although challenging, the investigation of adsorption of organic molecules on metals using DFT is considered enormously valuable [153]. Due to this, DFT is highly relevant in studying the mechanisms of corrosion inhibitors on metal surfaces. Studying the adsorption properties of inhibitors on metal surfaces can help in predicting the corrosion inhibition properties of different inhibitor molecules on the metal surface. The experimental methods of corrosion inhibition require greater time and resources as compared to modeling methods. Thus, this thesis will highlight how DFT can be used to study the mechanisms of corrosion inhibition in presence of different inhibitor molecules. The calculations of adsorption energy for different inhibitor molecules and differences in adsorption energy of inhibitor molecule and water on Fe

surface with and without corrosion product are shown in the respective chapters appended as journal manuscripts published or intended for publication.

2.9.2. Theoretical background

This section will focus on the theoretical background behind the electronic structure calculations. Mainly to study the adsorption process on the surfaces and its effects, one needs to understand it from atomistic view. The DFT is an appropriate tool to study the electronic structure and adsorption process from an atomistic view. The DFT was developed by Hohenberg and Kohn in 1964 [151]. According to the DFT, the ground state density of particles is considered as the “basic variable”. All other properties of the system are considered unique “*functional*” of the ground state density. A *functional* is considered as a function of *functions*. As a *function*, it is considered to map the value of a variable to a singular number, a *functional* maps the function to a singular value [154].

Visualization of a material with a full quantum-mechanical perspective requires a calculation of the many-nuclei, and many-electron wave function of that material. The nuclei have a relatively larger mass, requiring their decoupling from the electrons for a vast majority of simulations of their behavior. As a result, the nuclei may be treated as classical point-like particles (The Born-Oppenheimer approximation). Unlike nuclei, the electrons have a lower mass requiring full quantum-mechanical way for understanding their behavior. However, the computational complexity of the many-body Schrödinger equation makes the solution highly complex and beyond the current technologies for almost all material problems [153].

As mentioned earlier, the DFT considers that the total energy of the system is a unique functional of the electron density eliminating the need to compute the full many-body wave function of the system [151]. However, the challenge is that the precise functional dependence of the energy on the density is not known. The Kohn & Sham equations solve this issue of computing the ground state energy and particle density of an N-electron system using independent-particle equations [155]. These equations consist of N single-particle, 3-dimensional Schrödinger-like equations with a *modified effective potential* and are much easier to solve than the original (3N-dimensional) many-body problem. This *modified effective potential* is itself a functional of the total particle density, which follows the principle of DFT. The *modified effective potential* receives a contribution from the quantum-mechanical exchange and correlation of the particles. Although there is no expression for this exchange–correlation (XC) potential, but it is relatively small compared to the single-particle kinetic. The importance of this XC term is central to the success of DFT. The local density approximation (LDA) is the first general approximation for exchange and correlation [155]. In the LDA, the XC energy density at any position depends only on the particle density at that point. This density dependence must be identical to that of a *homogeneous* electron gas of the same density. Since this has been calculated accurately, it offers a usable approximate density functional [156,157]. An important property of any density functional is the exchange–correlation hole, the region around any particle in which the probability of finding another identical particle is reduced. The extensions to the LDA, such as the generalized-gradient approximations (GGAs), include a dependence on the local density gradient, e.g. the PW91[158], and Perdew, Becke and Ernzerhof (PBE) functionals [159]. The GGAs systematically improve the atomization or cohesive energies of hydrogen-bonded solids [160]. There are several approximations beyond the GGA; such as: (i) meta-GGAs (ii) hybrid functionals and (iii) DFT + *U*. In meta-GGAs, the Laplacian of the density, expressed as the Laplacian of the wave function is included. The

hybrid functionals includes an empirical fraction of Hartree Fock exchange to overcome the band-gap problem. The DFT+U includes Hubbard-U potential to enhance localization of electrons, to the d or f shells to improve the magnetic properties of materials [153]. Once the XC potential is finalized, the choice of basis for the single-particle wave functions needs to be determined. The Bloch's theorem can be used to express the wave function as a periodic Bloch function multiplied by a complex phase factor whose wavevector is drawn from the first Brillouin zone of the reciprocal lattice. These Brillouin zones are integrated and approximated numerically, with Bloch functions sampled on a discrete mesh of wavevectors often referred to as k-points. For metals, the abrupt change in the *occupancy* of each state with wavevector means that much denser grids are required.

The Bloch functions can be mathematically represented in the form of *basis functions*. The coefficients of these *basis functions* are the primary values used to build a computational representation. Different forms of the Bloch functions are available for the use in periodic solid-state calculations, such as plane-waves, augmented plane-waves, muffin-tin orbitals, numerical and mixed basis sets [161]. Amongst these, the plane-waves method is most used method [161,162] and has been used for this report. Each Bloch state is expressed as a Fourier series that are based on plane-waves (basis states) and reciprocal lattice vector (wave vector). The plane-waves state is thought to have advantages over the other sets, where functions are centered on atomic positions, which reflects the periodicity of an ordered material [153]. Other advantages include - efficient computing of matrix elements, orthonormal basis set, and its size is controlled by a single parameter, the cut-off energy E_{cut} . The disadvantages of the plane-waves state are: requirement of large function, higher energy cut-off, and corresponding increase in the computational cost.

2.9.3. Materials and methods for calculations

Periodic plane wave density functional theory calculations are performed using the Quantum Espresso package [163]. Electronic exchange-correlation effects were modeled within the generalized gradient approximation (GGA) by the revPBE functional [164]. The revPBE gives better atomization and adsorption energies than PBE. In all calculations, we used the projector augmented wave (PAW) method [165,166], with pseudopotentials available in the Quantum Espresso pseudopotential library [167]. The DFT does not include dispersion forces, which can be corrected using different methods. A simple method for including dispersion is by use of semiempirical corrections [168], which have proven very efficient and accurate for molecular systems. In this thesis, London dispersion corrections were included through the semiempirical DFT-D2 approach [169,170] with modified C6 parameters for ionic solids [171]. This semi-empirical approach performs well for adsorption properties of molecules on ionic solid surfaces.

The adsorption energy calculation for different types of inhibitor molecules (alkanolamines, imidazoline, aloin, etc.) were compared to water molecules for most stable surfaces such as Fe(110), FeCO₃(104) and Fe₃C (001). The comparison with water molecules is important as the inhibitors need to get adsorbed on the metal surface from an aqueous phase. Due to time limitation, only alkanolamines molecules adsorption energy values are calculated on FeCO₃(104) and Fe₃C(001) surface.

Initially, geometry optimization calculations for the conventional bulk unit cell of Fe, Fe₃C and FeCO₃ were performed. In order to perform slab calculations on Fe(110), FeCO₃(104) and Fe₃C(001), 15-20 Å of vacuum between the material slabs was inserted. The slabs for each of

the materials consisted of four molecular layers (shown in Fig. 2.18). It was assumed that all atoms of the surface molecular layer of the material is a potential site for the adsorption of the inhibitor molecule. All atoms in the first three molecular layers of the substrate and the adsorbed molecules were allowed to relax, and the fourth molecular layer (furthest from the side of the adsorbates) was frozen during the geometry optimizations. The lattice parameters used for each material were found by optimizing the cell parameters for the corresponding bulk material, using the same pseudopotentials, exchange-correlation functional that was later used for calculating adsorption energies, in order to minimize the effects of surface strain on adsorption properties. Fe and Fe₃C are metallic and therefore the need for k-points is higher. For example, for FeCO₃(104), only the gamma point was used during geometry optimizations, for Fe(110) a $4 \times 4 \times 1$ k-point sampling was used and for Fe₃C(001) a $6 \times 6 \times 1$ k-point sampling was used.

The revPBE functional [164] with added semi-empirical dispersion corrections were employed in the DFT-D2 implementation [169,170,172]. The s6 parameter for revPBE was 1.25, and a 12 Bohr cutoff was used for Fe calculations [168]. The C6 vdw parameter for Fe and Fe₃C was set to be 159.927, the same as the noble gas in the row above, Ar, as described in [168,173]. The C6 vdw parameters for FeCO₃(104) were reduced by a factor of 33 to take into account the decreased polarizability of cations when they are bonded within an ionic material [171,174,175]. All pseudopotentials were ultrasoft (or PAW), generated using revPBE, and were taken from PS Library 0.2.5 [167,176]. The kinetic energy cutoff was 40 Ry, and the density cutoff was 400 Ry, which has been shown for similar setups to provide converged adsorption energies [174,175].

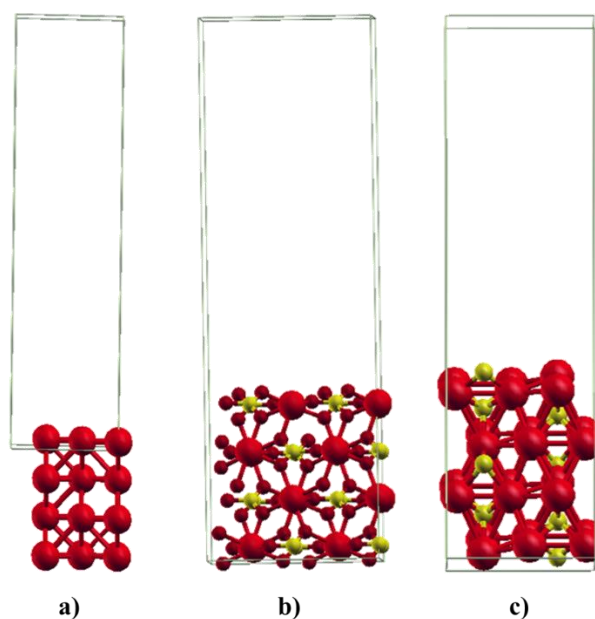


Figure 2.18. Slab with four molecular layer and vacuum for (a): Fe(110), (b): FeCO₃(104) and (c): Fe₃C(001).

In order to assess the specific molecular interaction with the model surfaces, the adsorption energy was calculated using equation (29).

$$E_{\text{adsorption}} = E_{\text{surface+inhibitor}} - (E_{\text{surface}}) - (E_{\text{inhibitor}}) \quad (29)$$

Where, E_{surface} , $E_{\text{inhibitor}}$ and $E_{\text{surface + inhibitor}}$ represent the total energies of a clean slab, a molecule, and a system with the molecule adsorbed on the slab. A negative adsorption energy determined in this way corresponds to an exothermic process and a stronger adsorption with the surface.

Accordingly, adsorption energy was determined using equation 1, for converged geometry of each structure. To find the most stable adsorption geometry for a particular molecule, calculations were made for a number of starting geometries, where the molecule was placed on the surface to promote several possible interactions between the functional group and the surface atoms.

2.10. Summary

Corrosion in oil and gas industry can lead to failures and shutdown of production, which amounts to huge economic losses and safety incidents. To help mitigate these losses, there is a need for effective corrosion inhibition strategies. The use of corrosion inhibitors is one such mitigation technique, which is cost effective and can be used on different surfaces and different environments. In addition, green alternatives of the corrosion inhibitors offer environmental-friendly ways of corrosion mitigation. Lastly, there is a limited understanding of molecular mechanisms underlying corrosion inhibition in oil and gas industry. Due to these gaps, more studies are warranted on corrosion prevention strategies using corrosion inhibitor in oil and gas industry.

In oil and gas industry, there can be extreme environment conditions. These include, the presence of sea water in production fluid, high temperature, highly acidic pH, and exposure to gases like CO_2 and H_2S . These extreme conditions make metal more susceptible to corrosion. The commonly used metal surface in oil and gas industry is carbon steel, which is more affordable and has desirable structural integrity. However, the corrosive resistance properties of carbon steel are not high enough to sustain adverse environment conditions over long periods.

Corrosion in presence of CO_2 and H_2S leads to formation of FeCO_3 and FeS corrosion products, respectively. These corrosion products form layer on the metal surface. The formation of these corrosion products also depends on the environmental factors such as temperature, pH and water chemistry. In addition, precipitation processes of corrosion products also influence the corrosion mechanism. The precipitation of the protective FeCO_3 is dependent on the temperature. At $T > 60\text{ }^\circ\text{C}$ and $\text{pH} \geq 6.5$, a protective layer of FeCO_3 is formed and can reduce significantly the corrosion rate. In case of H_2S or $\text{H}_2\text{S}/\text{CO}_2$ environment, the formation of FeS scale is dependent on the concentration of H_2S . Higher concentration of H_2S leads to a higher corrosion rate. The type of corrosion product formed as the first layer is Mackinawite film. At higher temperatures ($>90\text{ }^\circ\text{C}$), a protective FeS film is formed, which reduces the corrosion rate.

Commonly used corrosion inhibitors include amines and imidazoline derivatives. Depending on the structure and their pendent group, these inhibitors can offer high corrosion inhibition efficiencies ($>80\%$). These inhibitors also show synergistic effects with certain other compounds such as KI and ethylene glycol. The corrosion inhibition properties of these compounds result from the O, N, P, S heteroatom groups present in the inhibitors. These heteroatoms bind to the metal surface leading to adsorption of the inhibitor. The adsorption

leads for formation of inhibitor film on the metal surface, which forms the primary mechanism of corrosion inhibition.

These O, N, P, S heteroatoms are also present in the compounds that are naturally present in green inhibitors, for example, aloe emodins, aloin and tannins. These green inhibitors offer environmental friendly ways of corrosion mitigation. Over the time the corrosion inhibitors degrade and their effects are attenuated. Therefore, determining their optimal initial dosage, and frequency and dosing of the subsequent reinjections is important to maintain their corrosion inhibition properties.

Despite of extensive work on corrosion inhibition properties of inhibitors there are gaps that need to be addressed in order to progress the understanding of corrosion prevention in the oil and gas industry. There is a need for investigation of corrosion inhibition properties of amines and imidazolines on corrosion inhibition of 1 Cr steel in CO₂ environment with or without the presence of H₂S. Additionally, to limit the toxicity of chemical inhibitors, there is a need to study the effects of green inhibitors on corrosion prevention. Molecular modeling can compute the adsorption energy values and predict the corrosion behavior of various organic molecules. The knowledge of adsorption energy for different inhibitor molecules helps in understanding their affinity to bind to the metal surface and also their capacity to replace water molecules. These molecular level predictions help to understand the mechanisms of the corrosion inhibition behavior observed during experiments. In addition, the effect of these inhibitors using re-injections or in combination with other organic compounds need to be studied to understand the ways of improving corrosion inhibition efficiency of the inhibitors.

This thesis investigates the corrosion inhibition properties of amines, imidazolines, and green inhibitors on L-80 1-Cr steel in CO₂ and H₂S environments. Various electrochemical and molecular modelling techniques are utilized to study the corrosion behavior in the presence of different inhibitors and their adsorption properties (DFT molecular modeling), respectively. The inhibitors are tested in the pure form and in combination with mono-ethylene glycol to understand their synergistic effects on corrosion efficiencies. In addition, the effect of repeated injections of inhibitors is studied to understand the effect of subsequent doses on the replenishment of degrading initial doses of inhibitors. Correlating with this absorption characteristics on metal surface and corrosion scales are investigated using molecular modelling to understand relative adsorption of inhibitor molecules on metal surface and on corrosion products.

References

- [1] Y.T. Al-Janabi, An overview of corrosion in oil and gas industry: upstream, midstream, and downstream sectors, *Corros. Inhib. Oil Gas Ind.* (2020) 1–39.
- [2] A.P.I. Spec, 5CT: Specification for casing and tubing, (2001).
- [3] R. Rizzo, Investigation of oil production well corrosion issues and prevention: Role of seawater ingress on the corrosion behavior of 1Cr carbon steel used as production tubing material, (2020).
- [4] M. Askari, M. Aliofkhazraei, R. Jafari, P. Hamghalam, A. Hajizadeh, Downhole corrosion inhibitors for oil and gas production—a review, *Appl. Surf. Sci. Adv.* 6 (2021) 100128.
- [5] Satyendra, ISPAT Guru, *Corros. Carbon Steels.* (2020).
- [6] A. Bhardwaj, Fundamentals of Corrosion and Corrosion Control in Oil and Gas Sectors, *Corros. Inhib. Oil Gas Ind.* (2020) 41–76.
- [7] T. Hara, H. Asahi, H. Kaneda, Galvanic corrosion in oil and gas environments, in: *Corros.* 96, OnePetro, 1996.
- [8] E. Bardal, *Corrosion and protection*, Springer Science & Business Media, 2007.
- [9] M.M. Stack, G.H. Abdulrahman, Mapping erosion-corrosion of carbon steel in oil exploration conditions: Some new approaches to characterizing mechanisms and synergies, *Tribol. Int.* 43 (2010) 1268–1277.
- [10] L.T. Popoola, A.S. Grema, G.K. Latinwo, B. Gutti, A.S. Balogun, Corrosion problems during oil and gas production and its mitigation, *Int. J. Ind. Chem.* 4 (2013) 1–15.
- [11] H. De Reus, L.J.A. Hendriksen, M. Wilms, Y.N. Al-Habsi, W. Durnie, M. Gough, Test methodologies and field verification of corrosion inhibitors to address under deposit corrosion in oil and gas production systems, in: *Corros.* 2005, OnePetro, 2005.
- [12] C.I. Ossai, Advances in asset management techniques: An overview of corrosion mechanisms and mitigation strategies for oil and gas pipelines, *Int. Sch. Res. Not.* 2012 (2012).
- [13] P.B. Crawford, Possible reservoir damage from microbial enhanced oil recovery, in: *Proc. 1982 Int. Conf. Microb. Enhanc. Oil Recover.*, Bartlesville Energy Technology Center, Bartlesville, OK, 1983: pp. 76–79.
- [14] G.P.L. Gates, C.F. Parent, Water quality control presents challenge in giant Wilmington Field, *Oil Gas J.* 74 (1976) 115–126.
- [15] I. Lazar, P. Constantinescu, Field trials results of microbial enhanced oil recovery, *Microbes Oil Recover.* 1 (1985) 122–143.
- [16] AlAbbas, M. Faisal, “Corrosion of Linepipe Carbon Steel (API 5L X52) Influenced by A SRB Consortium Isolated From A Sour Oil Well,” *Corrosion* (2013), Paper# 2275, NACE, (n.d.).
- [17] C.D.W. and D. E.Milliams, Carbonic acid corrosion of steel, *Corrosion-NACE.* 31 (1975) 177–181.
- [18] R.H. Hausler, H.P. Gaddart, *Advances in CO₂ corrosion vol. 1*, Houston TX, 1985.
- [19] R.H. Hausler, H.P. Gaddart, *Advances in CO₂ corrosion vol. 2*, Houston TX, 1986.
- [20] A. Kahyarian, M. Achour, S. Nesic, CO₂ corrosion of mild steel, *Trends Oil Gas Corros. Res. Technol.* (2017) 149–190.
- [21] S. Nešić, Key issues related to modelling of internal corrosion of oil and gas pipelines - A review, *Corros. Sci.* 49 (2007) 4308–4338.
- [22] A. Dugstad, Fundamental aspects of CO₂ metal loss corrosion, Part I: mechanism, *Corrosion.* (2015).
- [23] Z. Duan, R. Sun, An improved model calculating CO₂ solubility in pure water and

- aqueous NaCl solutions from 273 to 533 K and from 0 to 2000 bar, *Chem. Geol.* 193 (2003) 257–271.
- [24] Z. Duan, D. Li, Coupled phase and aqueous species equilibrium of the H₂O–CO₂–NaCl–CaCO₃ system from 0 to 250 C, 1 to 1000 bar with NaCl concentrations up to saturation of halite, *Geochim. Cosmochim. Acta.* 72 (2008) 5128–5145.
- [25] Z. Duan, R. Sun, C. Zhu, I.-M. Chou, An improved model for the calculation of CO₂ solubility in aqueous solutions containing Na⁺, K⁺, Ca²⁺, Mg²⁺, Cl⁻, and SO₄²⁻, *Mar. Chem.* 98 (2006) 131–139.
- [26] D. Li, Z. Duan, The speciation equilibrium coupling with phase equilibrium in the H₂O–CO₂–NaCl system from 0 to 250 C, from 0 to 1000 bar, and from 0 to 5 molality of NaCl, *Chem. Geol.* 244 (2007) 730–751.
- [27] M. Nordsveen, S. Nešić, R. Nyborg, A. Stangeland, A mechanistic model for carbon dioxide corrosion of mild steel in the presence of protective iron carbonate films - Part 1: Theory and verification, *Corrosion.* 59 (2003) 443–456.
- [28] B.R. Linter, G.T. Burstein, Reactions of pipeline steels in carbon dioxide solutions, *Corros. Sci.* 41 (1999) 117–139.
- [29] R. Barker, D. Burkle, T. Charpentier, H. Thompson, A. Neville, A review of iron carbonate (FeCO₃) formation in the oil and gas industry, *Corros. Sci.* 142 (2018) 312–341.
- [30] J. Bockris, J. McBreen, L. Nanis, The hydrogen evolution kinetics and hydrogen entry into α -iron, *J. Electrochem. Soc.* 112 (1965) 1025.
- [31] J. Bockris, E.C. Potter, The mechanism of the cathodic hydrogen evolution reaction, *J. Electrochem. Soc.* 99 (1952) 169.
- [32] M.A. V Devanathan, Z. Stachurski, The mechanism of hydrogen evolution on iron in acid solutions by determination of permeation rates, *J. Electrochem. Soc.* 111 (1964) 619.
- [33] N. Pentland, J. Bockris, E. Sheldon, Hydrogen evolution reaction on copper, gold, molybdenum, palladium, rhodium, and iron: mechanism and measurement technique under high purity conditions, *J. Electrochem. Soc.* 104 (1957) 182.
- [34] A. Kahyarian, S. Nestic, A new narrative for CO₂ corrosion of mild steel, *J. Electrochem. Soc.* 166 (2019) C3048.
- [35] E. Remita, B. Tribollet, E. Sutter, V. Vivier, F. Ropital, J. Kittel, Hydrogen evolution in aqueous solutions containing dissolved CO₂: Quantitative contribution of the buffering effect, *Corros. Sci.* 50 (2008) 1433–1440.
- [36] R. Elgaddafi, R. Ahmed, S. Shah, Modeling and experimental studies on CO₂-H₂S corrosion of API carbon steels under high-pressure, *J. Pet. Sci. Eng.* 156 (2017) 682–696.
- [37] J. Han, J. Zhang, J.W. Carey, Effect of bicarbonate on corrosion of carbon steel in CO₂ saturated brines, *Int. J. Greenh. Gas Control.* 5 (2011) 1680–1683.
- [38] B. JO'M, D. Drazic, The kinetics of deposition and dissolution of iron: Effect of alloying impurities, *Electrochim. Acta.* 7 (1962) 293–313.
- [39] F. Hilbert, Y. Miyoshi, G. Eichkorn, W.J. Lorenz, Correlations between the kinetics of electrolytic dissolution and deposition of iron: I. The anodic dissolution of iron, *J. Electrochem. Soc.* 118 (1971) 1919.
- [40] A. Atkinson, A. Marshall, Anodic dissolution of iron in acidic chloride solutions, *Corros. Sci.* 18 (1978) 427–439.
- [41] A.A. El Miligy, D. Geana, W.J. Lorenz, A theoretical treatment of the kinetics of iron dissolution and passivation, *Electrochim. Acta.* 20 (1975) 273–281.
- [42] S. Nestic, N. Thevenot, J.L. Crolet, D. Drazic, Electrochemical properties of iron dissolution in the presence of CO₂-basics revisited, in: *Corros.* 96, OnePetro, 1996.

- [43] M. Keddam, O.R. Mattos, H. Takenouti, Reaction model for iron dissolution studied by electrode impedance: I. Experimental results and reaction model, *J. Electrochem. Soc.* 128 (1981) 257.
- [44] M. Keddam, O.R. Mattos, H. Takenouti, Reaction model for iron dissolution studied by electrode impedance: II. Determination of the reaction model, *J. Electrochem. Soc.* 128 (1981) 266.
- [45] B. JO'M, D. Drazic, A.R. Despic, The electrode kinetics of the deposition and dissolution of iron, *Electrochim. Acta.* 4 (1961) 325–361.
- [46] J. Garside, Advances in the characterization of crystal growth, in: *AIChE Symp. Ser.*, 1984: pp. 23–38.
- [47] S. Guo, L. Xu, L. Zhang, W. Chang, M. Lu, Corrosion of alloy steels containing 2% chromium in CO₂ environments, *Corros. Sci.* 63 (2012) 246–258.
- [48] A.C. Lasaga, 2. Transition State Theory, in: *Kinet. Theory Earth Sci.*, Princeton University Press, 2014: pp. 152–219.
- [49] Y. Yang, Removal mechanisms of protective iron carbonate layer in flowing solutions, (2012).
- [50] S. Nestic, Effects of multiphase flow on internal CO₂ corrosion of mild steel pipelines, *Energy & Fuels.* 26 (2012) 4098–4111.
- [51] J. Greenberg, M. Tomson, Precipitation and dissolution kinetics and equilibria of aqueous ferrous carbonate vs temperature, *Appl. Geochemistry.* 7 (1992) 185–190.
- [52] J.L. GREENBERG, High temperature kinetics of precipitation and dissolution of ferrous-carbonate, (1987).
- [53] R.D. Braun, Solubility of iron (II) carbonate at temperatures between 30 and 80, *Talanta.* 38 (1991) 205–211.
- [54] P. Benezeth, J.L. Dandurand, J.C. Harrichoury, Solubility product of siderite (FeCO₃) as a function of temperature (25? 250i; ½i; ½C), *Chem. Geol.* 265 (2009) 3–12.
- [55] W. Preis, H. Gamsjäger, Critical evaluation of solubility data: enthalpy of formation of siderite, *Phys. Chem. Chem. Phys.* 4 (2002) 4014–4019.
- [56] H.C. Helgeson, Thermodynamics of hydrothermal systems at elevated temperatures and pressures, *Am. J. Sci.* 267 (1969) 729–804.
- [57] J.K. Heuer, J.F. Stubbins, Microstructure analysis of coupons exposed to carbon dioxide corrosion in multiphase flow, *Corrosion.* 54 (1998).
- [58] M. Gopal, S. Rajappa, R. Zhang, Modeling the diffusion effects through the iron carbonate layer in the carbon dioxide corrosion of carbon steel, in: *Corros.* 98, OnePetro, 1998.
- [59] W. Sun, Kinetics of iron carbonate and iron sulfide scale formation in CO₂/H₂S corrosion, (2006).
- [60] A. Dugstad, L. Lunde, K. Videm, Influence of alloying elements upon the CO₂ corrosion rate of low alloyed carbon steels, A. Dugstad, L. Lunde, K. Videm, *Corros.* 91/473, NACE, Houston, TX. Per Copy\$ 5. (1991).
- [61] A. Dugstad, L. Lunde, K. Videm, Parametric study of CO₂ corrosion of carbon steel, NACE International, Houston, TX (United States), 1994.
- [62] M. Ueda, H. Takabe, Effect of environmental factor and microstructure on morphology of corrosion products in CO₂ environments, in: *Corros.* 99, OnePetro, 1999.
- [63] A. Dugstad, Mechanism of protective film formation during CO₂ corrosion of carbon steel, *Corrosion.* (1998) 1–11.
- [64] Y. Hua, R. Barker, T. Charpentier, M. Ward, A. Neville, Relating iron carbonate morphology to corrosion characteristics for water-saturated supercritical CO₂ systems, *J. Supercrit. Fluids.* 98 (2015) 183–193.
- [65] S. Nešić, M. Nordsveen, R. Nyborg, A. Stangeland, A mechanistic model for carbon

- dioxide corrosion of mild steel in the presence of protective iron carbonate films—part 2: a numerical experiment, *Corrosion*. 59 (2003) 489–497.
- [66] F. Pessu, R. Barker, A. Neville, The influence of pH on localized corrosion behavior of X65 carbon steel in CO₂-saturated brines, *Corrosion*. 71 (2015) 1452–1466.
- [67] E. Van Hunnik, E. Hendriksen, B.F.M. Pots, The formation of protective FeCO₃ corrosion product layers in CO₂ corrosion, in: *Corros.* 96, OnePetro, 1996.
- [68] M.H. Nazari, S.R. Allahkaram, M.B. Kermani, The effects of temperature and pH on the characteristics of corrosion product in CO₂ corrosion of grade X70 steel, *Mater. Des.* 31 (2010) 3559–3563.
- [69] S. Nestic, J. Lee, V. Ruzic, A mechanistic model of iron carbonate film growth and the effect on CO₂ corrosion of mild steel, in: *Corros.* 2002, OnePetro, 2002.
- [70] M.B. Kermani, A. Morshed, Carbon dioxide corrosion in oil and gas production—A compendium, *Corros. Sci. Eng.* 59 (2003) 659–683.
- [71] C. De Waard, D.E. Milliams, Carbonic acid corrosion of steel, *Corrosion*. 31 (1975) 177–181.
- [72] K. Videm, A. Dugstad, Film covered corrosion, film breakdown and pitting attack of carbon steels in aqueous CO₂ environments, K. Videm A. Dugstad, *Corros.* 88/186, NACE, Houston, Tx., Per Copy\$ 4. 00. (1988).
- [73] C. De Waard, U. Lotz, D.E. Milliams, Predictive model for CO₂ corrosion engineering in wet natural gas pipelines, *Corrosion*. 47 (1991) 976–985.
- [74] I.B. Obot, M.M. Solomon, S.A. Umoren, R. Suleiman, M. Elanany, N.M. Alanazi, A.A. Sorour, Progress in the development of sour corrosion inhibitors: Past, present, and future perspectives, *J. Ind. Eng. Chem.* 79 (2019) 1–18.
- [75] D.E. Milliams, D. Cottage, R.N. Tuttle, ISO 15156/NACE MR0175-A new international Standard for metallic materials for use in oil and gas production in sour environments, in: *Corros.* 2003, OnePetro, 2003.
- [76] S.A. Umoren, M.M. Solomon, V.S. Saji, Corrosion Inhibitors for Sour Oilfield Environment (H₂S Corrosion), *Corros. Inhib. Oil Gas Ind.* (2020) 229–254.
- [77] W. Sun, D. V Pugh, S.N. Smith, S. Ling, J.L. Pacheco, R.J. Franco, A Parametric Study Of Sour Corrosion Of Carbon Steela, in: *Corros.* 2010, OnePetro, 2010.
- [78] X. Wen, P. Bai, B. Luo, S. Zheng, C. Chen, Review of recent progress in the study of corrosion products of steels in a hydrogen sulphide environment, *Corros. Sci.* 139 (2018) 124–140.
- [79] G.A. Zhang, Y. Zeng, X.P. Guo, F. Jiang, D.Y. Shi, Z.Y. Chen, Electrochemical corrosion behavior of carbon steel under dynamic high pressure H₂S/CO₂ environment, *Corros. Sci.* 65 (2012) 37–47.
- [80] M.A. Lucio-Garcia, J.G. Gonzalez-Rodriguez, M. Casales, L. Martinez, J.G. Chacon-Nava, M.A. Neri-Flores, A. Martinez-Villafañe, Effect of heat treatment on H₂S corrosion of a micro-alloyed C–Mn steel, *Corros. Sci.* 51 (2009) 2380–2386.
- [81] X.L. Cheng, H.Y. Ma, J.P. Zhang, X. Chen, S.H. Chen, H.Q. Yang, Corrosion of iron in acid solutions with hydrogen sulfide, *Corrosion*. 54 (1998) 369–376.
- [82] A. Traidia, M. Alfano, G. Lubineau, S. Duval, A. Sherik, An effective finite element model for the prediction of hydrogen induced cracking in steel pipelines, *Int. J. Hydrogen Energy*. 37 (2012) 16214–16230.
- [83] D.W. Shoesmith, P. Taylor, M.G. Bailey, D.G. Owen, The formation of ferrous monosulfide polymorphs during the corrosion of iron by aqueous hydrogen sulfide at 21 C, *J. Electrochem. Soc.* 127 (1980) 1007.
- [84] D.W. Shoesmith, Formation, transformation and dissolution of phases formed on surfaces, Atomic Energy of Canada Ltd., 1983.
- [85] W. Sun, S. Nestic, A mechanistic model of H₂S corrosion of mild steel, in: *Corros.* 2007,

- OnePetro, 2007.
- [86] J.S. Smith, J.D.A. Miller, Nature of sulphides and their corrosive effect on ferrous metals: a review, *Br. Corros. J.* 10 (1975) 136–143.
- [87] R.A. Berner, Thermodynamic stability of sedimentary iron sulfides, *Am. J. Sci.* 265 (1967) 773–785.
- [88] A.D. Wadsley, *Non-stoichiometric compounds* ed. L. Mandelcorn, (1964).
- [89] R.G. Arnold, L.E. Reichen, Measurement of the metal content of naturally occurring, metal-deficient, hexagonal pyrrhotite by an X-ray spacing method, *Am. Mineral. J. Earth Planet. Mater.* 47 (1962) 105–111.
- [90] R.C. Erd, H.T. Evans Jr, D.H. Richter, Smythite, a new iron sulfide, and associated pyrrhotite from Indiana, *Am. Mineral. J. Earth Planet. Mater.* 42 (1957) 309–333.
- [91] J. Tang, Y. Shao, J. Guo, T. Zhang, G. Meng, F. Wang, The effect of H₂S concentration on the corrosion behavior of carbon steel at 90 C, *Corros. Sci.* 52 (2010) 2050–2058.
- [92] H. Taheri, S. Kakooei, M.C. Ismail, A. Dolati, The effect of H₂S concentration and temperature on corrosion behavior of pipeline steel A516-Gr70, *Casp. J. Appl. Sci. Res.* 1 (2012) 41–47.
- [93] B. Brown, S. Nesic, S.R. Parakala, CO₂ Corrosion in the Presence of Trace Amounts of H₂S, in: *Corros. 2004*, OnePetro, 2004.
- [94] D. Li, L. Zhang, J. Yang, M. Lu, J. Ding, M. Liu, Effect of H₂S concentration on the corrosion behavior of pipeline steel under the coexistence of H₂S and CO₂, *Int. J. Miner. Metall. Mater.* 21 (2014) 388–394.
- [95] K.-M. Yap, S. Srinivasan, Key factors in development of a CO₂/H₂S corrosion prediction model for multiphase oil/gas production systems, in: *Corros. 2010*, OnePetro, 2010.
- [96] Y. Zheng, J. Ning, B. Brown, S. Nešić, Advancement in predictive modeling of mild steel corrosion in CO₂-and H₂S-containing environments, *Corrosion.* 72 (2016) 679–691.
- [97] J. Ning, Investigation of polymorphous iron sulfide in H₂S corrosion of mild steel, in: *Ohio Univ. Advis. Board Meet. Ohio Univ.*, 2013.
- [98] D. Abayarathna, A.R. Naraghi, S. Wang, The effect of surface films on corrosion of carbon steel in a CO₂-H₂S-H₂O system, in: *Corros. 2005*, OnePetro, 2005.
- [99] L. Zhang, W. Zhong, J. Yang, T. Gu, X. Xiao, M. Lu, Effects of temperature and partial pressure on H₂S/CO₂ corrosion of pipeline steel in sour conditions, in: *Corros. 2011*, OnePetro, 2011.
- [100] S. Papavinasam, A. Doiron, J. Li, D.-Y. Park, P. Liu, Sour and Sweet Corrosion of Carbon Steel: General or Pitting or Localized or all of the above?, in: *Corros. 2010*, OnePetro, 2010.
- [101] S.N. Smith, B. Brown, W. Sun, Corrosion at higher H₂S concentrations and moderate temperatures, in: *Corros. 2011*, OnePetro, 2011.
- [102] S. Nešić, H. Li, J. Huang, D. Sormaz, An open source mechanistic model for CO₂/H₂S corrosion of carbon steel, in: *Corros. 2009*, OnePetro, 2009.
- [103] B. Brown, S. Nešić, Aspects of localized corrosion in an H₂S/CO₂ environment, in: *Corros. 2012*, OnePetro, 2012.
- [104] Y. Zheng, B. Brown, S. Nešić, Electrochemical study and modeling of H₂S corrosion of mild steel, *Corrosion.* 70 (2014) 351–365.
- [105] Y. Zheng, J. Ning, B. Brown, S. Nešić, Electrochemical model of mild steel corrosion in a mixed H₂S/CO₂ aqueous environment in the absence of protective corrosion product layers, *Corrosion.* 71 (2015) 316–325.
- [106] R.E. Lewis, D.K. Barbin, Selecting internal coatings for sweet oil well tubing service, in: *Corros. 99*, OnePetro, 1999.
- [107] R.E. Lewis, D.K. Barbin, Selecting Internal Coatings For Gas Well Tubulabs, in:

- Corrosion97, OnePetro, 1997.
- [108] S.A. Maksoud, D.W. Berger, Water-soluble corrosion inhibitors for downhole batch applications, (2008).
- [109] N.G. Park, L. Morello, G. Abriam, Understanding Inhibition Of Sour Systems With Water Soluble Corrosion Inhibitors, in: Corros. 2009, OnePetro, 2009.
- [110] J. Yang, V. Jovancicevic, S. Mancuso, J. Mitchell, High performance batch treating corrosion inhibitor, in: Corros. 2007, OnePetro, 2007.
- [111] G. Zhang, C. Chen, M. Lu, C. Chai, Y. Wu, Evaluation of inhibition efficiency of an imidazoline derivative in CO₂-containing aqueous solution, Mater. Chem. Phys. 105 (2007) 331–340.
- [112] L.D.L. León, M.A.V. Rodríguez, V.E.R. Cruz, S.A.P. García, A.L.L. León, Inhibition on Carbon Steel Corrosion in Presence of Hydrocarbon, Int. J. Electrochem. Sci. 6 (2011) 5134–5145.
- [113] B.G. Clubley, Chemical inhibitors for corrosion control, (1990).
- [114] R.W. Revie, Uhlig's corrosion handbook, John Wiley & Sons, 2011.
- [115] M.A. Migahed, A.A. Attia, R.E. Habib, Study on the efficiency of some amine derivatives as corrosion and scale inhibitors in cooling water systems, RSC Adv. 5 (2015) 57254–57262.
- [116] H.A. Nasr-El-Din, M. Al-Katheeri, Application of CE and CE-MS to Assay Corrosion Inhibitors Used in Well Stimulation Treatments, in: SPE Int. Symp. Oilf. Corros., OnePetro, 2005.
- [117] C.W. Crows, S.S. Minor, Acid Corrosion Inhibitor Adsorption and Its Effect on Matrix Stimulation Results, in: SPE Form. Damage Control Symp., OnePetro, 1982.
- [118] C.F. Smith, F.E. Dollarhide, N.J. Byth, Acid corrosion inhibitors-are we getting what we need?, J. Pet. Technol. 30 (1978) 737–746.
- [119] D.A. Williams, P.K. Holifield, J.R. Looney, L.A. McDougall, Method of inhibiting corrosion in acidizing wells, (1993).
- [120] D.G. Hill, H. Romijn, Reduction of Risk to the Marine Environment From Oilfield Chemicals û Environmentally Improved Acid Corrosion Inhibition for Well Stimulation, in: Corros. 2000, OnePetro, 2000.
- [121] A.A. Farag, M.R.N. El-Din, The adsorption and corrosion inhibition of some nonionic surfactants on API X65 steel surface in hydrochloric acid, Corros. Sci. 64 (2012) 174–183.
- [122] M.A. Malik, M.A. Hashim, F. Nabi, S.A. Al-Thabaiti, Z. Khan, Anti-corrosion ability of surfactants: a review, Int. J. Electrochem. Sci. 6 (2011) 1927–1948.
- [123] M.M. Brezinski, New environmental options for corrosion inhibitor intensifiers, in: SPE/EPA Explor. Prod. Environ. Conf., OnePetro, 1999.
- [124] M. Askari, M. Aliofkhazraei, S. Ghaffari, A. Hajizadeh, Film former corrosion inhibitors for oil and gas pipelines-A technical review, J. Nat. Gas Sci. Eng. 58 (2018) 92–114.
- [125] K. Khanari, N. Grah, M. Finšgar, R. Fuchs-Godec, U. Maver, Corrosion inhibition and surface analysis of amines on mild steel in chloride medium, Chem. Pap. 71 (2017) 81–89.
- [126] I. Jevremović, V. Misković-Stanković, The inhibitive effect of ethanolamine on corrosion behavior of aluminium in NaCl solution saturated with CO₂, Metall. Mater. Eng. 18 (2012) 241–257. <http://scindeks.ceon.rs/article.aspx?artid=2217-89611204241J>.
- [127] X. Zhang, F. Wang, Y. He, Y. Du, Study of the inhibition mechanism of imidazoline amide on CO₂ corrosion of Armco iron, Corros. Sci. 43 (2001) 1417–1431.
- [128] A. Edwards, C. Osborne, S. Webster, D. Klenerman, M. Joseph, P. Ostovar, M. Doyle,

- Mechanistic studies of the corrosion inhibitor oleic imidazoline, *Corros. Sci.* 36 (1994) 315–325.
- [129] Y. Ding, Mechanistic Understanding of CO₂ Corrosion Inhibition at Elevated Temperatures, (2019).
- [130] X. He, Y. Jiang, C. Li, W. Wang, B. Hou, L. Wu, Inhibition properties and adsorption behavior of imidazole and 2-phenyl-2-imidazoline on AA5052 in 1.0 M HCl solution, *Corros. Sci.* 83 (2014) 124–136.
- [131] M.A. Quraishi, M.Z.A. Rafiquee, S. Khan, N. Saxena, Corrosion inhibition of aluminium in acid solutions by some imidazoline derivatives, *J. Appl. Electrochem.* 37 (2007) 1153–1162.
- [132] P.C. Okafor, C.B. Liu, X. Liu, Y.G. Zheng, F. Wang, C.Y. Liu, Corrosion inhibition and adsorption behavior of imidazoline salt on N80 carbon steel in CO₂-saturated solutions and its synergism with thiourea, *J. Solid State Electrochem.* 14 (2010) 1367–1376.
- [133] P.C. Okafor, X. Liu, Y.G. Zheng, Corrosion inhibition of mild steel by ethylamino imidazoline derivative in CO₂-saturated solution, *Corros. Sci.* 51 (2009) 761–768.
- [134] M. Heydari, M. Javidi, Corrosion inhibition and adsorption behaviour of an amido-imidazoline derivative on API 5L X52 steel in CO₂-saturated solution and synergistic effect of iodide ions, *Corros. Sci.* 61 (2012) 148–155.
- [135] D.M. Ortega-Sotelo, J.G. Gonzalez-Rodriguez, M.A. Neri-Flores, M. Casales, L. Martinez, A. Martinez-Villafañe, CO₂ corrosion inhibition of X-70 pipeline steel by carboxyamido imidazoline, *J. Solid State Electrochem.* 15 (2011) 1997–2004.
- [136] K. Xhanari, Y. Wang, Z. Yang, M. Finšgar, A Review of Recent Advances in the Inhibition of Sweet Corrosion, *Chem. Rec.* (2021).
- [137] K.R.G. Bacca, N.F. Lopes, J.B. Marcolino, F. dos Santos Grasel, E.M. da Costa, Performance of Quebracho extract as eco-friendly corrosion inhibitor for SAE 1010 steel in the oil field environment, *Mater. Corros.* 71 (2020) 155–165.
- [138] T. Ibrahim, E. Gomes, I.B. Obot, M. Khamis, M. Abou Zour, Corrosion inhibition of mild steel by *Calotropis p. roceria* leaves extract in a CO₂ saturated sodium chloride solution, *J. Adhes. Sci. Technol.* 30 (2016) 2523–2543.
- [139] A. Singh, Y. Lin, W. Liu, E.E. Ebenso, J. Pan, Extract of *Momordica charantia* (Karela) seeds as corrosion inhibitor for P110SS steel in CO₂ saturated 3.5% NaCl solution, *Int. J. Electrochem. Sci.* 8 (2013) 812–884.
- [140] S. Aribo, S.J. Olusegun, L.J. Ibhadiyi, A. Oyetunji, D.O. Folorunso, Green inhibitors for corrosion protection in acidizing oilfield environment, *J. Assoc. Arab Univ. Basic Appl. Sci.* 24 (2017) 34–38.
- [141] S.B. Amir, N.A. Sallehudin, M.N. Azmi, H. Mohd Hussin, A.A. Rahim, H. Osman, K. Awang, P.B. Raja, *Murraya koenigii* as green corrosion inhibitor for mild steel in CO₂-saturated 3.5% NaCl medium, *Malaysian J. Chem.* 22 (2020) 25–32.
- [142] A. Peimani, M. Nasr-Esfahani, Application of Anise Extract for Corrosion Inhibition of Carbon Steel in CO₂ Saturated 3.0% NaCl Solution, *Prot. Met. Phys. Chem. Surfaces.* 54 (2018) 122–134.
- [143] J. Zhao, H. Duan, R. Jiang, Synergistic corrosion inhibition effects of coptis extract/berberine and thiourea on the corrosion of mild steel in carbon dioxide saturated brine solution, *Int. J. Electrochem. Sci.* 10 (2015) 2716–2739.
- [144] T. Ibrahim, Y. Chehade, M. Abou Zour, Corrosion inhibition of mild steel using potato peel extract in 2M HCL solution, (2011).
- [145] M. Sangeetha, S. Rajendran, J. Sathiyabama, P. Prabhakar, Eco friendly extract of Banana peel as corrosion inhibitor for carbon steel in sea water, *J Nat Prod Plant Resour.* 2 (2012) 601–610.
- [146] A.E.-A.S. Fouda, A.A. Nazeer, M. Ibrahim, M. Fakih, Ginger extract as green corrosion

- inhibitor for steel in sulfide polluted salt water, *J. Korean Chem. Soc.* 57 (2013) 272–278.
- [147] M. Stern, A.L. Geary, Electrochemical polarization: I. A theoretical analysis of the shape of polarization curves, *J. Electrochem. Soc.* 104 (1957) 56.
- [148] H. Kuzuya, I. Tamai, H. Beppu, K. Shimpo, T. Chihara, Determination of aloenin, barbaloin and isobarbaloin in Aloe species by micellar electrokinetic chromatography, *J. Chromatogr. B Biomed. Sci. Appl.* 752 (2001) 91–97.
- [149] N.O. Eddy, S.A. Odoemelam, Inhibition of corrosion of mild steel in acidic medium using ethanol extract of Aloe vera, *Pigment Resin Technol.* (2009).
- [150] A.O. James, A.O. Atela, Aloe vera: an inhibitor of aluminium corrosion in hydrochloric acid solution, *Int. J. Pure Appl. Chem.* 3 (2008) 159–163.
- [151] P. Hohenberg, W. Kohn, Inhomogeneous electron gas, *Phys. Rev.* 136 (1964) B864.
- [152] Wikipedia, Density functional theory, https://en.wikipedia.org/wiki/Density_functional_theory. (n.d.).
- [153] P.J. Hasnip, K. Refson, M.I.J. Probert, J.R. Yates, S.J. Clark, C.J. Pickard, Density functional theory in the solid state, *Philos. Trans. R. Soc. A Math. Phys. Eng. Sci.* 372 (2014) 20130270.
- [154] N. Mulakaluri, Density functional theory investigation of water adsorption on the Fe₃O₄ (001) surface, LMU, 2010.
- [155] W. Kohn, L.J. Sham, Self-consistent equations including exchange and correlation effects, *Phys. Rev.* 140 (1965) A1133.
- [156] J.P. Perdew, A. Zunger, Self-interaction correction to density-functional approximations for many-electron systems, *Phys. Rev. B.* 23 (1981) 5048.
- [157] D.M. Ceperley, B.J. Alder, Ground state of the electron gas by a stochastic method, *Phys. Rev. Lett.* 45 (1980) 566.
- [158] J.P. Perdew, Y. Wang, Accurate and simple analytic representation of the electron-gas correlation energy, *Phys. Rev. B.* 45 (1992) 13244.
- [159] J.P. Perdew, K. Burke, M. Ernzerhof, Generalized gradient approximation made simple, *Phys. Rev. Lett.* 77 (1996) 3865.
- [160] B. Winkler, V. Milman, B. Hennion, M.C. Payne, M.-H. Lee, J.S. Lin, Ab initio total energy study of brucite, diaspore and hypothetical hydrous wadsleyite, *Phys. Chem. Miner.* 22 (1995) 461–467.
- [161] R. Martin, *Electronic Structure—Basic Theory and Practical Methods*, Cambridge Univ. Pr., West Nyack, NY. (2004).
- [162] M.C. Payne, M.P. Teter, D.C. Allan, T.A. Arias, and J.D. Joannopoulos, Iterative minimization techniques for ab initio total-energy calculations: molecular dynamics and conjugate gradients, *Rev. Mod. Phys.* 64 (1992) 1045.
- [163] P. Giannozzi, S. Baroni, N. Bonini, M. Calandra, R. Car, C. Cavazzoni, D. Ceresoli, G.L. Chiarotti, M. Cococcioni, I. Dabo, A. Dal Corso, S. de Gironcoli, S. Fabris, G. Fratesi, R. Gebauer, U. Gerstmann, C. Gougoussis, A. Kokalj, M. Lazzeri, L. Martin-Samos, N. Marzari, F. Mauri, R. Mazzarello, S. Paolini, A. Pasquarello, L. Paulatto, C. Sbraccia, S. Scandolo, G. Sclauzero, A.P. Seitsonen, A. Smogunov, P. Umari, R.M. Wentzcovitch, QUANTUM ESPRESSO: a modular and open-source software project for quantum simulations of materials., *J. Phys. Condens. Matter.* (2009) 1–36.
- [164] Y. Zhang, W. Yang, Comment on “generalized gradient approximation made simple,” *Phys. Rev. Lett.* 80 (1998) 890. <https://doi.org/10.1103/PhysRevLett.80.890>.
- [165] P.E. Blöchl, Generalized separable potentials for electronic-structure calculations, *Phys. Rev. B.* 41 (1990) 5414.
- [166] G. Kresse, D. Joubert, From ultrasoft pseudopotentials to the projector augmented-wave method, *Phys. Rev. B.* 59 (1999) 1758.

-
- [167] A. Dal Corso, PSLibrary: A library of ultrasoft and PAW pseudopotentials, (2020).
- [168] M.P. Andersson, Density functional theory with modified dispersion correction for metals applied to molecular adsorption on Pt (111), *Phys. Chem. Chem. Phys.* 18 (2016) 19118–19122.
- [169] S. Grimme, Semiempirical GGA-type density functional constructed with a long-range dispersion correction, *J. Comput. Chem.* 27 (2006) 1787–1799.
- [170] V. Barone, M. Casarin, D. Forrer, M. Pavone, M. Sambri, A. Vittadini, Role and effective treatment of dispersive forces in materials: Polyethylene and graphite crystals as test cases, *J. Comput. Chem.* 30 (2009) 934–939.
- [171] S. Ehrlich, J. Moellmann, W. Reckien, T. Bredow, S. Grimme, System-dependent dispersion coefficients for the DFT-D3 treatment of adsorption processes on ionic surfaces, *ChemPhysChem*. 12 (2011) 3414–3420.
- [172] M.P. Andersson, Density Functional Theory with Modified Dispersion Correction for Metals Applied to Self-Assembled Monolayers of Thiols on Au(111), *J. Theor. Chem.* 2013 (2013) 1–9. <https://doi.org/10.1155/2013/327839>.
- [173] M.P. Andersson, Density functional theory with modified dispersion correction for metals applied to self-assembled monolayers of thiols on Au(111), *J. Theor. Chem.* 2013 (2013) 1–9.
- [174] E. Ataman, M.P. Andersson, M. Ceccato, N. Bovet, S.L.S. Stipp, Functional Group Adsorption on Calcite: I. Oxygen Containing and Nonpolar Organic Molecules, *J. Phys. Chem. C*. 120 (2016) 16586–16596.
- [175] E. Ataman, M.P. Andersson, M. Ceccato, N. Bovet, S.L.S. Stipp, Functional group adsorption on calcite: II. Nitrogen and sulfur containing organic molecules, *J. Phys. Chem. C*. 120 (2016) 16597–16607.
- [176] A. Dal Corso, Pseudopotentials periodic table: From H to Pu, *Comput. Mater. Sci.* 95 (2014) 337–350.





3. Materials and methods

This section provides an overview of the material, electrochemical method and other characterization methods, used in the thesis. Detailed description on the preparation of the natural inhibitors and experimental procedures can be found in the respective chapters added as journal manuscripts published or intended for publication.

3.1. Material and specimen preparation

The metallic material used for all the investigation in this thesis were made of a martensitic 1Cr steel (L80) in the quenched & tempered condition with a chemical composition listed in Table 3.1 and martensitic microstructure is shown in Fig. 3.1. This is one of the commonly used well tube material for Danish North Sea wells. The specimen were machined into cylinders with a diameter of 10 mm and a height of 10 mm which accounts for total surface area of 3.9 cm². The surface of the sample was mechanically polished with SiC paper grades of P220, P320, P500, and P1000 while being cooled with de-ionized water continuously. Immediately after polishing, the specimen were chemically degreased with ethanol, rinsed with de-ionized water, and then air-dried. The prepared and dried specimens were used for electrochemical experiments. At the end of the experiment, the specimens were taken out from the cell and then rinsed with de-ionized water and ethanol, dried in air, and stored in a desiccator for further characterization.

Table 3.1. Chemical composition in wt % of the L80-1 Cr material.

Material	C	Cr	Mn	Mo	P	Si	S	Fe
L-80 1 Cr (API 5CT)	0.40	1.10	0.75	0.20	≤0.035	0.20	≤0.040	base

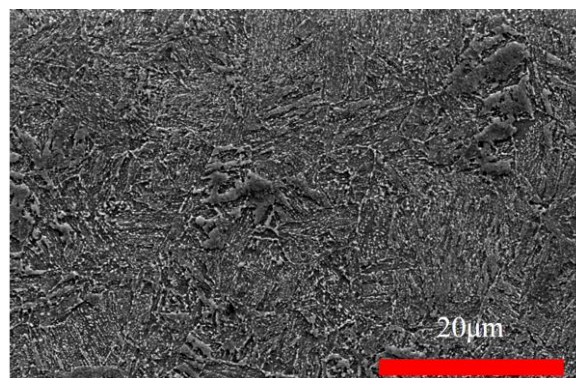


Figure 3.1. Microstructure of the 1Cr steel after etching with Nital with 2000 magnification.

3.2. Electrochemical corrosion testing

3.2.1. Electrochemical glass cell setup

The corrosion tests were carried out in an airtight 1.5 L glass cell (Fig.3.2b) using a standard three-electrode cell. An Ag/AgCl reference electrode was placed in contact with the solution through a glass-luggin capillary and a concentric platinum wire ring was used as the counter electrode. Whilst the material used for testing was placed as working electrode. A thermocouple was placed inside a glass jacket to monitor the temperature. In order to measure pH of the solution, in situ pH electrode (Mettler-Toledo InPro 3250i) was placed on the side inlet of the glass cell as shown in Fig. 3.2a.

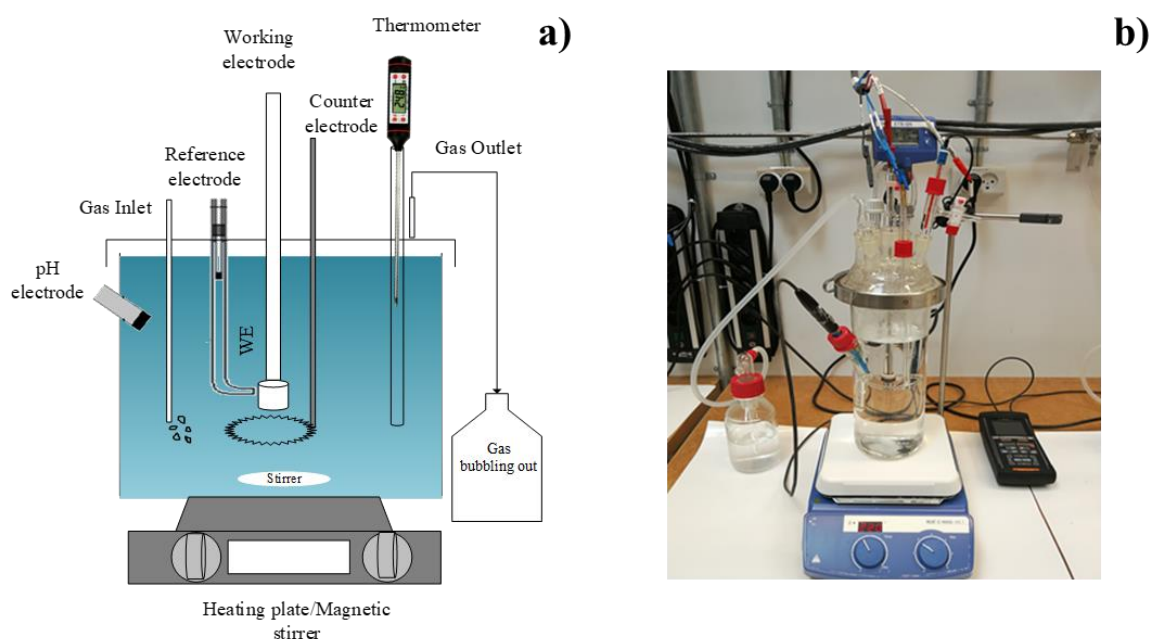


Figure 3.2. Electrochemical cell for experiments: (a) schematic of the experimental cell and (b) real corrosion cell.

3.2.2. Electrolyte preparation

All the electrochemical experiments were conducted in a CO₂-saturated 1 wt.% NaCl solution. Before immersing the specimen in the solution, the electrolyte was sparged with nitrogen for about 12 hours to deoxygenate the solution. The gas was then switched to CO₂ and bubbled for at least 4 hours in order to saturate the solution and temperature was increased. Further inhibitors were injected into the solution as required based on the experiments. Additional deaeration time was given for (at least 30 minutes) in order to remove possible trapped oxygen during the injection of inhibitors into the solution.

In another phase of this work, in order to study the effects of the inhibitors on the iron carbonate layer, NaHCO₃ was added to adjust the pH of the solution to 6.5 in order to facilitate iron carbonate precipitation. After pH adjustment, the solution was again de-aerated for at least one

hour with CO₂ gas bubbling. During testing, CO₂ gas was continuously bubbled through the solution to maintain its saturation and avoid any oxygen entrance.

3.3. Types of inhibitors investigated

In this research work, different types of inhibitors were investigated. The molecular structures of those inhibitor are shown in Fig. 3.3. For some investigations, inhibitors are tested alone (example experiments related to amine, chapter 5) and imidazoline types inhibitors were tested alone as well as in combination with ethylene glycol (Chapter 6).

For green inhibitor investigations, aloe vera extract was used as inhibitor. As discussed before in section 2.8.3 that aloe vera contains several rich organic compounds and aloin is one such compound which contributes for corrosion inhibition. Thus along with aloe vera extract, aloin was also tested for corrosion inhibition. Further, the concentrations used for different experiments are explained in the respective chapters.

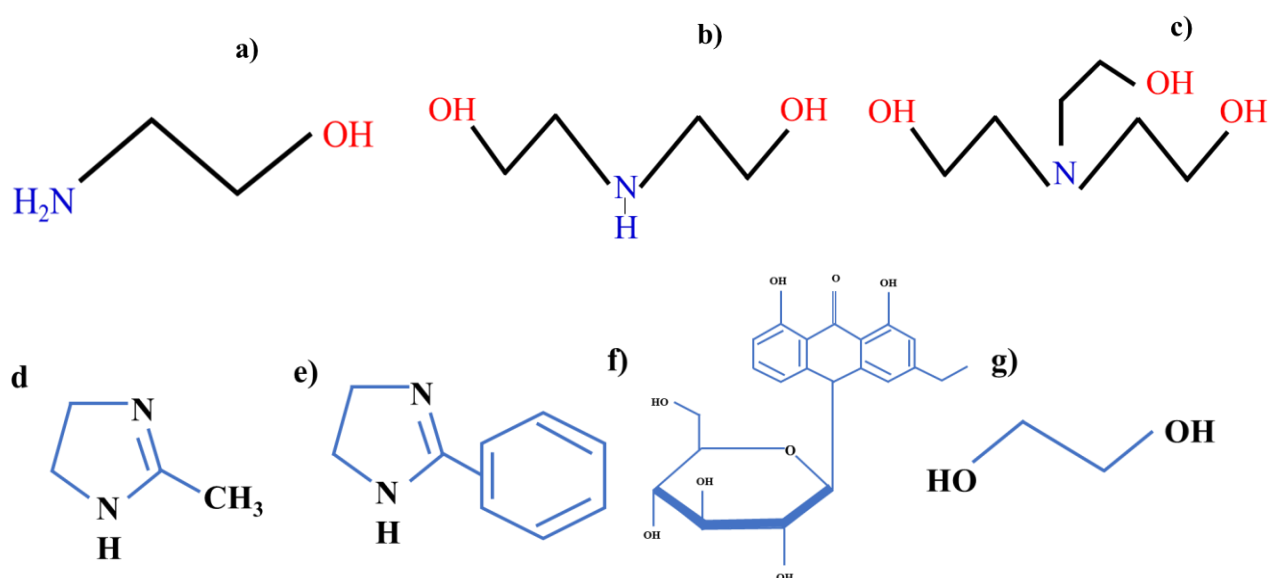


Figure 3.3. Molecular structure of used inhibitors (a) Ethanolamine, (b) Diethanolamine, (c) Triethanolamine, (d) 2-Methyl-2-imidazoline, (e) 2-Phenyl-2-imidazoline, (f) Aloin and (g) Mono ethylene glycol.

3.4. Electrochemical techniques

A Biologic VSP potentiostat was used to perform electrochemical tests. The electrochemical measurements conducted include linear polarization resistance (LPR), electrochemical impedance spectroscopy (EIS), and potentiodynamic sweeps or cyclic. The parameters chosen for each technique are described in the specific chapters. Further, data were analyzed using the EC-Lab software.

3.4.1. Linear Polarization Resistance (LPR) and inhibitor efficiency

The linear polarization resistance is an effective electrochemical technique used to measure instantaneous corrosion rate, where small potential is applied between the electrode, and the resulting current is measured. The small amplitude perturbation voltage will keep the electrochemical system under steady state condition allowing the technique to be useful for long term corrosion monitoring. Thus, the LPR technique can be used to assess the corrosion rate non-destructively.

Using linear polarization, one can obtain Polarization resistance (R_p), which is the transition resistance for the metal ions dissolution from the electrode surface to solution. Therefore, R_p is inversely proportional to corrosion rate. Using Stern Geary equation, one can convert R_p to corrosion rate if Tafel slopes for anodic and cathodic reaction is known. However, in absence of Tafel slopes, R_p can be taken as the direct measure of corrosion rate.

For work in this thesis, LPR results were obtained by polarizing the working electrode ± 10 mV versus the open circuit potential at a scan rate of 0.167 mV /s. Since the cathodic Tafel region had diffusion limited current behavior, it was difficult obtain slope value. Therefore the R_p values were reported directly as a measure of the corrosion rate.

The inhibition efficiency values are also calculated using R_p values. By using formula:

$$\text{Inhibitor efficiency (\%)} = \frac{(R_{p_{\text{uninhibited}}} - R_{p_{\text{inhibited}}})}{R_{p_{\text{uninhibited}}}} \times 100$$

3.4.2. Electrochemical Impedance Spectroscopy (EIS)

EIS has shown to be a powerful technique to understand the interfacial process happening during the inhibitor adsorption on steel surface. In the current research work, EIS is used to study protective films and scale analysis to provide information about corrosion and the protection mechanism together with inhibitor film persistency [2].

EIS experiments were carried out by applying a sinusoidal potential with an amplitude of ± 10 mV vs. OCP at a frequency range from 10 kHz to 10 mHz. The impedance response was modelled by fitting the equivalent circuit model presented in Fig. 3.4. Fig. 3.4a represents simple system when samples are tested without inhibitor (no film formation) and Fig. 3.4b represents system when samples are tested in presence of inhibitors, in which:

- R_s is the solution resistance
- R_{pr} is the pore resistance of the film layer
- C_{fc} is the film capacitance
- R_{ct} is the charge-transfer resistance
- C_{dl} is the double layer capacitance

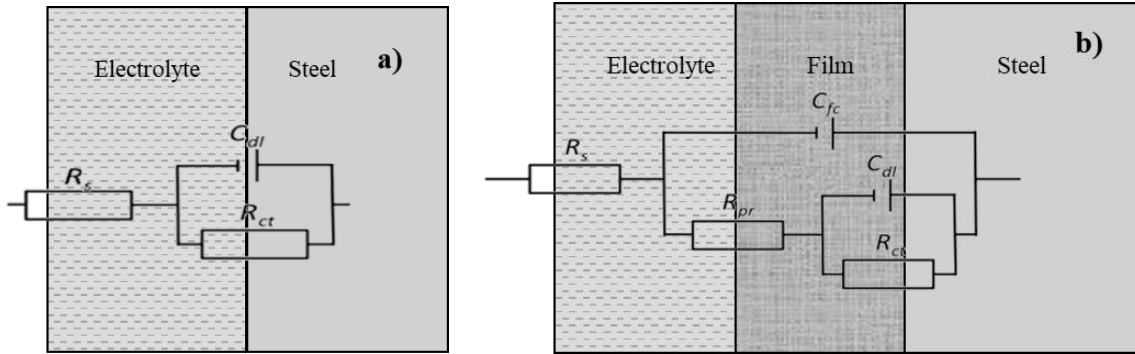


Figure 3.4. Equivalent circuit (EC) used for modelling of EIS data.

More detailed discussion on EIS data and circuit fitting are explained in individual chapters.

3.4.3. Potentiodynamic Sweep

Potentiodynamic scans were performed in order to obtain information about the electrochemical corrosion behavior of the sample over large potential range covering the Tafel region and beyond. The potentiodynamic sweep test was conducted using a potential range from -250 mV to +1000 mV with respect to OCP with a sweep rate of 0.167mV/min. The cathodic portion of the Tafel plot was scanned from -250 mV to 0 with respect to OCP while the anodic portion was scanned from 0 to +1000 mV with respect to OCP.

3.5. Surface Characterization and phase analysis

3.5.1. Scanning Electron Microscopy (SEM)

The surface morphology of the corroded surface, cross-section of the samples and elemental analysis of the corrosion products were investigated using high resolution scanning electron microscopy (SEM) on Quanta FEG 200, which is equipped with energy dispersive X-ray spectroscopy (EDS) using Oxford Instruments X-Max Silicon Drift Detector. In order to do cross section analysis, the samples were cold embedded and cut along the cross section. After cutting, water free (ethanol 100% purity) sample polishing was conducted with SiC grade P220, P320, P500, P1000, P4000 followed by 1 μ m and 3 μ m abrasive particles and then rinsed with ethanol and dried. Further samples were sputtered with gold to prevent charging of the samples. All images were obtained using Everhart- Thornley (ET) detector.

3.5.2. X-ray Diffraction

X-Ray Diffraction (XRD) was used to determine the phase composition of the formed layer using a Bruker D8 Advance. The instrument was operated at 35 kV and 50 mA with Cr-K α radiation ($\lambda=0.22909$ nm). The 2θ ranged was selected from 35° to 85°, with the step size of 0.05°, and a 10 s count time at each step.

3.5.3. X-ray Photoelectron Spectroscopy

X-ray photoelectron spectroscopy (XPS) spectra were recorded using a commercial XPS-Thermo Scientific system. The base pressure in the experimental chamber was below 10^{-9} mbar. The spectra were collected using Al K α X-ray source (1486.6 eV) radiation and the overall energy resolution was about 0.8 eV. High-resolution scans with 0.1 eV steps were conducted over the interesting regions. XPS spectra were deconvoluted using a non-linear least-squares algorithm with a Shirley baseline and a Gaussian–Lorentzian combination. Thermo Avantage software, version 5.9913, was used for all XPS data processing.

References

- [1] CAPROCO, Linear Polarization Resistance (LPR) General Information, (n.d.). <http://www.caproco.com/catalog/pdf/Probes-Instruments/Linear-Polarization-Resistance/LPR-General-Information.pdf> (accessed October 18, 2021).
- [2] G. Zhang, C. Chen, M. Lu, C. Chai, Y. Wu, Evaluation of inhibition efficiency of an imidazoline derivative in CO₂-containing aqueous solution, *Mater. Chem. Phys.* 105 (2007) 331–340.



4. Summary of the experimental chapters

This chapter includes summary of all manuscripts presented in chapters 5-9.

Paper I

Electrochemical and molecular modelling studies of CO₂ corrosion inhibition characteristics of alkanolamine molecules for the protection of 1Cr steel

The first study investigated the effects of alkanolamine molecules on the corrosion inhibition of L80–1Cr steel in CO₂-saturated 1 wt% NaCl solution at well downhole temperatures of 20 °C and 80 °C. When CO₂ dissolves in water and hydrates to carbonic acid (H₂CO₃), it promotes electrochemical reactions between the steel surface and the aqueous phase, leading to iron dissolution. At higher temperatures (80 °C), corrosion products such as iron carbonate in the form of siderite (FeCO₃) precipitate on the surface, which likely influences the corrosion mechanism. However, the formation of FeCO₃ corrosion product layer is unpredictable and offers unreliable protection against corrosion. Thus, there is reliance on use of corrosion inhibitors, which are considered as efficient and economical methods for corrosion inhibition in oil and gas production wells. Inhibitors on the metal surface mainly act as a competitive adsorbate against the aggressive ions. Alkanolamines (ethanolamine, diethanolamine and triethanolamine) are organic molecules possessing N hetero-atoms. These organic corrosion inhibitors are layer-forming agents and are usually adsorbed on the surface of metals. In this study, the effect of amine-based organic corrosion inhibitors on 1Cr steel and the pre-formed FeCO₃ corrosion layer were investigated using electrochemical techniques and molecular modelling. The corrosion rates were lower at 20 °C and were also influenced by alkanolamines. At 80 °C, there was a lower efficiency of alkanolamines inhibitors, due to higher corrosion kinetics and more desorption of alkanolamines from the surfaces. The molecular modelling revealed that alkanolamine adsorption/desorption influenced the kinetics and characteristics of FeCO₃ formation. The formation of FeCO₃ was delayed due to the alkanolamine injection. When the alkanolamines were injected at the beginning of the experiment, a porous FeCO₃ corrosion product layer was formed, leading to a lower polarization resistance value (shown in Fig. 4.1).

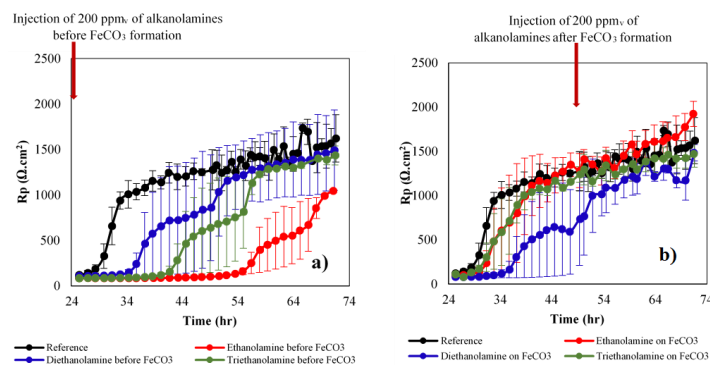


Figure 4.1. Variations of polarization resistance vs time for L80-1 Cr steel exposed to 1 wt % NaCl solution at 80°C, with different types of alkanolamines at 200 ppmv concentration injected (a): before FeCO₃ products formation and (b): after FeCO₃ formation.

Paper II

Electrochemical and molecular modelling studies of corrosion inhibition characteristics of Imidazoline based inhibitors on 1Cr steel under sweet conditions and annexure to the investigation of corrosion inhibition effects of 2-Phenyl-2-Imidazoline on 1Cr steel with CO₂: Effect of H₂S

This study investigated the corrosion inhibition properties of imidazoline-based inhibitors on 1Cr steel in pure CO₂ environment. This study builds on the results of the first study by including inhibitors with N hetero-atom, but with different chemical structures. The 2-methyl-2-Imidazoline (2-MI) and 2-phenyl-2-Imidazoline (2-PI) are two isomeric forms of imidazoline that are highly preferred due to their high corrosion inhibition efficiency and low toxicity. This study investigated the corrosion inhibition behavior of 2-MI and 2-PI on L80-1Cr steel in CO₂ environment using electrochemical techniques such as Open Circuit Potential (OCP), Linear Polarization resistance (LPR) and Electrochemical Impedance Spectroscopy (EIS). The adsorption of these inhibitors on the Fe surface was studied using molecular modelling technique. In addition, this study investigated the additive effects of mono-ethylene glycol (MEG) on corrosion efficiency of 2-MI and 2-PI. Lastly, this study investigated the effects of inhibitor reinjection on corrosion inhibition.

Imidazoline with methyl (2-MI) and phenyl (2-PI) structures led to corrosion inhibition with 28% and 93% efficiency, respectively. Higher efficiency of 2-PI was due to stronger adsorption of the phenyl group on the steel surface as supported by molecular modelling showing higher adsorption energy for 2-PI (-189 KJ/mol) than 2-MI (-76KJ/mol).

Addition of MEG increased the corrosion efficiency of 2-MI and 2-PI to 50% and 96%, respectively, suggesting synergistic effects from increased surface coverage due to ion-pair interactions between MEG anions and imidazoline cations. Re-injection of 2-PI at 48 hours led to a partial increase in the R_p values shown in Fig. 4.2, suggesting prevention of further degradation of the initially formed layer of 2-PI inhibitor. The 2-PI inhibitor was also found to be effective (efficiency of 88% alone and 90% in combination with MEG) in the presence of 200 ppm of H₂S in the CO₂ environment.

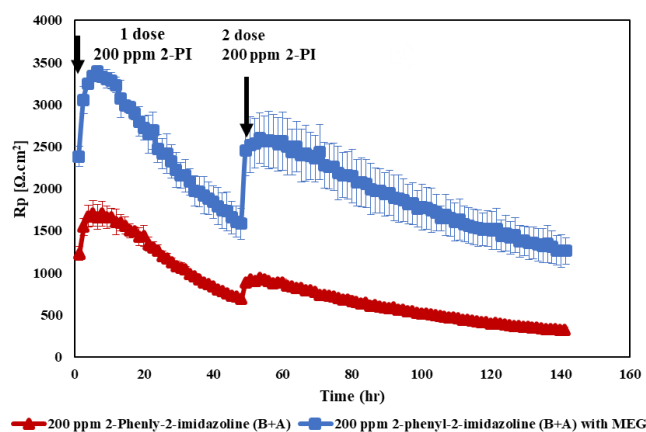


Figure 4.2. Effect of subsequent re-injection of 2-PI inhibitor on corrosion inhibition of L80-1 Cr steel when exposed to 1 wt % NaCl solution at 40 °C.

Paper III

CO₂ corrosion inhibition capability of an eco-friendly inhibitor containing green aloe vera plant extract on 1Cr steel: experimental and molecular modelling studies

Inhibitors typically offer a cost effective and efficient way of corrosion prevention; however, they potentially lead to environmental hazards. Eco-friendly (green) inhibitors such as aloe vera may favorably offer similar cost effective inhibitory effects without the environmental hazards and pollution. In addition, in combination with commercial inhibitors such as Mono Ethylene Glycol (MEG), aloe vera may offer high corrosion efficiency. Therefore, the focus of this study was to investigate the corrosion inhibition properties and underlying mechanisms of corrosion inhibition of aloe vera alone and in combination with MEG on L80-1Cr steel surface in CO₂ environment. Different electrochemical techniques (OCP, LPR and impedance) and molecular modelling were utilized to investigate the corrosion inhibition properties. The result from this study shows that aloe vera (4000 ppm) led to 45% increase in corrosion resistance as compared to the reference sample, suggesting an efficiency of 10%, see Fig.5.3a. In combination with MEG, the efficiency of aloe vera (4000 ppm) increased substantially (~8 times) as compared to that without MEG. Highest corrosion efficiency (88.7%) was seen due to synergistic effects of aloe vera (8000 ppm) and MEG, shown in Fig. 4.3b.

The molecular modelling, on the basis of adsorption energy calculations and estimation of water replacement, help explain the mechanisms underlying the corrosion inhibition behavior of different inhibitors as observed in the experimental findings. Highest adsorption energy was observed for aloin (-110 kJ/mol), the main constituent of aloe vera that contributes to corrosion inhibition.

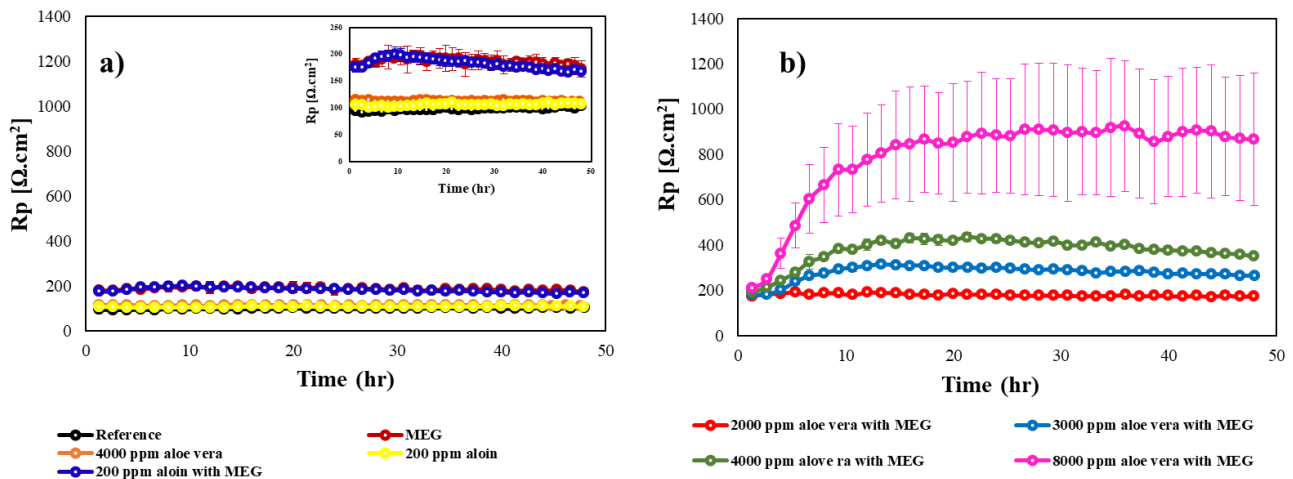


Figure 4.3. Polarization resistance for L80-1Cr steel exposed to 1 wt % NaCl solution at 40 °C, for 48 hours (a): without and with the addition of green inhibitor and (b): at different concentration of aloe vera together with MEG.

Paper IV

Corrosion inhibition properties of eco-friendly green inhibitors containing aloe vera plant extract on 1 Cr steel under H₂S conditions with CO₂

This study established the synergistic effect of aloe vera upon addition of MEG for corrosion inhibition in CO₂ environment. However, H₂S is commonly found as a component of natural gas and as a dissolved constituent of oil and water that is produced in the well. The H₂S is toxic, highly corrosive and frequently leads to the precipitation of metal sulfides in both the subsurface and in above ground piping. Wells with levels of H₂S of more than 10 ppm are classified as sour. Therefore, this study investigated the effect of aloe vera alone and in combination with MEG in sour environment. The specific objectives of the paper were: (1) to study the corrosion inhibition properties of aloe vera extract on steel surface at different concentrations of H₂S in CO₂-H₂S environment, and (2) to investigate the corrosion inhibition effects of combination of aloe vera and MEG. Electrochemical and surface characterization techniques were utilized to study the corrosion inhibition behavior and corrosion product layer analysis. The SEM analysis confirmed that in the absence of inhibitors (see Fig. 4.4 (a-f)), there was more corrosion and pitting (larger pits) on the steel surface than that seen in the presence of aloe vera (See Fig. 4.5 (a-f)). There was an effect of H₂S concentration on corrosion of L80-1Cr steel. In the absence of inhibitors, higher concentration of H₂S led to higher R_p values up to 400 ppm of H₂S. Higher R_p values were explained by a denser layer of FeS that was formed on the metal surface at higher concentrations of H₂S. The effects of aloe vera and MEG also varied with the concentration of the H₂S; however aloe vera alone and in combination with MEG had high efficiency values (up to 70%) in the H₂S environment.

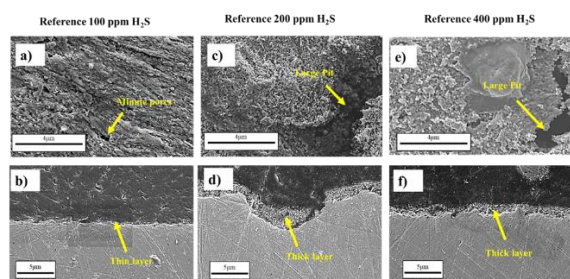


Figure 4.4. SEM images (top view and cross-sectional view) for L80-1Cr steel exposed to 1 wt% NaCl solution, without inhibitor (Reference) at 40 °C (a-b): 100 ppm H₂S, (c-d): 200 ppm H₂S and (e-f): 400 ppm H₂S.

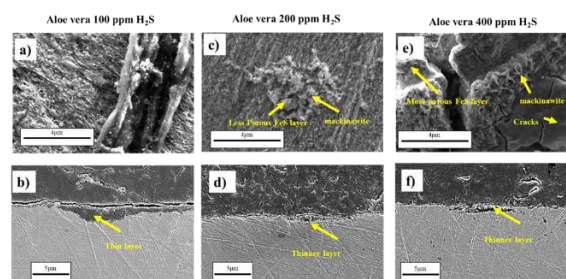


Figure 4.5. SEM images (top view and cross-sectional view) for L80-1Cr steel exposed to 1 wt% NaCl solution, with 4000 ppm aloe vera at 40 °C (a-b): 100 ppm H₂S, (c-d): 200 ppm H₂S and (e-f): 400 ppm H₂S.





5. Paper I: Electrochemical and molecular modelling studies of CO₂ corrosion inhibition characteristics of alkanolamine molecules for the protection of 1Cr steel

Shivangi Gupta, Kapil Kumar Gupta, Martin Andersson, Rouhollah Yazdi, Rajan Ambat, Electrochemical and molecular modelling studies of CO₂ corrosion inhibition characteristics of alkanolamine molecules for the protection of 1Cr steel, Corrosion Science 195 (2022) 10999. doi.org/10.1016/j.corsci.2021.109999.

This is the published version of the following article: Electrochemical and molecular modelling studies of CO₂ corrosion inhibition characteristics of alkanolamine molecules for the protection of 1Cr steel, which will published in final form at

<https://doi.org/10.1016/j.corsci.2021.109999>

This article may be used for non-commercial purposes in accordance with Elsevier Copyright Policies.



Electrochemical and molecular modelling studies of CO₂ corrosion inhibition characteristics of alkanolamine molecules for the protection of 1Cr steel

Shivangi Gupta^{a,*}, Kapil Kumar Gupta^a, Martin Andersson^b, Rouhollah Yazdi^a, Rajan Ambat^a

^a Section of Materials and Surface Engineering, Department of Mechanical Engineering, Technical University of Denmark, Produktionstorvet, 2800 Kongens Lyngby, Denmark

^b Department of Chemical Engineering, Technical University of Denmark, Produktionstorvet, Kongens Lyngby 2800, Denmark

ARTICLE INFO

Keywords:

- A. Steel
- B. Polarization
- B. EIS
- B. XPS
- B. modelling studies

ABSTRACT

Effects of alkanolamine molecules on the corrosion inhibition of L80–1Cr steel were studied in a CO₂-saturated 1 wt% NaCl solution at well downhole temperatures of 20 and 80 °C. The electrochemical results showed lower corrosion rates at 20 °C, for which corrosion rates were more influenced by the alkanolamine injection. The experimental results and molecular modelling calculations using DFT revealed that alkanolamine adsorption/desorption played a determining role in the kinetics and characteristics of FeCO₃ formation. Additionally, the dependency of inhibitor efficiency on both chemical structures and adsorption energy on Fe(110), FeCO₃(104) and Fe₃C(001) was demonstrated, resulting in the highest efficiency provided by ethanolamine.

1. Introduction

Despite their susceptibility to CO₂ corrosion, carbon and low alloy steels are the most commonly used materials in oil and gas production/transmission infrastructure; due to their relatively low price, availability, mechanical characteristics, ease of use in construction, and economic effectiveness by corrosion inhibition [1]. When CO₂ dissolves in water and hydrates to carbonic acid (H₂CO₃), it promotes electrochemical reactions between the steel surface and the aqueous phase, leading to iron dissolution [2–7]. In some circumstances, corrosion products or mineral scales can precipitate on the surface, which likely has a significant influence on the corrosion mechanism(s). This electrochemical process has been under investigation for more than four decades, but the corrosion mechanisms occurring at the metal-electrolyte interface are still the main subject of research [8,9].

Iron carbonate formation in the form of siderite (FeCO₃) is the most commonly observed corrosion product in an aqueous NaCl-containing medium saturated with CO₂. This has been proved to be one of the most important factors governing the rate of corrosion [1,10]. The influence of this layer on the corrosion rate of steel has been researched and documented in the literature [11–15]. Indeed, the iron carbonate layer can slow the general corrosion process by acting as a physical barrier to the diffusion of ionic species involved, covering up a portion of

the steel surface, and preventing the underlying steel from further dissolution. In other words, under certain conditions, FeCO₃ precipitation on the steel surface blocks the active sites of dissolution and creates a barrier to the diffusion of the electrochemically active species, resulting in a significant reduction in the corrosion rate. Iron carbonate layer growth depends primarily on the kinetics of the electrochemical reactions. As more iron carbonate precipitates, the layer grows in a higher density and thickness. However, the steel surface continuously corrodes under the layer, creating “voids” between the layer and the steel surface. When the rate of precipitation at the steel surface equals or exceeds the rate of corrosion, dense, protective layers form, which are sometimes very thin but still protective. The opposite scenario occurs when the corrosion process undermines the newly formed layer faster than precipitation can fill in the voids, and a porous and unprotective layer forms which can be sometimes very thick [16].

The protectiveness of the iron carbonate layer is strongly dependent on several parameters such as CO₂ partial pressure [11–14], concentration of ionic species [17,18], pH and temperature [19–22]. Temperature is one of the most crucial parameters that influences the corrosion of mild steel in CO₂ environments. At low pH values (when the solubility of FeCO₃ is high), an increase in temperature accelerates both the mass transport in the bulk solutions and the kinetics of chemical and electrochemical reactions at the metal-electrolyte interface. This leads to an

* Corresponding author.

E-mail address: shig@mek.dtu.dk (S. Gupta).

<https://doi.org/10.1016/j.corsci.2021.109999>

Received 30 June 2021; Received in revised form 21 November 2021; Accepted 29 November 2021

Available online 1 December 2021

0010-938X/© 2021 Elsevier Ltd. All rights reserved.

increase in the corrosion rate [23,24]. The peak in the corrosion rate has been reported in the literature to be between 60 °C and 80 °C [20–22]. Below ~ 60 °C, no protective layer is formed and the corrosion products are porous and not well adherent to the steel surface. At temperatures higher than about 60 °C, the FeCO₃ layer becomes denser and more adherent to the surface, creating a solid barrier between the metal and the electrolyte, which reduces the corrosion rate of the steel [25–29].

Due to the formation of various corrosion products with unpredictable and uncertain levels of protectiveness, the use of corrosion inhibitors is considered as one of the suitable and economical methods for reliable production of oil and gas [30,31]. The addition of corrosion inhibitors effectively secures the metal against an acid attack. Inhibitors on the metal surface mainly act as a competitive adsorbant against the aggressive ions. The adsorption on the metal surface is influenced by the surface nature and its charge-transfer properties, the type of aggressive electrolyte, and the chemical structure of inhibitors [32]. Most inhibitors are organic molecules possessing N, S, P and O hetero-atoms. There are different types of inhibitors of which organic corrosion inhibitors are mostly applied in the oil and gas industry. The organic corrosion inhibitors are layer-forming agents and are usually adsorbed on the surface of metals through a physical or chemical process. The mechanism of adsorption of most corrosion inhibitors can be understood by the determination of the adsorption properties of organic corrosion inhibitors [33]. The adsorption energy of inhibitor molecules can be calculated at the electronic level using Density Functional Theory (DFT). Most of the commercial organic corrosion inhibitors comprise of N-containing molecules amines, quarts, imidazoline, etc. which effectively adsorb on the metal surface and inhibits the corrosion processes. There are various factors which influence the adsorption and efficiency of corrosion inhibitors, such as the molecular structure of the inhibitors, inhibitor concentration, exposure time, electrolyte chemistry, temperature of the system, etc. [34].

Despite the existence of several studies, discussing the inhibitive effects of N- containing organic molecules on mild steel [35,36], the atomic interaction of the inhibitors with the steel surface is still unclear in the present literature especially when iron carbonate is formed at high temperatures. Thus, it is an important subject to understand whether amine-based corrosion inhibitors have a complementary effect on iron carbonate or are detrimental to its formation. The aim of this comprehensive study is to investigate the effect of amine-based organic corrosion inhibitors on bare 1Cr steel and the pre-formed FeCO₃ using electrochemical techniques as well as molecular modelling. In addition, inhibitor injection frequency experiments were studied to understand the role of the application method in corrosion mitigation. For this purpose, the electrochemical behavior of steel grade L80–1Cr has been investigated at 20 °C and 80 °C, the typical temperatures of oil production wells of the Danish sector of the North Sea. To assess the electrochemical behavior of the material and to measure corrosion rate, different electrochemical techniques such as Open Circuit Potential (OCP), Linear Polarization Resistance (LPR) and Electrochemical Impedance Spectroscopy (EIS) were used. Furthermore, for a comprehensive understanding of the inhibitor adsorption mechanism, different surface characterization techniques, including Scanning Electron Microscopy (SEM) equipped with Energy Dispersive Spectroscopy (EDS), and X-ray Photoelectron Spectroscopy (XPS) were employed.

2. Material and methods

2.1. Material and specimen preparation

The specimens used in this study were made of a martensitic 1Cr steel (L80) in the quenched & tempered condition with a chemical composition listed in Table 1. The specimens were machined into a cylindrical shape with a total surface area of 3.95 cm². The surface of the specimens was mechanically polished with SiC papers up to P1000 grade. Immediately after polishing, the specimens were degreased using ethanol,

Table 1
Chemical composition in wt% of the L80–1 Cr steel.

Material	C	Cr	Mn	Mo	P	Si	S	Fe
API 5CT L80 – 1Cr Steel	0.40	1.10	0.75	0.20	≤ 0.035	0.20	≤ 0.040	base

rinsed with de-ionized water, and then air-dried. The dried specimens were then mounted on a specimen holder and immersed in the test solution. At the end of the tests, the specimens were immediately retrieved, rinsed with ethanol, dried in air and stored in a desiccator for further assessments.

2.2. Electrolyte preparation

The electrochemical experiments were conducted on the 1Cr steel samples in a CO₂-saturated 1 wt% NaCl solution at 20 °C and 80 °C. Before immersing the specimen in the solution, the electrolyte was sparged with nitrogen for about 12 h to deoxygenate. The gas was then switched to CO₂ and bubbled for 4 h in order to saturate the solution. After gas bubbling, the pH of the solution was measured to be 3.9 for 20 °C and pH 4.2 for 80 °C. Three alkanolamines (possessing alcohol and amine functional groups) including ethanolamine, diethanolamine and triethanolamine with pKa values (at 25 °C) of 9.5, 8.88, 7.8, respectively, were used in the current study. An amount of 200 parts per million by volume (ppm_v) of inhibitors was injected into the solution. After inhibitor injection and before the immersion of the bare 1Cr steel samples, the solution was de-aerated again for at least 30 min in order to remove possible trapped oxygen during the injection. In another phase of this work, in order to study the effects of the inhibitors on the iron carbonate layer, NaHCO₃ was added to adjust the pH of the solution to 6.5 in order to facilitate iron carbonate precipitation prior to the alkanolamines injection. After pH adjustment, the solution was again de-aerated for at least one hour with CO₂ gas bubbling. During testing, CO₂ gas was continuously bubbled to the solution to maintain its saturation and avoid any oxygen entrance.

2.3. Electrochemical and weight loss measurements

The corrosion tests were carried out in an airtight 1.5 L glass container using a standard three-electrode cell. An Ag/AgCl reference electrode was placed in contact with the solution through a glass-luggin capillary and a concentric platinum wire ring was used as the counter electrode. The corrosion potential (E_{corr}) was monitored and the linear polarization resistance (LPR) was measured every 1.5 h. During LPR measurements, the potential was scanned in a potential range of ± 10 mV vs. open-circuit potential (OCP) at a scan rate of 0.167 mV/s. Based on our previous experience, a duration of 1 h was chosen for the system to stabilize the initial OCP. After the OCP stabilization, the EIS measurements were performed by applying an AC signal amplitude of 10 mV vs OCP in a frequency range of 10 mHz – 10 kHz.

The weight loss method was employed to calculate the corrosion rate for the steel samples in the CO₂-saturated 1 wt% NaCl solution without and with alkanolamines injection at 20 and 80 °C after 24 hr. For this purpose, after rinsing and drying, the initial weight of pre-immersed specimens was measured by a calibrated weighing tool with the accuracy of 10⁻⁵ gr. After the immersion tests, the corrosion products on the surface, if any, were removed using Clark's solution in accordance with the standard procedure mentioned in ASTM G1–03, and then the final weight and weight loss were (W) obtained. The corrosion rate was eventually obtained based on the following equation:

$$\text{Corrosion rate (mm/yr)} = 8.76 \times 10^4 \frac{W}{A.T.D} \quad (1)$$

where “W” is mass loss in grams; “T” is time of exposure in hour, “A” is the exposing surface area in cm^2 , and “D” is density in gr/cm^3 .

2.4. Experimental conditions and procedure

As listed in Table 2, initially, the effect of the alkanolamines on L80–1 Cr steel at two temperatures of 20 °C and 80 °C was studied in the CO_2 -saturated electrolyte. A 200 ppm_v concentration of the alkanolamine was injected into the solution at the beginning of the experiment and then electrochemical experiments were conducted. To understand the injection frequency of the inhibitors, another set of experiments was carried out in the NaCl solution in which the alkanolamines were intermittently injected to observe their effects on the corrosion behavior of L80–1 Cr steel. In this strategy, three different procedures were established as shown in Fig. 1a. In case I, the 200 ppm_v inhibitor was initially injected before immersing the sample in the solution. In case II, the same amount of inhibitor was injected after 12 hrs of the immersion, which means that the sample was pre-corroded for 12 hrs. In case III, a two-time injection of the inhibitors was done; (1) initial injection, 30 min before electrochemical measurements and, (2) final injection after 12 hrs of electrochemical measurement. All electrochemical experiments were performed at least twice and the average values with error bars are reported in the Results section.

As iron carbonate is the main corrosion product that may form over the steel material in a CO_2 environment, therefore, the inhibitive effect of alkanolamines on iron carbonate formation was also studied. For this purpose, two injection frequency cases were selected as shown in Fig. 1b. In the first case, the sample was anodically polarized with the current density of 61.1 $\mu\text{A}/\text{cm}^2$ in the NaCl solution at 80 °C and pH 6.5 for 24 hrs in order to accelerate Fe^{2+} ion dissolution into the solution. Then, the alkanolamines were injected under the OCP conditions to observe how they influence the formation and growth of FeCO_3 . In the second, after the anodic polarization, the OCP condition was applied on the sample in the solution for 24 hrs before injecting the alkanolamines. This enables the system to get saturated with Fe^{2+} ions and as a result, FeCO_3 was formed on the surface. Then, the effect of the alkanolamines on the corrosion behavior of the pre-formed FeCO_3 layer was studied. After each experiment, the samples were cleaned in deionized water, flushed with ethanol and air-dried. All samples were stored in a desiccator before further characterization analyses.

2.5. Surface characterization and phase analysis

The morphological and elemental analysis of the corrosion products were investigated using a Zeiss Supra FEG-SEM using 20 kV acceleration voltage, assisted with Energy Dispersive X-ray spectroscopy (EDS) analysis equipment. Grazing Incidence X-Ray Diffraction (GIXRD) was also used to determine the phase composition of the formed layer using a Bruker D8 Advance. The instrument was operated at 35 kV and 50 mA with Cr-K α radiation ($\lambda = 0.22909$ nm). The incidence angle was 3° and the 2 θ ranged was selected from 35° to 85°, with the step size of 0.05°, and a 10 s count time at each step.

X-ray photoelectron spectroscopy (XPS) spectra were recorded using a commercial XPS-Thermo Scientific system. The base pressure in the experimental chamber was below 10^{-9} mbar. The spectra were collected

Table 2
Experimental conditions of electrochemical experiments used in this study.

Parameter	Condition
Material	1Cr steel
Solution	1 wt% NaCl in Deionized water, CO_2 Saturated
Temperature	20 °C and 80 °C
CO_2 partial pressure	0.98 bar at 20 °C and 0.53 bar at 80 °C
Rotation	300 rpm
Inhibitor concentration	200 ppm _v
Test duration	24 and 72 hrs

using Al K α X-ray source (1486.6 eV) radiation and the overall energy resolution was about 0.8 eV. High-resolution scans with 0.1 eV steps were conducted over the following regions of interest: C 1 s, N 1 s and O 1 s. Surface charging effects were compensated by referencing the binding energy (BE) to the C 1 s line of residual carbon set at 285.0 eV BE. XPS spectra were deconvoluted using a non-linear least-squares algorithm with a Shirley baseline and a Gaussian–Lorentzian combination. Thermo Advantage software, version 5.9913, was used for all XPS data processing.

2.6. Computational details

The DFT calculations were performed in a pseudopotential plane-wave formalism with the Quantum Espresso package [37]. The adsorption energies for water, ethanolamine, diethanolamine and triethanolamine on a Fe(110) surface and a $\text{FeCO}_3(104)$ surface were calculated to model the different behavior of water and the alkanolamines on pristine and CO_2 corroded iron. The adsorption energy of ethanolamine was also calculated on a $\text{Fe}_3\text{C}(001)$ surface.

To perform slab calculations on Fe(110), $\text{FeCO}_3(104)$ and $\text{Fe}_3\text{C}(001)$, 15–20 Å of vacuum between the material slabs was inserted. The slabs for each of the materials consisted of four molecular layers. The fourth molecular layer (furthest from the side of the adsorbates) was frozen during the geometry optimizations. The lattice parameters used for each material were found by optimizing the cell parameters for the corresponding bulk material, using the same pseudopotentials, exchange-correlation functional that was later used for calculating adsorption energies, in order to minimize the effects of surface strain on adsorption properties. For $\text{FeCO}_3(104)$, only the gamma point was used during geometry optimizations, for Fe(110) a $4 \times 4 \times 1$ k-point sampling was used and for $\text{Fe}_3\text{C}(001)$ a $6 \times 6 \times 1$ k-point sampling was used. The revPBE functional [38] with added semi-empirical dispersion corrections were employed in the DFT-D2 implementation [39–41]. The s6 parameter for revPBE was 1.25, and a 12 Bohr cutoff was used for Fe calculations [39]. The C6 vdW parameters for Fe were reduced by a factor of 33 to take into account the decreased polarizability of cations when they are bonded within an ionic material [42–44]. All pseudopotentials were ultrasoft (US), Projector-Augmented Wave (PAW) and Norm-Conserving (NC) were generated using revPBE, and were taken from PS Library 0.2.5 [45, 46]. The kinetic energy cutoff was 40 Ry, and the density cutoff was 400 Ry, which has been shown for similar setups to provide converged adsorption energies [43,44].

In order to assess the specific molecular interaction with the model surfaces, the adsorption energy was calculated using Eq. (2).

$$E_{\text{adsorption}} = E_{\text{surface+inhibitor}} - (E_{\text{surface}}) - (E_{\text{inhibitor}}) \quad (2)$$

The dual functional groups of the alkanolamines allow for the adsorption with either group to the solid surfaces. The adsorption energies of both binding geometries were calculated. Using this convention, the more negative the adsorption energy, the stronger is the bond between the molecule and the surface.

3. Results

3.1. Molecular modelling simulation using density functional theory (DFT)

Amines contain a sp³ hybridized nitrogen atom on which another element or functional group can be bonded with three single bonds. Ethanolamine, commonly named monoethanolamine (MEA), is an organic chemical compound that has both primary amine and alcohol functionalities and acts as a weak base. All amines have a lone pair of electrons. However, the readiness with which the lone pair of electrons is available for co-ordination with a proton determines the basic strength of amines. The inhibitive effect of ethanolamine is achieved by donating the unshared pair of electrons from the nitrogen atom,

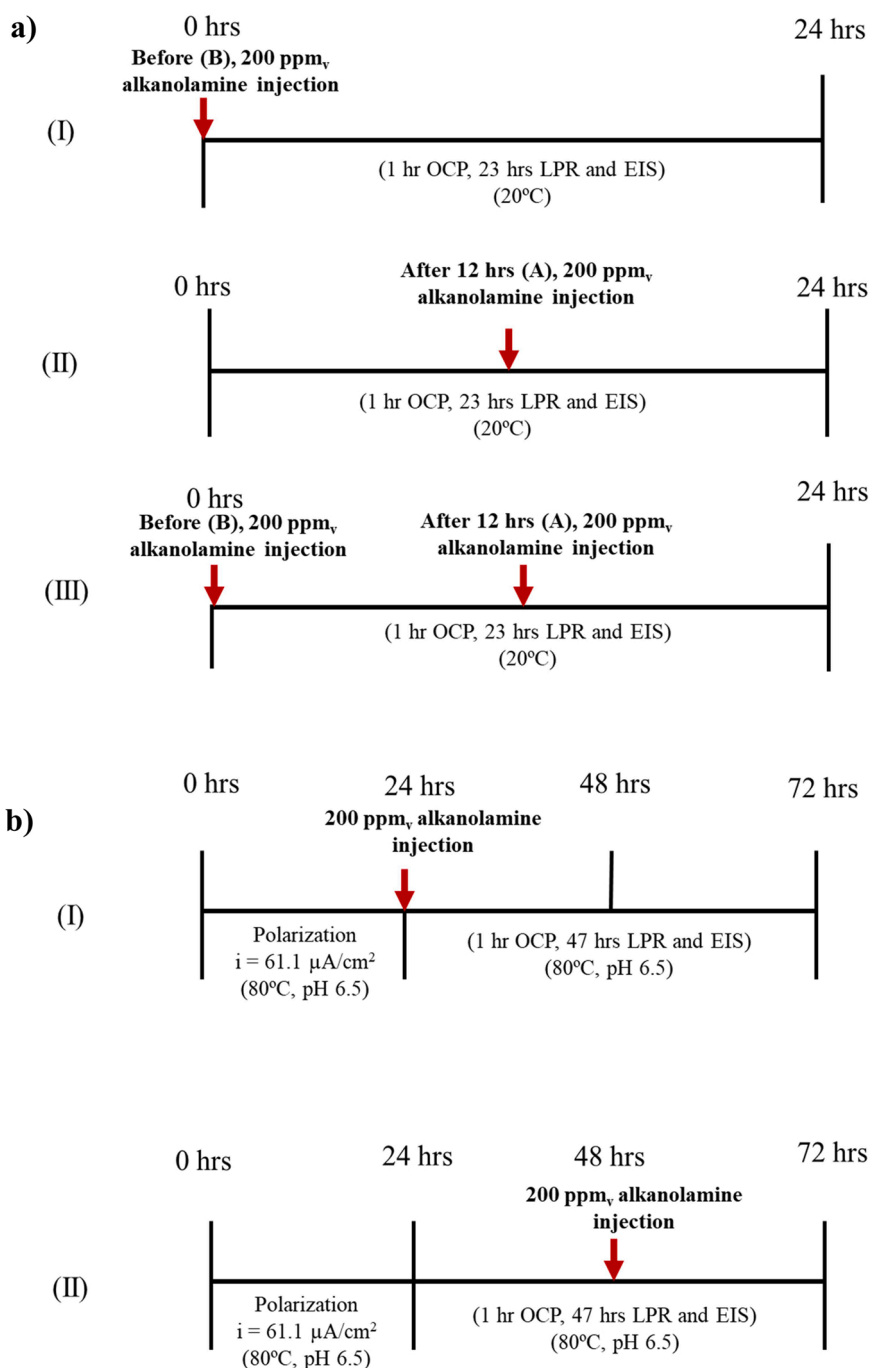


Fig. 1. . (a): Inhibitor injection frequency on L80- 1Cr steel, (b) Inhibitor injection frequency on the steel covered with iron carbonate (FeCO₃) corrosion products.

followed by a surface complex-forming [32]. Adsorption energy calculations using DFT were conducted to further study the interaction between tested inhibitors and Fe(110) and FeCO₃(104) stable surfaces in the gas phase. In Table 3, the calculated adsorption energies of the most stable bonding geometry of each alkanolamine on the surfaces are shown. When comparing the adsorption energy on Fe and FeCO₃ surfaces, water as well as all alkanolamines had more negative values for the FeCO₃ surface indicating a stronger bond. On Fe surfaces, however, water had the least negative (−31 kJ/mol) adsorption energy value representing the weakest bond with Fe surface in comparison to the alkanolamines. Among different alkanolamines, diethanolamine had the most negative adsorption energy value (−122 kJ/mol) on the Fe surface, thus formed the strongest bond. The adsorption energy value trend for the FeCO₃ surface was slightly different than the Fe surface. Water still

had the least negative value (−106 kJ/mol); however, amongst the alkanolamines, ethanolamine and diethanolamine had more negative values (−152 and −151 kJ/mol, respectively) than triethanolamine.

The inhibitor adsorption energy was estimated in water by comparing the adsorption energy of the inhibitor with that of water in Table 3. This estimation is based on the fact that an inhibitor molecule needs to replace water molecule(s) already bonded at the interface. The size of the inhibitor molecule at the interface can govern either one or two water molecules need to be displaced from the surface. For ethanolamine, one water molecule was chosen, and for diethanolamine, however, a single and couple of water molecule(s) were selected for the -OH and -NH anchoring group, respectively.

Table 3

Adsorption energy values of the alkanolamines as the inhibitors and the difference in the adsorption energy of the alkanolamines and water ($\Delta E_{\text{adsorption}}$) on Fe(110), Fe₃C(001) and FeCO₃(104) surfaces using DFT (in kJ/mol).

Molecule	Anchoring group	$E_{\text{adsorption}}$ Fe (110)	$E_{\text{adsorption}}$ FeCO ₃ (104)	$E_{\text{adsorption}}$ Fe ₃ C (001)	
Water	–OH	– 31	– 106	– 62	
Ethanolamine (C ₂ H ₇ NO)	–NH ₂	– 84	– 152	– 125	
	–OH	– 59	– 123	–	
Diethanolamine (C ₄ H ₁₁ NO ₂)	–NH	– 122	– 151	–	
	–OH	– 69	– 129	–	
Triethanolamine(C ₆ H ₁₅ NO ₃)	–N	^a	– 141	–	
	–OH	– 73	– 134	–	
Differences in adsorption energy between inhibitor and water					
Molecule	# water molecules replaced	Anchoring group	$\Delta E_{\text{adsorption}}$ Fe(110)	$\Delta E_{\text{adsorption}}$ FeCO ₃ (104)	$\Delta E_{\text{adsorption}}$ Fe ₃ C(001)
Ethanolamine (C ₂ H ₇ NO)	1	–NH ₂	– 53	– 46	– 63
Diethanolamine (C ₄ H ₁₁ NO ₂)	1	–OH	– 38	– 23	–
	2	–NH	– 60	+ 61	–

^a The chosen unit cell of the Fe(110) surface was too small to fit an N-bonded triethanolamine without artefacts from interactions with the periodic images.

3.2. Binding energy calculation using XPS at 20 °C

To confirm the assumption of the alkanolamine chemisorption and elucidate the nature of the organic thin-layer formed on the Fe surface, X-ray photoelectron spectroscopy (XPS) analyses were carried out. For comparison purposes, the XPS spectra as shown in Fig. 2 were obtained on the steel surfaces, which were previously immersed in the pure alkanolamines. All XPS spectra show complex forms, which were assigned to the corresponding species through a deconvolution fitting procedure. The high-resolution N 1s spectrum of the sample treated by the alkanolamines shows the peaks indicative of the presence of different nitrogen-containing molecules on the steel surface. The deconvoluted N 1s spectrum for pure ethanolamine shows two main peaks (Fig. 2a). The first peak located at approx. 397.0 eV has the largest contribution and is attributed to the coordinate nitrogen in ethanolamine bonded with the steel surface and the second peak at the binding energy of 399.5 eV corresponds to the bonds of C-N and the unprotonated N atoms in the ethanolamine structure. In Fig. 2b, the first peak is located at approx. 402.1 eV which is at a higher binding energy, attributed to positively charged nitrogen, and could be related to a protonated nitrogen atom (=N⁺H[–]) in the diethanolamine structure. A similar trend has been observed in Fig. 2c for triethanolamine.

3.3. Electrochemical responses at 20 °C and 80 °C

3.3.1. LPR measurements

The results obtained from the LPR measurements (corrosion potential and polarization resistance) on 1Cr steel at the temperatures of 20 °C and 80 °C are shown in Fig. 3. The comparison of Figs. 3a and 3b shows that the evolution of the corrosion potential depends on the exposure temperature. In Fig. 3a, the samples tested in the alkanolamine-containing solution at 20 °C show different corrosion potential trends without a significant variation over the period of the experiment. Only the reference sample shows a slight OCP delay from – 630 mV to about – 650 mV, probably due to the breakdown of the pre-immersion, residual air-formed oxide film [47], leaving more active sites on the surface which somewhat increased the corrosion tendency of the sample. At 80 °C, however, the corrosion potential for all samples slightly increased with time (Fig. 3b), suggesting the formation of a protective layer by electrochemical redox reactions. For instance, the E_{corr} for the sample (i. e. reference sample) at 80 °C increased in the solution with ethanolamine injection from approximately – 660 mV to – 640 mV and then remained unchanged. In comparison, the injection of the alkanolamines resulted in a nobler corrosion potential for the steel sample, indicating a less thermodynamic tendency to corrosion.

The corrosion rates of the 1Cr steel samples in the uninhibited and inhibited conditions were acquired after 24 h of immersion in the solution at 20 and 80 °C based on the weight loss technique and are presented in Fig. 3e and f. The corrosion rates of the samples at 20 °C were

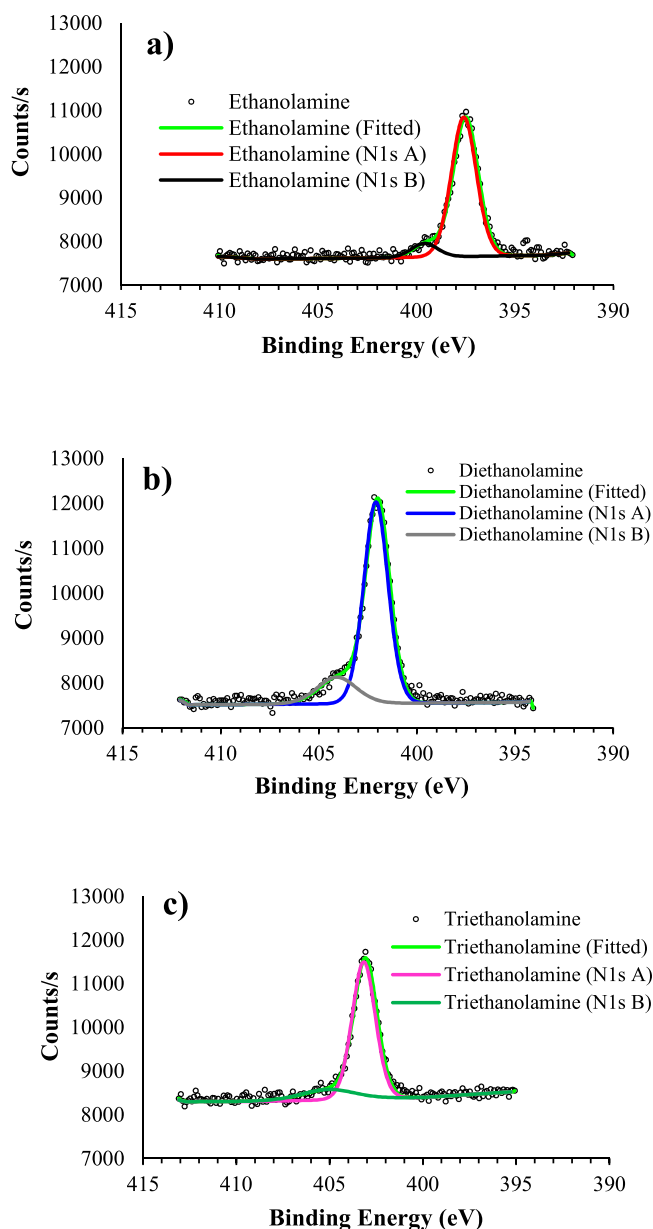


Fig. 2. The XPS deconvoluted profiles of N 1s for pure (a): ethanolamine, (b): diethanolamine and (c): triethanolamine.

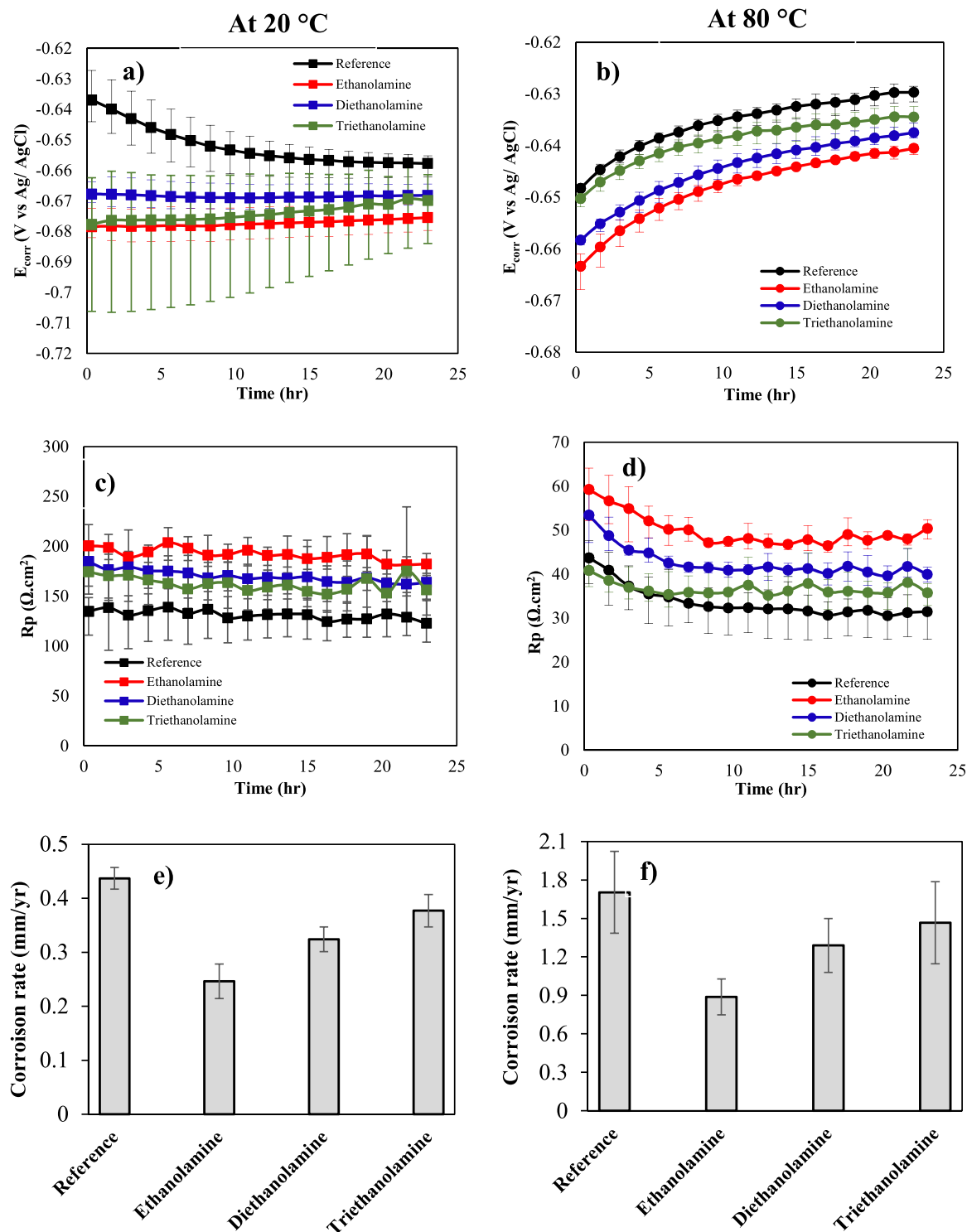


Fig. 3. Variations of: (a, b) E_{corr} as a function of time, (c, d) polarization resistance as a function of time, and (e, f) the corrosion rate (mm/yr) obtained by weight loss technique; for the L80-1 Cr steel samples in 1 wt% NaCl solution for 24 hrs without and with the addition of 200 ppmv of different alkanolamines at 20 °C and 80 °C, respectively.

about 4.4, 2.5, 3.2 and 3.8 mm/yr for the uninhibited sample and those inhibited by ethanolamine, diethanolamine and triethanolamine, respectively. Indeed, the results show a lower corrosion rate for inhibited samples in Fig. 3e, which are found to be consistent with the higher final polarization in Fig. 3c. For instance, the polarization resistance of the reference sample as a function of time for L80-1 Cr steel at 20 °C in Fig. 3c shows an about constant corrosion resistance of 130 $\Omega \cdot \text{cm}^2$,

whereas ethanolamine shows the highest resistance value (i.e., the lowest corrosion rate in Fig. 3e) of approx. 200 $\Omega \cdot \text{cm}^2$ corresponding to 70% increase in comparison to the reference sample. In addition, diethanolamine and triethanolamine exhibit a corrosion resistance of 170 $\Omega \cdot \text{cm}^2$ (60% increase) and 160 $\Omega \cdot \text{cm}^2$ (50% increase), respectively. Whereas, at 80 °C, both R_p values and corrosion rates reveal a comparably lower corrosion resistance even with the addition of the

alkanolamines see Fig. 3d and f. This means that the samples exposed to the amines-containing solution at the higher temperature show only 10–20% increase in corrosion resistance compared to the reference sample. The inhibition efficiency for the different alkanolamines at 20 °C was calculated based on Eq. (3) and is listed in Table 4. The table confirms the lower efficiency of the inhibitors at the high temperature, which is likely attributed to the less controllable acceleration of electrochemical reactions.

$$\text{Inhibitor efficiency (\%)} = \frac{(R_{p\text{Inhibited}} - R_{p\text{Uninhibited}})}{R_{p\text{Inhibited}}} \times 100 \quad (3)$$

Due to the better corrosion inhibition of ethanolamine and diethanolamine in comparison to triethanolamine (Fig. 3c and d), it was also planned to study the injection frequency effect of these two alkanolamines on the corrosion behavior of the steel surface. Fig. 4 shows the LPR results of 1Cr steel at 20 °C. Two different frequency strategies were considered (see Fig. 4a and b). In the first case, when alkanolamines were injected after 12 h of corrosion, (Fig. 4a), the resistance value was sharply increased from about 125–185 and 170 $\Omega\cdot\text{cm}^2$ for ethanolamine and diethanolamine, respectively. In the second one, the alkanolamines were injected two times, (Fig. 5b) before starting the experiment and after 12 h of immersion. Despite the effective initial inhibition levels provided by the alkanolamines similar to the previous condition, the results in Fig. 4b show that there is no significant change in the resistance value when the alkanolamines were reinjected after 12 hours. The polarization resistance is approximately 190 $\Omega\cdot\text{cm}^2$ for both ethanolamine and diethanolamine. The proposed mechanisms of inhibitions provided by the alkanolamines in the various injection frequencies will be discussed in the Discussion section.

During higher temperatures (60–80 °C), the possibility of iron carbonate formation in CO₂-saturated solutions increases [23,24], which sometimes protects the steel surface from further corrosion. Therefore, in the presence of the alkanolamines, their effect on the formation of iron carbonate products was also worth study. To form a FeCO₃ layer, it is important to maintain optimal temperature and pH conditions for the NaCl solution which were selected to be 80 °C and 6.5, respectively. The results from LPR measurements (polarization resistance) for the samples under these conditions are shown in Fig. 5. In Fig. 5a, when the alkanolamines were injected from the very beginning (just after polarization), the protectiveness provided by FeCO₃ formation was postponed to a longer immersion time (i.e., once there was a sharp increase in R_p value) as compared with the reference sample. In the reference sample, for example, the significant rise in the R_p value induced by the protective FeCO₃ formation starts after 4 hrs, however, the sample exposed to ethanolamine delayed by 26 hrs. Also by injecting diethanolamine and triethanolamine, the FeCO₃ layer was delayed to effectively protect the substrate by 6 and 14 hrs, respectively. In the other scenario, the sample was initially polarized at an anodic current density of 61.1 $\mu\text{A}/\text{cm}^2$ for 24 h to form a FeCO₃ layer (after 24 hrs) and then the alkanolamines were injected into the system. In Fig. 5b, it can be seen from the LPR trends that there is a small effect on the R_p value by alkanolamine injection, suggesting no significant inhibitor efficiency in this case.

3.3.2. Electrochemical impedance spectroscopy investigation

Fig. 6 presents the results of the EIS measurements of the samples in the solution without and with alkanolamine injection at 20 °C and 80 °C

Table 4
Comparison in the inhibition efficiency of the various alkanolamines at different temperatures of 20 °C and 80 °C.

Inhibitor type	Inhibitor efficiency (%) at 20 °C	Inhibitor efficiency (%) at 80 °C
Ethanolamine	46.7	35.5
Diethanolamine	33.1	22.2
Triethanolamine	26.1	6.6

after 24 hrs immersion. The Nyquist plot for the samples exposed at 80 °C shows two incomplete and depressed semicircles, one at high-medium (HF-MF) frequencies and one at low frequencies (LF), which are partly overlapped with each other. Samples in alkanolamine-containing solutions show a higher diameter for both semicircles compared to the reference sample. Whereas, the Nyquist plot for the sample exposed to the solution at 20 °C in Fig. 6 presents one oval semicircle. At both temperatures, the diameter of the semicircles, which indicates the polarization resistance, is the highest for ethanolamine. The EIS results of the experiments at 20 °C and 80 °C were further analyzed using the numerical fitting with the most commonly used equivalent electrical systems related to corroding steel. The electrochemical system shown in Fig. 7a is a simple Randle's system with a single time constant, representing a homogeneous interface. The system has a solution resistance (R_s), a double layer capacitance (C_{dl}) and a charge transfer resistance (R_{ct}). This corresponding electrical equivalent circuit system was used to fit Nyquist plots results for the uninhibited sample at 20 °C experiments. Fig. 7b represents the second system well fitted with experimental data obtained at 20 °C for the inhibited sample and at 80 °C (Fig. 6) for all samples. The system has a double-time constant, signifying the presence of two layers. The system has a solution resistance (R_s), a film capacitance (C_{fc}), a pore resistance (R_{pr}), a double layer capacitance (C_{dl}) and a charge transfer resistance (R_{ct}). Different circuit element values as shown in Fig. 7 were fitted on the EIS data (Fig. 6) obtained in the solution without and with the initial injection of the alkanolamines at 20 and 80 °C and the results are listed in Table 5. The fitted data are discussed below.

Furthermore, to understand the effect of inhibitor injection on the kinetics of FeCO₃ formation, EIS measurements were conducted and the obtained Nyquist data are shown in Fig. 8 at various immersion times. Fig. 8a presents the Nyquist plots for the reference sample, note that an abrupt change in impedance values occurred before 32 hrs, which can be considered as the initial point for the formation of FeCO₃ corrosion product. Similarly, Fig. 8b and c show the cases for ethanolamine injected before and after the formation of FeCO₃ corrosion products, respectively. In Fig. 8b, when ethanolamine was injected and before the formation of FeCO₃, there is a gradual change in the impedance results with time until 52 hrs which is also consistent with LPR results (Fig. 5a), confirming the delay in FeCO₃ formation caused by an antagonistic steel surface/inhibitor interaction. However, in the third case when ethanolamine was injected after the formation of FeCO₃, the impedance trends were comparable to the reference sample. After 48 hrs, the amplitude for both cases is similar which may indicate a similar protectiveness conferred by the corrosion product layer on both samples. The evolution of various interfaces on the sample surface after the alkanolamine addition can be characterized with the fitted EIS parameters, as typically listed for triethanolamine injection in Table 6, using the equivalent circuit in Fig. 7b, which is commonly used to simulate the surface of an electrode with a top layer having a low conductivity [24, 25].

3.3.3. Surface characterizations

Fig. 9 shows the XRD patterns of the corrosion products formed on the specimens during the electrochemical experiments in the 1 wt% NaCl solution. Peaks corresponding to cementite (Fe₃C) were detected in the corrosion products at both 20 °C and 80 °C, whereas, siderite (FeCO₃) was only detected on the corroded surface at 80 °C. For injection frequency of the alkanolamines on steel at 20 °C, only Fe₃C was discovered along with the main GIXRD peak corresponding to the martensite. At 80 °C and pH 6.5, both Fe₃C and FeCO₃ (siderite) were identified in the GIXRD pattern. The high-intensity peak for siderite which was recorded at $2\theta = 48.40^\circ$ on the corroded samples at 80 °C corresponded to the (104) plane [48].

Fig. 10a, b and c represent cross-sectional SEM images of reference and ethanolamine and triethanolamine samples, respectively, after 24 hrs immersion in the solution at 80 °C. The SEM images show a

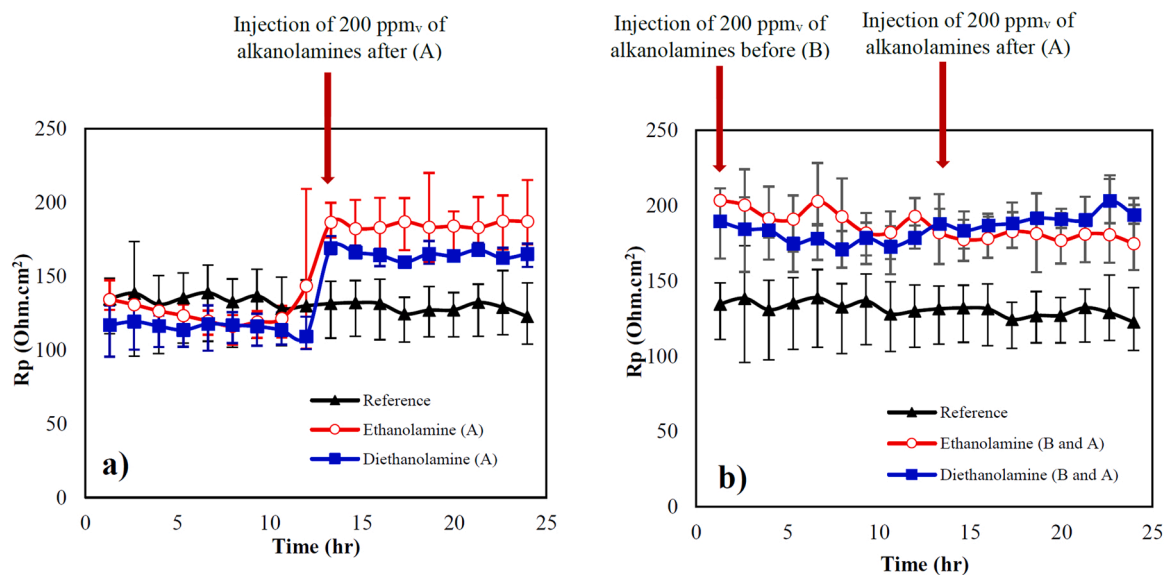


Fig. 4. Variations of polarization resistance vs time for L80-1 Cr steel exposed to 1 wt% NaCl solution at 20 °C, with different types of alkanolamines at 200 ppm_v concentration injected (a) injected after 12 hrs (A) and (b) injected initially and after 12 hrs (B and A) for 24 hrs experimental study.

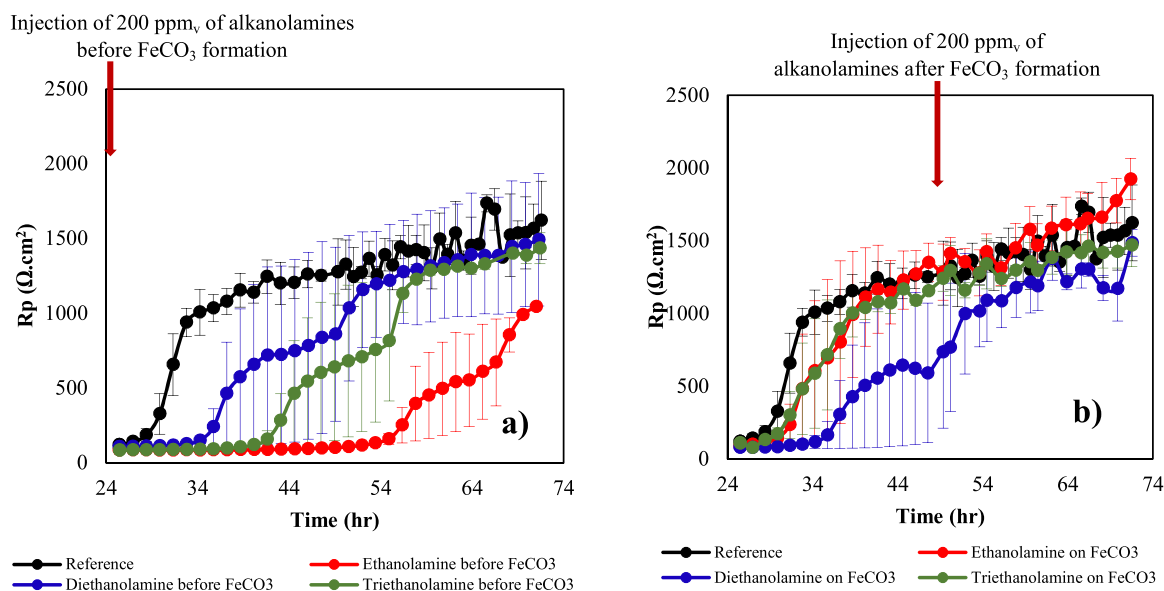


Fig. 5. Variations of polarization resistance vs time for L80-1 Cr steel exposed to 1 wt% NaCl solution at 80 °C, with different types of alkanolamines at 200 ppm_v concentration injected (a): before FeCO₃ products formation and (b): after FeCO₃ formation.

corrosion product layer with a similar thickness of about 30 μm for the samples, while the layers on the reference and triethanolamine samples (Fig. 11a and c) seem to be less dense (more porous) compared with ethanolamine. Fig. 10d typically represents the morphology of the corrosion products formed on the reference sample at 80 °C. The figure shows a layer with prismatic shape crystals covered the surface, which reveals the characteristic feature for iron carbonate as previously reported in the literature [29,49].

Fig. 11 shows the SEM images of the cross-section of the samples after implementing the inhibitor injection frequency cases at a temperature of 20 °C as explained in Fig. 1a. Based on the GIXRD patterns in Fig. 9, at 20 °C, no corrosion products were formed on the surface, and the thin layers presented on the surfaces in Fig. 11 are the Fe₃C that remained after ferrite oxidative dissolution. In Fig. 11a and b, when ethanolamine and diethanolamine were injected after 12 hrs of pre-corrosion, a thin adherent layer of Fe₃C was observed. In Fig. 11c and

d, however, when the alkanolamines were injected twice before and after 12 hrs, a more porous and non-adherent layer of Fe₃C is observable. Intermittent (cracked) porosities were also visible within the top layer (Fig. 11a and d).

Fig. 12 shows the cross-sectional and top-view SEM images of the anodically polarized sample exposed to the solution without and with triethanolamine at a temperature of 80 °C and pH 6.5. The EDS elemental maps of iron, carbon and oxygen taken from the cross-section of the sample inhibited by triethanolamine are also prepared in Fig. 12d. The results in Fig. 12 in conjunction with the GIXRD patterns indicate the presence of FeCO₃ corrosion products together with a residual Fe₃C network in the samples. Fig. 12a represents the reference sample, which shows a thick layer of FeCO₃ corrosion products (approx. 16 μm), where Fe₃C is incorporated between the surrounding FeCO₃ corrosion products. Fig. 12b and c represent the sample exposed to triethanolamine after and before the formation of FeCO₃ corrosion products,

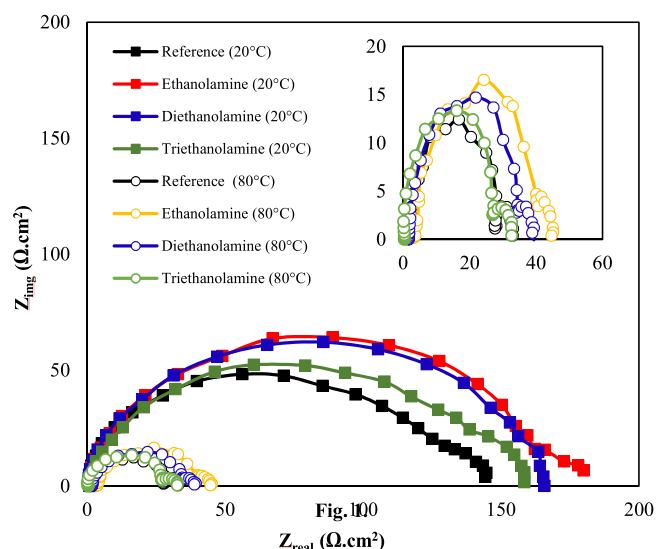


Fig. 6. Results of electrochemical impedance measurements: Nyquist plot for L80-1 Cr steel exposed to 1 wt% NaCl solution at 20 °C and 80 °C, without and with the addition of 200 ppmv of different alkanolamines after 24 hrs.

respectively. When triethanolamine was injected before (Fig. 12c), the FeCO_3 corrosion products are more porous and thicker (approx 0.18 μm) compared to the sample exposed with ethanolamine after the layer formation (Fig. 12b).

4. Discussion

The temperature variations between the limiting ranges of 20 – 80 °C in the oil production wells in the Danish sector can significantly change the corrosion resistance of utilized steel tubes. In general terms, the results presented in this paper confirm the importance of the temperature variations as one of the governing factors, which affects

both the nature and morphology of the corrosion products, influencing the corrosion behavior of 1Cr steel in a CO_2 environment. The results also showed how the use of the inhibitors and the injection times can alter the corrosion behavior and the kinetics of FeCO_3 formation (Figs. 3, 4, 5 and 8). This effect was linked to the characteristics of the FeCO_3 layer developed at higher temperatures influencing their protectiveness.

Although amines can act as the pH modifier of the solution, by which the corrosion behavior slightly changes; the basic inhibitive mechanism of amines is that they get chemically adsorbed (chemisorbed) on the steel surface [50,51]. The XPS spectra in Fig. 2 demonstrated that the interaction between the inhibitor and the steel surface is mainly due to the formation of a bond between the N electron pair and the electron cloud at the metal surface. In this interaction, the N-containing functional groups of amines act as the predominant unshared electron pair donors to the electron-depleted dehydrated steel surface [52]. The DFT calculations are consistent with this viewpoint, because the adsorption energies in Table 3 for binding with the nitrogen functional group are stronger than water and the alcohol functional group of the amines. As a

Table 5

EIS parameters obtained based on the fitted curves on experimental data according to equivalent circuit presented in Figs. 7a and 8b for L80-1 Cr steel exposed to 1 wt% NaCl solution at 20 °C and 80 °C, without and with the addition of 200 ppm_v of the different alkanolamines after 24 hrs.

Sample	R_{ct} Ω. cm ²	C_{dl} μΩ ⁻¹ . cm ⁻² .s ⁿ	n_1	R_{pr} Ω. cm ²	C_{fc} μΩ ⁻¹ . cm ⁻² .s ⁿ	n_2
At the temperature of 20 °C						
Reference	128	1235	0.77	–	–	–
Ethanolamine	19	110×10^3	0.84	170	747	1
Diethanolamine	17	64×10^3	0.85	141	700	0.98
Triethanolamine	12	199×10^3	0.81	136	861	0.99
At the temperature of 80 °C						
Reference	5	646×10^3	1.00	25	1104	0.99
Ethanolamine	12	893×10^3	0.86	31	1168	0.94
Diethanolamine	4	666×10^3	1.00	36	1158	0.95
Triethanolamine	4	632×10^3	0.91	30	1237	0.95

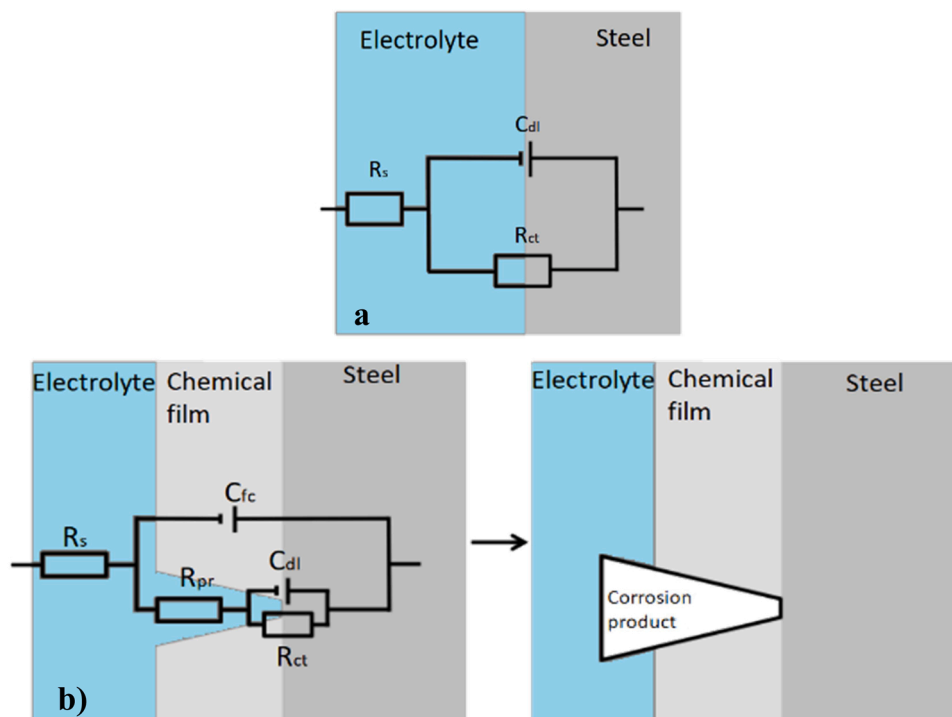


Fig. 7. (a) Simplified Randle's system showing a single layer interface, (b) a double-time constant circuit showing a perforated film interface or perforations filled with corrosion product.

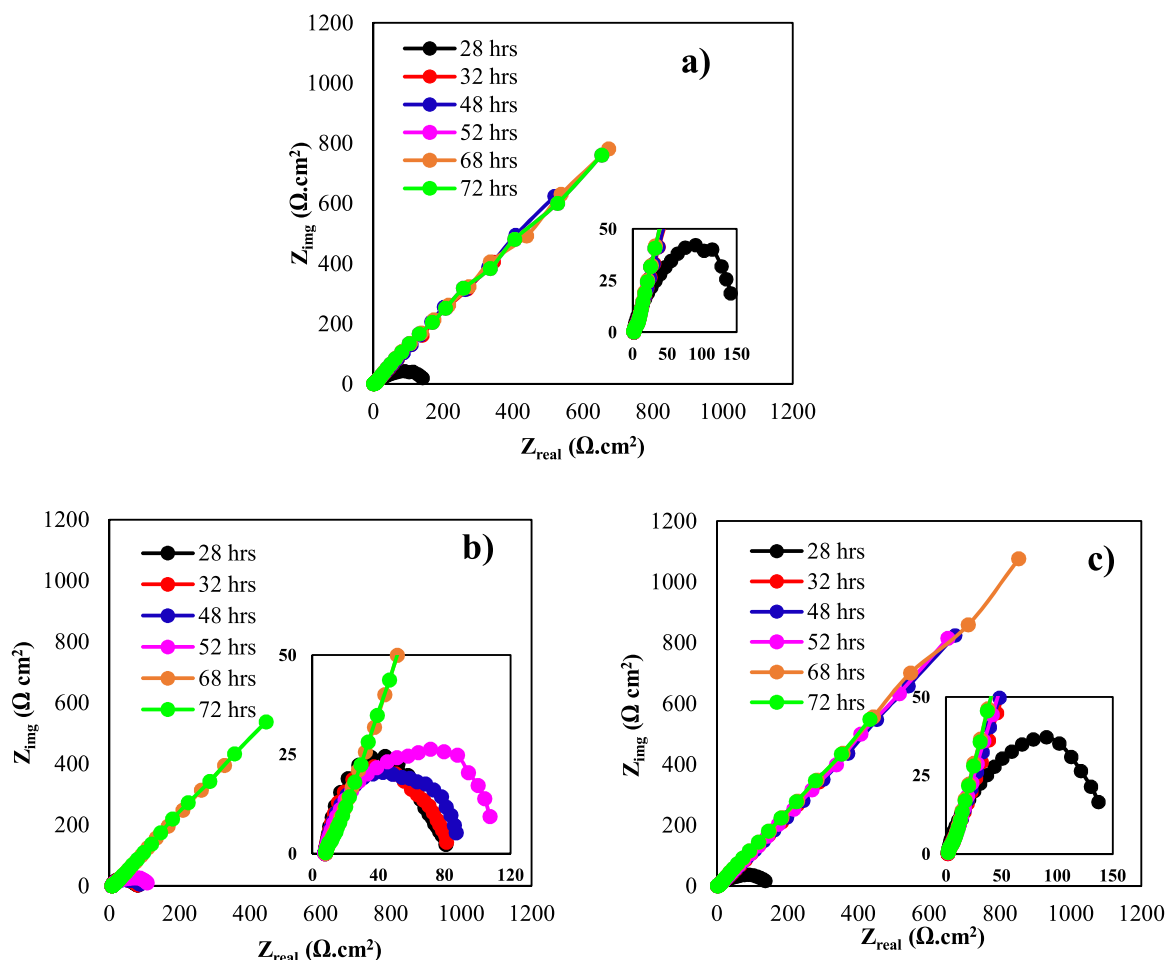


Fig. 8. Nyquist plots at different time intervals for (a) reference sample, (b) ethanolamine injected before the formation of FeCO_3 corrosion products and (c) ethanolamine injected after the FeCO_3 products were formed; on L80-1 Cr steel in 1 wt% NaCl solution at 80 °C.

Table 6

EIS spectra results based on fitted curves on experimental data obtained at various immersion times according to equivalent circuit in Fig. 7b for injection frequency experiments for L80-1 Cr steel exposed to 1 wt% NaCl solution at 80 °C, with triethanolamine at 200 ppm, concentration injected before and after the formation of the FeCO_3 corrosion products.

Test condition	Immersion time, hrs	R_{ct} $\Omega \cdot \text{cm}^2$	C_{dl} $\mu\Omega^{-1} \cdot \text{cm}^{-2} \cdot \text{s}^n$	n_1	R_{pr} $\Omega \cdot \text{cm}^2$	C_{fc} $\mu\Omega^{-1} \cdot \text{cm}^{-2} \cdot \text{s}^n$	n_2
Triethanolamine injection on FeCO_3	28	1466	17158	0.92	363	4489	0.95
	48	1658	15399	1.00	410	4015	1.00
	72	1783	9039	0.92	453	3783	0.86
Triethanolamine injection before FeCO_3 formation	28	19	59427	0.79	58	1083	0.95
	48	71	24455	0.87	68	1547	1.00
	72	1732	14097	0.92	432	3121	0.91

result of the strong surface bonds, in particular the negative difference in adsorption energy between the amine and water (Table 3), a durable top layer can potentially be formed and the iron dissolution on the underlying steel substrate can be limited. The calculations are consistent with the alkanolamine binding stronger than water for all surface models. This leads to the establishment of a higher corrosion resistance of 1Cr steel in the alkanolamine-containing NaCl solution as compared to the reference sample (see Fig. 3c, d, e and f). The iron dissolution resulted in a residual Fe_3C layer on the corroded surface (Fig. 11). When the alkanolamines were injected initially and after 12 hrs (Fig. 11c and d), the surface layer was more porous compared to that injected once at the beginning of the experiment (Fig. 11a and b). When the alkanolamines were injected for the first time, they immediately bind at the active sites on the steel surface (adsorption), leading to less iron dissolution. But, the subsequent desorption of the initially injected inhibitors happened after

the alkanolamines reinjection could cause the layer detachment as shown in Fig. 11c and d.

However, at the higher temperature (i.e., 80 °C), while the alkanolamines play a role in the morphology of FeCO_3 corrosion products (Fig. 12), the efficiency for the alkanolamines is comparatively low (Fig. 3c, d and Table 4). Table 5 shows that there is a difference in R_{ct} values at 20 °C and 80 °C in which the lower R_{ct} value is observed at a temperature of 80 °C. It should be pointed out that the overall adsorption property of nitrogen groups on the steel surface mainly depends on the bulkiness of the attaching groups [39]. But, the groups attached to N in all types of the alkanolamines used in this experiment are not bulky enough to strongly bond with the steel surface. On the other hand, the entropy of molecules adsorbing on a solid surface is about 2/3 of their corresponding gas or liquid phase entropy [53,54]. This means that for small inhibitor molecules, such as alkanolamines, which only replace

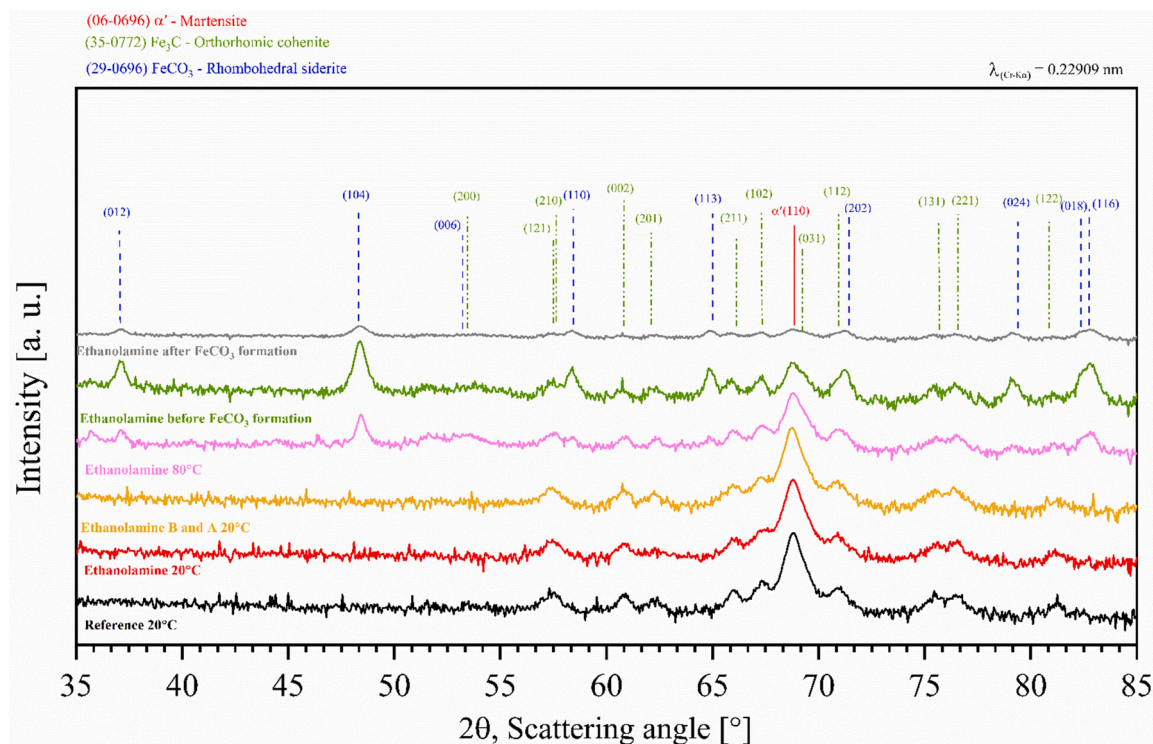


Fig. 9. Grazing incidence X-ray diffraction patterns for the corrosion products formed on steel surface at (a) 20 °C, pH 3.92, (b) 80 °C, pH 4.2 (c) 20 °C and pH 3.92 when alkanolamines were injected before and after 12 hrs, (d): 80 °C, pH 6.5 when alkanolamines were injected before FeCO₃ formation and (e): 80 °C, pH 6.5 when the alkanolamines were injected on a pre-formed FeCO₃ layer. The Cr-K α radiation with a wavelength (λ) of 0.22909 nm was used during the GIXRD experiments.

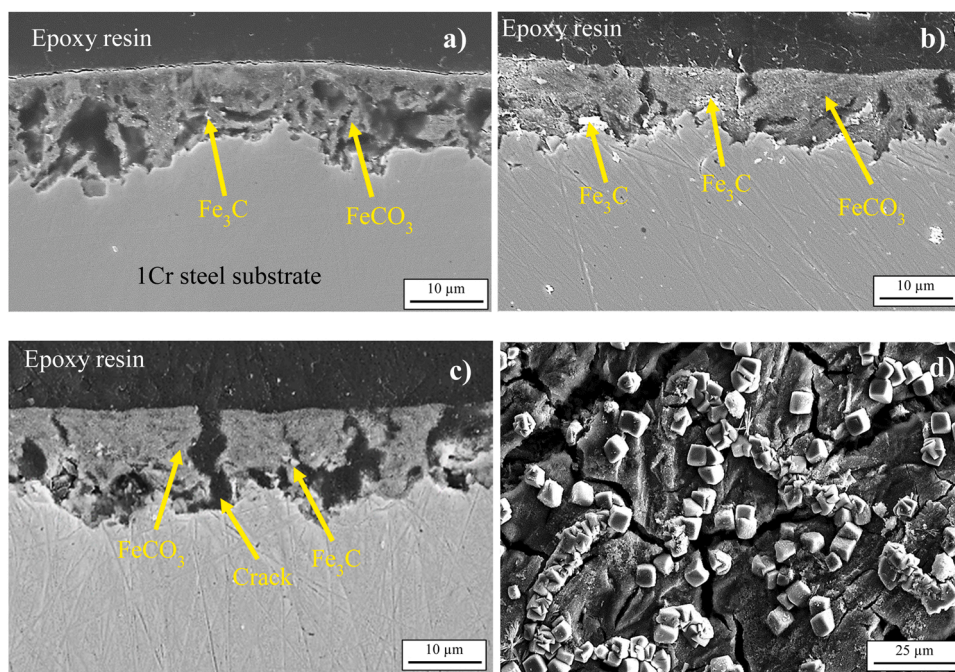


Fig. 10. SEM images for L80-1 Cr steel exposed to 1 wt% NaCl solution, (a): cross-sectional view of the sample without amine injection at 80 °C, (b): cross-sectional view of the sample exposed to the ethanolamine-containing solution at 80 °C, (c): cross-sectional view of the sample exposed to the triethanolamine-containing solution at 80 °C, (d): surface morphology of the reference sample without amine injection at 80 °C.

one (ethanolamine) and one or two (diethanolamine) water molecules from the surface, the entropy of the adsorption is negligible, because the loss of entropy of the adsorbing alkanolamines is almost cancelled by the entropy gaining by desorbing water molecule(s). However, since the alkanolamine molecule is bulkier than the water, the entropy of

adsorption can be slightly negative which disfavors the adsorption at the higher temperature. Therefore, the small alkanolamines in this study could easily desorb from the metal surface with time. Especially at elevated temperatures, the adsorption/desorption occurs faster and the free energy of the adsorption is weaker because of the unfavorable

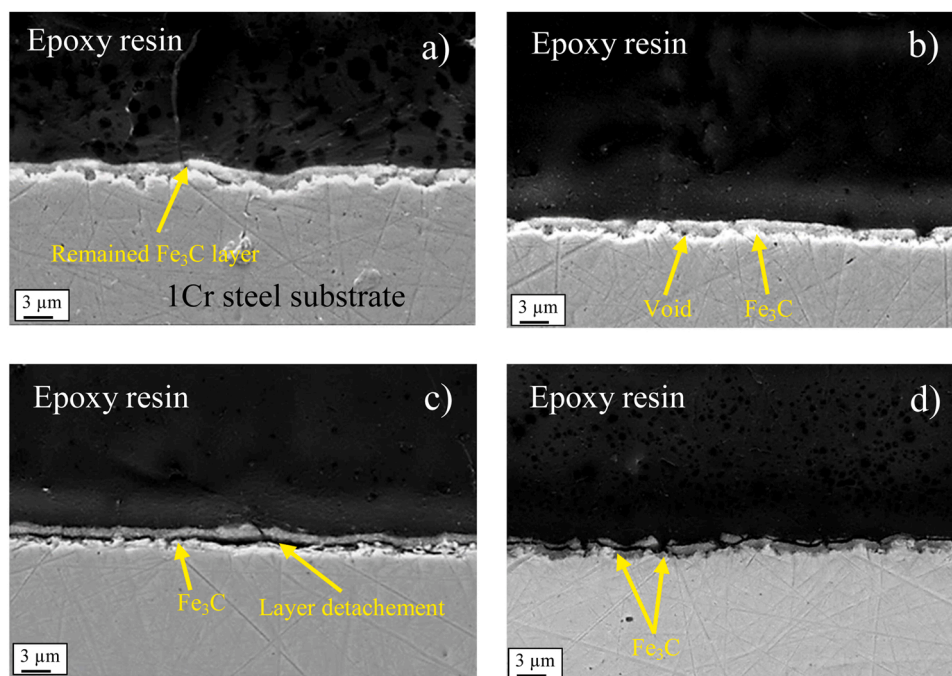


Fig. 11. Cross-sectional SEM images for L80-1 Cr steel exposed to 1 wt% NaCl solution at 20 °C, (a) ethanolamine injected after 12 hrs of the immersion, (b) diethanolamine injected after 12 hrs of the immersion, (c) ethanolamine injected before and after 12 hrs of the experiment, (d) diethanolamine injected before and after 12 hrs of the experiment.

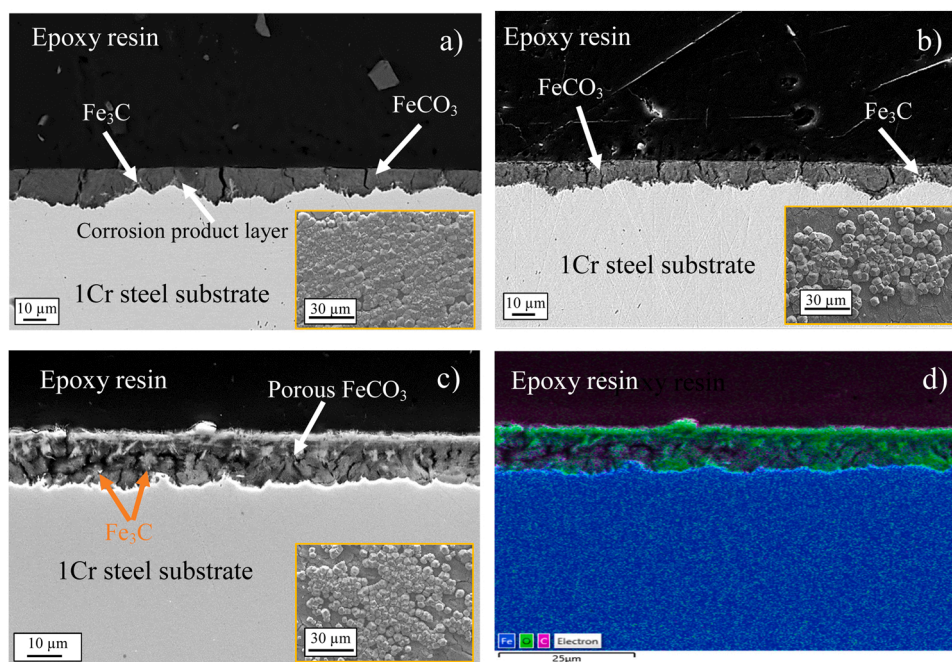


Fig. 12. Cross-sectional SEM images for L80-1 Cr steel exposed to 1 wt% NaCl solution at 80 °C; (a) without alkanolamines injection, (b) with triethanolamine injected on FeCO_3 corrosion products, (c) with triethanolamine injected before FeCO_3 corrosion products formation. The top view images are also inserted in the figures (d) EDS elemental map of iron, carbon and oxygen taken from the cross-section of the sample inhibited by triethanolamine presented in Fig. 12c.

entropy of adsorption. The easy desorption of the alkanolamines molecules from the surface resulted in a less corrosion inhibition at the higher temperature. Consequently, when the electrochemical conditions were provided for iron carbonate precipitation, a porous layer was formed (Fig. 12c). Therefore, the FeCO_3 layers did not provide any kind of protection to the steel surface (Fig. 5). As a result, the solution could readily penetrate the porosities and continued the dissolution of the underlying steel layer.

The calculated adsorption energy for ethanolamine is less negative than diethanolamine (see, Table 3). The reason is that the more bulky group attached to the N atom, the more the steric effect can be, leading to a weaker bond between amines and the steel surface. It means that among the different alkanolamines used in this study, ethanolamine has the less negative absorption energy level due to the nature of the attaching group to the N atom ($-\text{NH}$). However, the results show the highest R_{ct} value (Fig. 3 and Table 5) and efficiency (Table 4) for

ethanolamine, which is in contradiction to its absorption energy level. It is believed that depending on the size of the inhibitor molecules, water can be replaced from the steel surface by the inhibitor molecule, leading to a net increase in entropy, which in turn would lead to stronger binding. This has been observed e.g. for the amphiphilic molecule TOFA/DETA imidazoline molecule [55]. The bonding geometries of the inhibitor molecules on the Fe(110), Fe₃C(001) and FeCO₃(104) planes are presented in Fig. 13a-j. Generally, the atomic-scale distance between inhibitor molecules and those of the substrate provides an appropriate condition for the chemical bonding. The chemical structure of ethanolamine and diethanolamine bonded on the surface with the N-containing functional group is also schematically shown in Fig. 13k and l, respectively. Since ethanolamine has a single linear arrangement of atoms, if two molecules of ethanolamine cover the sample surface, then

the gap between both molecules is not enough (Fig. 13k) for the water molecule to come to contact with the sample surface on both Fe(110) (i. e., anode site) and Fe₃C(001) (cathode site) as shown in Fig. 13b and f, respectively. This limits the exposed areas of the surface to the solution and provides a better efficiency for corrosion inhibition. However, in the case of diethanolamine in Fig. 13l, the gap between two diethanolamine molecules is big enough for the water molecule to go in and contact with the sample surface. This means that although diethanolamine more strongly binds with the Fe surface, it results in a poorer corrosion resistance than ethanolamine, due to the interference of water molecules against the performance of diethanolamine.

In Table 3, the adsorption energy values for all three alkanolamines bonded to FeCO₃ corrosion products is similar regardless of the bonding geometries of the different inhibitor molecules on FeCO₃(104) in Fig. 13.

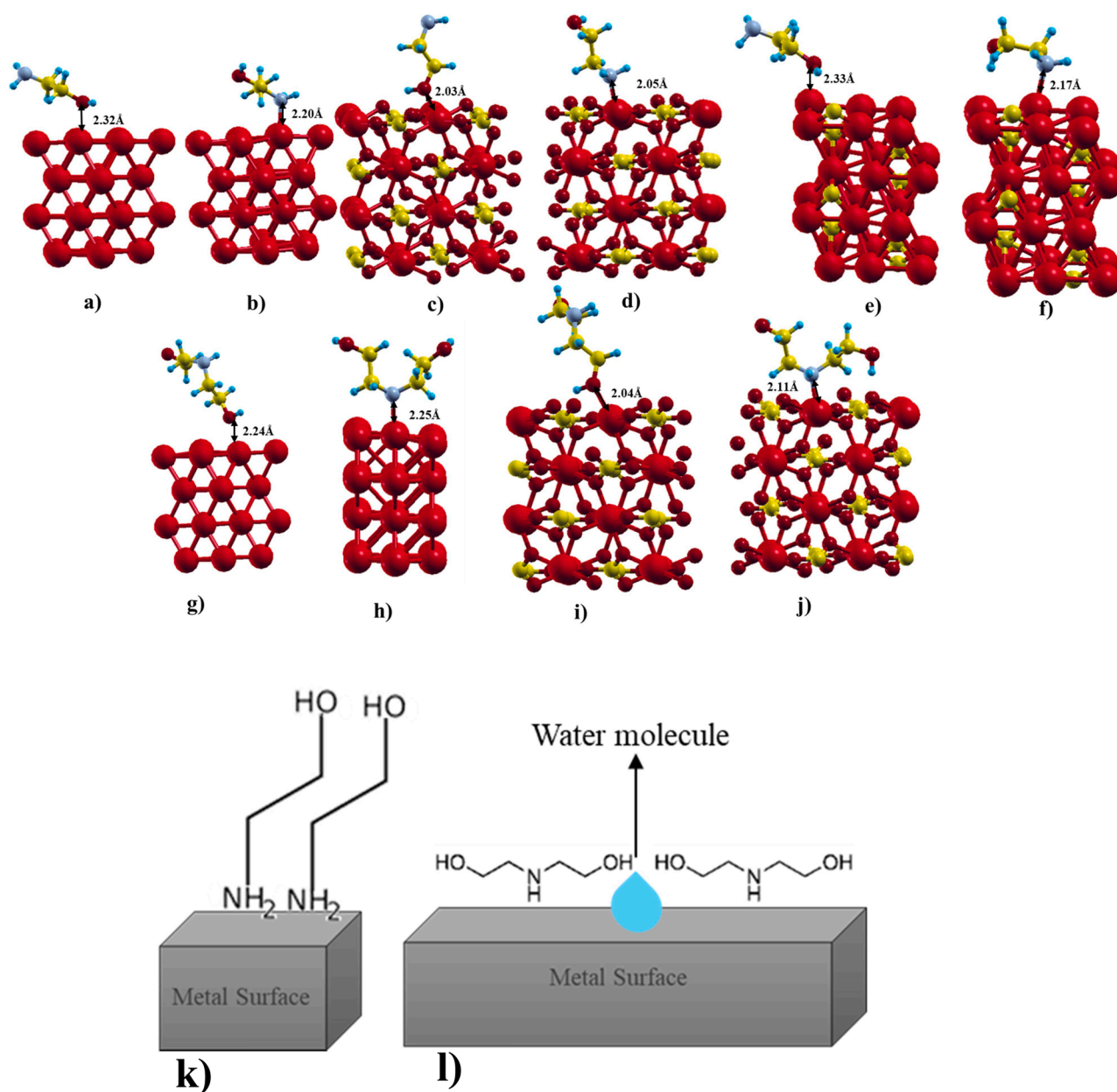


Fig. 13. Optimized bonding geometries for some inhibitor molecules on various model surfaces (a-j) and schematic view of packing efficiency difference between ethanolamine and diethanolamine (k-l). The bonding geometries are: ethanolamine bonded to (a) Fe(110) with -OH, (b) Fe(110) with -NH₂, (c) FeCO₃(104) with -OH, (d) FeCO₃(104) with -NH₂ group, (e) Fe₃C(001) with -OH, (f) Fe₃C(001) with -NH₂; diethanolamine bonded to: (g) Fe(110) with -OH, (h) Fe(110) with -NH group, (i) FeCO₃(104) with -OH, (j) FeCO₃(104) with -NH. The color code: bright red (large radius) = Fe, dark red (small radius) = O, blue-grey = N, yellow = C, aqua = H.

This led to no significant difference in the polarization resistance value after the injection of alkanolamines (Fig. 5b). For the samples with the pre-formed FeCO_3 top layer, the C_{fc} values in Table 6 gradually decreased, which indicates the further precipitation of the FeCO_3 layer as reported by Farelas et al. [56]. The C_{fc} decrease has been linked to the layer becoming denser and less porous [57], as confirmed by the increasing values of R_{pr} (see, Table 6), which also is consistent with the corrosion rate obtained by LPR with time (Fig. 5b). On the other hand, the solution could have penetrated the porosities and continued the dissolution of the underlying steel reflected by the decrease in C_{dl} . The slight increase in R_{ct} with time from $1466 \Omega \cdot \text{cm}^2$ to $1658 \Omega \cdot \text{cm}^2$ suggests that the precipitated FeCO_3 may have still given some degree of protection. However, the increase is too low for claiming a further protectiveness by this layer, and the fitted data confirm the LPR corrosion rate observed in Fig. 5a, which was almost constant.

However, when the alkanolamines were injected on the steel surface from the beginning of the experiment at the higher temperature, its molecules cover the metal surface and the saturation of Fe^{2+} is postponed to a longer time, thus the limited dissolution of the underlying steel layer continues as reflected by the decrease in C_{dl} with time (Table 6). Due to the absence of a protective corrosion product layer, R_{ct} insignificantly increased from the initial value of $19 \Omega \cdot \text{cm}^2$ to $71 \Omega \cdot \text{cm}^2$ after the immersion time of 48 hrs. Furthermore, once the solution was saturated with Fe^{2+} , the iron carbonate was formed on the surface sites other than those areas blocked by the triethanolamine, leading to a significant R_{ct} increase to $1732 \Omega \cdot \text{cm}^2$ after 72 hrs (Table 6). Later on, the triethanolamine desorption from the surface during FeCO_3 formation caused the generation of porosity within the corrosion product layer (Fig. 12c) [58].

5. Conclusions

Different electrochemical methods along with molecular modelling were used to study the effect of temperature (20°C and 80°C) on L80–1 Cr steel in the CO_2 -saturated 1 wt% NaCl electrolyte without and with the injection of different types of alkanolamines. The following main conclusions were drawn from this study:

- The chemical structures of the alkanolamines and adsorption energy of both $\text{Fe}(110)$ and $\text{FeCO}_3(104)$ played determining role in efficiently inhibiting the corrosion occurrence. Among the alkanolamines, ethanolamine had the best efficiency compared to the other alkanolamines, increasing the R_p value by about 70%.
- The DFT modelling showed that the observed inhibitor efficiency for the ethanolamine and diethanolamine correlated with the adsorption energy of the inhibitors on the model surfaces. Ethanolamine adsorption energy compared to water adsorption energy was favorable on all model surfaces. Ethanolamine was found to be significantly better at replacing water than diethanolamine was on the surface of the corrosion product FeCO_3 .
- The temperature of the solution also plays a role in the inhibitor efficiency of the alkanolamines. At the higher temperature, there was a lower efficiency of alkanolamines inhibitors, due to higher corrosion kinetics and more desorption of alkanolamines from the surfaces.
- The formation of the corrosion products (FeCO_3) was postponed due to the alkanolamine injection. When the alkanolamines were injected at the beginning of the experiment, a porous FeCO_3 corrosion product layer was formed, leading to a lower polarization resistance value.
- In the cases of injection frequencies, the reinjection of the alkanolamines did not provide more protectiveness than that by the pre-formed FeCO_3 layer.

CRedit authorship contribution statement

Shivangi Gupta: Conceptualization, Methodology, Investigation, Formal analysis, Writing - Original Draft, **Kapil Kumar Gupta:** Methodology, Investigation, Formal analysis, **Martin Andersson:** Validation, Writing - Original Draft, Writing - Review & Editing, Supervision, **Rouhollah Yazdi:** Conceptualization, Formal analysis, Supervision, Writing - Original Draft, Writing - Review & Editing, **Rajan Ambat:** Conceptualization, Supervision, Writing - Review & Editing, Project administration.

Declaration of Competing Interest

The authors declare that they have no known competing financial interests or personal relationships that could have appeared to influence the work reported in this paper.

Acknowledgements

The authors would like to thank the Danish Hydrocarbon Research and Technology Center (DHRTC) for providing financial funding and technical supports to this work. The Mechanical Engineering Department at the Technical University of Denmark is appreciatively acknowledged.

References

- [1] M.B. Kermani, A. Morshed, Carbon dioxide corrosion in oil and gas production—A compendium, *Corros. Sci. Eng.* 59 (2003) 659–683.
- [2] C. De Waard, D.E. Milliams, Carbonic acid corrosion of steel, *Corrosion* 31 (1975) 177–181.
- [3] R.H. Hausler, H.P. Gaddart, *Advances in CO₂ corrosion vol. 1*, Houston TX, 1985.
- [4] R.H. Hausler, H.P. Gaddart, *Advances in CO₂ corrosion vol. 2*, Houston TX, 1986.
- [5] M. Rogowska, J. Gudme, A. Rubin, K. Pantleon, R. Ambat, Effect of Fe ion concentration on fatigue life of carbon steel in aqueous CO_2 environment, *Corros. Eng. Sci. Technol.* 51 (2016) 90–103.
- [6] M. Rogowska, J. Gudme, A. Rubin, K. Pantleon, R. Ambat, Effect of Fe ion concentration on corrosion of carbon steel in CO_2 environment, *Corros. Eng. Sci. Technol.* 51 (2016) 25–36.
- [7] S. Nešić, Key issues related to modelling of internal corrosion of oil and gas pipelines - A review, *Corros. Sci.* 49 (2007) 4308–4338.
- [8] A. Kahyarian, B. Brown, S. Nestic, Mechanism of CO_2 corrosion of mild steel: A new narrative, in: *NACE - Int. Corros. Conf. Ser.*, 2018: pp. 1–16.
- [9] T. das, C. Almeida, M.C.E. Bandeira, R.M. Moreira, O.R. Mattos, New insights on the role of CO_2 in the mechanism of carbon steel corrosion, *Corros. Sci.* 120 (2017) 239–250.
- [10] H. Fang, S. Nestic, B. Brown, S. Wang, General CO_2 corrosion in high salinity brines, in: *NACE - Int. Corros. Conf. Ser.*, 2006: pp. 1–15.
- [11] M. Nordsveen, S. Nešić, R. Nyborg, A. Stangeland, A mechanistic model for carbon dioxide corrosion of mild steel in the presence of protective iron carbonate films - Part 1: Theory and verification, *Corrosion* 59 (2003) 443–456.
- [12] S. Nešić, M. Nordsveen, R. Nyborg, A. Stangeland, A mechanistic model for carbon dioxide corrosion of mild steel in the presence of protective iron carbonate films—part 2: a numerical experiment, *Corrosion* 59 (2003) 489–497.
- [13] D.A. López, W.H. Schreiner, S.R. De Sánchez, S.N. Simison, The influence of carbon steel microstructure on corrosion layers: An XPS and SEM characterization, *Appl. Surf. Sci.* 207 (2003) 69–85.
- [14] Z.D. Cui, S.L. Wu, C.F. Li, S.L. Zhu, X.J. Yang, Corrosion behavior of oil tube steels under conditions of multiphase flow saturated with super-critical carbon dioxide, *Mater. Lett.* 58 (2004) 1035–1040.
- [15] M.B. Valcarce, M. Vázquez, Carbon steel passivity examined in alkaline solutions: The effect of chloride and nitrite ions, *Electrochim. Acta* 53 (2008) 5007–5015.
- [16] W. Sun, K. Chokshi, S. Nestic, D.A. Gulino, A study of protective iron carbonate scale formation in CO_2 corrosion, *AIChE Annu. Meet. Conf. Proc.* (2004) 5063–5071.
- [17] J.B. Sun, G.A. Zhang, W. Liu, M.X. Lu, The formation mechanism of corrosion scale and electrochemical characteristic of low alloy steel in carbon dioxide-saturated solution, *Corros. Sci.* 57 (2012) 131–138.
- [18] T. Li, Y. Yang, K. Gao, M. Lu, Mechanism of protective film formation during CO_2 corrosion of X65 pipeline steel, *J. Univ. Sci. Technol. Beijing Miner. Metall. Mater. (Eng. Ed.)* 15 (2008) 702–706.
- [19] W. Sun, S. Nešić, Kinetics of corrosion layer formation: Part 1 - Iron carbonate layers in carbon dioxide corrosion, *Corrosion* 64 (2008) 334–346.
- [20] V. Ruzic, M. Veidt, S. Nešić, Protective iron carbonate films -Part 2: Chemical removal by dissolution in single-phase aqueous flow, *Corrosion* 62 (2006) 598–611.

- [21] V. Ruzic, M. Veidt, S. Nešić, Protective iron carbonate films - Part 3: Simultaneous chemo-mechanical removal in single-phase aqueous flow, *Corrosion* 63 (2007) 758–769.
- [22] V. Ruzic, M. Veidt, S. Nešić, Protective iron carbonate films — Part 1: Mechanical removal in single-phase aqueous flow, *Corrosion* 62 (2006) 419–432.
- [23] S. Wang, K. George, S. Nestic, High pressure CO₂ corrosion electrochemistry and the effect of acetic acid, *Corrosion* (2004) 1–17.
- [24] K. George, S. Nestic, C. De Waard, Electrochemical investigation and modeling of carbon dioxide corrosion of carbon steel in the presence of acetic acid, in: *NACE Meet. Pap.*, 2004: pp. 1–25.
- [25] Z.F. Yin, Y.R. Feng, W.Z. Zhao, Z.Q. Bai, G.F. Lin, Effect of temperature on CO₂ corrosion of carbon steel, *Surf. Interface Anal.* 41 (2009) 517–523.
- [26] M.B. Tomson, M.L. Johnson, How ferrous carbonate kinetics impacts oilfield corrosion, *Soc. Pet. Eng.* (1991) 257–264.
- [27] F. de Moraes, J.R. Shadley, J. Chen, E.F. Rybicki, Characterization of CO₂ corrosion product scales related to environmental conditions, *Corrosion* (2000).
- [28] A. Munoz, J. Genesca, R. Duran, J. Mendoza, Mechanism of FeCO₃ formation on API X70 pipeline steel in brine solutions containing CO₂, *Proc. Corros.* (2005) 1–14.
- [29] A. Dugstad, Mechanism of protective film formation during CO₂ corrosion of carbon steel, *Corrosion* (1998) 1–11.
- [30] B.M. Miksic, A.Y. Furman, M.A. Kharshan, Effectiveness of the corrosion inhibitors for the petroleum industry under various flow conditions, in: *NACE - Int. Corros. Conf. Ser.*, 2009: pp. 1–9.
- [31] M.N. Rahuma, M.B. EL-Sabbah, I.M. Hamad, Effect of serine and methionine on electrochemical behavior of the corrosion of mild steel in aqueous solutions, *ISRN Corros.* (2013) 1–7.
- [32] I. Jevremović, V. Misković-Stanković, The inhibitive effect of ethanolamine on corrosion behavior of aluminium in NaCl solution saturated with CO₂, *Metall. Mater. Eng.* 18 (2012) 241–257.
- [33] I.C. Ivonye, *Corrosion processes and mechanisms in the presence of monoethylene glycol (MEG)*, The University of Leeds, 2014.
- [34] M.P. Desimone, G. Gordillo, S.N. Simison, The effect of temperature and concentration on the corrosion inhibition mechanism of an amphiphilic amido-amine in CO₂ saturated solution, *Corros. Sci.* 53 (2011) 4033–4043.
- [35] K. Khanari, N. Grah, M. Finšgar, R. Fuchs-Godec, U. Maver, Corrosion inhibition and surface analysis of amines on mild steel in chloride medium, *Chem. Pap.* 71 (2017) 81–89.
- [36] R. Rihaan, R. Shawabkeh, N. Al-Bakr, The effect of two amine-based corrosion inhibitors in improving the corrosion resistance of carbon steel in sea water, *J. Mater. Eng. Perform.* 23 (2014) 693–699.
- [37] P. Giannozzi, S. Baroni, N. Bonini, M. Calandra, R. Car, C. Cavazzoni, D. Ceresoli, G.L. Chiarotti, M. Cococcioni, I. Dabo, A. Dal Corso, S. de Gironcoli, S. Fabris, G. Fratesi, R. Gebauer, U. Gerstmann, C. Gougousis, A. Kokalj, M. Lazzeri, L. Martin-Samos, N. Marzari, F. Mauri, R. Mazzarello, S. Paolini, A. Pasquarello, L. Paulatto, C. Sbraccia, S. Scandolo, G. Sclauzero, A.P. Seitsonen, A. Smogunov, P. Umari, R.M. Wentzcovitch, QUANTUM ESPRESSO: a modular and open-source software project for quantum simulations of materials, *J. Phys. Condens. Matter* (2009) 1–36.
- [38] Y. Zhang, W. Yang, Comment on “generalized gradient approximation made simple”, *Phys. Rev. Lett.* 80 (1998) 890.
- [39] M.P. Andersson, Density functional theory with modified dispersion correction for metals applied to self-assembled monolayers of thiols on Au(111), *J. Theor. Chem.* (2013) 1–9.
- [40] S. Grimme, Semiempirical GGA-type density functional constructed with a long-range dispersion correction, *J. Comput. Chem.* 27 (2006) 1787–1799.
- [41] V. Barone, M. Casarin, D. Forrer, M. Pavone, M. Sambri, A. Vittadini, Role and effective treatment of dispersive forces in materials: Polyethylene and graphite crystals as test cases, *J. Comput. Chem.* 30 (2009) 934–939.
- [42] S. Ehrlich, J. Moellmann, W. Reckien, T. Bredow, S. Grimme, System-dependent dispersion coefficients for the DFT-D3 treatment of adsorption processes on ionic surfaces, *ChemPhysChem* 12 (2011) 3414–3420.
- [43] E. Ataman, M.P. Andersson, M. Ceccato, N. Bovet, S.L.S. Stipp, Functional group adsorption on calcite: I. oxygen containing and nonpolar organic molecules, *J. Phys. Chem. C* 120 (2016) 16586–16596.
- [44] E. Ataman, M.P. Andersson, M. Ceccato, N. Bovet, S.L.S. Stipp, Functional group adsorption on calcite: II. Nitrogen and sulfur containing organic molecules, *J. Phys. Chem. C* 120 (2016) 16597–16607.
- [45] A. Dal Corso, Pseudopotentials periodic table: From H to Pu, *Comput. Mater. Sci.* 95 (2014) 337–350.
- [46] A. Dal Corso, *PSLibrary: A library of ultrasoft and PAW pseudopotentials*, (2020).
- [47] M.A. Amin, S.S. Abd El-Rehim, E.E.F. El-Sherbini, R.S. Bayoumi, The inhibition of low carbon steel corrosion in hydrochloric acid solutions by succinic acid: Part I. Weight loss, polarization, EIS, PZC, EDX and SEM studies, *Electrochim. Acta* 52 (2007) 3588–3600.
- [48] R. Rizzo, S. Gupta, M. Rogowska, R. Ambat, Corrosion of carbon steel under CO₂ conditions: Effect of CaCO₃ precipitation on the stability of the FeCO₃ protective layer, *Corros. Sci.* 162 (2020) 1–12.
- [49] A. Dugstad, Fundamental aspects of CO₂ metal loss corrosion, Part I: mechanism, *Corrosion* (2015) 1–12.
- [50] L. Bin Zhao, R. Huang, M.X. Bai, D.Y. Wu, Z.Q. Tian, Effect of aromatic amine-metal interaction on surface vibrational Raman spectroscopy of adsorbed molecules investigated by density functional theory, *J. Phys. Chem. C* 115 (2011) 4174–4183.
- [51] R. Banerjee, S.N. Malhotra, Contribution to adsorption of aromatic amines on mild steel surface from HCl solutions by impedance, UV, and Raman spectroscopy, *Corrosion* 48 (1992) 10–15.
- [52] N. Goudarzi, M. Peikari, M. Reza Zahiri, H. Reza Mousavi, Adsorption and corrosion inhibition behavior of stainless steel 316 by aliphatic amine compounds in acidic solution, *Arch. Metall. Mater.* 57 (2012) 845–851.
- [53] C.T. Campbell, J.R.V. Sellers, The entropies of adsorbed molecules, *J. Am. Chem. Soc.* 134 (2012) 18109–18115.
- [54] A. Budi, S.L.S. Stipp, M.P. Andersson, Calculation of entropy of adsorption for small molecules on mineral surfaces, *J. Phys. Chem. C* 122 (2018) 8236–8243.
- [55] I. Jevremović, M. Singer, S. Nešić, V. Misković-Stanković, Inhibition properties of self-assembled corrosion inhibitor talloil diethylenetriamine imidazole for mild steel corrosion in chloride solution saturated with carbon dioxide, *Corros. Sci.* 77 (2013) 265–272.
- [56] F. Farelàs, M. Galicia, B. Brown, S. Nestic, H. Castaneda, Evolution of dissolution processes at the interface of carbon steel corroding in a CO₂ environment studied by EIS, *Corros. Sci.* 52 (2010) 509–517.
- [57] C. Liu, Q. Bi, A. Leyland, A. Matthews, An electrochemical impedance spectroscopy study of the corrosion behavior of PVD coated steels in 0.5 N NaCl aqueous solution: part I. Establishment of equivalent circuits for EIS data modelling, *Corros. Sci.* 45 (2003) 1243–1256.
- [58] C. Liu, Q. Bi, A. Leyland, A. Matthews, An electrochemical impedance spectroscopy study of the corrosion behavior of PVD coated steels in 0.5 N NaCl aqueous solution: Part II. EIS interpretation of corrosion behaviour, *Corros. Sci.* 45 (2003) 1257–1273.





6. Paper II: Electrochemical and molecular modelling studies of corrosion inhibition characteristics of Imidazolines on 1Cr steel under sweet conditions and annexure to the investigation of corrosion inhibition effects of 2-Phenyl-2-Imidazoline on 1Cr steel with CO₂: Effect of H₂S

Shivangi Gupta, Martin Andersson, Rajan Ambat, Electrochemical and molecular modelling studies of corrosion inhibition characteristics of Imidazolines on 1Cr steel under sweet conditions, submitted to *Electrochimica Acta*, 2022

Electrochemical and molecular modelling studies of corrosion inhibition characteristics of Imidazolines on 1Cr steel under sweet conditions

Shivangi Gupta^{a*}, Martin Andersson^b, Rajan Ambat^a

^a Section of Materials and Surface Engineering, Department of Mechanical Engineering, Technical University of Denmark, Produktionstorvet, Kongens Lyngby, 2800 Denmark

^b Department of Chemical Engineering, Technical University of Denmark, Produktionstorvet, Kongens Lyngby, 2800 Denmark

*Corresponding author. Tel: +45 60773762, E-mail address: shig@mek.dtu.dk (S. Gupta).

Abstract

Organic compounds such as imidazoline derivatives are commonly used as corrosion inhibitors. The objective of this study was to characterize the corrosion inhibition properties of two different forms of imidazoline, 2-Methyl-2-imidazoline (2-MI), and 2-Phenyl-2-imidazoline (2-PI), with and without the presence of mono ethylene glycol (MEG) on a steel surface under CO₂ corrosion condition. Electrochemical, surface characterization, and molecular modelling methods were used to study the corrosion inhibition properties and underlying mechanisms. In the pure form, 2-PI had higher corrosion inhibition efficiency than 2-MI, likely due to stronger adsorption to the steel surface, as confirmed by molecular modelling. The addition of MEG improved the inhibitor efficiency of both 2-MI and 2-PI.

Keywords: A. Steel, B. Polarization, B. EIS, B. XPS, C. Oxidation.

1. Introduction

Corrosion in CO₂ environment is of great relevance in oil and gas industry as it leads to frequent maintenance issues and safety hazards. One of the materials that is frequently used in oil and gas industry is low carbon steel due to its low cost. However, low carbon steel is prone to corrosion under CO₂ environment, warranting investigation of corrosion prevention methods. Use of inhibitors is one of the methods that can be utilized for corrosion inhibition of steel surfaces in CO₂ environment.

Among the various organic compounds that are currently being used for corrosion inhibition, derivatives of imidazoline are highly preferred due to their high corrosion inhibition efficiency and low toxicity. The imidazoline adheres to the metallic surface and also repels substances that are present in the medium [1]. Therefore, minimal concentrations of inhibitors are required for better efficiencies, leading to lower environmental toxicity [1].

Imidazoline commonly exist in 3 isomeric forms – 2-imidazoline, 3-imidazoline, and 4-imidazoline and the 2-imidazoline isomer is the most commonly found [2,3]. The derivatives of imidazoline like 2-Methyl-2-imidazoline and 2-Phenyl-2-imidazoline have shown to provide high efficiencies in different environments on different metals [1,4–6]. For example, high corrosion inhibition efficiency (> 80%) have been reported for 2-MI and 2-PI on 1018 Carbon Steel in sulphuric environment [7]. The inhibition properties of imidazoline is thought to depend on the adsorption of the hydrophilic group of the inhibitor molecule to the metal surface. The adsorption behavior is specific to both - the functional group of the inhibitor, and the nature of the metal surface on which the molecules are adsorbed [8]. The corrosion inhibition of 2-PI is larger than 2-MI, which is likely due to stronger adsorption of the larger phenyl group than the methyl group on the steel surface [7]. The corrosion inhibition of imidazoline inhibitors and their adsorption mechanisms are yet to be investigated on steel in a CO₂ environment.

Some imidazoline can be prone to hydrolysis, especially in highly acidic environment and at higher temperatures due to breaking of the C-N bond by protonation [9]. The hydrolysis can reduce the corrosion inhibition ability of these inhibitors over time after the initial injection [9,10]. The decline in inhibition properties of imidazoline may be mitigated by re-injecting another dose of these inhibitors over time. The effects of re-injection of imidazoline also on the steel surface in CO₂ environment still needs to be investigated.

Lastly, addition of other organic compounds such as mono ethylene glycol (MEG) have shown to improve the efficiency of imidazoline derivatives in different environments [7,11,20,21,12–19]. These improvements are thought to result from improved coverage of the metal surface with the inhibitor complex (imidazoline with MEG). Therefore, it is important to understand the synergistic effect of ethylene glycol and imidazoline on corrosion of steel in the CO₂ environment.

Therefore, the objectives of this study was to investigate the corrosion inhibition properties of imidazoline derivatives such 2-MI and 2-PI alone and in combination with ethylene glycol on steel surface in CO₂ environment. In addition, this study investigated the effect of injection frequency on corrosion inhibition properties of imidazoline to understand if subsequent doses of inhibitor can help mitigate the lowering of corrosion rate over time. This study utilized experimental methods such as Open Circuit Potential (OCP), Linear Polarization Resistance (LPR) and Electrochemical Impedance Spectroscopy (EIS). In addition, molecular modelling using density functional theory (DFT) was used to study the adsorption behavior of different functional groups of the desired molecule on steel surface. Lastly, surface characterization techniques such as scanning electron microscopy (SEM) equipped with energy dispersive spectroscopy (EDS), X-ray diffraction (XRD), and X-ray photoelectron spectroscopy (XPS) were utilized to understand scale formation and inhibitor adsorption.

2. Materials and methods

2.1. Specimen preparation for the experimental study

Low carbon steel (L-80 1Cr steel) samples were used for this study (chemical composition listed in Table 1). Specimens of 10mm x 10mm cylinders were machined with a total surface area of 3.9 cm². The sample surface was polished mechanically using SiC paper (grades P220, P320, P500, and P1000) with de-ionized water as lubricant. The specimens were then cleaned with ethanol and de-ionized water, and air-dried. Electrochemical experiments were conducted on the prepared samples following which the specimens were cleaned again using the same process and stored in a desiccator for further characterization.

Table 1. Chemical composition in wt % of the L80-1 Cr material.

Material	C	Cr	Mn	Mo	P	Si	S	Fe
API 5CT L80	0.40	1.10	0.75	0.20	≤0.035	0.20	≤0.040	base

2.2. Electrolyte preparation

The electrochemical experiments were carried out with and without 2-MI and 2-PI in 1 wt. % NaCl solution saturated with CO₂. In some experiments, the NaCl solution was mixed with 20 volume % MEG (300 ml) of total cell solution.

The solution was deaerated by sparging the nitrogen gas overnight before running the experiment. The solution was then saturated with CO₂ for 4 hours. The initial pH of the NaCl solution without and with MEG was measured to be 3.9 and 4.2, respectively at 40 °C. The solution was then injected with 200 parts per million by volume (ppm_v) of the test inhibitor. After inhibitor injection, the solution was de-aerated again for at least 30 minutes. The CO₂ gas was continuously purged into the solution to maintain its saturation and avoid any oxygen entrance during the electrochemical tests.

Inhibitors used

2-Methyl-2-imidazoline (purity of 95%), 2-Phenyl-2-imidazoline (purity of ≥ 96%) and MEG of spectrophotometric grade (≥ 99%) was purchased from Sigma Aldrich (chemical structures shown in Fig. 1).

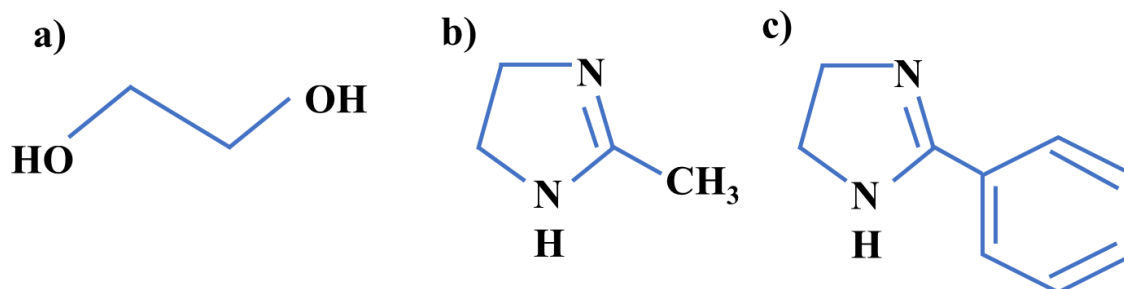


Figure 1. Structure of (a): Ethylene glycol, (b): 2-Methyl-2-imidazoline, (c): 2-Phenyl-2-imidazoline.

2.3. Electrochemical measurement

A standard three-electrode glass cell (1.5 L) setup was used for the electrochemical corrosion tests. The reference Ag/AgCl electrode was placed in the solution using a glass-luggin capillary. The counter electrode was made of concentric ring of platinum wire. Linear Polarization Resistance technique was used to measure the corrosion potential (E_{corr}) and the corrosion rate every 1.5 hours. A potential range of ± 10 mV vs. open-circuit potential (OCP) at a scan rate of 0.167 mV/s was used during the LPR measurements. OCP stabilization was achieved in 1 hour and the EIS measurements were performed by applying ± 10 mV AC signal vs OCP in a frequency range of 10 mHz -10 kHz.

2.4. Experimental conditions and procedure

The inhibitive effects of 2-MI(200 ppm), 2-PI(200 ppm), MEG (20 vol% of total cell solution = 300ml) and a combination of MEG-2-MI and MEG-2-PI were studied on the CO₂ corrosion of L80-1 Cr steel samples at 40 °C (see Table 2 for experimental conditions). For electrochemical experiments, the inhibitors were injected 30 minutes before the immersion of specimens. Both types of imidazoline were injected alone or in combination with MEG to study their effects on corrosion inhibition. In another set of experiment, the 2-PI was intermittently injected (Fig. 2) in the NaCl solution to study the effect of injection frequency on the corrosion behavior of L80-1 Cr steel. This was achieved by comparing the effects of single injection (case I) of 200 ppm_v inhibitor that was injected 30 minutes before the sample immersion in the NaCl solution with the repeated injections (case II) of the inhibitors. For the repeated injections, after the initial dose, another 200ppm of inhibitor was injected after 48 hours of sample immersion. All electrochemical experiments were performed at least twice and the error bars represent the maximum and minimum values observed in repeated experiments are reported in the results section.

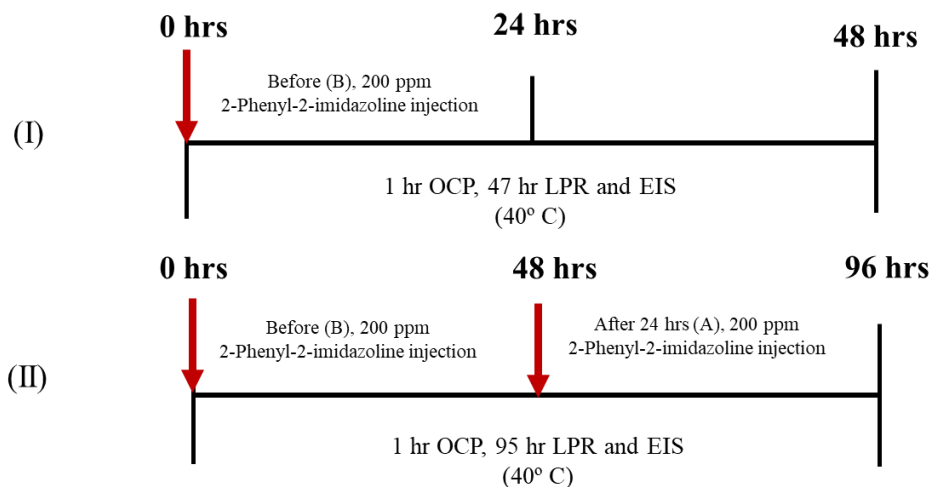


Figure 2. Inhibitor injection frequency (2-PI) on L80-1Cr steel in 1% NaCl solution at 40° C.

Table 2. Experimental conditions of electrochemical experiments used in this study.

Parameter	Condition
Material	Q&T 1Cr steel
Solution	1 wt.% NaCl in deionized distilled water, CO ₂ saturated
Temperature	40 °C
CO ₂ partial pressure	0.93 bar
Rotation	350 rpm
Inhibitor concentration	200ppm
Test duration	48 and 140 hrs

2.5. Surface characterization and phase analysis

The surface morphology of the corroded samples were investigated using a Zeiss Supra FEG-SEM using 5 kV acceleration voltage, assisted with energy dispersive X-ray (EDS) analysis equipment. Phase analysis of the corrosion layer was performed using a Bruker D8 Advance X-ray Diffractometer (XRD) technique. The operating parameters for XRD were 35 kV and 50 mA with Cr-K α radiation ($\lambda=0.22909$ nm). The 2θ ranged between 45° and 85° with a step size of 0.05° , and a 10 s count time at each step.

X-ray photoelectron spectroscopy (XPS) was recorded using a commercial XPS-Thermo Scientific system. The base pressure in the experimental chamber was below 10^{-9} mbar. The spectra were collected using Al K α X-ray source (1486.6 eV) radiation and the overall energy resolution was about 0.8 eV. High-resolution scans with 0.1 eV steps were conducted over the following regions of interest: C 1s, N 1s, Fe 2ps and O 1s. Surface charging effects were compensated by referencing the binding energy (BE) to the C 1s line of residual carbon set at 285.0 eV BE. XPS spectra were deconvoluted using a non-linear least-squares algorithm with a Shirley baseline and a Gaussian–Lorentzian combination. Thermo Avantage software, version 5.9913, was used for all XPS data processing.

2.6. Computational details

The Quantum Espresso package was used to perform DFT calculations in a pseudopotential plane wave formalism [22]. The adsorption energies for water, MEG and the different types of imidazoline on Fe(110) were calculated. The DFT-D2 method was used with the revPBE functional [23] and additional semi-empirical dispersion corrections [24–26]. In particular, appropriate methods for adsorption on metal surfaces was used [24][27]. The modelling parameters used for Fe calculations in this study were same as the previous study on alkanolamine [28]: s_6 for revPBE = 1.25; Bohr cutoff for Fe calculations = 12 ; and C6 vdw parameter for Fe = 159.927 [24]. The revPBE functional was used to generate all pseudopotentials (ultrasoft or PAW) and were taken from the PS Library 0.2.5 [29,30]. The cutoff values for kinetic energy and density were 40 Ry and 400 Ry, respectively [31,32].

The 2-MI and 2-PI molecules are large and bulky, requiring very large unit cells, which makes calculations of adsorption very slow. The adsorption energies for water, MEG, 2-MI, and 2-PI on a 2x3 unit cell of an Fe (110) surface were calculated to model their behaviors on iron surface as shown in Table 3a. The surface model in this study consisted of 4 molecular layers for performing slab calculations on Fe (110) surface. A 17 Å vacuum was inserted between the material slabs. To retain the bulk atomic positions, the fourth layer was kept frozen during the geometry optimizations.

Similar to the previous study [28], the following equation was used to calculate of adsorption energy of different inhibitor molecules:

$$E_{adsorption} = E_{surface+inhibitor} - (E_{surface}) - (E_{inhibitor}) \quad (1)$$

The more negative the adsorption energy, the stronger is the bond between the molecule and the surface. The MEG, 2-MI and 2-PI have different functional groups that can bind to the Fe surface

(see chemical structure in Fig. 1b and 1c). To model the behavior of different functional groups of different inhibitors on Fe(110), the adsorption energies were calculated and compared. The imidazolines are large in size in comparison to water and MEG. Thus, when they were adsorbed to the 2x3 Fe(110) surface, unexpected bond breaking and errors from interactions between the periodic images occurred. To avoid these interactions, the adsorption energy for 2-PI and 2-MI was also performed on 4x3 Fe(110) unit cell.

The contact angles were calculated using the method based on DFT and COSMO-RS theory[33], which involves calculating the solid-liquid and liquid-liquid interfacial tensions and estimating the contact angle from Young's equation. The DFT calculations for the contact angle calculations involved calculating molecular models for MEG, 2-MI and 2-PI, which were done in Turbomole [34], v 7.4, with the BP functional [35,36] and the TZVP basis set [37] for geometry optimization, followed by a single point energy calculation using the TZVPD basis set. The BP-TZVPD-FINE-21 parameterization for the COSMO-RS calculations and hexadecane as the model oil was used. The hexadecane, the Na⁺ and the Cl⁻ ions were taken from the internal database in COSMOtherm.

2.7. Methodology of contact angle measurement

Before conducting the contact angle measurements, the specimen surface was polished using SiC paper grades of P220, P320, P500, and P1000. The polished samples were rinsed (with ethanol) and dried. The samples were then immersed in inhibitors for 15 minutes. Once the samples dried, the inhibitor film was observed on the same surface. Using a pipette, a drop of 1% NaCl solution was placed on the sample surface. Contact angle measurement were taken at both ends of drop (θ_{C1} and θ_{C2}). Each measurement was repeated for 5-times.

3. Results

3.1. Adsorption energy using density functional theory (DFT)

Table 3a shows the adsorption energy values for water, MEG, and different types of imidazoline (2-PI and 2MI). The weakest adsorption energy was observed for the water molecule (-31 kJ/mol with -OH), which makes it replaceable by the inhibitors due to their higher adsorption energies. The adsorption energy value for 2-MI and the vertically adsorbed 2-PI on 2x3 Fe(110) surface (-76 KJ/mol and -43 KJ/mol, respectively) were weaker by ~10 KJ/mol as compared to that on 4x3 Fe(110) surface (-61 KJ/mol and -32 KJ/mol, respectively), see Table 3a. In 2-PI, the bond formed by the -CH of phenyl ring parallel to the surface was stronger than the -CH of imidazoline ring when adsorbed vertically. This is also reflected in the smaller distance of binding Fe(110) molecules from the -CH of phenyl ring (2.62 Å) as compared to -CH of imidazoline ring (3.59 Å). In some instances, the inhibitor molecules bonded to Fe(110) surface with two functional groups, which led to stronger bonds with corresponding high adsorption energies. For example, the highest adsorption (-189 kJ/mol) was observed for phenyl imidazoline when it bonded to 4x3 Fe(110) with -N- of the imidazoline ring and the aromatic phenyl ring. The strong influence of the aromatic entity is seen by comparing the results to the 2-MI adsorbing similarly with the -N-functional group, but with a much weaker adsorption (-76 kJ/mol). The phenyl ring thus is actively involved in the bonding to the surface, and it is known that dispersion can be quite strong forces for binding similar molecules to other metals [27,38].

Similar to that reported for alkanolamines [28], the inhibitor adsorption energy in water was estimated by comparing the adsorption energy of the inhibitor with that of water in Table 3a. This estimation is based on the fact that the inhibitor molecules need to replace the water molecules already bonded at the interface. The size of the inhibitor molecule at the interface and the way it binds to the iron surface (vertical v/s parallel orientation) can govern the number of water molecules that can be displaced from the Fe(110) surface (see Fig. 3e and 3g for example of inhibitor molecule interaction direction). Table 3b also shows the differences in the adsorption energy between inhibitor and one or more molecules of water i.e. $\Delta E_{\text{adsorption}}$ on Fe(110) surface. The negative $\Delta E_{\text{adsorption}}$ means that replacing of water molecules is favorable (from an energy/enthalpy point of view). Based on the $\Delta E_{\text{adsorption}}$ results, the MEG ($-\text{OH}/-\text{CH}$) and 2-PI ($-\text{CH}$ of imidazoline ring) can replace only one molecule of water. The 2-MI ($-\text{N}-$) can replace two molecules of water, whereas the vertically bonded 2-PI ($-\text{CH}$ of phenyl ring and $-\text{N}-$ imidazole ring) can replace five molecules of water. The increase in entropy from releasing five water molecules for each 2-PI adsorbed will lead to a further decrease in the adsorption free energy, which should favor adsorption even more at elevated temperatures.

Table 3a. Adsorption energy values of different types of imidazoline inhibitors on Fe surfaces using DFT (in kJ/mol).

Molecule	Anchoring group	$E_{\text{adsorption}}$ on 2x3 Fe(110)	$E_{\text{adsorption}}$ on 4x3 Fe(110)	Optimized geometry shown in Figure
Water	$-\text{OH}$	-31	---	3a
MEG ($\text{C}_2\text{H}_6\text{O}_2$)	$-\text{OH}/-\text{CH}_2$	-50	---	3b
2-Methyl-2-imidazoline ($\text{C}_4\text{H}_8\text{N}_2$)	$-\text{NH}$ (imidazoline ring)	-76	-61	3c and 3d
2-Phenyl-2-imidazoline ($\text{C}_9\text{H}_{10}\text{N}_2$)	$-\text{CH}$ (imidazoline ring)	-43	-32	3e and 3f
	$-\text{CH}$ (phenyl ring) and $-\text{N}-$ (imidazoline ring)	-112*	-189	3g and 3h

* the small unit cell only made it possible for the 2-PI molecule to bind to the Fe(110) with the phenyl ring, hence the weaker adsorption energy compared to the 4x3 Fe(110) unit cell.

Table 3b. Differences in the adsorption energy between different types of imidazoline and water ($\Delta E_{\text{adsorption}}$) on Fe (110) surfaces using DFT (in kJ/mol).

Differences in adsorption energy between inhibitor and water				
Molecule	# Water molecules replaced	Anchoring group	$\Delta E_{\text{adsorption}}$ on 2x3 Fe(110)	$\Delta E_{\text{adsorption}}$ on 4x3 Fe(110)
MEG ($\text{C}_2\text{H}_6\text{O}_2$)	1	$-\text{OH}/-\text{CH}_2$	-19	---
	2		+12	---
2-Methyl-2-imidazoline ($\text{C}_4\text{H}_8\text{N}_2$)	1	$-\text{NH}$ (imidazoline ring)	-45	-30
	2		-14	+1
	3		+17	+32
2-Phenyl-2-imidazoline	1	$-\text{CH}$ (imidazoline ring)	-12	-1
	2		+19	+30

(C ₉ H ₁₀ N ₂)	1	-CH (phenyl ring) and -N- (imidazoline ring)	---	-158
	2		---	-127
	3		---	-96
	4		---	-65
	5		---	-34
	6		---	-3
	7		---	+28

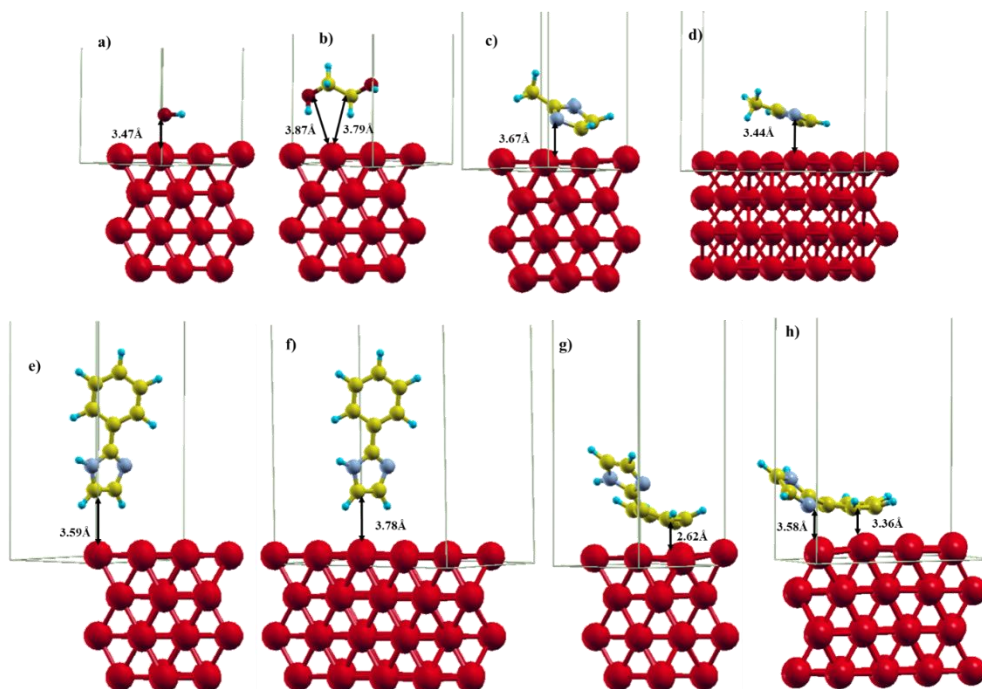


Figure 3. Optimized bonding geometries for some inhibitor molecules on various model surfaces (a): Water bonded to 2x3 Fe(110) with -OH, (b): MEG bonded to 2x3 Fe(110) with -OH/-CH₂, (c): 2-MI bonded to 2x3 Fe (110) with -NH (Imidazoline ring) (d): 2-MI bonded to 4x3 Fe (110) with -NH (Imidazoline ring), (e): 2-PI bonded to 2x3 Fe (110) with -CH (Imidazoline ring), (f): 2-PI bonded to 4x3 Fe (110) with -CH (Imidazoline ring), (g): 2-PI bonded to 2x3 Fe (110) with -CH (Phenyl ring) (h): 2-PI bonded to 4x3 Fe(110) with -CH (Phenyl ring) and -NH (Imidazoline ring).

Color code: bright red (large radius) = Fe, dark red (small radius) = O, yellow = C and aqua= H.

3.2. Binding energy calculation using XPS

The XPS analysis was carried out to confirm the hypothesis of the imidazoline and MEG chemisorption behavior, and interpret the nature of the organic thin-layer formed on the Fe surface. The film was formed in 1% NaCl solution saturated with CO₂ in the presence of different types of imidazoline in combination with MEG with a 48 hrs immersion time. For comparison purposes, the XPS spectra for 2-MI combined with MEG and 2-PI combined with MEG are shown in Fig.4. All XPS spectra show complex forms, which were assigned to the corresponding species through a deconvolution fitting procedure. The peaks in individual spectra showed evidence of the presence of C, N, O and Fe, where the O, C and Fe contents displayed the highest amount, while

the signals of N were detected with small intensities in comparison to other three elements. The XPS spectra of C1s ranging from 282.0 eV to 300.0 eV. The peaks around 285.02 eV in Fig. 4 a and 4d ascribed to C–N and peak at 288.0 in Fig. 4d corresponds to C=O. A less intensive peak at 289.8 eV in Fig. 4a relates to C=O [4], [39]. The Fe 2p spectra was composed of two peaks (Fe2p_{1/2} at 724.0 eV and Fe2p_{3/2} at 710.0 eV). The Fe2p_{3/2} peak shows multiple splitting composed of three peaks at 710.0 eV, 714.0 eV and 718.0 eV. These peaks could be assigned to Fe of Fe₂O₃ or Fe₃O₄, which means that a certain amount of oxidation of Fe occurred [11]. It was expected for Fe to be oxidized during the process of analysis. The N1s spectra from the range 395 to 413 eV was fitted by two peaks one with Fe(II)/ Fe(III) nitrate at 405 eV and other with C–NH₂ bond at 400.0 eV [40]. These peaks provided evidence that the 2-MI and 2-PI was really adsorbed on the steel surface. The area for N1s peak is shown in Table 4.

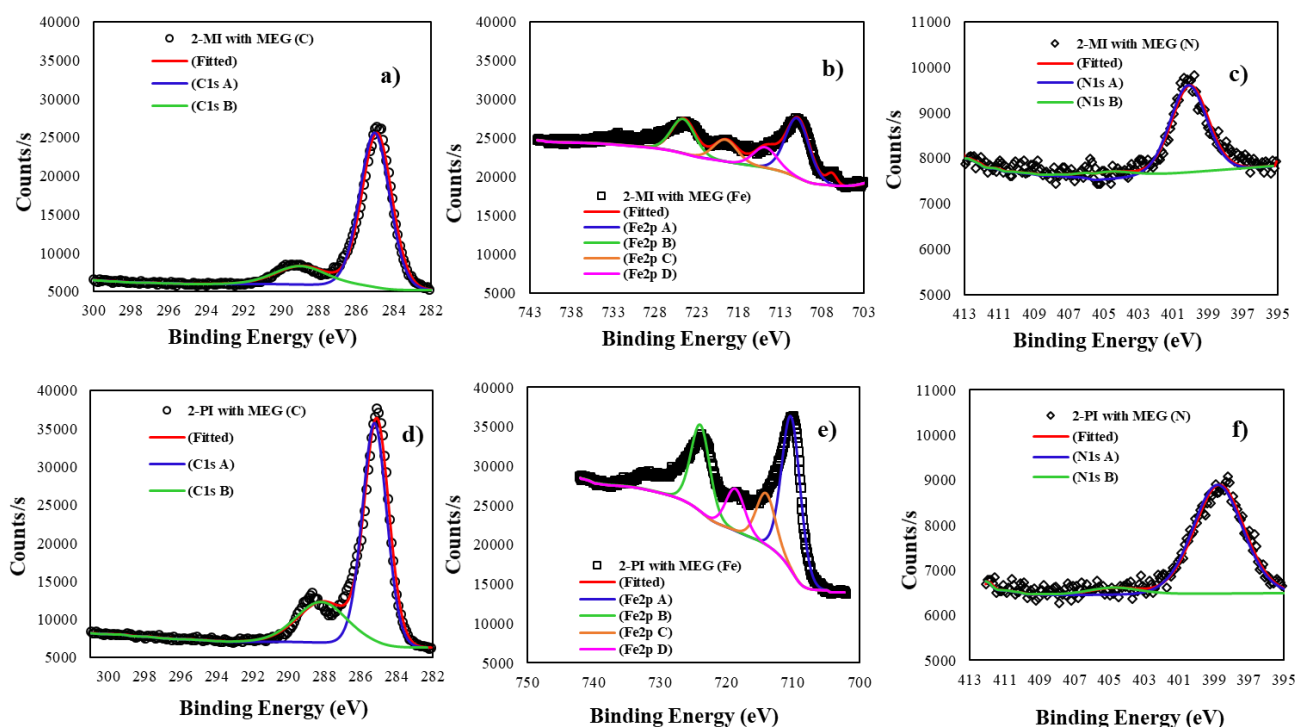


Figure 4. XPS spectrum of (a and d): C 1s, (b and e): Fe2p and (c and f): N 1s in corrosion products of NaCl-contaminated L-80 1 Cr steel specimens after 48 h exposure to 40°C in the presence of 2-MI inhibitor and 2-PI inhibitor in combination with MEG respectively.

Table 4. Area under N1s peaks using XPS analysis on L80-1Cr steel exposed in 1% NaCl solution in presence of 2-MI with MEG and 2-PI with MEG after 48 h exposure at 40°C.

Area (CPS.eV)	2-MI with MEG	2-PI with MEG
N1s Scan A	5145	8807
N1s Scan B	548	557

3.3. Electrochemical studies on the effect of 2-MI and 2-PI together with MEG on L 80- 1 Cr at 40°C

3.3.1. OCP monitoring

The shift in the OCP values of working electrode with and without inhibitor is shown in Fig. 5. A positive shift in the OCP indicates reduction in the driving force for corrosion steel. A pseudo-steady state was achieved after around 30 min of immersion time. Relative to the reference sample (-0.658 V to -0.659 V), a positive shift in OCP was observed for a combination of 2-PI and MEG (-0.646 V to -0.636 V), MEG (-0.641 V to -0.649 V), and 2-PI (-0.661 V to -0.643 V). A negative shift in OCP was observed for 2-MI alone (-0.674 V to -0.679 V) and in combination with MEG (-0.664 V to -0.672 V).

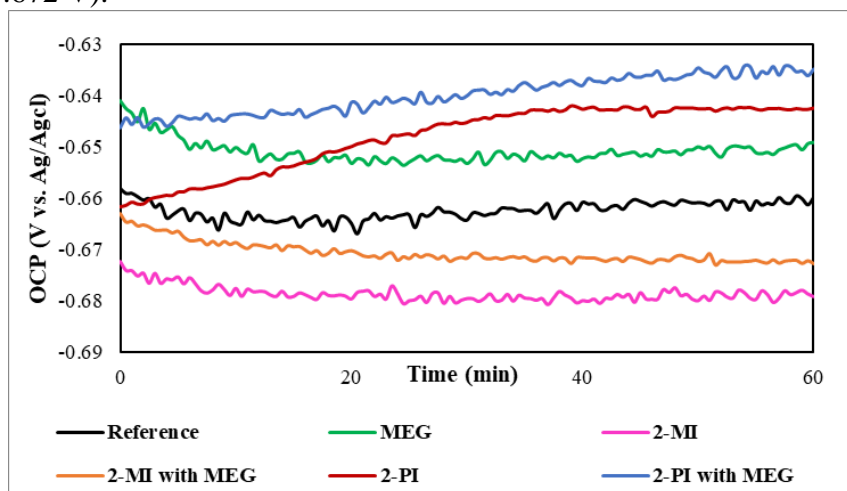


Figure 5. OCP measurement of L-80 1 Cr steel with and without inhibitor imidazolines types of inhibitor in 1% NaCl solution at 40°C.

3.3.2. LPR measurements at 40°C

Fig.6a represents the LPR (time vs Rp) results for L-80 1 Cr steel in NaCl solution with and without inhibitors. The polarization resistance value for 2-MI and MEG ($153 \Omega \cdot \text{cm}^2$) was 1.5 times that of the reference ($99 \Omega \cdot \text{cm}^2$). However, the Rp value for MEG was quite stable over 48 hrs, whereas the Rp value for 2-MI decreased with time and reached to the reference value by the end. When 2-MI was mixed with MEG, the Rp value increased to $220 \Omega \cdot \text{cm}^2$. The Rp value of 2-PI was (~5 times) higher than MEG, 2-MI alone, and MEG and 2-MI combination. Further, the combination of MEG and 2-PI provided the highest (10 times) Rp value in comparison to MEG, 2-MI alone, and MEG and 2-MI combination.

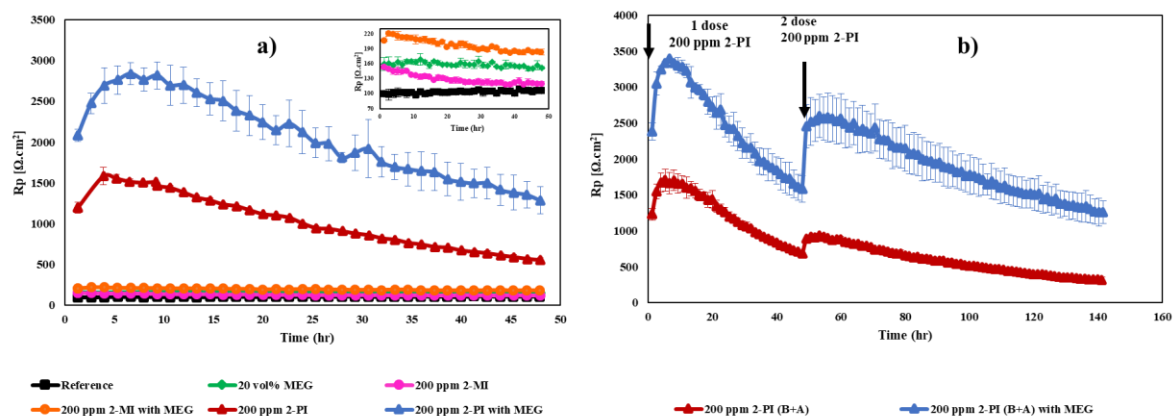


Figure 6. (a): Polarization resistance for L80-1 Cr steel exposed to 1 wt % NaCl solution at 40 °C, without and with the addition of 200 ppm of imidazolines, MEG and combination of imidazolines and MEG inhibitor for 48 hrs, (b): Effect of subsequent re-injection of 2-PI inhibitor L80-1 Cr steel exposed to 1 wt % NaCl solution at 40 °C.

During initial injection of 2-PI alone and in combination with MEG, there was an incubation time of 5-6 hours. By the time for re-injection i.e. 48 hrs, the R_p values for 2-PI alone and in combination with MEG had reduced to a level below their initial values at time 0 hrs. Upon re-injection, there was an increase in the R_p values (within 1-2 hours) to 922 $\Omega \cdot \text{cm}^2$ and 2576 $\Omega \cdot \text{cm}^2$ for the two solutions, respectively. However, the increased values were either smaller or slightly greater than their initial values, suggesting the re-injection just prevented further degradation of the inhibitor film.

The maximum value of the polarization resistance was used to calculate the inhibitor efficiency of the solution using Eq. (2). The MEG alone had a better efficiency than 2-MI alone, but lower efficiency than 2-PI alone. The addition of MEG substantially improved the efficiency of 2-MI (82%), but did not lead to much change in the efficiency of 2-PI (< 1%). These efficiency values (reported in Table 5) were in fair agreement with polarization resistance values in Fig. 6.

$$\text{Inhibitor efficiency (\%)} = \frac{(R_{p_{\text{inhibited}}} - R_{p_{\text{Uninhibited}}})}{R_{p_{\text{inhibited}}}} \times 100 \quad (2)$$

Table 5. Comparison of efficiency between different types of inhibitors at 40 °C.

Inhibitor type	Inhibitor efficiency (%) at 40 °C
MEG	35
2-MI	28
2-MI with MEG	50
2-PI	93
2-PI with MEG	96
2-PI (B+A)	93 and 88
2-PI (B+A) with MEG	96 and 95

3.3.3. Electrochemical impedance spectroscopy investigation

The impedance responses of the sample (L-80 1 Cr steel) at 40 °C in the form on Nyquist plots at hours 2, 24, and 48 are shown in Fig. 7. The responses were recorded in the presence of the inhibitors (2-PI and 2-MI) in the pure form and when mixed with MEG.

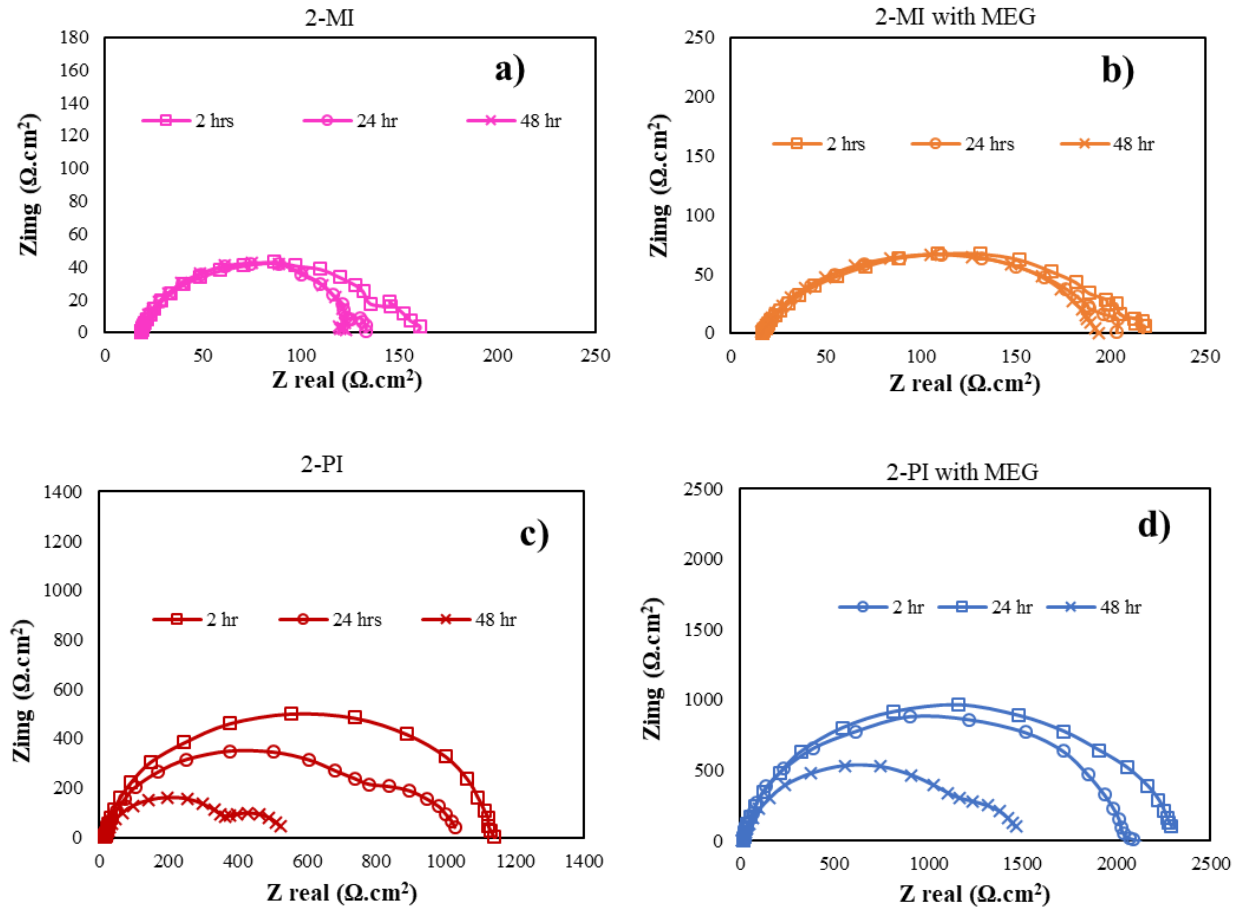


Figure 7. Results of electrochemical impedance measurements: Nyquist plot (a): pure 2-MI inhibitor, (b): 2-MI inhibitor in combination with MEG, (C): Pure 2-PI inhibitor and (d): 2-PI inhibitor in combination with MEG on L80-1 Cr steel exposed to 1 wt % NaCl solution at 40 °C for 48 hrs.

In the Nyquist plots, the effect of inhibitors is characterized by the diameter of capacitive loop such that a higher value indicating better formation of an adsorption film on the metal surface [11,13]. In this study, the addition of 2-PI led to higher values of the capacitive loop diameters when compared to the 2-MI. Similarly, addition of MEG yielded capacitive loops of larger diameters for both 2-PI and 2-MI conditions. Irrespective of the inhibitor used, the diameter of the capacitive loops reduced with increase in time from 2 hours to 48 hours indicating the disintegration of adsorption film over the time. The equivalent circuits that were used to fit the impedance experimental data from the steel surface in the presence of inhibitors is shown in Fig. 8. The equivalent circuit consists of single time constant whereas a double layer capacitance (C_{dl}) in parallel with a charge transfer resistance (R_{ct}) was used for the solution resistance (R_s). In the

presence of inhibitors, another film capacitance (C_{fc}) and a film pore resistance (R_{pr}) was added to account for an adsorbed inhibitor layer–solution interface. The R_{ct} is a measure of the polarization resistance of the corroding metal. The value of capacitance present in the electric double layer at the metal–solution interface are modified by the species adsorbed or desorbed on the metal surface. Therefore Fig. 8 represents system for inhibitors (film formation) and fits well with experimental data in presence of inhibitor (Fig. 6) with a double-time constant, signifying either two layers or a porous film. Table 6 represents fitting of impedance data at 2, 24, and 48 hrs that shows maximum corrosion resistance value in Fig. 6a and 6b.

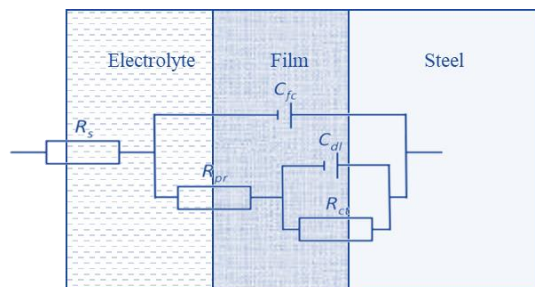


Fig. 8. A double-time constant circuit showing a perforated film interface or perforations filled with corrosion product.

Table 6. EIS parameters obtained based on the fitted curves on experimental data according to equivalent circuit presented in Fig. 8, for L80-1 Cr steel exposed to 1 wt % NaCl solution at 40 °C, with the addition of 200 ppm of the different types of imidazoline alone and in combination with MEG at time 2, 24 and 48 hrs.

Sample	Immersion time (hrs)	R_{ct} $\Omega.cm^2$	C_{dl} $\mu\Omega^{-1}.cm^{-2}.s^n$	n_1	R_{pr} $\Omega.cm^2$	C_{fc} $\mu\Omega^{-1}.cm^{-2}.s^n$	n_2
2-MI	2	13	71001	0.97	127	885	0.76
	24	6	343731	0.87	109	628	0.83
	48	1	497838	0.99	104	538	0.87
2-MI with MEG	2	76	3051	0.75	133	585	0.78
	24	7	61149	0.55	180	580	0.79
	48	7	1960	0.87	169	555	0.83
2-PI	2	3	2245	0.93	1117	101	0.93
	24	174	13751	0.97	827	233	0.92
	48	192	20862	0.88	404	550	0.93
2-PI with MEG	2	13	13013	0.97	2054	94	0.91
	24	253	3936	0.77	2036	141	0.93
	48	481	3711	0.73	1028	177	0.99

3.4. Change in water drop contact angle measurements on L80-1Cr steel samples covered with a layer of inhibitors

Fig. 9 shows the contact angle measurement for different inhibitors. A smaller contact angle ($< 90^\circ$) correspond to hydrophilic characteristics, whereas a larger contact angle suggests a more hydrophobic nature of the surface. Small contact angle values were found for uninhibited ($31^\circ - 10^\circ$), 2-MI ($38^\circ - 25^\circ$), and MEG ($51^\circ - 37^\circ$). The contact value was larger for (in decreasing order) combination of MEG and 2-PI ($107^\circ - 91^\circ$), 2-PI ($91^\circ - 82^\circ$), and a combination of MEG and 2-MI ($67^\circ - 60^\circ$). Corresponding contact angles were calculated for a hexadecane/water system and compared to the experimental systems in Table 7. The highest contact angle for the 2-PI is consistent with the strong adsorption of 2-PI on Fe(110) as predicted from the DFT calculations, and is also consistent with the highest predicted contact angle from the DFT calculations. Both point to a strongly covered surface. The order of the predicted contact angles is consistent with the experimental order, with the exception of 2-MI, which (on its own) has a lower contact angle than MEG. The contact angle predictions for 2-MI are significantly higher than the corresponding experimental values. The surface coverage by 2-MI is not particularly high, unless supported with MEG in solution. The same trend can be observed in the corrosion inhibition efficiencies, Table 5, where the combination of 2-MI with MEG is substantially better than either on their own.

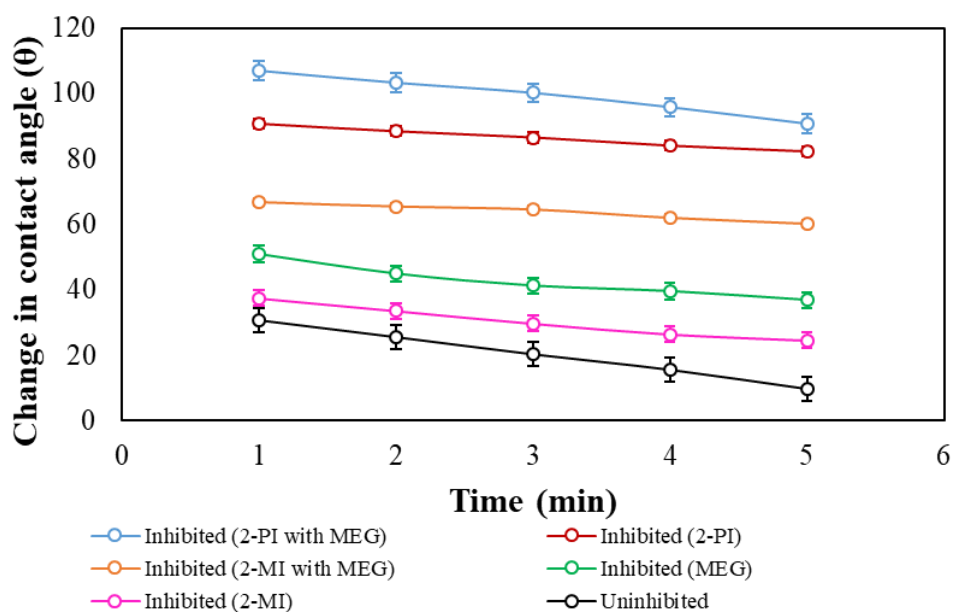


Figure 9. Change in water drop contact angle measurements on L80-1Cr steel in 1% NaCl solution with and without inhibitors.

Table 7. Comparison of computed oil/water contact angle and measured water-in-air contact angles (in degrees). The calculated oil/water contact angle used hexadecane as the model oil and 1 wt% NaCl in water.

Surface chemistry (S)	Solid-liquid (SL) interfacial tension (mN/m)		Contact angle (θ)		
	L = Water	L = hexadecane	Calc.	Exp. (t=0 min)	Calc. – Exp.
2-PI	13.6	10.3	93	91	2
2-MI	5.9	12.3	83	38	45
MEG	-1.2	17.5	71	51	20
water	3.8	30.8	61	31	30

3.5. Surface characterization

The XRD analysis of the scale/film formed on the specimen during the electrochemical experiments is shown in Fig. 10. The Fe α peak and Cementite (Fe_3C) peaks were observed in all corroded samples with and without inhibitors. However, the diffracted intensity of Fe_3C peaks decreased with the addition of inhibitors. In case of pure and mixed (with MEG) forms of 2-PI, the Fe_3C formation was substantially less as indicated by disappearance of all of the peaks, except two reflections (210 and 221). The peak Fe_3C intensities were also decreased for a combination of MEG and 2-MI for six (002, 211, 102, 131, 221, and 122) out of nine reflections. Overall, when inhibitors are added, Fe_3C reflection significantly reduced showing reduction in corrosion and enrichment of Fe_3C on the surface.

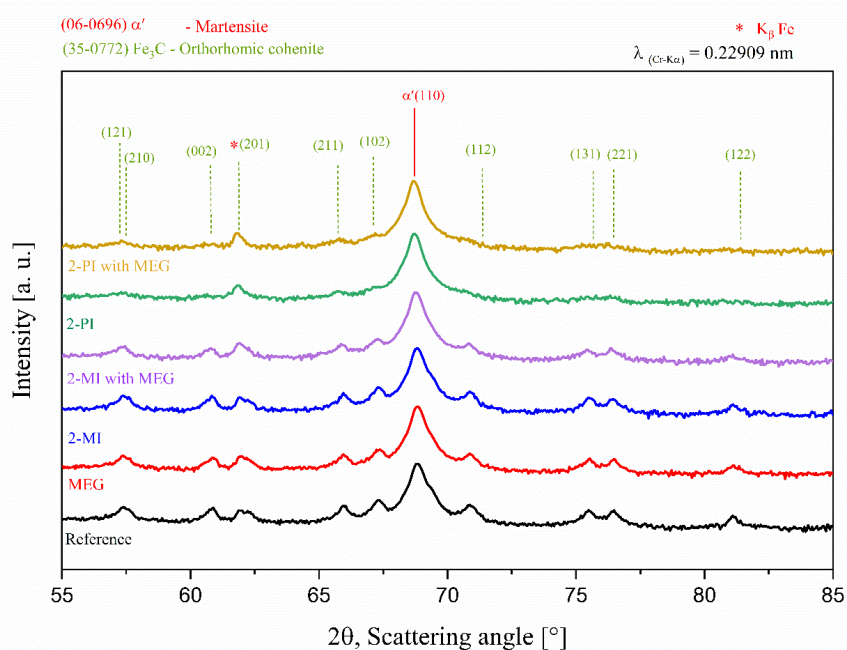


Fig. 10. Results of X-ray diffraction of the scale formed on L-80 1 Cr steel surface with and without imidazoline types of inhibitor at 40 °C.

The top-view and the cross-sectional SEM images of the reference and different inhibitors immersed in the NaCl solution at 40°C are shown in Fig. 11. The reference sample had the thickest corrosion product layer (6.15 μm), followed by MEG (3.84 μm), 2-MI (4.61 μm) (Fig. 11a, 11c, and 11e). In combination with MEG, the corrosion product layer was less thick with 2-MI (3.08 μm) (Fig. 11g). In 2-PI alone and in combination with MEG, a corrosion product of negligible thickness (1.53 μm and 0.76) was formed (Fig. 11i and 11k) respectively. As shown in top view, a surface with coarse cracks was found in the reference sample highlights severe damage to the surface caused by bulky corrosion products without inhibitors (Fig. 11b). Less coarse cracks were found in the samples treated with MEG and 2-MI in pure forms (Fig. 11d and 11f). Whereas 2-MI in combination with MEG (Fig. 11h) led to fine cracks. The extent of cracks was also lesser in the combined 2-MI and MEG specimen in comparison to pure MEG. Highly fine corrosion pits with scratches reflecting light were observed for the pure 2-PI (Fig. 11j). Least corrosion with a smoother surface and localized pits with reflection of light was observed for the mix of 2-PI and MEG specimen (Fig. 11l)

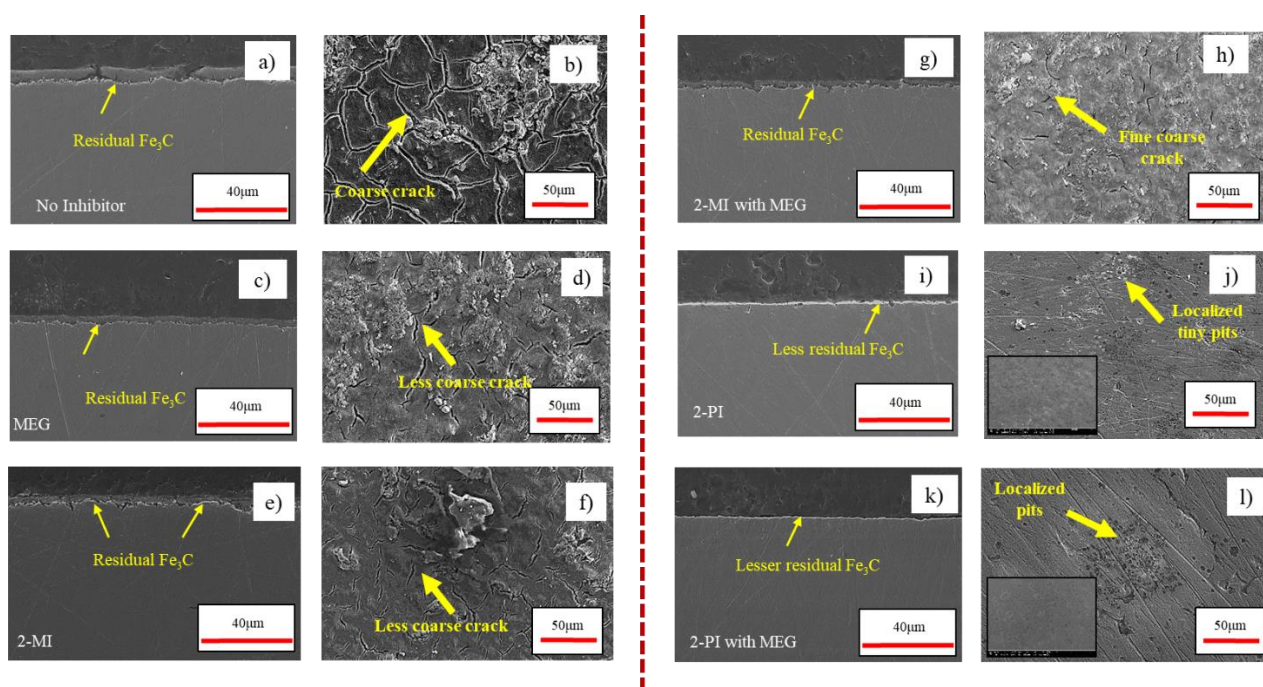


Figure 11. SEM images (Cross-sectional and top view) for L80-1 Cr steel exposed to 1 wt% NaCl solution, (a and b): specimen without inhibitor, (c and d): specimen with MEG, (e and f): specimen with 200 ppm 2-MI, (g and h): specimen with combination of MEG and 2-MI, (i and j): specimen with 200 ppm 2-PI, (k and l): specimen with combination of MEG and 2-PI at 40 °C.

4. Discussion

This study investigated the corrosion inhibition properties of two specific imidazoline compounds 2-MI and 2-PI in CO₂ environment on L-18 1Cr steel surface using a combination of molecular modelling and electrochemical techniques. Overall, 2-PI was found to have significantly better corrosion inhibition properties than 2-MI as reflected by a lower polarization resistance, stronger adsorption energy, and a larger capacitive loop diameter values that were observed for the former. Also, the addition of MEG improved the corrosion inhibition properties of both forms of imidazoline, although less so for the 2-PI.

In this study, OCP measurement (Fig. 5) was used to understand the corrosion behavior of the steel surface with and without inhibitors. The displacement of OCP in inhibited system relative to uninhibited can be used as a basis for inhibitor categorization [41–43]. By observing difference in OCP values, it is justifiable to claim that inhibitors used in this study demonstrated principal corrosion inhibitory effect. A pseudo-steady state of potential in this study was reached at around 30-minutes with all inhibitors, which is slightly longer than a previous study (16-minutes) that used another derivative of imidazoline [44]. In the blank solution, a more negative steady state value of OCP (-0.659 V) is indicative of the corrosion process, which is thought to result from negative chloride absorption and activation of the metal surface [44]. A positive shift in the OCP values in the presence of 2-PI (-0.642 V), MEG (-0.649V), and in combination of 2-PI and MEG (-0.634 V) could be associated with the adsorption of inhibitor molecules on the electrode surface [45]. In a previous study, a similar positive shift in the OCP values was observed with addition of imidazoline derivatives such that a greater shift was observed with an increase in concentration of the inhibitor [44]. In the current study, the concentrations of the inhibitors kept constant; however, addition of MEG led to a positive shift in the OCP values. Surprisingly, the OCP values in the presence of 2-MI (-0.679 V) in its pure form and in combination with MEG (-0.672 V) were more negative than the reference values that attribute to the lesser corrosion inhibition in comparison to 2-PI.

The corrosion behavior observed using the OCP values were confirmed by the R_p values (Fig.6). The maximum R_p value for the reference ($109 \Omega \cdot \text{cm}^2$) was significantly lower than for the inhibitors. When comparing two imidazoline type, a higher R_p value was observed for 2-PI ($1582 \Omega \cdot \text{cm}^2$) than 2-MI ($154 \Omega \cdot \text{cm}^2$) suggesting a strong adsorption of the former on the metal surface. The presence of a bulkier phenyl group for 2-PI is likely contributed to stronger attachment with the Fe surface with higher R_p values. The MEG alone had R_p value ($169 \Omega \cdot \text{cm}^2$) higher than the reference; however, the value was smaller than 2-PI suggesting MEG film was adsorbed on the surface, but did not form as strong bond with the Fe surface as seen with 2-PI. Interestingly, addition of MEG to both 2-PI and 2-MI led to higher R_p values ($2837 \Omega \cdot \text{cm}^2$ and $169 \Omega \cdot \text{cm}^2$) than their pure forms suggesting synergistic effects of MEG and imidazolines. The R_p values also were higher for 2-PI (93%) as compared with 2-MI (28%). The addition of MEG increased the corrosion inhibition efficiency slightly for 2-PI (96%) and substantially for 2-MI (50%). The observed corrosion inhibition efficiency of 2-MI in combination with MEG could be a result from increased surface coverage arising from ion-pair interactions between MEG anions and imidazoline cations [7].

Over time, the R_p value of 2-PI reduced, which might be attributed to the desorption of inhibitor molecules making the inhibitor film porous or less dense with time. The formation of porous film in case of 2-PI inhibitor was supported by impedance parameters as shown in Table 6. For 2-PI, the R_{pr} value decreased from 2 hrs ($1117 \Omega \cdot \text{cm}^2$) to 48 hrs ($404 \Omega \cdot \text{cm}^2$) confirming increase in porosity of the inhibitor film, which is also supported by the increase in C_{fc} values (suggesting decrease in film thickness). Due to increase in porosity of the layer as the exposed area increases more anodic sites were available for iron dissolution, which is indicated by the increase in C_{dl} values over the time. Despite the increased porosity, decrease in thickness and availability of more anodic sites, the R_{ct} values continued to increase suggesting the inhibitor layer was intact, limiting the corrosion reactions on the sample surface. This situation would be possible if there was localized corrosion in certain areas, but the whole film stayed more or less intact elsewhere. With

addition of MEG to 2-PI, similar impedance results were observed, except that the C_{dl} values decreased, suggesting fewer anodic sites were available for corrosion reaction.

In the case of 2-MI alone, over time, the inhibitor film turned more porous and less intact causing more charge transfer resistance and availability of more anodic sites as indicated by reducing R_{pr} and R_{ct} values and increasing C_{dl} values, respectively. Although the film turned more porous, the thickness of the film increased as indicated by a decrease in C_{fc} value. In case of 2-MI in combination with MEG, similar impedance results were observed, except the R_{pr} and C_{dl} values initially increased until 24 hours and then subsequently decreased (Table 6). Overall, the impedance results suggest that 2-PI led to porous and thin film that was intact, whereas 2-MI led to porous and thick film, which was less intact than 2-PI.

The impedance results were supported by the XRD and SEM images. Due to less corrosion upon addition of different types of imidazoline, less iron (Fe^{2+} ions) dissolution occur from the ferritic phase, which results in less residual cementite (Fe_3C) on the steel surface as shown in XRD analysis in Fig. 10. The SEM images confirmed that the reference sample had more coarse cracks as compared to inhibitors likely due to bulky corrosion products (Fig. 11b).

The addition of imidazoline inhibitors resulted in smaller cracks and pits when compared to the reference suggesting the corrosion inhibition tendency of the two inhibitors. The addition of 2-PI led to a lesser extent of corrosion as compared to 2-MI as seen in SEM images that showed no cracks and localized corrosion in case of 2-PI (Fig. 11e and 11f vs. 11i and 11j). Addition of MEG to the imidazoline led to fine cracks, localized pits and a thinner layer of corrosion for both imidazoline inhibitors – 2-MI (Fig. 11g and 11h) and 2-PI (Fig. 11k and 11l). The XPS results (Fig. 4c and 4f) also confirm that the intensity of the N1s A peaks in case of 2-PI with MEG is higher in comparison to 2-MI in combination with MEG. Hence, we deduced that the N atom in the case of 2-PI with MEG and Fe atom on the steel surface occurred strong chemical coordination and the 2-PI molecules chemically adsorbed on sample surface forming a protective film in comparison to 2-MI with MEG to inhibit the samples from CO_2 corrosion.

The electrochemical results were supported by the molecular modelling. The adsorption energy calculations from the molecular modeling shows that the presence of the aromatic phenyl group in 2-PI yields significantly stronger adsorption energy (-189 kJ/mol) as compared to the 2-MI (-76 kJ/mol), suggesting significantly stronger capacity for forming a stable protective film. A previous study has also shown comparable adsorption energy values (-155 kJ/mol) for 2-PI on $Cu_2O(001)$ surface [5].

The adsorption energy depends strongly on the chemistry of the inhibitor molecule that formed a bond on the Fe surface. The phenyl group in 2-PI has a strong electron donor tendency [31], which adds to the strength of the bond, although dispersion forces certainly also play a role [27,38,46]. This offers two bonds between 2-PI and the steel surface – first between the -N- group of the imidazoline ring and the steel surface, and second between the phenyl group and the steel surface. The orientation of the bond also played a role in adsorption energy values. For example, parallel orientation of -CH of imidazoline ring on the Fe surface led to a stronger bond than the vertical orientation of -CH of imidazoline ring (Table 3a, Fig. 3f and 3h). There were small differences (~10 kJ/mol) in the adsorption energy values between the two Fe unit cells (2x3 and 4x3) for 2-MI and 2-PI (Table 3a). These differences between the two unit cells may have resulted from

attractive adsorbate-adsorbate interactions via dispersion at the higher coverage modelled with the smaller 2x3 unit cell. For the inhibitors, the adsorption energy depended strongly on the anchoring group that binds to the Fe(110) surface, see Table 3a.

The adsorption influences the replacement of water molecules on the corroding surface, which can markedly change the corrosion resisting property of the metal. Due to its bulkier size and higher adsorption energy, 2-PI could replace up to at least five water molecules, whereas 2-MI could replace a maximum of 2 water molecules (Table 3b), based solely on adsorption energy considerations.

Previous studies have found that the steel surface without inhibitor has lower contact angle, which suggests that the surface is hydrophilic i.e. attracting more water, which leads to higher corrosion [12,44]. Such findings were supported in this study as the contact angle measurement of water was smallest for the uninhibited steel surface (31° to 10°). The smaller contact angle is due to the hydrophilic nature of the surface and increase of the surface roughness under corrosive attack by the media [47,48]. With the addition of 2-MI (38° to 25°) and MEG (51° to 37°) alone, or in combination (67° to 60°), the contact angle of water was slightly increased, suggesting the steel surface was more water repellent than without inhibitor. In the case of PI in its pure form (91° to 82°) and in combination MEG (107° to 91°), a large increase in contact angle was observed, which confirms that the surface became more water repellent. Another previous study found high contact angle measurement (82°) for water on AA5052 when immersed in 2-PI for 72 hours [20]. The results of this study demonstrate (at least in this case) a correlation between contact angle and the inhibitor efficiencies (Table 4). This result was further corroborated by predicted oil/water contact angles using molecular modelling (see Table 7). The most notable discrepancy between calculations and experiments occur for 2-MI, which can be rationalized by the 2-MI adsorption energy, which is substantially weaker than for the 2-PI (Table 3). The predicted contact angle thus demonstrates that the surface is not well covered/protected by the 2-MI inhibitor alone.

Lastly, re-injection of another dose of same concentration of inhibitors improved the R_p values for 2-PI alone ($686 \Omega \cdot \text{cm}^2$ to $938 \Omega \cdot \text{cm}^2$) and in combination with MEG ($1583 \Omega \cdot \text{cm}^2$ to $2597 \Omega \cdot \text{cm}^2$) (Fig. 6b). Imidazolines can be prone to hydrolysis due to breaking of the C-N bond by protonation [9]. The second dose of 2-PI likely prevented the loss of inhibitor film that may have resulted from hydrolysis of the inhibitors from the first dose.

5. Conclusions

- Imidazoline with methyl (2-MI) and phenyl (2-PI) structures found to be good corrosion inhibitor for steel surface in NaCl solution under saturated CO_2 conditions. The addition of imidazoline inhibitors resulted in smaller cracks and pits when compared to the reference.
- The corrosion inhibition properties (efficiency and R_p values) of 2-PI are greater than that of 2-MI, which is likely due to the presence of the phenyl group which provides another site for bonding with the steel surface as confirmed by higher adsorption energy values for 2-PI during molecular modelling calculations.
- Addition of MEG to the imidazolines improves their corrosion inhibition properties, especially with 2-MI, likely due to increased surface coverage arising from ion-pair interactions between MEG anions and imidazoline cations.

- Lesser residual cementite (Fe_3C) peaks were found on the steel surface when treated with 2-PI as compared to 2-MI (alone and in combination with MEG) confirming lesser corrosion in the presence of 2-PI.
- The XPS results also confirmed that in the case of 2-PI with MEG, a strong chemical coordination occurred between the N atom and the Fe atom (higher intensity of N1s A peaks) leading to stronger adsorption than 2-MI and MEG.
- The higher contact angle observed for 2-PI than 2-MI alone and with MEG also suggest stronger coverage on the metal surface.
- The Incubation time was observed for 2-PI, which reduced upon addition of MEG from 4 hours to 2 hours. Re-injection of another dose of inhibitors (2-PI) at 48 hours increased the R_p values partially suggesting prevention of further degradation of the initially formed layer of 2-PI inhibitor.

ACKNOWLEDGEMENTS

The authors would like to thank the Danish Hydrocarbon Research and Technology Center (DHRTC) for providing financial funding and technical supports to this work.

References

- [1] G.C. Díaz, A. Espinoza-Vázquez, F.J. Rodríguez-Gómez, Electrochemical Evaluation of 2-Methyl-2-Imidazole and 2-Phenyl-2-Imidazole in a Sulphuric Medium, *ECS Trans.* 84 (2018) 89.
- [2] H. Liu, D. Du, Recent advances in the synthesis of 2-imidazolines and their applications in homogeneous catalysis, *Adv. Synth. Catal.* 351 (2009) 489–519.
- [3] C. Dardonville, I. Rozas, Imidazoline binding sites and their ligands: an overview of the different chemical structures, *Med. Res. Rev.* 24 (2004) 639–661.
- [4] S. Wan, X.-Z. Ma, C.-H. Miao, X.-X. Zhang, Z.-H. Dong, Inhibition of 2-phenyl imidazoline on chloride-induced initial atmospheric corrosion of copper by quartz crystal microbalance and electrochemical impedance, *Corros. Sci.* 170 (2020) 108692.
- [5] S. Wan, Z. Dong, X. Guo, Investigation on initial atmospheric corrosion of copper and inhibition performance of 2-phenyl imidazoline based on electrical resistance sensors, *Mater. Chem. Phys.* 262 (2021) 124321.
- [6] M. Finšgar, 2-Phenylimidazole Corrosion Inhibitor on Copper: An XPS and ToF-SIMS Surface Analytical Study, *Coatings.* 11 (2021) 966.
- [7] S. Salimi, M. Nasr-Esfahani, S.A. Umoren, E. Saebnoori, Complexes of imidazole with Poly (ethylene glycol) as a corrosion inhibitor for carbon steel in sulphuric acid, *J. Mater. Eng. Perform.* 24 (2015) 4696–4709.
- [8] B.J. Usman, S.A. Ali, Carbon dioxide corrosion inhibitors: a review, *Arab. J. Sci. Eng.* 43 (2018) 1–22.
- [9] M.M. Watts, Imidazoline hydrolysis in alkaline and acidic media—A review, *J. Am. Oil Chem. Soc.* 67 (1990) 993–995.
- [10] G.R. Meyer, *Corrosion Inhibitor Compositions*, 2001.
<https://patentimages.storage.googleapis.com/fe/17/25/dc239f4b5f53c9/US6303079.pdf>.
- [11] B. Wang, M. Du, J. Zhang, C.J. Gao, Electrochemical and surface analysis studies on corrosion inhibition of Q235 steel by imidazoline derivative against CO₂ corrosion, *Corros. Sci.* 53 (2011) 353–361.
- [12] A. Singh, K.R. Ansari, A. Kumar, W. Liu, C. Songsong, Y. Lin, Electrochemical, surface and quantum chemical studies of novel imidazole derivatives as corrosion inhibitors for J55 steel in sweet corrosive environment, *J. Alloys Compd.* 712 (2017) 121–133.
- [13] H. Zhang, K. Gao, L. Yan, X. Pang, Inhibition of the corrosion of X70 and Q235 steel in CO₂-saturated brine by imidazoline-based inhibitor, *J. Electroanal. Chem.* 791 (2017) 83–94.
- [14] J. Marsh, J.W. Palmer, R.C. Newman, Evaluation of inhibitor performance for protection against localized corrosion, *NACE - Int. Corros. Conf. Ser.* 2002-April (2002) 1–16.

- [15] R. Barker, B. Pickles, A. Neville, General corrosion of X65 steel under silica sand deposits in CO₂-saturated environments in the presence of corrosion inhibitor components, *Corrosion*. (2014) 1–19.
- [16] W.H. Durnie, M.A. Gough, J.A.M. De Reus, Development of corrosion inhibitors to address under deposit corrosion in oil and gas production systems, *NACE - Int. Corros. Conf. Ser.* 2005-April (2005) 1–20.
- [17] A. Neville, W. Lane, Investigation of pitting corrosion and inhibition in sweet conditions, in: *NACE - Int. Corros. Conf. Ser.*, 2013: pp. 1–15.
- [18] H.J. Chen, W.P. Jepson, T. Hong, High temperature corrosion inhibition performance of imidazoline and amide, *Corrosion*. (2000).
- [19] L. Zhang, Y. He, Y. Zhou, R. Yang, Q. Yang, D. Qing, Q. Niu, A novel imidazoline derivative as corrosion inhibitor for P110 carbon steel in hydrochloric acid environment, *Petroleum*. 1 (2015) 237–243.
- [20] X. He, Y. Jiang, C. Li, W. Wang, B. Hou, L. Wu, Inhibition properties and adsorption behavior of imidazole and 2-phenyl-2-imidazoline on AA5052 in 1.0 M HCl solution, *Corros. Sci.* 83 (2014) 124–136.
- [21] M.M. Solomon, S.A. Umoren, M.A. Quraishi, M. Salman, Myristic acid based imidazoline derivative as effective corrosion inhibitor for steel in 15% HCl medium, *J. Colloid Interface Sci.* 551 (2019) 47–60.
- [22] P. Giannozzi, S. Baroni, N. Bonini, M. Calandra, R. Car, C. Cavazzoni, D. Ceresoli, G.L. Chiarotti, M. Cococcioni, I. Dabo, A. Dal Corso, S. de Gironcoli, S. Fabris, G. Fratesi, R. Gebauer, U. Gerstmann, C. Gougoussis, A. Kokalj, M. Lazzeri, L. Martin-Samos, N. Marzari, F. Mauri, R. Mazzarello, S. Paolini, A. Pasquarello, L. Paulatto, C. Sbraccia, S. Scandolo, G. Sclauzero, A.P. Seitsonen, A. Smogunov, P. Umari, R.M. Wentzcovitch, QUANTUM ESPRESSO: a modular and open-source software project for quantum simulations of materials., *J. Phys. Condens. Matter*. (2009) 1–36.
- [23] Y. Zhang, W. Yang, Comment on “generalized gradient approximation made simple,” *Phys. Rev. Lett.* 80 (1998) 890. <https://doi.org/10.1103/PhysRevLett.80.890>.
- [24] M.P. Andersson, Density Functional Theory with Modified Dispersion Correction for Metals Applied to Self-Assembled Monolayers of Thiols on Au(111), *J. Theor. Chem.* 2013 (2013) 1–9. <https://doi.org/10.1155/2013/327839>.
- [25] S. Grimme, Semiempirical GGA-type density functional constructed with a long-range dispersion correction, *J. Comput. Chem.* 27 (2006) 1787–1799.
- [26] V. Barone, M. Casarin, D. Forrer, M. Pavone, M. Sambi, A. Vittadini, Role and effective treatment of dispersive forces in materials: Polyethylene and graphite crystals as test cases, *J. Comput. Chem.* 30 (2009) 934–939.
- [27] M.P. Andersson, Density functional theory with modified dispersion correction for metals applied to molecular adsorption on Pt (111), *Phys. Chem. Chem. Phys.* 18 (2016) 19118–19122.

- [28] S. Gupta, K.K. Gupta, M. Andersson, R. Yazdi, R. Ambat, Electrochemical and molecular modelling studies of CO₂ corrosion inhibition characteristics of alkanolamine molecules for the protection of 1Cr steel, *Corros. Sci.* (2021).
- [29] A. Dal Corso, Pseudopotentials periodic table: From H to Pu, *Comput. Mater. Sci.* 95 (2014) 337–350.
- [30] A. Dal Corso, PSLibrary: A library of ultrasoft and PAW pseudopotentials, (2020).
- [31] E. Ataman, M.P. Andersson, M. Ceccato, N. Bovet, S.L.S. Stipp, Functional Group Adsorption on Calcite: I. Oxygen Containing and Nonpolar Organic Molecules, *J. Phys. Chem. C* 120 (2016) 16586–16596.
- [32] E. Ataman, M.P. Andersson, M. Ceccato, N. Bovet, S.L.S. Stipp, Functional group adsorption on calcite: II. Nitrogen and sulfur containing organic molecules, *J. Phys. Chem. C* 120 (2016) 16597–16607.
- [33] M.P. Andersson, T. Hassenkam, J. Matthiesen, L. V Nikolajsen, D. V Okhrimenko, S. Dobberschütz, S.L.S. Stipp, First-principles prediction of surface wetting, *Langmuir* 36 (2020) 12451–12459.
- [34] R. Ahlrichs, M. Bär, M. Häser, H. Horn, C. Kölmel, Electronic structure calculations on workstation computers: The program system turbomole, *Chem. Phys. Lett.* 162 (1989) 165–169.
- [35] A.D. Becke, Density-functional exchange-energy approximation with correct asymptotic behavior, *Phys. Rev. A* 38 (1988) 3098.
- [36] J.P. Perdew, Density-functional approximation for the correlation energy of the inhomogeneous electron gas, *Phys. Rev. B* 33 (1986) 8822.
- [37] F. Weigend, R. Ahlrichs, Balanced basis sets of split valence, triple zeta valence and quadruple zeta valence quality for H to Rn: Design and assessment of accuracy, *Phys. Chem. Chem. Phys.* 7 (2005) 3297–3305.
- [38] M.P. Andersson, Density functional theory with modified dispersion correction for metals applied to self-assembled monolayers of thiols on Au(111), *J. Theor. Chem.* 2013 (2013) 1–9.
- [39] N. Ochoa, C. Vega, N. Pébère, J. Lacaze, J.L. Brito, CO₂ corrosion resistance of carbon steel in relation with microstructure changes, *Mater. Chem. Phys.* 156 (2015) 198–205.
- [40] Thermo Scientific XPS, Nitrogen, (n.d.).
<https://www.jp.xpssimplified.com/elements/nitrogen.php>.
- [41] E.E. Oguzie, Y. Li, F.H. Wang, Corrosion inhibition and adsorption behavior of methionine on mild steel in sulfuric acid and synergistic effect of iodide ion, *J. Colloid Interface Sci.* 310 (2007) 90–98.
- [42] M.M. Solomon, S.A. Umoren, In-situ preparation, characterization and anticorrosion property of polypropylene glycol/silver nanoparticles composite for mild steel corrosion in acid solution, *J. Colloid Interface Sci.* 462 (2016) 29–41.

- [43] A.P. Srikanth, T.G. Sunitha, V. Raman, S. Nanjundan, N. Rajendran, Synthesis, characterization and corrosion protection properties of poly (N-(acryloyloxymethyl) benzotriazole-co-glycidyl methacrylate) coatings on mild steel, *Mater. Chem. Phys.* 103 (2007) 241–247.
- [44] A. Munis, T. Zhao, M. Zheng, A.U. Rehman, F. Wang, A newly synthesized green corrosion inhibitor imidazoline derivative for carbon steel in 7.5% NH₄Cl solution, *Sustain. Chem. Pharm.* 16 (2020) 100258.
- [45] G. Sığırcık, T. Tüken, M. Erbil, Assessment of the inhibition efficiency of 3, 4-diaminobenzonitrile against the corrosion of steel, *Corros. Sci.* 102 (2016) 437–445.
- [46] K. Toyoda, I. Hamada, S. Yanagisawa, Y. Morikawa, Adsorption of benzene on noble metal surfaces studied by density functional theory with Van der Waals correction, *J. Nanosci. Nanotechnol.* 11 (2011) 2836–2843.
- [47] R. Blossey, Self-cleaning surfaces—virtual realities, *Nat. Mater.* 2 (2003) 301–306.
- [48] T.-M. Wen, K.-H. Hou, C.-Y. Bai, M.-D. Ger, P.-H. Chien, S.-J. Lee, Corrosion behaviour and characteristics of reforming chromized coatings on SS 420 steel in the simulated environment of proton exchange membrane fuel cells, *Corros. Sci.* 52 (2010) 3599–3608.



7. Annexure to the investigation of corrosion inhibition effects of 2-Phenyl-2-Imidazoline on 1Cr steel with CO₂: Effect of H₂S

Annexure to the investigation of corrosion inhibition effects of 2-Phenyl-2-Imidazoline on 1Cr steel with CO₂: Effect of H₂S

This annexure supplements the findings on corrosion inhibition properties of imidazoline based inhibitor on 1Cr steel. When H₂S is present in the CO₂ environment, sour corrosion is observed that can affect corrosion inhibition properties of the inhibitors. This annexure reports the results from preliminary investigations on the corrosion inhibition properties of 2-Phenyl-2-imidazoline (2-PI) alone and in combination with mono ethylene glycol (MEG) on 1Cr steel surface in CO₂-H₂S environment. The electrochemical experimental methods and characterization techniques used in this study are same as those reported in the earlier appended paper.

1. Materials and methods

1.1. Specimen and electrolyte preparation

Same material and polishing methods were used as described in the previously appended paper [1]. In this study, 1wt. % NaCl, CO₂-H₂S saturated solution was used for the experiments. Before each electrochemical experiment, the solution was de-aerated with Nitrogen over the night. After de-aeration, the solution was saturated for 4-hours with 200 ppm of H₂S (92.63 mol% CO₂ & 0.02 mol% H₂S), which led to CO₂:H₂S partial pressure ratios of 4632. Then 200 ppm of 2-PI was injected into the CO₂-H₂S saturated solution, and the solution was de-aerated again for at least 60 minutes to remove any oxygen that may have entered the system. The specimen was then introduced in the solution for electrochemical testing. For experiments with combined 2-PI and MEG, 300ml MEG was added during solution preparation.

1.2. Electrochemical measurement and experimental conditions and procedure

Same as the previously appended paper. Table 2 lists the experimental parameters used in this study.

Table 1. Experimental conditions of electrochemical experiments used in this study.

Parameter	Condition
Material	Q&T 1Cr steel
Solution	1 wt.% NaCl in deionized distilled water, CO ₂ -H ₂ S saturated
Temperature	40 °C
CO ₂ -H ₂ S partial pressure	At 200 ppm H ₂ S (0.9263 bar CO ₂ and 2 x 10 ⁻⁴ bar H ₂ S)
Rotation	350 rpm
Inhibitor	2-PI and MEG
Inhibitor concentration	200 ppm 2-PI and 30 ml MEG
Test duration	2 days

2. Results and Discussion

2.1. Effect of 2-PI alone and together with MEG on L80-1Cr at 200 ppm H₂S, 40°C

2.1.1. LPR measurements

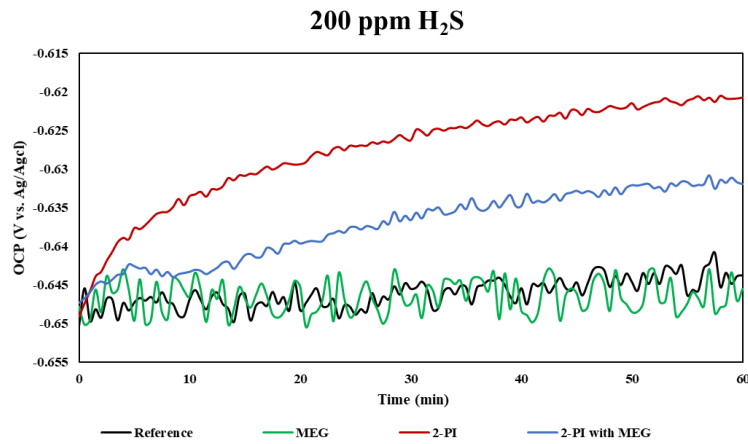


Figure 1. Variation of open circuit potential (OCP) with time for L80-1Cr steel in 1wt % NaCl solution without and with 200 ppm 2-PI and MEG at 40°C, 200 ppm H₂S.

In the presence of H₂S, the OCP values for the reference sample (-0.645 V to -0.643 V) were higher than pure CO₂ conditions (-0.658 V to -0.659 V) [1]. As compared to pure CO₂ environment, 2-PI led to higher OCP values (H₂S : - 0.649 V to - 0.620 V vs CO₂: 0.661 V to - 0.642 V); however, the OCP values for MEG alone (H₂S : - 0.647 V to - 0.645 V vs CO₂: 0.641 V to - 0.649 V) and in combination with 2-PI (H₂S : - 0.647 V to - 0.631 V vs CO₂: 0.646 V to - 0.634 V) were comparable with the pure CO₂ environment. In the CO₂-H₂S environment, highest OCP values were observed for 2-PI, whereas in the pure CO₂ environment, the combination of 2-PI and MEG led to the highest values [1].

In the CO₂-H₂S environment, a positive OCP shift in the presence of inhibitor suggests adsorption of the inhibitor molecules on the steel surface, which offers corrosion inhibition [2,3].

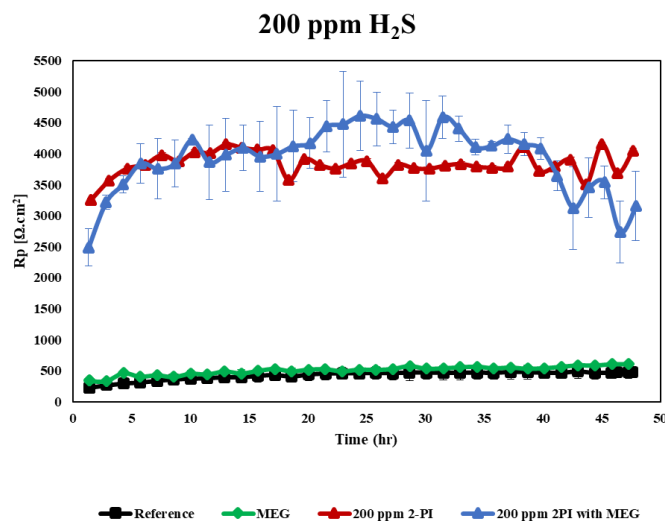


Figure 2. Polarization resistance for L80-1 Cr steel exposed to 1 wt % NaCl solution without and with the addition of 200 ppm of 2-PI, MEG and combination of 2-PI and MEG inhibitor at 40 °C, 200 ppm H₂S for 48 hrs.

The observed R_p values with and without inhibitors were higher in the $\text{CO}_2\text{-H}_2\text{S}$ environment in comparison to pure CO_2 environment [1]. The maximum R_p values for 2-PI alone ($4150 \Omega\cdot\text{cm}^2$ at 45 hours) and in combination with MEG ($4613 \Omega\cdot\text{cm}^2$ at 24 hours) were comparable, but higher than MEG ($604 \Omega\cdot\text{cm}^2$ at 46 hours) and the reference sample ($483 \Omega\cdot\text{cm}^2$ at 43 hours). These peak R_p values in $\text{CO}_2\text{-H}_2\text{S}$ environment were 2.6, 1.6, 3.5, and 4.4 times higher than the pure CO_2 environment, respectively [1]. Interestingly, the increase in R_p values was largest suggesting these results may have resulted from the formation of FeS layer on the sample surface, which is more protective against corrosion. Inhibitors may also have contributed to higher R_p values in $\text{CO}_2\text{-H}_2\text{S}$ environment as compared to pure CO_2 environment as inhibitors have higher affinity for residual Fe_3C , leading to lesser adsorption on the Fe surface in pure CO_2 environment [4].

The inhibitor efficiencies of all inhibitors appeared to decrease in $\text{CO}_2\text{-H}_2\text{S}$ environment as compared to pure CO_2 environment (Table 2). Since inhibitor efficiencies are calculated in reference to the R_p values of the uninhibited sample (equation 1), the decrease in efficiency in $\text{CO}_2\text{-H}_2\text{S}$ environment resulted from a greater increase in R_p values of the reference sample as compared to R_p values of the inhibitors.

$$\text{Inhibitor efficiency (\%)} = \frac{(R_{p_{\text{inhibited}}} - R_{p_{\text{Uninhibited}}})}{R_{p_{\text{inhibited}}}} \times 100 \quad (1)$$

Table 2. Comparison of efficiency between different types of inhibitors at 200 ppm H_2S , 40°C .

Inhibitor type	Inhibitor efficiency (%) at 200 ppm H_2S	Inhibitor efficiency (%) in pure CO_2 environment
2-PI	88	93
2-PI with MEG	90	96
MEG	20	35

2.1.2. Electrochemical impedance spectroscopy investigation

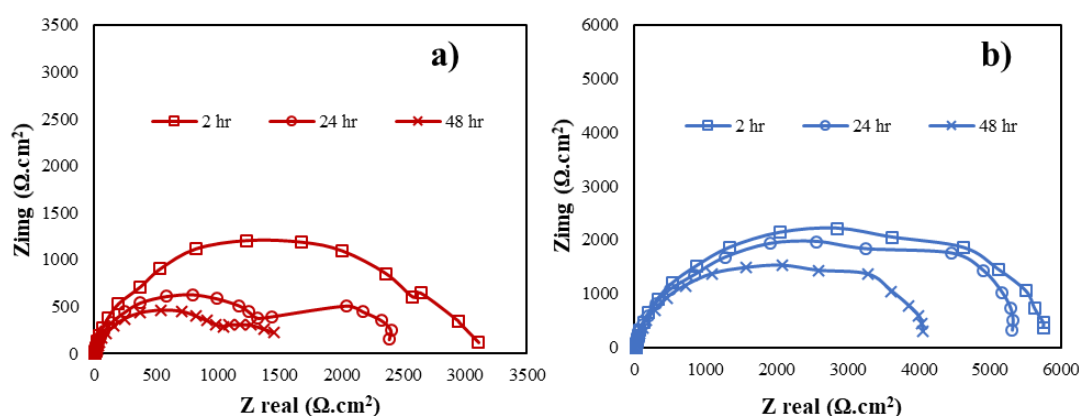


Figure 3. Results of electrochemical impedance measurements: Nyquist plot (a): pure 200 ppm 2-PI inhibitor and (b): 200 ppm 2-PI inhibitor in combination with MEG on L80-1 Cr steel exposed to 1 wt % NaCl solution at 200 ppm H_2S , 40°C .

Fig. 3 shows the impedance results in the form of Nyquist plot for 2-PI alone and in combination with MEG. The diameter of the capacitance loop for combination of 2-PI and

MEG is higher than pure 2-PI (Fig. 3a). In both cases, the diameter of the capacitance loop decreased with time together with the occurrence of a prominent double loop after 24 hours.

The Randle's electrochemical system with double time constant used to fit impedance results shown in Fig. 3 was same as used in the previously appended paper. Table 3 represents fitting of impedance data at the last cycle of impedance measure at different time points – 2 hrs, 24 hrs, and 48 hrs. The pattern of EIS data circuit fitting was similar for all inhibitors and comparable between pure CO₂ and CO₂-H₂S environments. The corrosion product layer became more porous and reduced in thickness over time as indicated by an increase R_{pr} and decrease in C_{fc} values. However, the corrosion product layer was still protective as indicated by an increase in R_{ct} and increase in C_{dl} values.

Table 3. Electrochemical impedance parameters obtained from the measured EIS data circuit fitting for L80-1 Cr steel exposed to 1 wt % NaCl solution at 40 °C, with the addition of 200 ppm 2-PI alone and combination of 200 ppm 2-PI and MEG at time 2, 24 and 48 hrs.

Sample	Immersion time (hrs)	R _{ct} Ω.cm ²	C _{dl} μΩ ⁻¹ .cm ⁻² .s ⁿ	n ₁	R _{pr} Ω.cm ²	C _{fc} μΩ ⁻¹ .cm ⁻² .s ⁿ	n ₂
2-PI	2	2671	907	0.97	3135	48	0.99
	24	3208	828	0.48	17	225	0.48
	48	6890	844	0.96	16	301	0.14
2-PI with MEG	2	1132	377	0.99	3366	129	0.98
	24	2185	366	0.97	3074	135	0.99
	48	2258	961	0.94	2913	189	0.97

2.1.3. Scanning electron microscopy, XRD and XPS

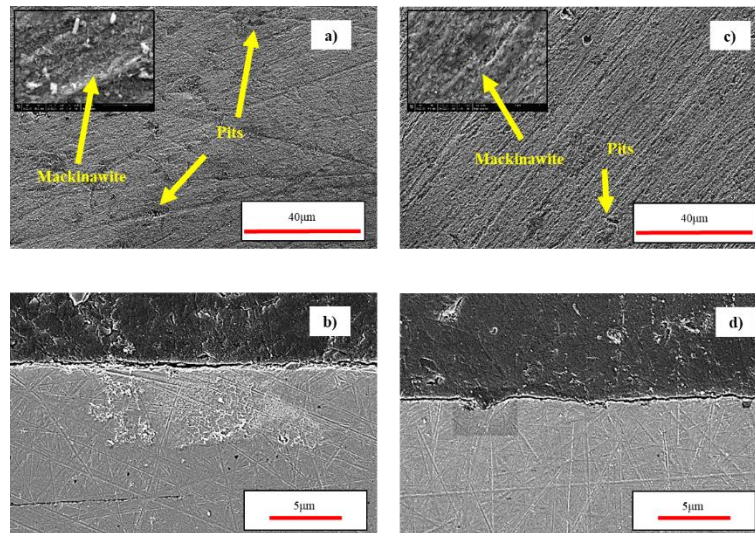


Figure 4. SEM images (Cross-sectional and top view) for L80-1 Cr steel exposed to 1 wt% NaCl solution, (a and b): specimen with 200 ppm 2-PI and (c and d): specimen with combination of MEG and 2-PI at 200 ppm H₂S, 40 °C.

The surface morphology for the reference sample in CO₂-H₂S environment was different than the pure CO₂ environment. In presence of 200 ppm H₂S, the corrosion product was thin, but more protective without any cracks [5], whereas in pure CO₂ environment, the corrosion product layer was thick with pores and cracks were observed [1]. These results support the observation of higher 4.4 times higher R_{pr} in the presence of H₂S as compared to pure CO₂ environment.

When comparing 2-PI alone and in combination with MEG in the CO₂-H₂S environment, the surface morphology of the sample was similar and showed few micro-pits. A thin layer of corrosion products was observed in both cases, with slightly higher thickness in case of 2-PI alone. The type of FeS corrosion product formed appeared to be Mackinawite type (Fig. 4a and 4c), which is also reported to be seen at low concentrations of H₂S by previous literature [6,7]. In pure CO₂ environment also, the surface morphology of 2-PI alone were like that of 2-PI combined with MEG; however, as compared to pure H₂S environment, more pitting was observed on the sample surface.

The XRD results (Fig. 5) confirmed the presence of Fe₃C (residual product) and low-intensity reflections of FeS (reflections 42.9, 73.4, and 88.9 only) on the sample in the CO₂-H₂S environment. With the addition of inhibitors, the intensity of the Fe₃C diffracted peaks were decreased. The highest change was observed for 2-PI, for example, the reflections (121), (210), (002), (211), (102), (112), (131), (221) and (122) almost disappeared suggesting lower iron dissolution in the presence of 2-PI alone.

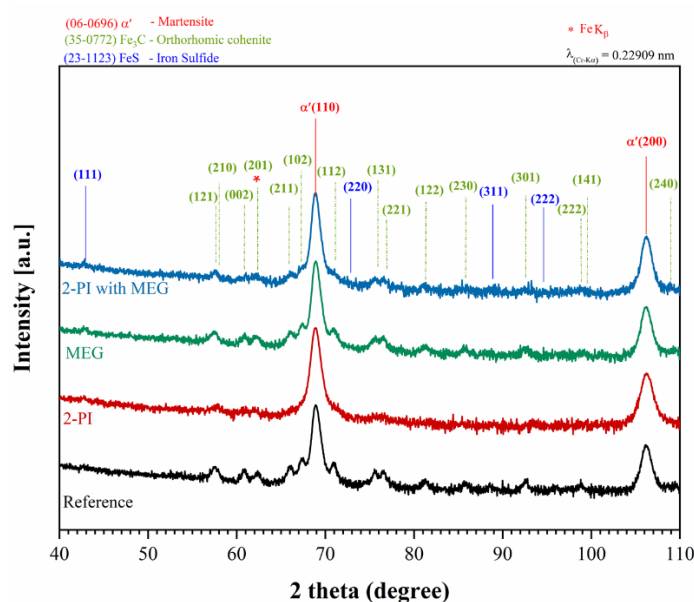


Figure 5. Results of X-ray diffraction of L80-1Cr steel corroded in 1 wt% NaCl without and with 2-PI, MEG and combination of 2-PI and MEG inhibitors at 200 ppm H₂S concentration, 40 °C.

The XPS results also confirm the presence of thin-layer of organic film (2-PI inhibitor) and FeS corrosion product layer over the steel sample surfaces in CO₂-H₂S environment. Wide-scan spectra of Fe2p, C1s, N1s and S2p of the corroded samples were observed at 200 ppm H₂S concentration with 2-PI alone (Figs. 6a-d) and 2-PI in combination with MEG (Figs. 6e-h). The peaks in individual spectra confirmed the presence of Fe, C, N, and S. The signals of C1s and N1s were mainly attributed to the inhibitors adsorbed on the steel surface, whereas the signals of S2p resulted from the corrosive products. The signal of Fe2p could be assigned to the iron matrix and its corrosion products.

Fe2p peak was composed of two peaks, Fe2p_{1/2} peak and Fe2p_{3/2} peak. Further, Fe2p_{3/2} peak shows multiple splitting and composed of three peaks. The Fe 2p_{3/2} peaks at 711.08 eV and 710.88 eV in Figs 6a and 6e corresponds to Fe (III)-S peak respectively [8]. The high-resolution spectra of C1s are shown in Fig. 6b, 6f and 6j. The high resolution carbon peaks then splits into three peaks, one at 284.58 eV which corresponds to carbon in iron carbide Fe-C bond [9] and other non-intensive peak at 286.28 eV and 288.38 eV attribute to binding energies of C-C

bond [10] and $-C=N$ bond [11,12] respectively. In Fig. 6c and 6g high-resolution spectra of N1s is presented. In case of 2-PI (Fig.6c), peaks at 398.68 eV and 405.98 eV relates to $C=N-C$ in 2-PI and Fe(II)/ Fe(III) nitrate respectively [9,13]. Whereas in case of 2-PI in combination with MEG, the peak is shifted to 400.38 which indicate $C-NH_2$ bond [14]. Two peaks can be observed in the high-resolution spectra of S2p. Peaks at (161.98 eV, and 162.18 eV) denote the presence of ferrous sulfide on steel surface in Figs. 6d and 6h respectively [15,16], and peaks at (168.58 eV and 168.38 eV) corresponds to the oxidation of sulfur [17,18]. The XPS results confirm the adsorption of 2-PI on the steel sample in the CO_2-H_2S environment.

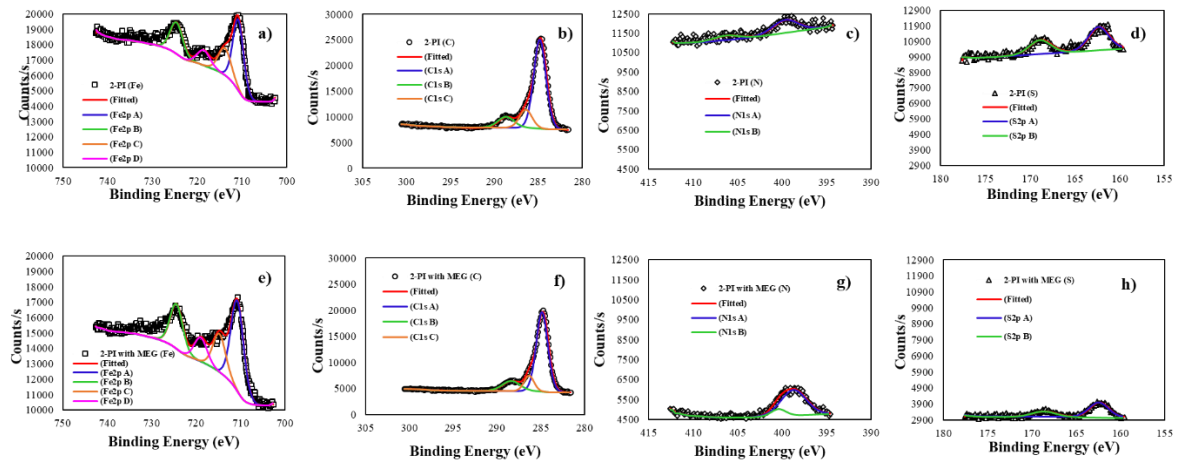


Figure 6. XPS spectrum for L-80 1 Cr steel specimens corroded (a, b, c and d): Fe2p, C 1s, N 1s and S2p in presence of 2-PI and (e, f, g and h): Fe2p, C 1s, N 1s and S2p in presence of 2-PI in combination with MEG in 1% NaCl solution at 200 ppm H_2S , 40°C.

3. Conclusions

- 200 ppm 2-PI alone was found to be effective (high R_p and corrosion inhibition efficiency) in corrosion inhibition of 1Cr steel in the presence of 200 ppm H_2S in CO_2 environment.
- No significant synergistic effect of MEG and 2-PI was found on corrosion inhibition of 1Cr steel in the presence of 200 ppm H_2S in CO_2 environment.
- Impedance results show that the corrosion product layer became porous and thin over the time, but was still protective against corrosion.
- The XPS confirm the presence of organic inhibitor (2-PI) film and FeS in the corrosion product layer on the steel sample at 200 ppm H_2S , which contributed to the corrosion inhibition effects.

References

- [1] G. Shivangi, A. Martin, A. Rajan, Electrochemical and molecular modelling studies of corrosion inhibition characteristics of Imidazolines on 1Cr steel under sweet conditions, Unpubl. Results. (2021).
- [2] A. Munis, T. Zhao, M. Zheng, A.U. Rehman, F. Wang, A newly synthesized green corrosion inhibitor imidazoline derivative for carbon steel in 7.5% NH₄Cl solution, *Sustain. Chem. Pharm.* 16 (2020) 100258.
- [3] G. Sığırcık, T. Tüken, M. Erbil, Assessment of the inhibition efficiency of 3, 4-diaminobenzonitrile against the corrosion of steel, *Corros. Sci.* 102 (2016) 437–445.
- [4] S. Gupta, K.K. Gupta, M. Andersson, R. Yazdi, R. Ambat, Electrochemical and molecular modelling studies of CO₂ corrosion inhibition characteristics of alkanolamine molecules for the protection of 1Cr steel, *Corros. Sci.* (2021).
- [5] G. Shivangi, A. Martin, A. Rajan, Corrosion inhibition properties of eco-friendly green inhibitors containing aloe vera plant extract on 1 Cr steel under H₂S conditions with CO₂, Unpubl. Results. (2021).
- [6] J.S. Smith, J.D.A. Miller, Nature of sulphides and their corrosive effect on ferrous metals: a review, *Br. Corros. J.* 10 (1975) 136–143.
- [7] H. Ohfuji, D. Rickard, High resolution transmission electron microscopic study of synthetic nanocrystalline mackinawite, *Earth Planet. Sci. Lett.* 241 (2006) 227–233.
- [8] M. Mullet, S. Boursiquot, M. Abdelmoula, J.-M. Génin, J.-J. Ehrhardt, Surface chemistry and structural properties of mackinawite prepared by reaction of sulfide ions with metallic iron, *Geochim. Cosmochim. Acta.* 66 (2002) 829–836.
- [9] S. Delpeux, F. Beguin, R. Benoit, R. Erre, N. Manolova, I. Rashkov, Fullerene core star-like polymers—1. Preparation from fullerenes and monoazidopolyethers, *Eur. Polym. J.* 34 (1998) 905–915.
- [10] N. Ochoa, C. Vega, N. Pébère, J. Lacaze, J.L. Brito, CO₂ corrosion resistance of carbon steel in relation with microstructure changes, *Mater. Chem. Phys.* 156 (2015) 198–205.
- [11] La Surface Database, (n.d.). <http://www.lasurface.com/accueil/index.php?lang=fr> (accessed November 30, 2021).
- [12] NIST X-ray Photoelectron Spectroscopy Database, (n.d.). <http://dx.doi.org/10.18434/T4T88K> (accessed November 30, 2021).
- [13] O. Olivares-Xometl, N. V Likhanova, M.A. Domínguez-Aguilar, J.M. Hallen, L.S. Zamudio, E. Arce, Surface analysis of inhibitor films formed by imidazolines and amides on mild steel in an acidic environment, *Appl. Surf. Sci.* 252 (2006) 2139–2152.
- [14] Thermo Scientific XPS, Nitrogen, (n.d.). <https://www.jp.xpssimplified.com/elements/nitrogen.php>.
- [15] J.M. Bonello, R.M. Lambert, The structure and reactivity of quinoline overlayers and the adsorption geometry of lepidine on Pt {1 1 1}: model molecules for chiral modifiers in enantioselective hydrogenation, *Surf. Sci.* 498 (2002) 212–228.
- [16] S. Nakamura, A. Yamamoto, Electrodeposition of pyrite (FeS₂) thin films for photovoltaic cells, *Sol. Energy Mater. Sol. Cells.* 65 (2001) 79–85.

- [17] B.C. Bostick, S. Fendorf, Arsenite sorption on troilite (FeS) and pyrite (FeS₂), *Geochim. Cosmochim. Acta.* 67 (2003) 909–921.
- [18] R. V Kashkovskiy, Y.I. Kuznetsov, L.P. Kazansky, Inhibition of hydrogen sulfide corrosion of steel in gas phase by tributylamine, *Corros. Sci.* 64 (2012) 126–136.



8. Paper III: CO₂ corrosion inhibition capability of an eco-friendly inhibitor containing green aloe vera plant extract on 1Cr steel: experimental and molecular modelling studies

Shivangi Gupta, Martin Andersson, Rouhollah Yazdi, Rajan Ambat, CO₂ corrosion inhibition capability of an eco-friendly inhibitor containing green aloe vera plant extract on 1Cr steel: experimental and molecular modelling studies, submitted to Corrosion Science 2022.

CO₂ corrosion inhibition capability of an eco-friendly inhibitor containing green aloe vera plant extract on 1Cr steel: experimental and molecular modelling studies

Shivangi Gupta^{a*}, Rouhollah Yazdi^a, Martin Andersson^b, Rajan Ambat^a

^a Section of Materials and Surface Engineering, Department of Mechanical Engineering, Technical University of Denmark, Produktionstorvet, Kongens Lyngby, 2800 Denmark

^b Department of Chemical Engineering, Technical University of Denmark, Produktionstorvet, Kongens Lyngby, 2800 Denmark

*Corresponding author. Tel: +45 60773762, E-mail address: shig@mek.dtu.dk (S. Gupta).

Abstract

Green inhibitors such as aloe vera offer alternate ways of corrosion inhibition in an environment-friendly manner. This study utilized electrochemical techniques and molecular modelling to study the corrosion inhibition properties and the underlying mechanisms of corrosion inhibition. The highest efficiency (88.7%) was seen due to the synergistic effects of aloe vera and mono ethylene glycol. Molecular modelling confirmed the highest adsorption energy (-110 kJ/mol) of aloin, the main constituent of aloe vera that contributes to its corrosion prevention properties. Aloe vera in combination with other organic inhibitors offers an efficient and “green” way of corrosion inhibition in the oil and gas industry.

Keywords: A. Steel, B. Polarization, B. EIS, B. XPS, C. Oxidation.

1. Introduction

Corrosion in the Oil and Gas industry can lead to undesirable incidents compromising safety at both an individual and environmental level. Interaction of carbon steel and carbon dioxide (CO₂) in the pipelines offers a favorable environment for sweet corrosion happening. Despite of its susceptibility to corrosion, carbon steel is generally the most commonly used alloy in pipelines; due to its cost effectiveness and excellent functional properties. As a result, increasing new ways are warranted to mitigate the risk of corrosion in the Oil and Gas industry.

The use of corrosion inhibitors is one of the commonly used methods for corrosion prevention. Heteroatoms (e.g., O, N) and π electrons presented in the inhibitors efficiently cause the adsorption of their molecules on the L80-1 Cr steel surface and offer protection from corrosion [1]. Inhibitors typically offer a cost effective and efficient way of corrosion prevention; however, they potentially lead to environmental hazards [2–4]. In addition, the inhibitors degrade gradually and require frequent injections to supplement the corrosion prevention effects of degrading inhibitors [5].

Green inhibitors that are more compatible with nature may favorably offer similar cost effective and efficient inhibitory effects without the environmental hazards and pollution [6]. For instance, some plant extracts have the adsorption properties of an effective inhibitor and can be used in a more eco-friendly manner due to both their biodegradability and non-toxic nature [7]. Aloe vera-containing chemical can potentially be one example of an environmentally friendly inhibitor that is rich in several organic compounds [8–10] of high molecular weight with heteroatom and π centers in their molecular structures. These organic constituents of aloe vera include tannins, saponins, steroids, arabinose, resins, galactose, carbohydrates, polysaccharides, anthraglycosides and anthraquinones. Furthermore, it also contains several biologically active compounds [7], such as aloin and aloe emodins. Aloin is responsible for corrosion inhibition and its molecular structure reveals an anthraquinone link to a pentose with 5 oxygen atoms, and aloe emodins show heterocyclic organic compounds with nitrogen or oxygen atoms [11]. Due to its constituent organic compounds, aloe vera offers to be a potential green inhibitor; however, its corrosion inhibition needs to be established before its commercial use. So far, the corrosion inhibition properties of the aloe vera extract have been established for the corrosion of mild steel [9,12–16], stainless steel [12,17] zinc [11], aluminum [10] and iron [18,19] in acid solutions, and also Bronze in 3% NaCl solution [20].

Commercial inhibitors consist of different organic compounds that work synergistically to achieve optimal inhibitory effects. Similarly, a combination of aloe vera and other organic compounds such as Mono Ethylene Glycol (MEG) may result in improved inhibition efficiency. However, to the best of our knowledge, there is no reported work on the inhibitive properties of aloe vera extract on the corrosion of low carbon steel in the CO₂ environment.

The objective of this study was to investigate the inhibitive properties of aloe vera on carbon steel surface. In addition, the synergistic corrosion inhibition properties provided by the combination of aloe vera extract and Mono Ethylene Glycol (MEG) were studied in this paper. In order to profoundly understand if aloe vera alone or in combination with MEG can be used to supplement the effects of degrading inhibitors, their inhibitive effects through subsequent injections were also evaluated. From an environmental point of view, glycol has a low toxicity and while it is not surface active nor bioaccumulable; it is degradable and recycled in the process. It serves a dual function: hydrate prevention and corrosion control [21]. This research utilized experimental techniques to study the corrosion inhibition behavior of different inhibitor molecules on L80-1Cr. In addition, this study utilized molecular modelling for the estimation of the adsorption energy on Fe(110) surface to help understand the molecular mechanisms underlying the corrosion inhibition behavior. Different electrochemical techniques such as Open Circuit Potential (OCP), Linear Polarization Resistance (LPR) and Electrochemical Impedance Spectroscopy (EIS) were employed to assess the electrochemical behavior of the material and to measure the corrosion rate. Furthermore, for a comprehensive understanding of the inhibitor adsorption mechanism, different surface characterization techniques, including Scanning Electron Microscopy (SEM) equipped with Energy Dispersive Spectroscopy (EDS), Fourier-Transform Infrared Spectroscopy (FTIR) were used.

2. Material and methods

2.1. Specimen preparation

The samples used in this study were made of 1Cr steel (L80) in a Quenched and Tempered (Q&T) condition with a chemical composition listed in Table 1. The specimens were machined into a cylindrical shape with a total surface area of 3.9 cm². The surface of the sample was mechanically polished with SiC paper grades of P220, P320, P500, and P1000 while being cooled with de-ionized distilled water simultaneously. Immediately after polishing, the specimens were chemically degreased with ethanol, rinsed with de-ionized distilled water, and then air-dried. The prepared and dried specimens were used for electrochemical experiments. At the end of the experiment, the specimens were taken out from the cell and then rinsed with de-ionized distilled water and ethanol, dried in air, and stored in a desiccator for further characterization.

Table 1. Chemical composition in wt % of the L80-1Cr steel.

Material	C	Cr	Mn	Mo	P	Si	S	Fe
API 5CT L80	0.40	1.10	0.75	0.20	≤0.035	0.20	≤0.040	base

2.2. Electrolyte preparation

1wt. % NaCl solution pre-saturated with CO₂ was used for all electrochemical experiments. In some cases, 20 volume percent MEG (300 ml) of total cell solution was added to the NaCl solution before running the experiments. Before immersing the specimen, nitrogen gas was sparged in the solution for about 12 hours in order to completely remove the dissolved and trapped oxygen gas (i.e., in order to obtain deaerated condition). The sparging gas was then switched to CO₂ for 4 hours to saturate the solution. The initial pH of the NaCl solution without and with MEG was measured to be 3.9 and 4.2, respectively at 40 °C. The inhibitors were injected into the CO₂-saturated solution. After inhibitor injection and before the immersion of specimens, the solution was de-aerated again for at least 30 minutes in order to remove any oxygen that might have entered during the injection. Furthermore, during electrochemical testing, CO₂ gas was continuously purged into the solution to maintain its saturation and avoid any oxygen entrance.

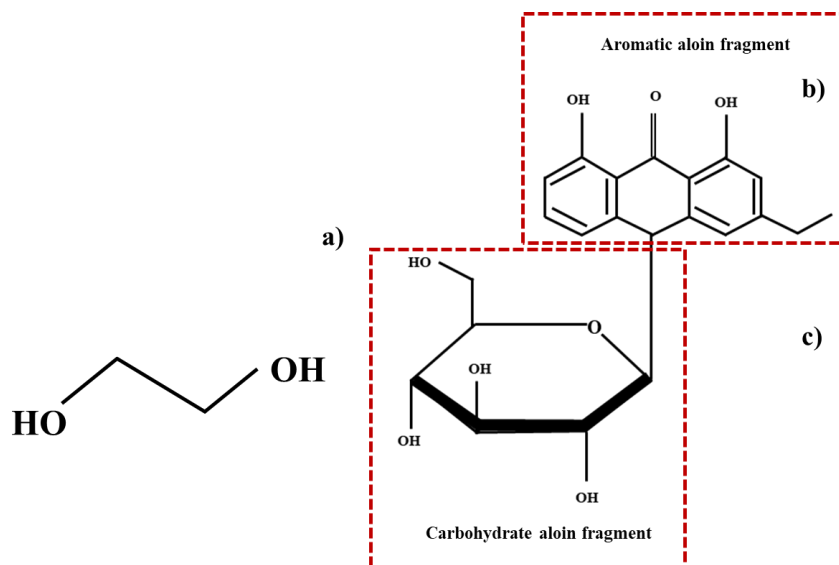


Figure 1. Structure of (a): Ethylene glycol, (b): Aromatic aloin fragment, (c): Carbohydrate aloin fragment.

2.3. Inhibitors

Aloin (purity of $\geq 97\%$) and MEG of spectrophotometric grade ($\geq 99\%$) was purchased from Sigma Aldrich, and aloe vera inhibitor was extracted from aloe vera plant. The chemical structure of the used inhibitors are shown in Fig. 1.

Preparation of aloe vera extract: Complete aloe vera extract extraction process is shown in Fig.2. Mature healthy and fresh leaves were taken from an aloe vera plant (see Fig. 2a). The leaves were washed with de-ionized water to remove any possible dirt and contaminations. The spikes were removed along the margins. Then, the leaves were transversely cut into pieces, and the thick epidermis was carefully separated from the parenchyma (Fig. 2b). The parenchyma was collected (Fig. 2c) and ground in a mechanical blender together with the de-ionized distilled water in the ratio of 1:2 (aloe vera: water) to form a homogenized gel extract. The extract was filtered through a filter paper (Fig. 2d) and stored in an air-tight bottle (Fig. 2e) in a refrigerator for a day prior to the experiment.

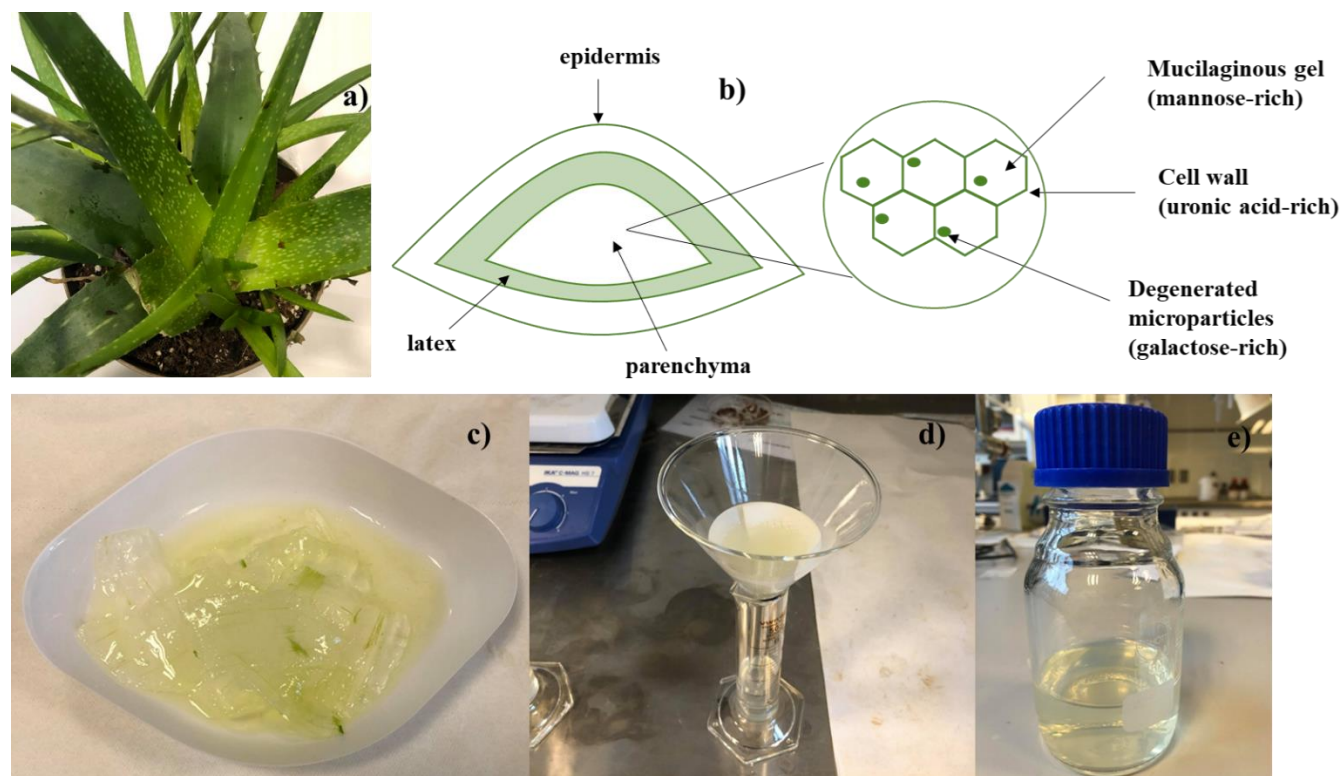


Figure 2. a): Typical aloë vera plant, b): Schematic cross-section of an aloë vera leaf and major components of the parenchyma, (c): aloë vera gel extracted from leaves, (d): Filtration of aloë vera extract and (e): stored aloë vera extract inhibitor.

2.4. Electrochemical measurement

The electrochemical corrosion tests were carried out using a standard three-electrode cell setup in a 1.5 L glass cell. An Ag/AgCl reference electrode was placed in contact with the solution through a glass-lug-in capillary and a concentric ring of platinum wire was used as the counter electrode. The corrosion potential (E_{corr}) and the polarization resistance were measured using Linear Polarization Resistance (LPR) every 1.5 hours. During LPR measurements, the potential was scanned in a potential range of ± 10 mV vs. Open-Circuit Potential (OCP) at a scan rate of 0.167 mV/s. Based on the previous experience, a duration of 1 hour was chosen for the OCP stabilization. After the OCP stabilization, the EIS measurements were performed by applying an AC signal amplitude of ± 10 mV vs OCP in a frequency range of 10 mHz -10 kHz.

2.5. Experimental conditions and procedure

As listed in Table 2, the inhibitive effects of aloin (200 ppm), different concentrations of aloë vera (2000, 3000, 4000 and 8000 ppm), MEG (300ml) and a mixture of MEG-aloin and MEG-aloe vera were studied on the CO₂ corrosion of L80-1Cr steel samples at a temperature of 40 °C. To understand if aloë vera alone or in combination with MEG can supplement the effects of degrading the initial dose of inhibitors, another set of long-term experiments was carried out for 14 days. In these experiments, initially the specimens were corroded in the NaCl solution in the presence of MEG and 4000 ppm of aloë vera extract for 4 days. After 4 days of electrochemical measurement,

again 4000 ppm of aloe vera was injected into the solution and the polarization resistance was monitored for 3 more days. The specimen was then shifted into new cell containing a fresh NaCl solution mixed with MEG and 4000 ppm of aloe vera and the polarization resistance was monitored for another 7 days. All electrochemical experiments were performed at least twice and the average values with error bars are reported in the results section.

Table 2. Experimental conditions of electrochemical experiments used in this study.

Parameter	Condition
Material	Q&T 1Cr steel
Solution	1 wt.% NaCl in deionized distilled water, CO ₂ saturated
Temperature	40 °C
CO ₂ partial pressure	0.93 bar
Rotation	350 rpm
Inhibitor	Aloe vera extract, Aloin and MEG
Inhibitor concentration	200, 2000, 3000, 4000 and 8000 ppm
Test duration	2 and 14 days

2.6. *SECM Electrochemical characterization*

Scanning electrochemical microscopy (M470, Biologic, France) was used to locally carry out electrochemical measurements using a three-electrode cell. The Pt tip with a diameter of 15 μm was selected for the SECM study, which was peripherally insulated by a glass sheath. In the electrochemical cell, both the tip and samples were used as the working electrodes, a Pt plate and Ag/AgCl was also employed as the counter and reference electrodes, respectively. The mode of intermittent contact (ic-AC-SECM) was selected to run during SECM measurements for eliminating the signals coming from the surface topography, which could interfere with the detected electrochemical signals. For this purpose, an integrated piezoelectric block and load cell were utilized to adjust the distance between the oscillating tip and the surface.

Before the experiments, the disks were embedded in an epoxy resin and they were mechanically polished using SiC papers up to #4000 and 1 μm diamond particle suspension. The SECM measurements were performed in a 0.01 M NaCl solution without and with 20% MEG, 200 ppm aloe vera over a surface area of 100 μm ×100 μm with a step size of 5 μm along x- and, y-axis. The measurements were made under the alternating potential of ± 50 mV over the OCP of Pt electrode at the fixed frequency of 100 kHz, while the sample surfaces were left potentially-unbiased. The impedance magnitudes as the outcome of the SECM experiments were plotted in 2D graphs. Indeed, SECM imaging in the AC mode was obtained by scanning the tip in the x; y-axis over the arrays and; monitoring and processing local impedances.

2.7. *Surface characterization and phase analysis*

The morphological and elemental analysis of the corrosion products were investigated using a Zeiss Supra FEG-SEM using 5 kV acceleration voltage, assisted with energy dispersive X-ray (EDS) analysis equipment. A Bruker D8 Advance X-Ray Diffractometer (XRD) was also employed to identify the phase composition of the formed layer. The instrument was operated at

35 kV and 50 mA with Cr-K α radiation ($\lambda=0.22909$ nm), and the 2θ ranged from 35° to 85° with a step size of 0.05° , and a 10 s count time at each step.

FTIR has been used in this study to identify inhibitors that are tenaciously adsorbed to L80-1Cr steel surface and corrosion film. FTIR measurements were carried using a NicoletTMiNTM10 MX infrared imaging microscope with a Mercury Cadmium-Telluride (MCT) detector cooled with liquid nitrogen. The samples were analyzed using an Attenuated Total Reflection (ATR) method. The spectra were recorded in the range of $4000\text{--}500\text{cm}^{-1}$ with a resolution of 4 cm^{-1} , which allows for the detection of multiple diagnostic bands in the obtained infrared (IR) spectrum.

2.8. Methodology of molecular modelling

The density functional theory (DFT) calculations were performed in a pseudopotential plane-wave formalism with the Quantum Espresso package [22]. The revPBE functional [23] and added semi-empirical dispersion corrections were used in the DFT-D2 implementation [24–26]. The s_6 parameter for revPBE was 1.25, and a 12 Bohr cutoff was used for Fe calculations [25]. The C6 vdw parameter for Fe was set to be 159.927, the same as the noble gas in the row above, Ar, as described in [27,28]. All pseudopotentials were ultrasoft (or PAW), generated using revPBE, and were taken from PS Library 0.2.5 [29,30]. The kinetic energy cutoff was 40 Ry, and the density cutoff was 400 Ry, which has been shown for similar setups to provide converged adsorption energies [31,32].

Alain is one of the key compounds present in aloe vera that contributes to its corrosion inhibition properties [11]. The chemical structure of alain is quite large and bulky, which makes calculations of adsorption in a periodic formalism difficult because the very large unit cell required would also lead to very slow calculations. Therefore, to avoid artifacts from interactions between the periodic images, the alain structure was split into two parts (see Fig. 1b) by breaking a C-C bond and each of the fragments was instead terminated by a hydrogen atom. The molecular interaction of both alain parts with a more moderately sized Fe(110) surface is shown in Figs. 3. The adsorption energies for both parts of alain, water and MEG on a 2×3 Fe (110) unit cell (and a 4×3 unit cell for large adsorbates) were calculated to model their behaviors on iron surface as shown in Table 3a. The Fe (110) iron surface used in this study is the most stable Fe surface termination.

To perform slab calculations on Fe (110) surface, 17 \AA vacuum was inserted between the material slabs, which consisted of four molecular layers. The fourth layer was kept frozen during the geometry optimizations to retain the bulk atomic positions. The lattice parameters for Fe (110) were initially relaxed for bulk fcc iron using the same functional as for calculating the adsorption energies to minimize the effects of surface strain on the adsorption properties.

The adsorption energies of different inhibitor molecules on model surfaces were obtained using the following equation (1).

$$E_{\text{adsorption}} = E_{\text{surface+inhibitor}} - (E_{\text{surface}}) - (E_{\text{inhibitor}}) \quad (1)$$

The different functional groups of MEG and alain allow for several possible adsorption geometries, with either group bonding to the Fe surface. The adsorption energies of both binding

geometries were calculated, using several different starting geometries. Using the definition of adsorption energy from Eq. (1) means that the more negative the adsorption energy, the stronger was the bond between the molecule and the surface.

2.9. Methodology of contact angle measurement

The surface of the specimens was polished with the same procedure as mentioned in the section 2.1. Then the specimens were immersed into the inhibitors for 15 minutes and then dried. The specimen was placed on the stage and then the camera and the illumination lamp were turned on. The specimen stage was levelled and a drop of test solution was drained from the pipette onto the specimen. The change in contact angle of the drop was measured with time at both ends of the drop (θ_{C1} and θ_{C2}). Each measurement was repeated for 5-times.

3. Results

3.1. Molecular modeling simulation using density functional theory (DFT)

DFT calculations of the adsorption behavior of water, aloin and MEG on the Fe (110) surface are shown in Table 3a. The adsorption energy values of aloin fragments were found to be greater than water (-31 kJ/mol) and MEG (-50 kJ/mol) molecules. When comparing the two parts of aloin, the adsorption energy values were generally higher for aromatic aloin fragment. For example, the adsorption energy of aromatic aloin fragment on a 2x3 Fe(110) unit cell (-OH; -92 kJ/mol) and on a 4x3 Fe(110) unit cell (-CH; -110 kJ/mol) were higher as compared to carbohydrate aloin fragment on 2x3 Fe unit cell (-OH of the ring; -71 kJ/mol and -OH of the side group; -62 kJ/mol) and on 4x3 Fe unit cell (-CH; -101 kJ/mol). Table 3b shows the difference in the adsorption energy between green inhibitors and one or more molecules of water ($\Delta E_{\text{adsorption}}$), in order to estimate the adsorption energy in an aqueous solution, where the inhibitor molecule needs to replace water molecule(s) at the interface. Both aromatic aloin fragment (-OH) and carbohydrate aloin fragment (-OH of the ring) had negative values for at least two water molecules when bonded to the 2x3 Fe(110) surface suggesting the favourable displacement of at least two water molecules based on energy alone. Whereas, when both aloin fragments bonded with -CH (of the ring) on 4x3 Fe(110) surface, they had a negative value for at least three water molecules indicating the displacement of at least three water molecules, again based on energy alone. For carbohydrate aloin fragment when binding to -OH side group only, displacement of one water molecule was favourable (-31 kJ/mol). In order to estimate the free energy of adsorption, the contribution to upon adsorption, with the entropy increase in principle proportional to the number of water molecules that are released [33,34]. The adsorption energy of a water molecule on Fe(110) compares reasonably well to the adsorption energy on kaolinite (Si side) from (Table 2 in [34]). Therefore it is assumed that the same entropy increase ($T\Delta S$) upon release from the surface can be applied in our case, which is 0.34 kJ/mol at room temperature (Table 3 in [34]). This means that the entropy increase is comparable to the adsorption energy of water, and that the free energy difference is almost 0 for removing a water molecule from the surface. This means that there is an entropic driving force for maximizing the adsorption area of a molecule on the surface, while there is an enthalpic driving force for minimizing adsorption area. The approximations used here, together with the fact that the calculations for the entropy of inhibitor molecules were not conducted which means that this discussion is qualitative at the moment. Further investigations focussing on modelling could take

into account the entropy change of the inhibitor molecule as well, and also the change in solvation energy upon adsorption for both water and the inhibitor molecules [35].

Figure 3 shows the most stable optimized adsorption geometries of the molecules. Two kind of binding geometry were observed – vertical and parallel to the Fe(110) surface. The inhibitors binding vertically to the Fe surface had lower adsorption energy value (e.g. aromatic aloin fragment bind with -OH of side group on 4x3 Fe(110) unit cell as shown Fig. 3 d), whereas those binding parallelly had higher adsorption energy values (e.g. aromatic aloin fragment bind with -CH on 4x3 Fe(110) unit cell as shown in Fig. 3 e). The distance between molecules forming the bond with the Fe(110) surface for different structures ranged between 2.22Å (aromatic aloin fragment bonded -CH on 4x3 Fe) – 4.25Å (carbohydrate aloin fragment bonded with -OH of the ring on 2x3 Fe). This distance between the bonding surfaces is apparently in the range that can lead to strong molecular bonds. Because the change in free energy of removing water from the surface is almost 0, the orientation of the molecule will not matter much (at room temperature), and the most stable geometry can be deduced directly from the adsorption energy, also in an aqueous solution.

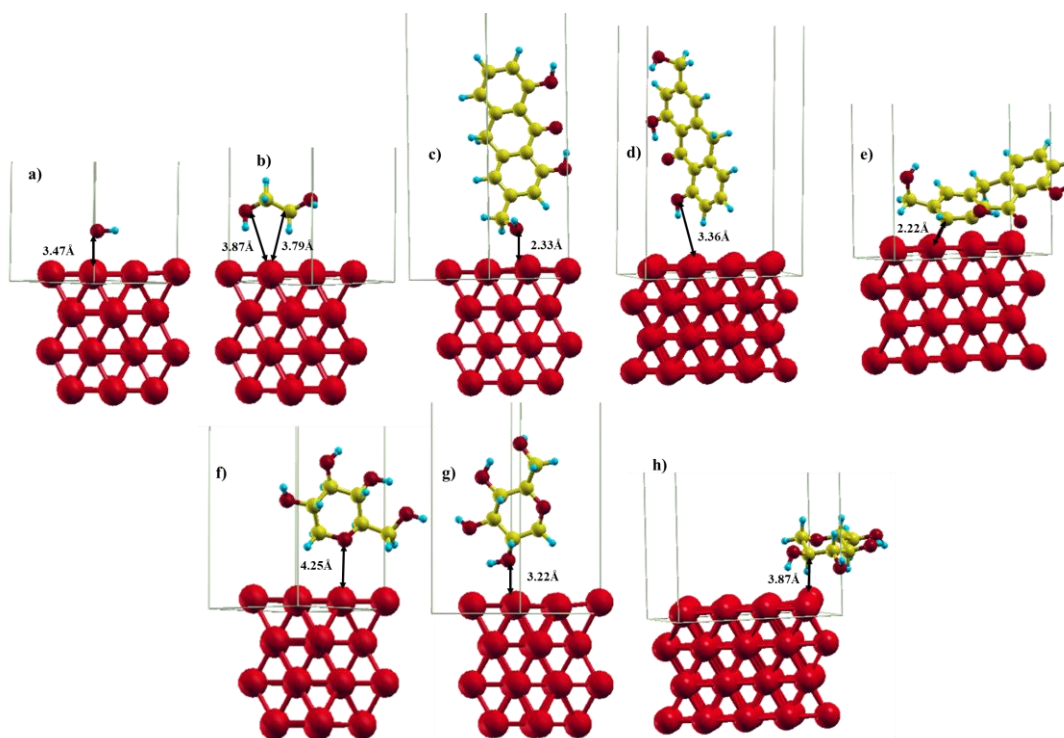


Figure 3. Optimized bonding geometries for some inhibitor molecules on various model surfaces (a): Water bonded to 2x3 Fe(110) with -OH, (b): MEG bonded to 2x3 Fe(110) with -OH/-CH₂, (c): Aromatic aloin fragment bonded to 2x3 Fe (110) with -OH (d): Aromatic aloin fragment bonded to 4x3 Fe(110) with -OH, (e): Aromatic aloin fragment bonded to 4x3 Fe(110) with -CH, (f): Carbohydrate aloin fragment bonded to 2x3 Fe(110) with -OH group of the ring and (g): Carbohydrate aloin fragment bonded to 2x3 Fe(110) with -OH and (h): Carbohydrate aloin fragment bonded to 4x3 Fe(110) with -CH of the ring.

Color code: bright red (large radius) = Fe, dark red (small radius) = O, yellow = C and aqua= H.

Table 3a. Adsorption energy values of Water, MEG and Green inhibitor (Aloin) on Fe(110) surfaces using DFT (in kJ/mol).

Molecule	Anchoring group	$E_{\text{adsorption}}$ on 2x3 Fe (110)	$E_{\text{adsorption}}$ on 4x3 Fe(110)	Optimized geometry shown in Figure
Water	-OH	-31	---	3a
MEG (C ₂ H ₆ O ₂)	-OH/-CH ₂	-50	---	3b
Aromatic aloin fragment	-OH	-92	-35	3c and 3d
	-CH	---	-110	3e
Carbohydrate aloin fragment	-OH (of the ring)	-71	---	3f
	-OH (side group)	-62	---	3g
	-CH (of the ring)	---	-101	3h

Table 3b. Differences in the adsorption energy between green inhibitors and water ($\Delta E_{\text{adsorption}}$) on Fe(110) surfaces using DFT (in kJ/mol).

Differences in adsorption energy between inhibitor and water				
Molecule	# water molecules replaced	Anchoring group	$\Delta E_{\text{adsorption}}$ on 2x3 Fe(110)	$\Delta E_{\text{adsorption}}$ on 4x3 Fe(110)
MEG (C ₂ H ₆ O ₂)	1	-OH/-CH ₂	-19	---
	2		+12	---
Aromatic aloin fragment	1	-OH	-61	-4
	2		-30	+27
	3		+1	+58
	1	-CH (of the ring)	---	-79
	2		---	-48
	3		---	-17
	4		---	+14
Carbohydrate aloin fragment	1	-OH (of the ring)	-40	---
	2		-9	---
	3		+22	---
	1	-OH (side group)	-31	---
	2		0	---
	3		+31	---
	1	-CH (of the ring)	---	-70
	2		---	-39
	3		---	-8
4	---		+23	

3.2. Change in water drop contact angle measurements on L80-1Cr steel samples covered with a layer of inhibitors

The contact angle measurements is an indicator of hydrophobic (water-repelling) and hydrophilic (water-loving) characteristics of the inhibitor [36]. A small contact angle ($\ll 90^\circ$) corresponds to hydrophilic characteristics, whereas a large contact angle ($\gg 90^\circ$) is indicative of the hydrophobic nature of the inhibitor. Figure 4 shows contact angle measurement using water on L80-1Cr bare surface, and after treating with different aloe vera, MEG, and combination of aloe vera and MEG. In Fig.4, all tested solutions show a small contact angle ($\ll 90^\circ$) which means that the solutions used in this study had hydrophilic characteristics. MEG and aloe vera mixture have comparatively the highest contact angle (97° - 86°) than water (31° - 10°), pure MEG (51° - 37°) and pure aloe vera (75° - 72°) suggesting the formation of a water-repellant or hydrophobic layer on the Fe surface in the presence of MEG and aloe vera mixture.

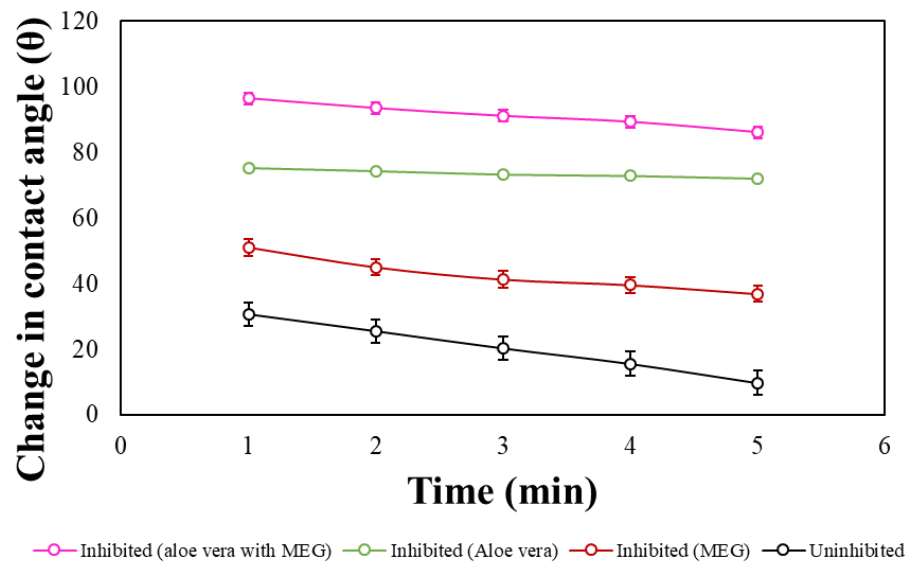


Figure 4. Change in water drop contact angle measurements on L80-1Cr steel in 1% NaCl solution with and without inhibitor.

3.3. Effect of aloe vera extract and organic compound on L80-1Cr at 40°C

3.3.1. OCP and LPR measurements

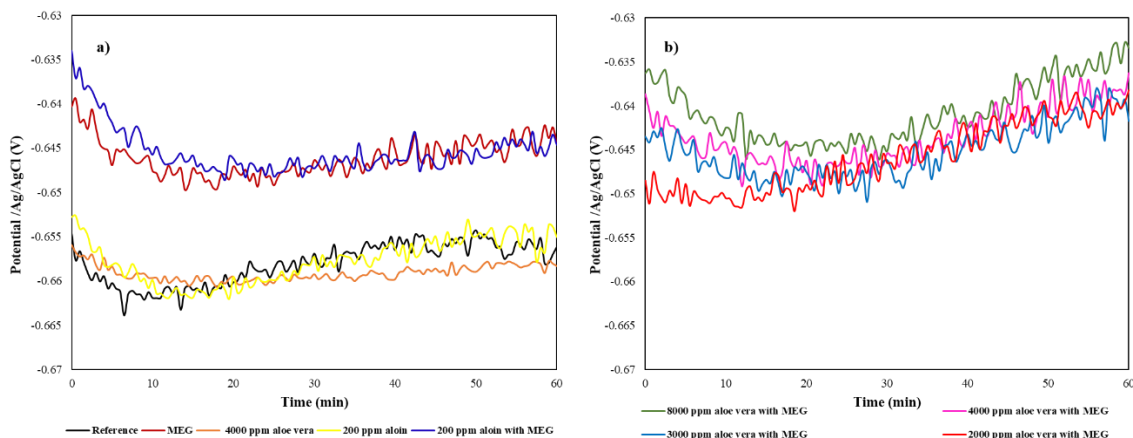


Figure 5. Variation of open circuit potential (OCP) with time for L80-1Cr steel in 1wt % NaCl solution (a): without and with MEG, aloin and aloe vera alone and (b): at different concentration of aloe vera together with MEG.

Fig. 5a shows the OCP values of the L80-1Cr steel sample over the period of 60 min in 1 wt% NaCl solution with and without the presence of the inhibitors at a temperature of 40 °C. The aloin and aloe vera inhibitors were found to have similar potential values to the reference specimen (-0.665V to -0.655 V vs Ag/AgCl). However, MEG alone and in combination with aloin was found to have higher potential values (-0.650 V to -0.635 V vs Ag/AgCl reference), which comparatively indicates a less thermodynamic tendency to corrosion. Similarly, as shown in Fig. 5b MEG in combination with different concentrations of aloe vera yielded higher potential values (-0.650 V to -0.635 V) than either the reference values or pure aloe vera and aloin.

Fig. 6 shows the LPR measurement results (polarization resistance) on L80-1Cr steel in the various solution systems without and with the addition of the various inhibitors. For LPR results, the Tafel slopes are not calculated because for the reference sample there is mass limitation in the cathodic process and taking slope of which is not correct thus all LPR results were presented as polarization resistance v/s time plots. When comparing LPR data in Figs. 6a and 6b, MEG in combination with different concentrations of aloe vera had higher R_p values than the reference specimen (i.e., uninhibited sample), MEG, aloe vera and aloin alone, or a combination of MEG and aloin (Fig. 6a). Aloe vera and aloin alone had marginally higher R_p values than the reference specimen, whereas Fig. 6a shows that MEG alone and in combination with aloin lead to higher values of R_p ($\sim 180 \Omega \cdot \text{cm}^2$) as compared to reference specimen ($90 \Omega \cdot \text{cm}^2$), and aloe vera and aloin alone ($\sim 110 \Omega \cdot \text{cm}^2$). Fig. 6b displays that the evolution of the polarization resistance induced by the inhibitors mainly depends on the concentration of the aloe vera extract. Whereas, when MEG and different concentrations of aloe vera are mixed, the results reveal remarkable higher corrosion resistance, with higher resistance values with increasing concentration of aloe vera (highest resistance polarization value of $900 \Omega \cdot \text{cm}^2$ observed with 8000ppm aloe vera) (see Fig. 6 b). However, notably, an incubation time of 9-10 hours was observed for inhibition to trigger a tangible corrosion decrease when aloe vera concentration of 3000ppm or more was injected into the solution.

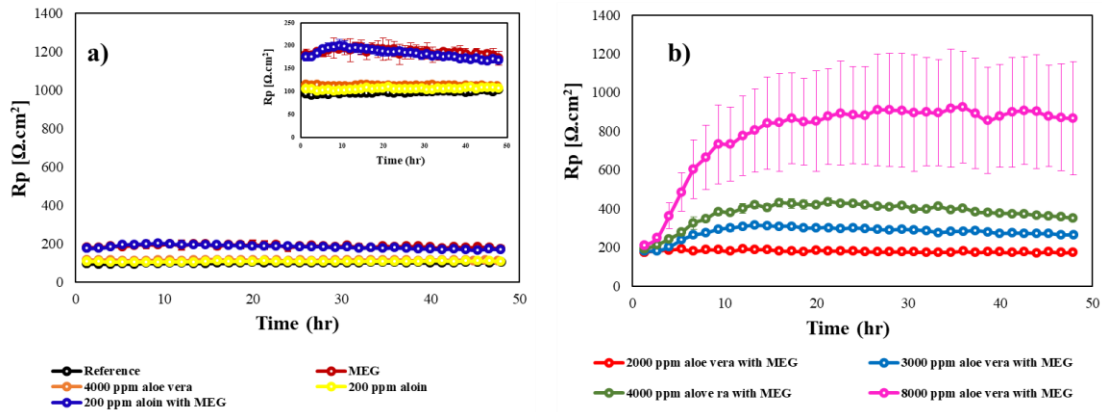


Fig. 6. Polarization resistance for L80-1Cr steel exposed to 1 wt % NaCl solution at 40 °C, for 48 hours (a): without and with the addition of MEG, aloin and alo vera alone (b): at different concentration of alo vera together with MEG.

The maximum value of the polarization resistance was used to calculate the inhibitor efficiency using Eq. (2). From the calculated values listed in Table 4, it was confirmed that pure MEG had a better efficiency than pure alo vera and pure aloin. However, in the combined inhibiting system, mixing 2000 ppm alo vera with 20 vol% of MEG increased the efficiency by 10% and further keeps increasing on increasing the concentration of alo vera. Increasing the alo vera concentration to 8000 ppm provided a remarkable efficiency of 89% which is 40% more than the mixture of 2000 ppm alo vera and MEG.

$$\text{Inhibitor efficiency (\%)} = \frac{(R_{p_{\text{inhibited}}} - R_{p_{\text{Uninhibited}}})}{R_{p_{\text{inhibited}}}} \times 100 \quad (2)$$

Table 4. Inhibitor efficiency values for green inhibitor at 40 °C.

Inhibitor type	Inhibitor efficiency (%) at 40 °C
4000 ppm alo vera	10
200 ppm aloin	6
MEG	47
2000 ppm alo vera with MEG	49
3000 ppm alo vera with MEG	67
4000 ppm alo vera with MEG	76
8000 ppm alo vera with MEG	89

3.3.2. Electrochemical impedance spectroscopy investigation

Figure 7 shows the EIS results obtained during the CO₂ corrosion of L80-1Cr steel at 40 °C in the NaCl solution without and with inhibitors at 15 hours. The Nyquist plots, in Figs. 7a and b, are depressed semi-circles both in the absence and presence of inhibitors. A higher solution resistance is observed for samples treated with either pure MEG or a mixture of MEG with aloin as compared to reference specimen, and pure aloin and aloe vera (Fig. 7a). The addition of aloe vera extract increases the size of the semi-circle and phase angle maxima relative to the reference specimen, which is more significant with the higher inhibitor concentration confirming the increased corrosion resistance with inhibitor concentration (Fig. 7b). Figs. 8 a and b represent the two equivalent electrical circuits that were used to model the impedance behavior of the L80-1Cr steel without and with the inhibitors in the NaCl solution, respectively. The Electrochemical system shown in Fig. 8a is a simple Randle's system, which is well fitted for the reference plot shown in Fig. 7a with a one-time constant representing a homogeneous interface. Fig. 8b represents the second system well fitted with all experimental data shown in Fig. 7 a and b (except reference sample), which has a double-time constant, signifying either two layers or a porous film. The equivalent circuit in Fig. 8a consists of on- time constant whereby a solution resistance (R_s), is connected to a double layer capacitance (C_{dl}), which is in parallel with a charge transfer resistance (R_{ct}). In the presence of aloe vera extract, however, an additional circuit (see Fig. 8b) consisting of a film capacitance (C_{fc}) and film pore resistance (R_{pr}) was added to account for an adsorbed inhibitor layer–solution interface, as applied elsewhere [20]. The R_{ct} is a measure of the polarization resistance of the corroding L80-1Cr steel. The adsorbed species on the steel surface modify the capacitance of charges presented in the electric double layer at the steel/solution interface. Thus, the double-layer capacitance (C_{dl}) provides a better validation of an equivalent circuit model.

Table 5 represents the fitting of impedance data at 15 hours which shows the maximum corrosion resistance value in fig 7a and 7b.

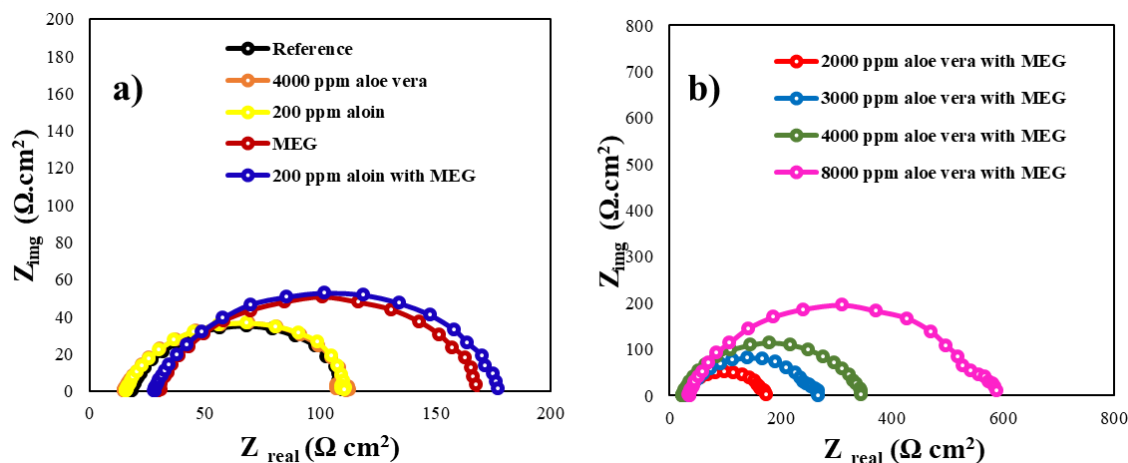


Figure 7. Results of Electrochemical impedance measurements: Nyquist plot for L80-1Cr steel exposed to 1 wt % NaCl solution at 40 °C(a): without and with the addition of MEG, aloin and aloe vera alone (b): at different concentration of aloe vera together with MEG at 15 hours time.

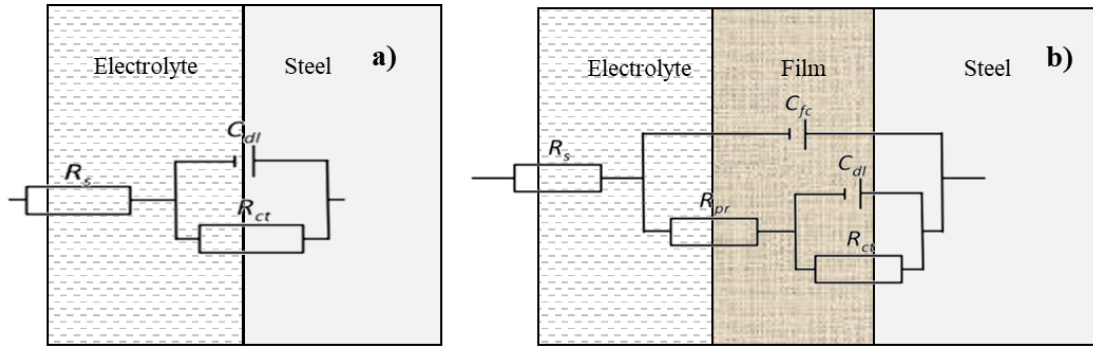


Fig. 8. (a): Simplified Randle's system showing a single layer interface, (b): a double-time constant circuit showing a perforated film interface or perforations filled with corrosion product.

Table 5. Circuit fitting elements: EIS parameters obtained based on the fitted curves on experimental data according to equivalent circuits presented in Fig. 8a and 8b for L80-1Cr steel exposed to 1 wt % NaCl solution at 40 °C, without and with the addition of inhibitors.

Sample	R_s $\Omega.cm^2$	C_{fc} $\mu\Omega^{-1}.cm^{-2}.s^n$	$n1$	R_{pr} $\Omega.cm^2$	C_{dl} $\mu\Omega^{-1}.cm^{-2}.s^n$	$n2$	R_{ct} $\Omega.cm^2$
Reference	14	907	0.79	8	-	-	-
4000 ppm aloe vera	15	512	0.85	17	1921	0.33	106
200 ppm aloin	16	579	0.24	18	913	0.77	89
MEG	29	799	0.75	23	843	0.68	121
200 ppm aloin with MEG	26	783	0.70	22	814	0.74	163
2000 ppm aloe vera with MEG	36	979	0.63	22	782	0.99	160
3000 ppm aloe vera with MEG	33	189	0.89	46	766	0.51	230
4000 ppm aloe vera with MEG	34	188	0.88	49	551	0.56	269
8000 ppm aloe vera with MEG	35	127	0.89	119	240	0.48	528

3.3.3. SECM Study

AC-SECM was explicitly introduced as a tool for localized EIS, having a powerful competency to visually detect the micro-scale conductivity/electrochemical activities at solid/liquid interfaces. Local impedance over the steel surface in the various solutions of 0.01 M NaCl, 0.01 NaCl with 200 ppm aloe vera, and 0.01 NaCl together with 20% MEG resulted from ic-AC-SECM measurements and are presented in Fig. 9. The figure shows a variation in the impedance magnitude of the Pt tip during scanning the steel surface in both uninhibited and inhibited conditions. The difference in the local impedance at various surface points indicates heterogeneous conductivity of the surface, which governs the resistance against the electron transfer from/to the counter electrode using the bulk of the sample. The impedance variation in the uninhibited solution in Fig. 9a could attribute to the probable formation of corrosion products on the surface with a conductivity different from the bare steel surface during SECM scanning. Comparing lower and upper limits of impedance in the SECM maps in Fig. 9 reveals that by the injection of aloe vera and MEG inhibitors to the NaCl solution, the averaged impedance value of the steel surface was increased by about 15% and 38%, respectively. It should be pointed out that

due to applying a high frequency of the alternating potential during the AC-SECM measurements, the impedance values mainly represent the solution resistance of the solution, in which the change in the conductivity of the surface by adsorbing the ionic species can partly play a role as well. The SECM results in Fig. 9c can confirm that the solution resistance remarkably increased as the MEG was injected into the solution, which is well consistent with the research studies.

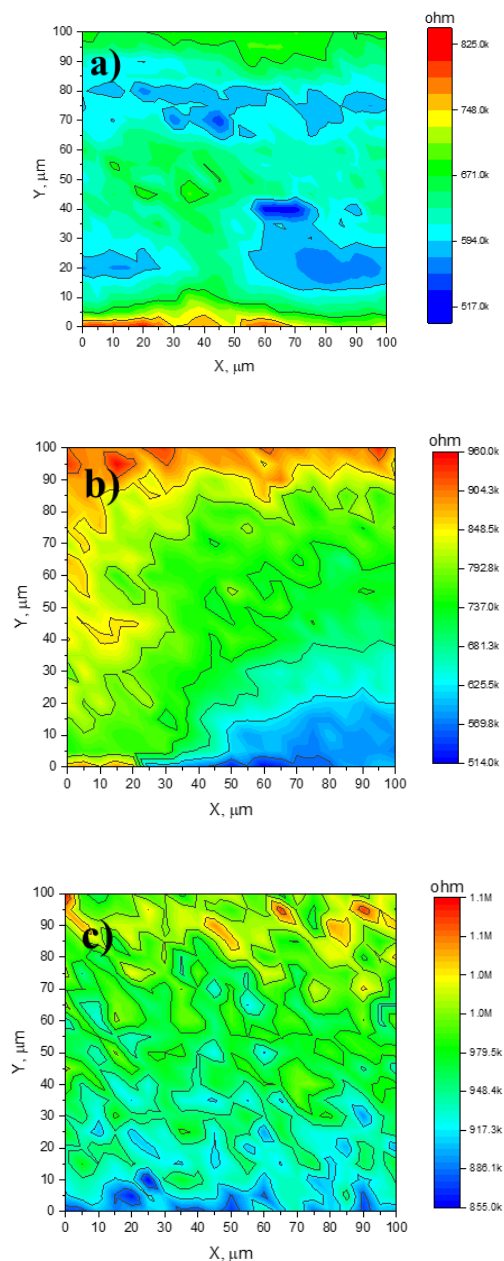


Figure 9. 2D SECM plots showing the variations of the impedance magnitude R (Ω) as a function of x- and y-positions in (a): 0.01 M NaCl solution, (b): 0.01 M NaCl with 200 ppm aloe vera and (c): 0.01 M NaCl containing 20% MEG solution. The alternating potential over the open-circuit potential was 50 mV at a frequency of 100 kHz.

3.3.4. Surface characterization

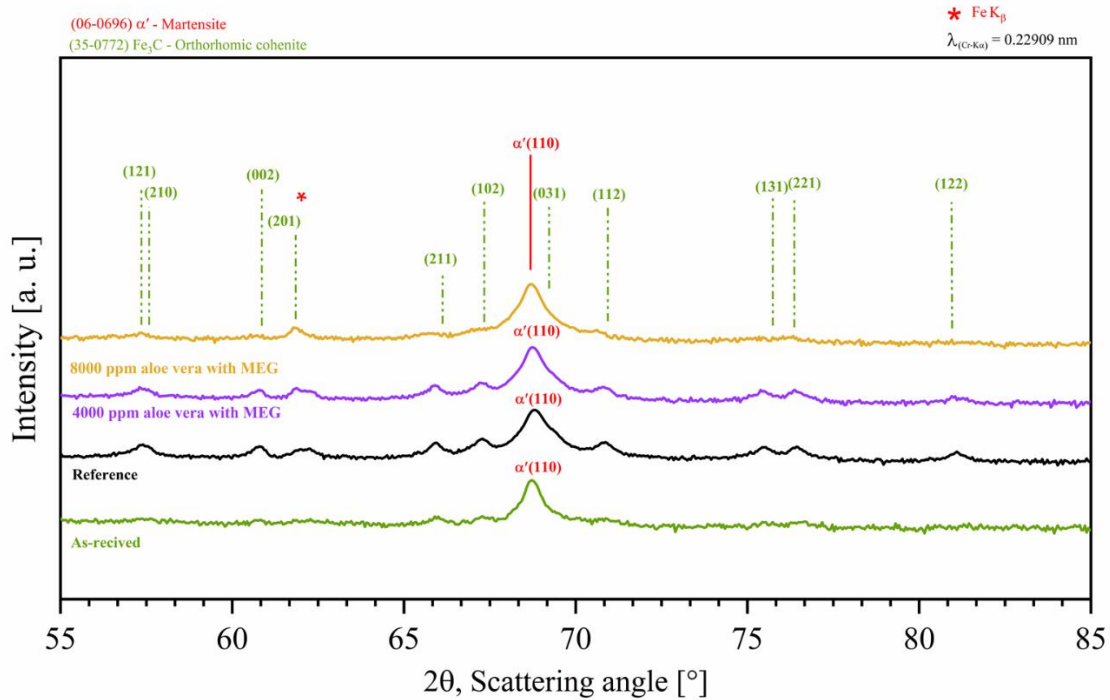


Fig. 10. Results of X-ray diffraction of L80-1Cr steel corroded at 40 °C in 1 wt% NaCl with and without green inhibitors.

Fig. 10 shows the XRD patterns of the scale formed on the specimens during the electrochemical experiments in the NaCl solution at 40 °C. Cementite (Fe_3C) was detected in all the samples scales; however, with an increase in the concentration of aloe vera (especially at 8000 ppm aloe vera), the intensity of Fe_3C diffracted peaks were decreased. For example, the peaks as seen in reflections (121), (210), (002), (211), (102), (112), (131), (221) and (122) were almost absent in aloe vera solution with 8000 ppm with MEG.

Figs. 11 a, c, e and g represent cross-sectional SEM images of reference, MEG, the mixture of MEG and 4000ppm aloe vera, and mixture of MEG and 8000ppm aloe vera, respectively, after 48 hours of immersion in the NaCl solution at 40°C. The SEM images show a corrosion product layer with varying thicknesses (8 μm to 20 μm) except for a mixture of MEG with 4000 and 8000 ppm aloe vera. The corrosion product scale formed on the reference specimen seems to be denser (less porous) compared with MEG. Figs. 11 b, d, f and h represent the top surface morphology of the corrosion products formed on the reference, MEG, the mixture of MEG and 4000ppm aloe vera, and the mixture of MEG and 8000ppm aloe vera, respectively. The L80-1Cr steel samples exposed in 1% NaCl solution in the absence of inhibitors (Fig. 11 a) show the formation and cracking of heavy deposits of corrosion products. The SEM images indicate that the reference specimen (Fig. 11b) and MEG (Fig. 11d) corroded homogeneously; however, the cracks in the reference specimen are coarser than the MEG. In case of aloe vera in combination with MEG, there is some shallow localized corrosion (Fig. 11f, 11h). In Fig. 11h that are non-uniformly distributed over the sample surface.

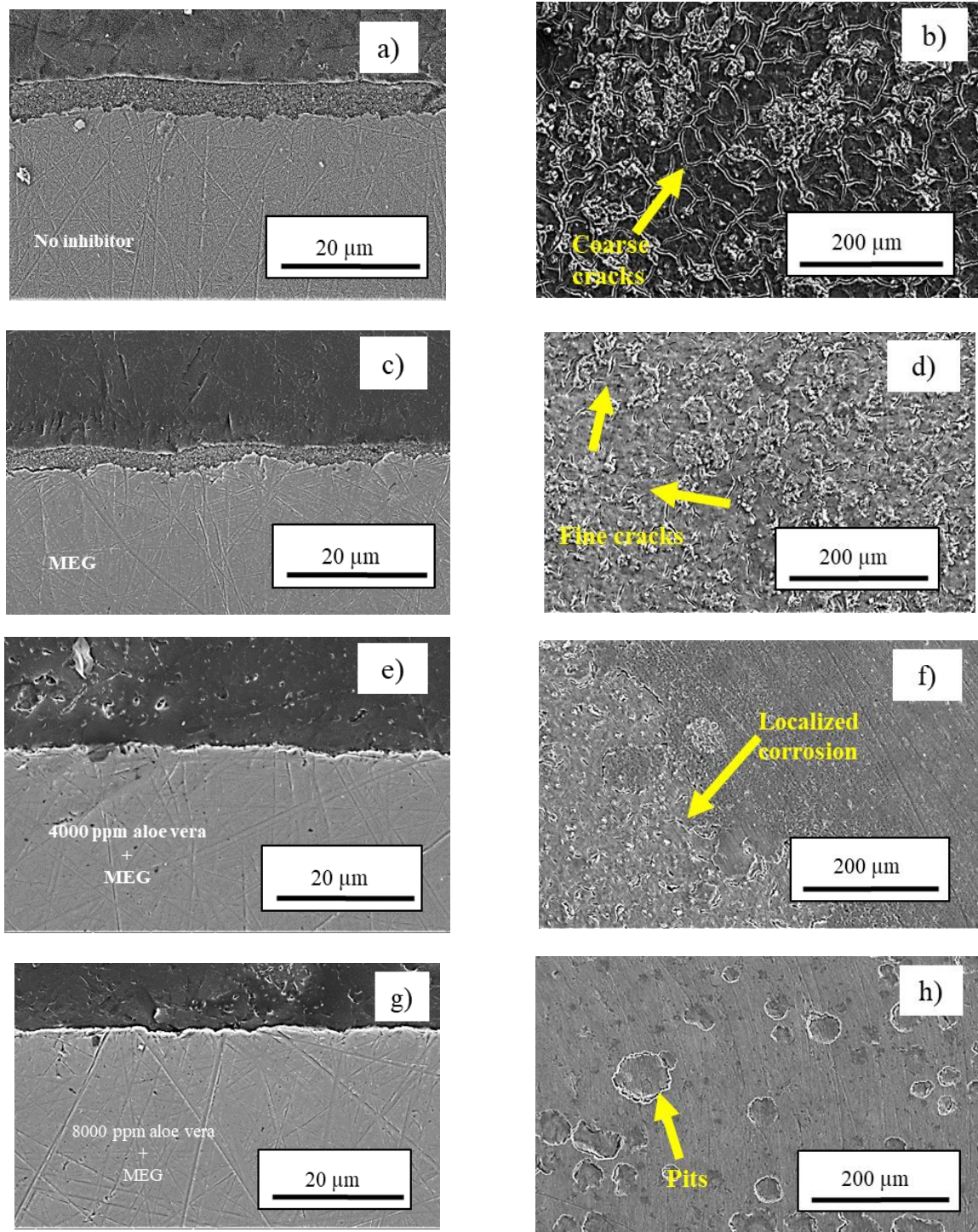


Figure 11. SEM images for L80-1Cr steel exposed to 1 wt% NaCl solution, (a and b): cross-sectional and top view of the specimen without inhibitor, (c and d): cross-sectional and top view of the specimen with MEG, (e and f): cross-sectional and top view of the specimen with MEG mixture of MEG and 4000 ppm aloe vera and (g and h): cross-sectional and top view of the specimen with MEG mixture of MEG and 8000 ppm aloe vera at 40 °C.

Fig. 12 shows the FTIR spectrums for aloin and aloe vera gel extract. A strong broad absorption band around 3399.3 cm^{-1} in aloe vera spectrum denotes the presence of hydrogen-bonded N–H stretching, characteristic of amino acids [37]. The absorption band at 2811.8 and 2118.0 cm^{-1} in aloe vera and 2917.3 cm^{-1} in aloin is due to the symmetrical and asymmetrical C–H stretching of the CH_2 groups. This band is also characteristic of the presence of aliphatic (–CH) groups in these compounds. The absorption band at 1640.2 cm^{-1} in aloe vera is characteristic of C=O stretching and indicates the presence of flavonoids groups, and another medium band at 1412.8 cm^{-1} in aloe vera and 1488.9 – 1429.4 cm^{-1} may be characteristic of C=C (aromatic ring) [38]. The absorption band at 1259.9 cm^{-1} is likely because of the stretching vibrations of C–O groups of esters and phenols have also reported similar results. The absorption band in the region 1080.5 cm^{-1} in aloe vera corresponds to the stretching vibrations of C=S. The strong absorption band at 709 cm^{-1} in aloe vera indicates the C–H out of plane deformation. However, in aloin only two major peaks were observed that are at 3341.1 cm^{-1} due to the presence of –OH group [39] and the strong absorption band at 1604.1 cm^{-1} in aloin is due to C=C stretching which indicates the presence of aloin compound [37,40,41].

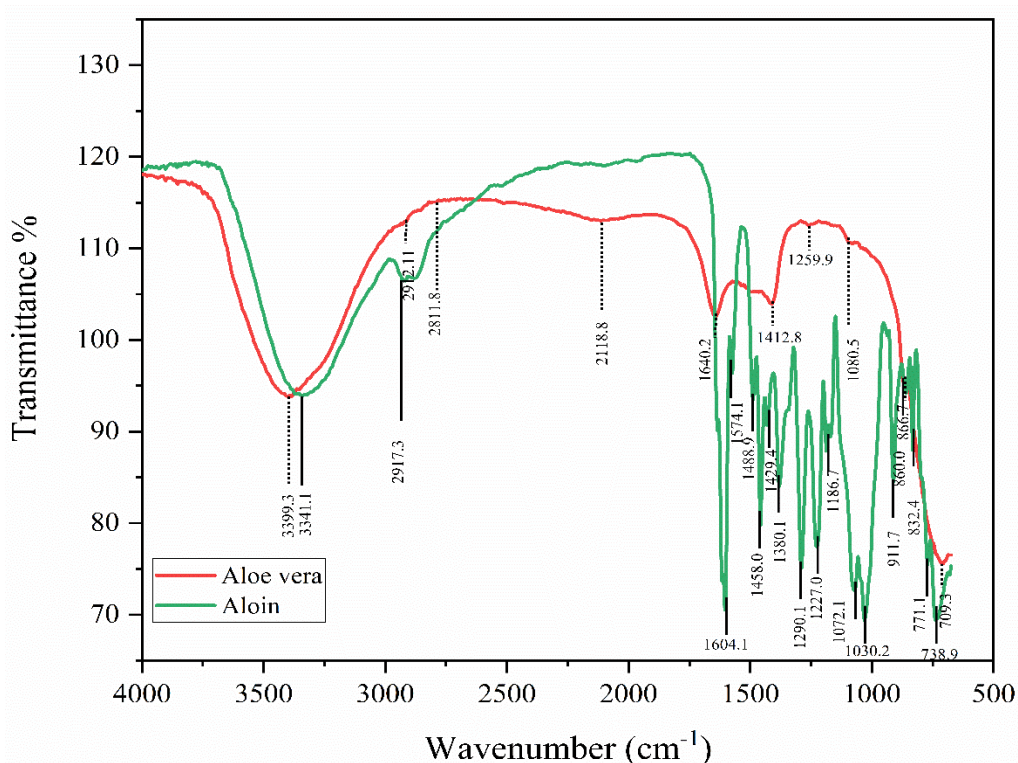


Figure 12. FTIR spectra of aloin and aloe vera.

3.3.5. Inhibitory properties upon subsequent injections

Fig. 13 shows the effect of subsequent injection of aloe vera alone and mixed with MEG. L80-1Cr specimen was typically tested in NaCl solution with MEG and 4000 ppm aloe vera. The polarization resistance value initially increased to $458\ \Omega\cdot\text{cm}^2$ in 17 hours and subsequently reduced

back to its starting value of $216 \Omega \cdot \text{cm}^2$ in 4 days. Injection of the second dose of 4000 ppm aloe vera on day 4 did not affect the decreasing trend of polarization resistance. The polarization resistance dropped to $150 \Omega \cdot \text{cm}^2$ within the next 3 days. When the same specimen was immersed into a new solution containing fresh NaCl with the mixture of MEG and 4000 ppm aloe vera on day 7, the polarization resistance increased and stabilized for the next 7 days in the range of $\sim 160 \Omega \cdot \text{cm}^2$ to $174 \Omega \cdot \text{cm}^2$.

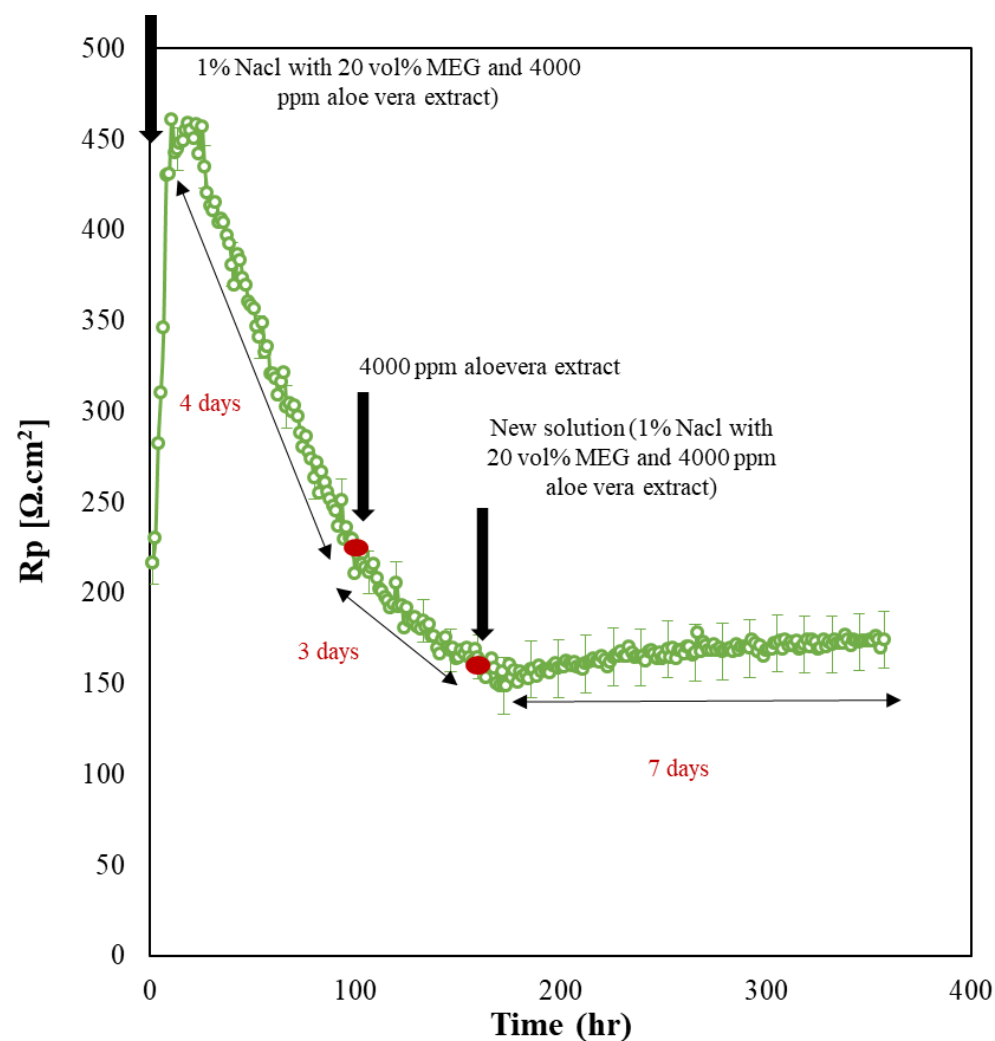


Figure 13. Effect of subsequent injection of aloe vera and mixture of aloe vera and MEG mixture for L80-1Cr steel exposed to 1 wt % NaCl solution at 40°C .

4. Discussion

In this paper, different electrochemical techniques were used to study the corrosion inhibition behavior of aloe vera extract as corrosion inhibitor alone or in combination with MEG. The corrosion inhibition effects of different concentrations of aloe vera were also investigated. In addition, molecular modelling was carried out to understand the adsorption behavior of the

inhibitors and their different functional groups on the Fe(110) surface in a CO₂ corrosive environment. Aloe vera extract containing solution was found to be effective in inhibiting the corrosion and its efficiency improved significantly with an increase in its concentration. Furthermore, aloe vera has a promising synergistic effect when combined with MEG leading to a higher efficiency of corrosion inhibition. In general term, the observed corrosion inhibition properties are mainly due to the interaction of the inhibitors with the steel surface, and in some cases due to changes in the properties of the solution.

The L80-1Cr steel displayed more positive OCP values (see Fig. 5a) in the presence of aloe vera indicating that the inhibitor lowers the propensity of the L80-1Cr steel for dissolution in the NaCl solution due to the inhibitor film formation [20]. The positive shift in OCP values (-0.635 V) upon addition of 8000 ppm of aloe vera in combination with MEG in Fig. 5 b highlights absorption of inhibitor molecules on the L80-1Cr steel surface [17], which was further supported by the results from other experiments. There was an increase in Rp values in the presence of aloin, aloe vera, and MEG in pure and combined forms (Fig. 6). These results confirm reduction in corrosion in the presence of these inhibitors. Aloe vera consists of organic compounds that have π centered electrons and functional groups of O, S or N/ or combination, which can contribute to its corrosion inhibitive properties [12,14,17]. The structure of aloin (the main constituent of aloe vera) has an anthraquinone link to a pentose with 5 oxygen atoms (shown in Fig. 1b) that can form a strong bond with the steel surface [11]. Previous studies have found that aloe vera gets adsorbed both chemically and physically on the metal surface (e.g. zinc, aluminium, mild steel, stainless steel, etc.) [9–11,17]. It should be noted that aloin is just one of the constituents of aloe vera among other molecules, therefore more amount in solution for inhibition compared to the pure form of aloin. The aloe vera spectrum in Fig. 12 confirms the presence of other constituents such as: amino acids (at 3399.3 cm⁻¹), phenols (at 1259.9 cm⁻¹) etc.; in addition to aloin. The molecular adsorption of aloe vera limits the steel surface area exposure to the solution largely by blocking active (anodic) sites and forming a layer of the inhibitor[17]. This limits the exposure of the solution to the anodic sites and protects the steel surface from being severely attacked by the aggressive ions (such as Cl⁻, CO₃²⁻, etc.) from the acid solution[11].

The corrosion inhibition effects were increased significantly upon the addition of MEG to aloe vera. The Rp values observed (Fig. 6) for combined aloe vera and MEG were higher than those observed for pure forms, which is well-consistent with the SECM results in Fig. 9, where MEG resulted in a highest impedance magnitude range. These findings reveal the synergistic corrosion inhibition effects of the two inhibitors when used in combination. The synergistic effects of combined aloe vera and MEG could come from impacts in adsorption properties because of changes in solvation energies [35], but could also come from additional mechanisms than just surface adsorption mechanisms, such as the changes in the properties of the solution [21]. For example, upon the addition of MEG, there is decreased CO₂ solubility, decreased CO₂ diffusivity / increased solution viscosity, decreased water activity and decreased solution polarity [21]. These changes in solution likely contribute to increases the resistance of the solution as shown by impedance results in Table 5 and SECM images in Fig. 9. Upon addition of MEG, the solution resistance was higher (29 $\Omega \cdot \text{cm}^2$) than the reference sample value without any inhibitor (14 $\Omega \cdot \text{cm}^2$). The solution resistance further increased to 36 $\Omega \cdot \text{cm}^2$ when MEG was mixed with 2000 ppm aloe vera. The solution resistance did not increase further with higher concentrations of aloe vera suggesting the solution resistance was mainly influenced due to the presence of MEG (as

confirmed by SECM results in Fig. 9) and any effects seen due to aloe vera were saturated at lower concentrations of aloe vera (2000 ppm) (Table 5).

Despite no further increase in solution resistance with a higher concentration of aloe vera, there was an increased corrosion inhibition with increasing concentration of aloe vera. The aloe vera concentration used in this study ranged between 2000 to 8000 ppm, with higher ppm resulting in higher R_p values (see Fig. 6b). Similar findings were seen in the inhibition efficiencies in Table 4. Higher concentration leads to a compact and coherent film on the L80-1Cr steel providing more protection from corrosion [14]. In addition, better inhibition efficiency at higher concentration (2000 ppm: 49% ; 3000 ppm: 67% ; 4000ppm: 76%; 8000 ppm:89%) may also attribute to a larger coverage of sample with inhibitor molecules [14]. Furthermore, in presence of MEG, as the concentration of aloe vera increased, the corresponding values of R_{pr} (2000 ppm = $22 \Omega \cdot \text{cm}^2$; 8000 ppm = $119 \Omega \cdot \text{cm}^2$) and R_{ct} (2000 ppm = $160 \Omega \cdot \text{cm}^2$; 8000 ppm = $528 \Omega \cdot \text{cm}^2$) also increased (Table 5). The R_{pr} increase corresponds to the formation of a denser film (fewer cracks) on the sample surface or localized corrosion (Figs. 11f and h) leading to a slower rate of charge transfer as indicated by an increase in R_{ct} values in Table 5. A higher concentration of aloe vera also led to an increase in thickness of inhibitor film, which is indicated by a decrease in C_{fc} value (2000 ppm: $979 \mu\Omega^{-1} \cdot \text{cm}^{-2} \cdot \text{s}^n$; 8000: ppm $127 \mu\Omega^{-1} \cdot \text{cm}^{-2} \cdot \text{s}^n$) in Table 5. The increased thickness of the inhibitor film is related to the double layer capacitance, C_{dl} on the basis of the Helmholtz model [$C_{dl} = A(\epsilon\epsilon_0/\delta)$] [42], Where A is the surface area, ϵ_0 is the permittivity of the vacuum, and δ is the surface layer thickness. which assumes the double layer can be taken as a parallel plate capacitor. The C_{dl} value also decreased (2000 ppm: $782 \mu\Omega^{-1} \cdot \text{cm}^{-2} \cdot \text{s}^n$ 3000 ppm: $551 \mu\Omega^{-1} \cdot \text{cm}^{-2} \cdot \text{s}^n$; 8000 ppm: $240 \mu\Omega^{-1} \cdot \text{cm}^{-2} \cdot \text{s}^n$) with an increase in aloe vera concentration supporting the increase in the thickness of the capacitive surface layer, which is also an indication of a gradual replacement of the surface water molecules with inhibitor adsorption. Overall, the impedance results suggest an increase in aloe vera concentration led to a more protective film formation on the L80-1Cr steel surface.

The XRD (Fig. 10) and SEM (Fig. 11) analysis also supported the experimental findings. An increase in aloe vera concentration led to less coarse, localized and non-uniform distribution of corrosion (Fig. 11 f and h). In addition, XRD analysis revealed less dissolution (anodic) of Fe^{2+} with increased concentration of aloe vera, which is indicated by the reduction in peak Fe_3C intensity. Previous studies have reported at very high concentrations of inhibitors, the protective layer itself can get desorbed leading to no further increase in the corrosion inhibition [42]. In the current study the highest aloe vera concentration that was used was 8000 ppm and the corrosion inhibition effects did not saturate at the highest aloe vera concentration.

The adsorption energy findings help explain the mechanisms underlying the corrosion inhibition behavior of the inhibitors observed in this study. Higher adsorption energy values were obtained for aloin (-110 kJ/mol) and MEG (-50 kJ/mol) as compared to water (-31 kJ/mol) suggesting that these inhibitor molecules are able to replace water on the Fe(110) surface limiting the corrosion. Table 3b shows the differences in the adsorption energy between the inhibitor and water molecules on Fe(110) surface. Based on the adsorption energy of the different functional groups that bind to the Fe(110) surface, the inhibitor molecules can replace different numbers of water molecules (Table 3b) that may contribute to their corrosion inhibition effects on the sample surface. The adsorption energy values of the different parts of the aloin also appear to depend on the binding geometry of the inhibitor molecules, which may have influenced their corrosion inhibition

properties. For example, a vertical binding geometry between -OH group of aromatic aloin fragment on 4x3 Fe(110) led to a low adsorption energy value of -35 kJ/mol, whereas a horizontal binding geometry between -CH group of carbohydrate aloin fragment led to the higher adsorption energy value of -110 kJ/mol. In addition, the corresponding distances between the above two groups from the Fe molecules were 3.36 Å and 2.22 Å. The observed relationship between the binding geometry and the adsorption energies supports the idea that adsorption energy values can be used to understand the molecular mechanisms of the corrosion inhibition of organic inhibitors, at least when the expected mechanism of inhibition is based on the formation of a protective film, hindering water molecule access to the surface. However, there can be a possibility where the aloin molecules cover most of the iron surface, but are not able to form a perfect protective film and that water can still get to the surface in between the adsorbed aloin. When combined with MEG, the MEG is only slightly smaller than water, and because it binds stronger, it can replace the water, acting as a “filler” between the adsorbed aloin, making the combined protective film stronger than aloin without MEG. This view is supported by our experimental observation that the contact angle is higher for a combination of aloin and MEG compared to aloin or MEG on their own, (see Fig. 4).

Contact angle measurements of different inhibitors were along the same lines as their adsorption energy behavior (Fig. 4). A higher contact angle measures were observed for aloe vera (75°-72°) as compared to MEG (51°-37) and water (30°- 10°) over a 5-minute period. The higher contact angle is indicative of hydrophobic (water repellent) property and suggests a higher affinity for water replacement for aloe vera as compared to MEG and water. The contact angle of a mixture of aloe vera and MEG was the highest (97°-86°) supporting the highest corrosion inhibition behavior of the combination of these molecules.

5. Conclusions

- A green corrosion inhibitor in form of aloe vera (4000 ppm) led to 45% increase in corrosion resistance as compared to the reference sample, suggesting an efficiency of 9.6%.
- In combination with MEG, the efficiency of aloe vera increased substantially, to ~8 times the result without MEG. The incubation time for a combination of aloe vera and MEG is 10-12 hours and is apparent only at aloe vera concentration of 3000ppm and above.
- There was a direct relationship between the concentration of aloe vera and the corrosion inhibition. The greatest inhibition was observed with the highest concentration of aloe vera (i.e. 8000 ppm) used in this study.
- The rise in efficiency with an increase in concentration did not plateau at 8000 ppm suggesting we may not have reached the highest levels of efficiency. Future studies may look at the efficiencies at higher concentrations of aloe vera.
- The addition of aloe vera extract, especially at higher concentrations, increases the impedance values (capacitive loop diameter), confirming higher corrosion inhibition due to increased thickness of inhibitor film.
- The average impedance values measured by the AC-SECM method at high frequency revealed an increase in the resistance of the aloe vera- and MEG-containing solutions by about 15% and

38%, respectively. This resulted from the lower conductivity of the surface by adsorbing the ionic species.

- The DFT modelling, on the basis of adsorption energy calculations and estimation of water replacement, help explain the mechanisms underlying the corrosion inhibition behavior of different inhibitors as observed in the experimental findings. The highest adsorption energy was observed for aloin, the main constituent of aloe vera that contributes to corrosion inhibition.

ACKNOWLEDGEMENTS

The authors would like to thank the Danish Hydrocarbon Research and Technology Center (DHRTC) for providing financial funding and technical supports to this work.

References

- [1] S. Şafak, B. Duran, A. Yurt, G. Türkoğlu, Schiff bases as corrosion inhibitor for aluminium in HCl solution, *Corros. Sci.* 54 (2012) 251–259.
- [2] P.B. Raja, M.G. Sethuraman, Studies on the inhibition of mild steel corrosion by *Rauvolfia serpentina* in acid media, *J. Mater. Eng. Perform.* 19 (2010) 761–766.
- [3] P.B. Raja, M.G. Sethuraman, Natural products as corrosion inhibitor for metals in corrosive media—a review, *Mater. Lett.* 62 (2008) 113–116.
- [4] E. Stupnišek-Lisac, S. Podbršček, T. Sorić, Non-toxic organic zinc corrosion inhibitors in hydrochloric acid, *J. Appl. Electrochem.* 24 (1994) 779–784.
- [5] Y.T. Al-Janabi, An overview of corrosion in oil and gas industry: upstream, midstream, and downstream sectors, *Corros. Inhib. Oil Gas Ind.* (2020) 1–39.
- [6] R.M. Palou, O. Olivares-Xomelt, N. V. Likhanova, Environmentally friendly corrosion inhibitors, *Dev. Corros. Prot.* 19 (2014) 431–432.
- [7] O.A. Omotosho, Inhibition evaluation of chemical and plant extracts on the corrosion of metallic alloys in acidic environment, (2016).
- [8] H. Kuzuya, I. Tamai, H. Beppu, K. Shimpo, T. Chihara, Determination of aloenin, barbaloin and isobarbaloin in Aloe species by micellar electrokinetic chromatography, *J. Chromatogr. B Biomed. Sci. Appl.* 752 (2001) 91–97.
- [9] N.O. Eddy, S.A. Odoemelam, Inhibition of corrosion of mild steel in acidic medium using ethanol extract of Aloe vera, *Pigment Resin Technol.* (2009).
- [10] A.O. James, A.O. Atela, Aloe vera: an inhibitor of aluminium corrosion in hydrochloric acid solution, *Int. J. Pure Appl. Chem.* 3 (2008) 159–163.
- [11] O.K. Abiola, A.O. James, The effects of Aloe vera extract on corrosion and kinetics of corrosion process of zinc in HCl solution, *Corros. Sci.* 52 (2010) 661–664.
- [12] A.A. Ayoola, O.S.I. Fayomi, I.G. Akande, O.A. Ayeni, O. Agboola, O.R. Obanla, O.G. Abatan, C.J. Chukwuka, Inhibitive corrosion performance of the eco-friendly aloe vera in acidic media of mild and stainless steels, *J Bio Tribo Corros.* 6 (2020) 1–13.
- [13] O.M. Ajayi, N.M. Everitt, K.T. Voisey, Evaluation of inulin and aloe vera as green corrosion inhibitors for mild steel in 15% HCl, (2016).
- [14] A.K. Singh, S. Mohapatra, B. Pani, Corrosion inhibition effect of Aloe Vera gel: gravimetric and electrochemical study, *J. Ind. Eng. Chem.* 33 (2016) 288–297.
- [15] S. Dahiya, S. Lata, P. Kumar, R. Kumar, A descriptive study for corrosion control of low-alloy steel by Aloe vera extract in acidic medium, *Corros. Rev.* 34 (2016) 241–248.
- [16] R.T. Vashi, H.G. Chaudhari, The study of aloe-vera gel extract as green corrosion inhibitor for mild steel in acetic acid, *Int J Innov Res Sci Eng Tech.* 6 (2017) 22081–22091.
- [17] M. Mehdipour, B. Ramezanzadeh, S.Y. Arman, Electrochemical noise investigation of Aloe plant extract as green inhibitor on the corrosion of stainless steel in 1 M H₂SO₄, *J. Ind. Eng. Chem.* 21 (2015) 318–327.
- [18] P. Shah, S. Agarwal, Aloe-Vera: A Green Corrosion Inhibitor, *Int. J. Res. Appl. Sci. Eng. Technol.* 2 (2014) 12–16.
- [19] T. Derbe, B. Yilma, Investigation of the anti-corrosion activities of aloe vera extract on iron metal sheets, *J. Nat. Sci. Res.* 5 (2015) 18–24.
- [20] B. Benzidia, H. Hammouch, A. Dermaj, H. Benassaoui, S. Abbout, N. Hajjaji, Investigation of green corrosion inhibitor based on aloe vera (*L. burm. F.*) for the protection of bronze B66 in 3% NaCl, *Anal. Bioanal. Electrochem.* 11 (2019) 165–177.

- [21] E. Gulbrandsen, J.H. Morard, Why does glycol inhibit CO₂ corrosion?, in: *Corros.* 98, OnePetro, 1998.
- [22] P. Giannozzi, S. Baroni, N. Bonini, M. Calandra, R. Car, C. Cavazzoni, D. Ceresoli, G.L. Chiarotti, M. Cococcioni, I. Dabo, A. Dal Corso, S. de Gironcoli, S. Fabris, G. Fratesi, R. Gebauer, U. Gerstmann, C. Gougoussis, A. Kokalj, M. Lazzeri, L. Martin-Samos, N. Marzari, F. Mauri, R. Mazzarello, S. Paolini, A. Pasquarello, L. Paulatto, C. Sbraccia, S. Scandolo, G. Sclauzero, A.P. Seitsonen, A. Smogunov, P. Umari, R.M. Wentzcovitch, QUANTUM ESPRESSO: a modular and open-source software project for quantum simulations of materials., *J. Phys. Condens. Matter.* (2009) 1–36.
- [23] Y. Zhang, W. Yang, Comment on “generalized gradient approximation made simple,” *Phys. Rev. Lett.* 80 (1998) 890. <https://doi.org/10.1103/PhysRevLett.80.890>.
- [24] M.P. Andersson, Density Functional Theory with Modified Dispersion Correction for Metals Applied to Self-Assembled Monolayers of Thiols on Au(111), *J. Theor. Chem.* 2013 (2013) 1–9. <https://doi.org/10.1155/2013/327839>.
- [25] S. Grimme, Semiempirical GGA-type density functional constructed with a long-range dispersion correction, *J. Comput. Chem.* 27 (2006) 1787–1799.
- [26] V. Barone, M. Casarin, D. Forrer, M. Pavone, M. Sambri, A. Vittadini, Role and effective treatment of dispersive forces in materials: Polyethylene and graphite crystals as test cases, *J. Comput. Chem.* 30 (2009) 934–939.
- [27] M.P. Andersson, Density functional theory with modified dispersion correction for metals applied to self-assembled monolayers of thiols on Au(111), *J. Theor. Chem.* 2013 (2013) 1–9.
- [28] M.P. Andersson, Density functional theory with modified dispersion correction for metals applied to molecular adsorption on Pt (111), *Phys. Chem. Chem. Phys.* 18 (2016) 19118–19122.
- [29] A. Dal Corso, Pseudopotentials periodic table: From H to Pu, *Comput. Mater. Sci.* 95 (2014) 337–350.
- [30] A. Dal Corso, PSLibrary: A library of ultrasoft and PAW pseudopotentials, (2020).
- [31] E. Ataman, M.P. Andersson, M. Ceccato, N. Bovet, S.L.S. Stipp, Functional Group Adsorption on Calcite: I. Oxygen Containing and Nonpolar Organic Molecules, *J. Phys. Chem. C.* 120 (2016) 16586–16596.
- [32] E. Ataman, M.P. Andersson, M. Ceccato, N. Bovet, S.L.S. Stipp, Functional group adsorption on calcite: II. Nitrogen and sulfur containing organic molecules, *J. Phys. Chem. C.* 120 (2016) 16597–16607.
- [33] C.T. Campbell, J.R. V Sellers, The entropies of adsorbed molecules, *J. Am. Chem. Soc.* 134 (2012) 18109–18115.
- [34] A. Budi, S.L.S. Stipp, M.P. Andersson, Calculation of entropy of adsorption for small molecules on mineral surfaces, *J. Phys. Chem. C.* 122 (2018) 8236–8243.
- [35] A. Budi, S.L.S. Stipp, M.P. Andersson, The effect of solvation and temperature on the adsorption of small organic molecules on calcite, *Phys. Chem. Chem. Phys.* 20 (2018) 7140–7147.
- [36] Y. Lin, A. Singh, E.E. Ebenso, M.A. Quraishi, Y. Zhou, Y. Huang, Use of HPHT autoclave to determine corrosion inhibition by berberine extract on carbon steels in 3.5% NaCl solution saturated with CO₂, *Int. J. Electrochem. Sci.* 10 (2015) 194–208.
- [37] R. Kumar, M. Gayathiri, S. Ravi, Spectroscopy studies on the status of aloin in Aloe vera and commercial samples, *J. Exp. Sci.* 2 (2011) 10–13.

- [38] P. Chauhan, A. Kumar, Development of a microbial coating for cellulosic surface using aloe vera and silane, *Carbohydr. Polym. Technol. Appl.* 1 (2020) 100015.
- [39] A.Y. Esmat, M.M. Said, S.A. Khalil, Aloin: A natural antitumor anthraquinone glycoside with iron chelating and non-atherogenic activities, *Pharm. Biol.* 53 (2015) 138–146.
- [40] M. Mahuli, R. Anandamoy, Development and formulation of Aloe vera emulgel, *GSC Biol. Pharm. Sci.* 12 (2020) 161–166.
- [41] Z. Badar, S. Khan, S. Ahmed, M.I. Choudhary, Enhanced Production of Aloe Mannan Using Plant Biotechnology, *Int. J. Biotech. Bioeng.* 3 (2017) 298–316.
- [42] A. Munis, T. Zhao, M. Zheng, A.U. Rehman, F. Wang, A newly synthesized green corrosion inhibitor imidazoline derivative for carbon steel in 7.5% NH₄Cl solution, *Sustain. Chem. Pharm.* 16 (2020) 100258.



Corrosion inhibition properties of eco-friendly green inhibitors containing aloe vera plant extract on 1 Cr steel under H₂S conditions with CO₂

Shivangi Gupta^{a*}, Rouhollah Yazdi^a, Martin Andersson^b, Rajan Ambat^a

^a Section of Materials and Surface Engineering, Department of Mechanical Engineering, Technical University of Denmark, Produktionstorvet, Kongens Lyngby, 2800 Denmark

^b Department of Chemical Engineering, Technical University of Denmark, Produktionstorvet, Kongens Lyngby, 2800 Denmark

*Corresponding author. Tel: +45 60773762, E-mail address: shig@mek.dtu.dk (S. Gupta).

Abstract

Aloe vera extract as corrosion inhibitors found to be environment-friendly corrosion inhibitor for oil and gas industry. The objective of this investigation was to characterize the corrosion inhibition properties of aloe vera extract on steel surface at different concentrations of H₂S under CO₂ saturated conditions. Investigations were carried out with and without mono ethylene glycol (MEG). The electrochemical and surface characterization techniques were used to study the corrosion inhibition properties. The Rp values for the reference sample increased with the concentration of H₂S, while with aloe vera extract under 400 ppm H₂S conditions showed almost 50% efficiency together with MEG.

Keywords: A. Steel, B. Polarization, B. EIS, B. XPS, C. Oxidation.

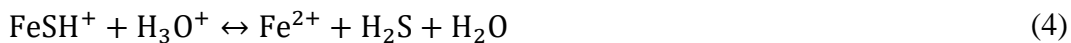
1. Introduction

Corrosion prevention is an unmet need of oil and gas industry worldwide. Accidents, maintenance, and production interruption resulting from corrosion-related failures adds to a huge economic loss in oil and gas industry [1]. The presence of CO₂ and H₂S mixture in the environment causes a severe form of attack on low carbon steel, which is the predominant alloy used for manufacturing in oil and gas industry [2–4]. The concentration of H₂S is a key determinant of extent of corrosion in CO₂-H₂S environment. Severe corrosion in CO₂-H₂S environment is of great concern as globally there is an increase in number of sour oil and gas fields (i.e. with high S content) [5]. Use of corrosion inhibitors is one of effective and economic way of preventing corrosion due to CO₂ and H₂S in oil and gas environment. Various types of organic or inorganic chemistries are used as corrosion inhibitors, therefore effect of these molecules on environment is a serious concern. Identifying environment friendly “green” inhibitors can help in offsetting the toxicity caused by the commercially available inhibitors. Investigating the inhibition efficiency of prospective green inhibitor chemistries under different corrosive conditions is the first step towards developing environmental friendly ways of corrosion prevention.

Aloe vera is one of the potential green inhibitors that have been used to study corrosion inhibition of steel [6] [7,8]. Aloe vera consist of organic compounds such as aloins, aloe emodins, tannins, saponins steroids, arabinose, resins, galactose, carbohydrates, polysaccharides, anthraglycosides and anthraquinones [9–12]. These compounds, due to their chemical structure offer corrosion inhibition properties to aloe vera. For example, aloin is key constituent of aloe vera and its structure conatins anthraquinone link to a pentose with 5 oxygen atoms [13]. Aloe vera has shown to be an efficient corrosion inhibitor on different surfaces including steel, zinc, aluminum, iron and bronze etc [7,8,11–20].

In our previous studies, aloe vera alone and in combination with ethylene glycol is shown to be efficient (aloe vera alone =10% combination = 76%) in corrosion prevention of steel surface in CO₂ environment at 40° C [6]. The inhibition properties of aloe vera are due to the adsorption of its key constituents (e.g. aloin) on the active anodic sites of the metal surface [13]. These results cannot be directly translated to CO₂-H₂S environment as the corrosion is influenced by the concentration of H₂S. Firstly, in H₂S environment the kinetics of reaction is faster and anodic reaction is a multistage reaction (see equation 1-6) which is different from pure CO₂ environment anodic reaction. Secondly, a key corrosion product of H₂S corrosion is FeS, which is different from FeCO₃ that is observed in pure CO₂ corrosion. The characteristics of FeS film that is formed in the presence of H₂S influences the corrosion of the steel samples, and may also have an impact on the inhibition effects of aloe vera. Depending on the concentration of H₂S and other environmental factors, the FeS layer can be stable offering corrosion prevention; however, unstable FeS layer can crack from internal stresses resulting in localized corrosion [21]. Secondly, the interaction of H₂S (and FeS) with inhibitors like aloe vera in CO₂-H₂S environment has not been investigated limiting the understanding of its corrosion inhibition characteristics in CO₂-H₂S environment.

On the anodic site, carbon steel oxidation takes place according to the following reactions [22–25]:



Therefore, the objectives of this paper is to investigate the corrosion inhibition behaviour of aloe vera extract for low carbon steel under CO₂ saturated conditions with different concentrations of H₂S at 40 °C. In our previous work under CO₂ condition, presence of MEG was found to be an important factor for efficient inhibition with aloe vera, therefore the investigations in this paper was carried both with and without MEG [6]. This study utilized the electrochemical experimental techniques such as LPR, Impedance, and potentiodynamic polarization to study corrosion and electrochemical behavior. Further, specimens after corrosion testing were characterized using SEM, XRD, and XPS.

2. Materials and methods

2.1. Specimen and electrolyte preparation

In all experiments, 1Cr steel (L80) in a Quenched and Tempered (Q&T) condition was used in this study. The chemical composition of the samples used are described in Table 1. The specimens were cylindrical in shape with dimension of 10mm diameter x 10mm height (Fig. 1), and a total surface area of 3.9 cm². The specimens were polished using SiC paper grades of P220, P320, P500, and P1000 and simultaneously being cooled with de-ionized distilled water. After polishing, the specimen were degreased with ethanol, rinsed with de-ionized distilled water, and then air-dried. Further, dried specimens were used for electrochemical experiments and at the end of the experiment, the specimens were rinsed with de-ionized distilled water and ethanol, dried in air, and stored in a desiccator for further characterization.

Table 1. Chemical composition in wt % of the L80-1Cr steel.

Material	C	Cr	Mn	Mo	P	Si	S	Fe
API 5CT L80	0.40	1.10	0.75	0.20	≤0.035	0.20	≤0.040	base

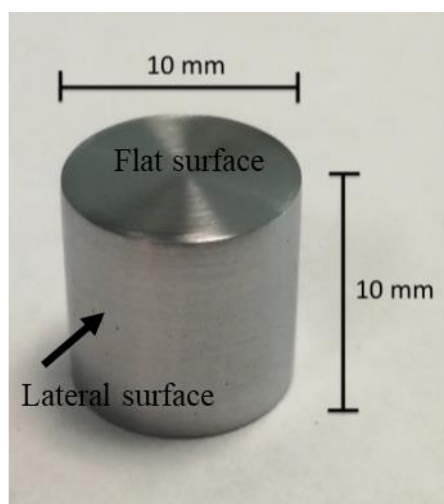


Figure 1. L80-1Cr steel sample used in all experiments.

The solution used in this study consisted of 1wt. % NaCl solution. Before each electrochemical experiment, the solution was de-aerated using the Nitrogen gas for about 12 hours. The de-aerated solution was then saturated with H₂S at different concentrations 100 ppm (92.64 mol% CO₂ and 0.01 mol% H₂S), 200 ppm (92.63 mol% CO₂ & 0.02 mol% H₂S), and 400ppm (92.62 mol% CO₂ and 0.05 mol% H₂S) for 4 hours. These concentrations (100 ppm, 200ppm, 400ppm) led to CO₂:H₂S partial pressure ratios of 9264, 4632, and 1852, respectively. The inhibitors were then injected into the CO₂-H₂S saturated solution, and the solution was de-aerated again for at least 60 minutes. The specimen was then introduced in the solution for electrochemical testing.

2.2. Inhibitors

Aloe vera (4000 ppm) and 30ml MEG (\geq spectrophotometric grade 99%) alone, and in combination with each other were used in this study. The chemical structure of MEG and aloin is shown in Fig.2.

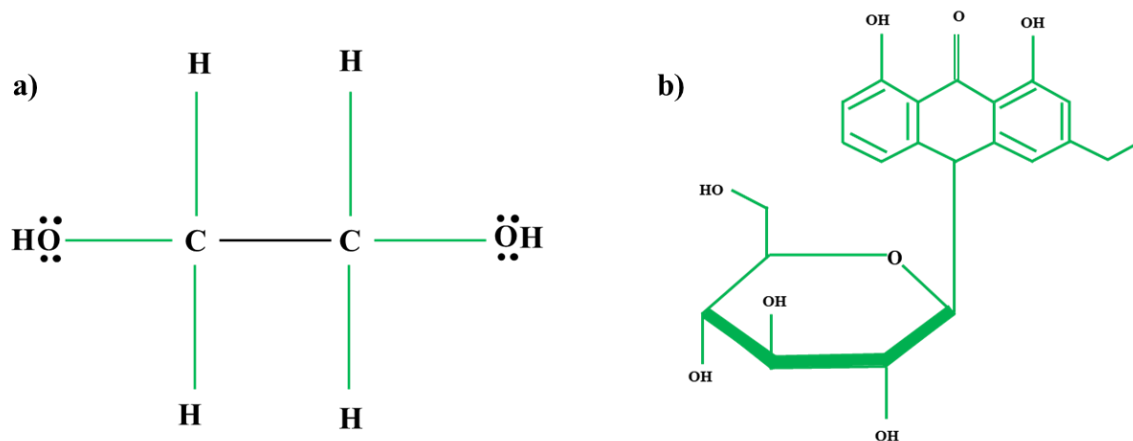


Figure 2. Structure of (a): Ethylene glycol and (b): Aloin.

Preparation of aloe vera extract

Fresh aloe vera leaves were washed and spikes were removed. The leaves were then cut into small pieces and the aloe vera gel was extracted. The gel was then blended with de-ionized distilled water in the ratio of 1:2 (aloe vera: water). The homogenized blended mixture was filtered and refrigerated in an air-tight bottle at most one day prior to the use in the experiment.

2.3. Electrochemical measurement

A standard three-electrode cell setup in a 1.5 L glass cell was used for the experiments. Ag/AgCl reference electrodes were used and a concentric ring of platinum wire was used as the counter electrode. For the linear polarization resistance measurement (LPR), the potential was scanned in a potential range of ± 10 mV vs. Open-Circuit Potential (OCP) at a scan rate of 0.167 mV/s. One-hour duration was used for the OCP stabilization. The electrochemical impedance spectroscopy (EIS) was performed using an AC signal amplitude of ± 10 mV vs OCP between 10 mHz and 10 kHz. The potentiodynamic sweep test was conducted using a range from -250 mV to +1000 mV with respect to OCP at a sweep rate of 0.167mV/min.

2.4. Experimental conditions and procedure

Table 2 lists the experimental parameters used in this study. In these experiments, the specimens were corroded in the NaCl solution at 40 °C with and without inhibitors at different concentrations of CO₂-H₂S (100, 200 and 400 ppm).

After saturation of solution with CO₂ and H₂S, the temperature was set to 40 °C. The inhibitor was injected, and the initial pH was measured. The specimen was then immersed into the solution for electrochemical experiments for 48 hours. The final pH values were obtained at the end of 48 hours of experimental measurements. The samples were then removed from the solution and rinsed first with di-water and then with ethanol. The samples were dried and then stored in desiccator for surface analysis. All electrochemical experiments were performed at

least twice and the results display average values with error bars. Further, the inhibitor efficiency was calculated using the maximum value of the polarization resistance using Eq. (7).

$$\text{Inhibitor efficiency (\%)} = \frac{(R_{p_{\text{inhibited}}} - R_{p_{\text{Uninhibited}}})}{R_{p_{\text{inhibited}}}} \times 100 \quad (7)$$

Table 2. Experimental conditions of electrochemical experiments used in this study.

Parameter	Condition
Material	Q&T 1Cr steel
Solution	1 wt.% NaCl in deionized distilled water, CO ₂ -H ₂ S saturated
Temperature	40 °C
CO ₂ -H ₂ S partial pressure	At 100 ppm H ₂ S (0.9264 bar CO ₂ and 1x10 ⁻⁴ bar H ₂ S) At 200 ppm H ₂ S (0.9263 bar CO ₂ and 2 x10 ⁻⁴ bar H ₂ S) At 400ppm H ₂ S (0.9262 bar CO ₂ and 5 x10 ⁻⁴ bar H ₂ S)
Rotation	350 rpm
Inhibitor	Aloe vera extract and MEG
Inhibitor concentration	4000 ppm and 30 ml
Test duration	2 days

2.5. Surface characterization and phase analysis

The morphological and elemental analysis of the corrosion products were investigated using a Zeiss Supra FEG-SEM using 5 kV acceleration voltage, assisted with energy dispersive X-ray (EDS) analysis equipment. For observing the cross section of the corroding steel, the samples were embedded in cold epoxy and cut longitudinally across the two ends of the cylinder. The sample was further polished using water free method (using ethanol) with SiC grade P220, P320, P500, P1000 and P4000, followed by 3 and 1µm abrasive particles. Gold was sputter coated to prevent charging of the sample. Grazing Incidence X-Ray Diffraction (GIXRD) was conducted on corroded samples with and without inhibitor by using Bruker D8 Advance X-Ray Diffractometer (XRD) to identify the phase composition of the corrosion product layer. The instrument was operated at 35 kV and 50 mA with Cr-K α radiation ($\lambda=0.22909$ nm).

The measurements were performed at 1.5° and 3° incidence angle in the 2 θ range 35° to 110° with a step size ($\Delta 2 \theta$) of 0.03 ° and a counting time per step 13 s were chosen. Since the results were similar at 1.5° and 3° incidence angle so results at 3° incidence angle are discussed.

X-ray photoelectron spectroscopy (XPS) spectra were recorded using a commercial XPS-Thermo Scientific system. The base pressure in the experimental chamber was below 10⁻⁹ mbar. The spectra were collected using Al K α X-ray source (1486.6 eV) radiation and the overall energy resolution was about 0.8 eV. High-resolution scans with 0.1 eV steps were conducted over the following regions of interest: Fe 2ps, C 1s, N 1s, and S 2p. Surface charging effects were compensated by referencing the binding energy (BE) to the C 1s line of residual

carbon set at 285.0 eV BE. XPS spectra were deconvoluted using a non-linear least-squares algorithm with a Shirley baseline and a Gaussian–Lorentzian combination. Thermo Advantage software, version 5.9913, was used for all XPS data processing.

3. Results

3.1. Effect of aloe vera extract and MEG on L80-1Cr at 40°C

3.1.1. OCP and LPR measurements

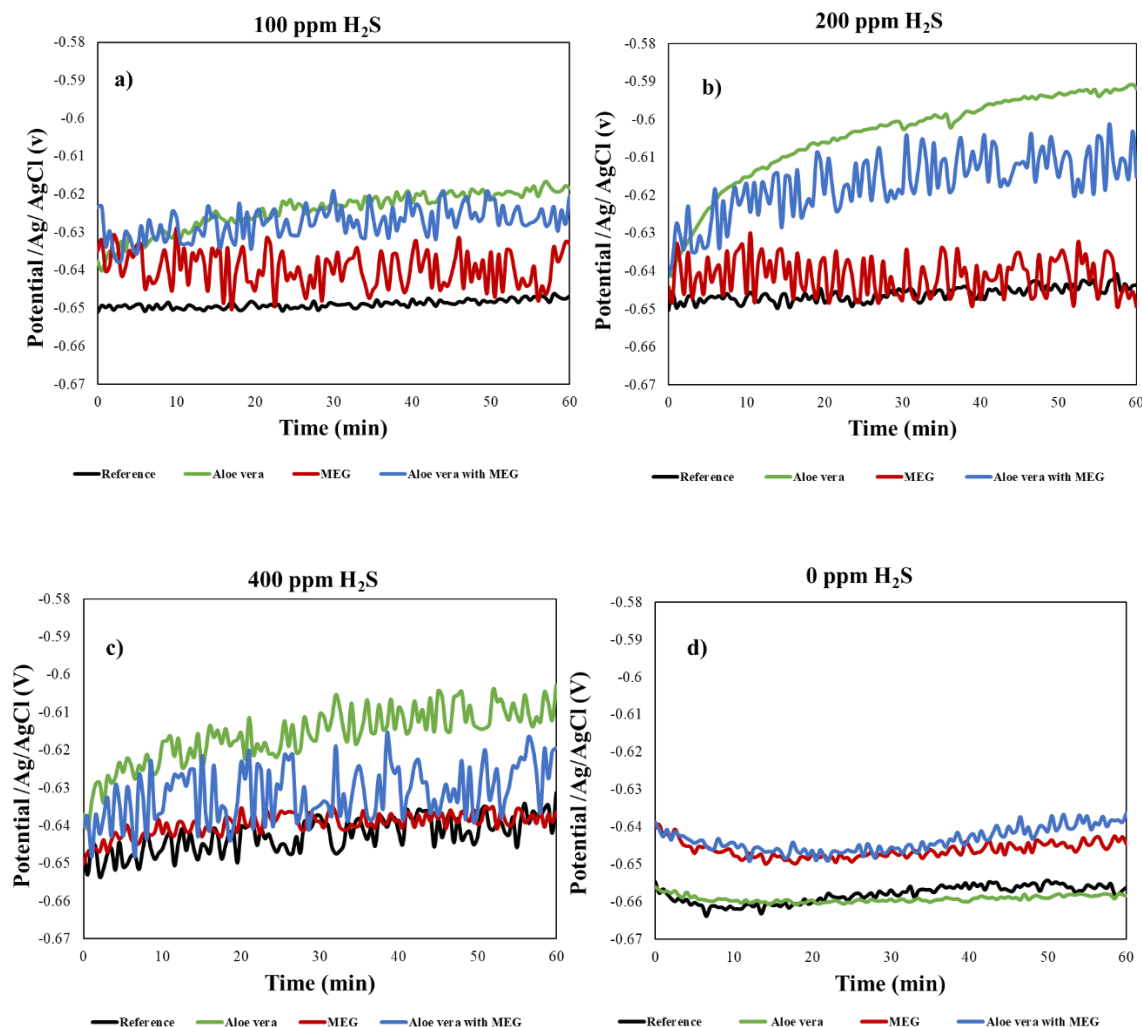


Figure 3. Variation of open circuit potential (OCP) with time for L80-1Cr steel in 1wt % NaCl solution without and with 4000 ppm aloe vera extract and MEG at 40 °C at (a): 100 ppm H₂S, (b):200 ppm H₂S, (c): 400 ppm H₂S and (d): 0 ppm H₂S concentration. Note: Results shown at 0 ppm H₂S are taken from previous study conducted using same methods in pure CO₂ environment [6].

The Fig. 3 shows the OCP values of the L80-1Cr steel sample over the period of 1 hour in 1 wt% NaCl solution with and without inhibitors (aloe vera and MEG alone, and in combination) at different H₂S concentrations. In the presence of H₂S, experiment using MEG showed OCP values close to the reference specimen. For example, at 200 ppm the OCP values for MEG ranged from -0.644V to -0.649 V vs Ag/AgCl, whereas the values for the reference specimen ranged from -0.650V to -0.644 V vs Ag/AgCl. However, aloe vera alone and in combination

with MEG shifted the potential toward noble direction with the highest shift at 200 ppm H₂S (aloe vera alone = -0.639 V to -0.591 V vs Ag/AgCl; aloe vera with MEG = 0.641 V to -0.615 V vs Ag/AgCl). Fig. 3d shows the OCP values from previous study in pure CO₂ environment (0 ppm H₂S) [6], Overall the OCP values at 0 ppm H₂S were lower than the CO₂-H₂S (200 ppm) without and with same concentration of inhibitors. Even at other concentration of H₂S (100 and 400 ppm) the OCP values with and without inhibitor were higher than those observed at 0 ppm H₂S.

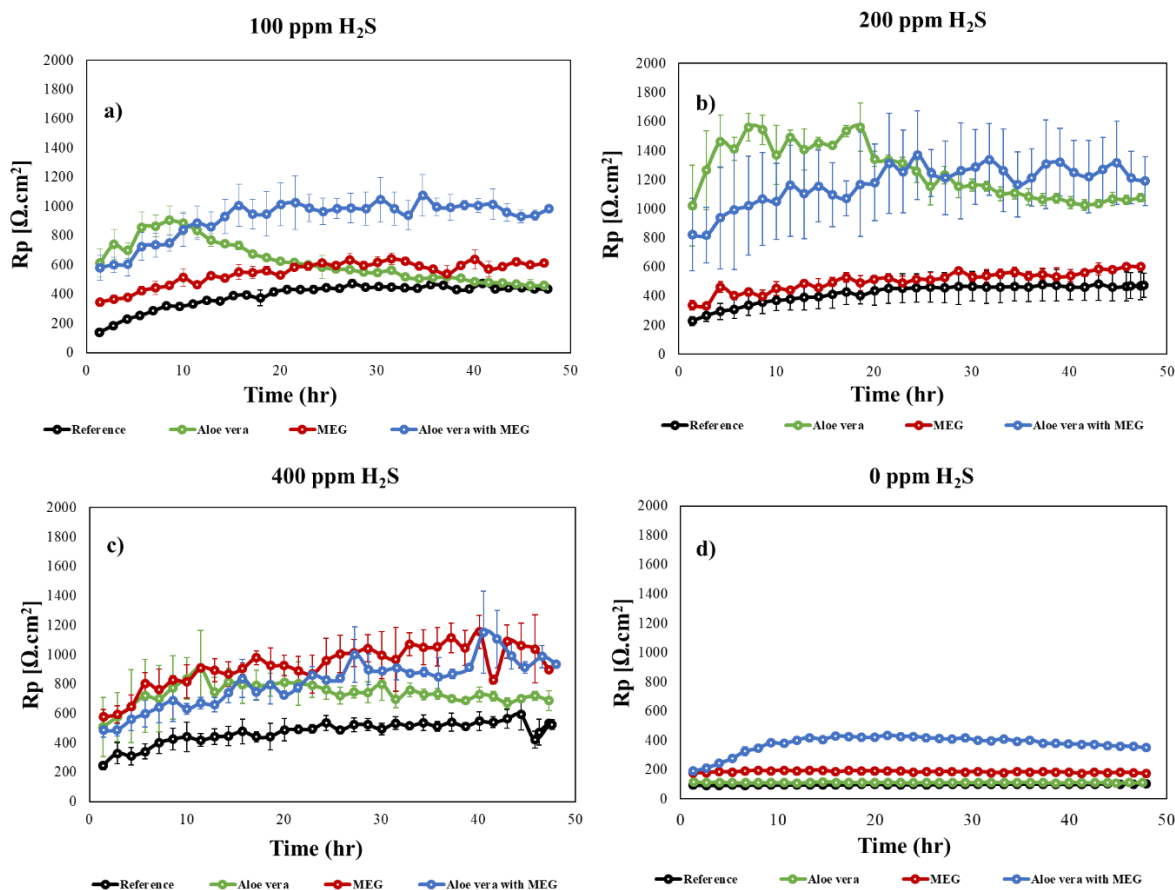


Figure 4. Polarization resistance for L80-1Cr steel exposed to 1 wt % NaCl solution without and with 4000 ppm aloe vera extract, MEG and combination of aloe vera and MEG inhibitor at 40 °C, for 48 hrs (a): 100 ppm H₂S (b): 200 ppm H₂S, (c): 400 ppm H₂S and (d): 0 ppm H₂S concentration. Note: Results shown at 0 ppm H₂S are taken from previous study conducted using same methods in pure CO₂ environment [6].

The polarization resistance values (R_p) from the LPR measurement on L80-1Cr steel with and without inhibitors at different concentrations of CO₂-H₂S are shown in Fig. 3. The R_p values for the reference sample (i.e. in absence of inhibitors) increased slightly with the concentration of H₂S from 100 ppm (476 $\Omega\cdot\text{cm}^2$ at 41 hour) to 200 ppm H₂S (483 $\Omega\cdot\text{cm}^2$ at 43 hour), and substantially at 400 ppm H₂S (593 $\Omega\cdot\text{cm}^2$ at 44 hour).

At 100 ppm H₂S (Fig. 4b), the R_p values of the reference remained lower than all other conditions and ranged from 138 $\Omega\cdot\text{cm}^2$ at 1 hour to 478 $\Omega\cdot\text{cm}^2$ at 41 hour with values remaining similar until 48 hour (435 $\Omega\cdot\text{cm}^2$). The highest R_p values at 100 ppm H₂S were observed for pure aloe vera, pure MEG, and combination of aloe vera and MEG were 807 $\Omega\cdot\text{cm}^2$ (at 10 hour), 643 $\Omega\cdot\text{cm}^2$ (at 31 hour), and 1075 $\Omega\cdot\text{cm}^2$ (at 34 hour), respectively (Fig. 4b). The initial R_p values of aloe vera in its pure form ranged from 519 $\Omega\cdot\text{cm}^2$ at 1 hour and were comparable to the trend seen with combination of aloe vera and MEG (580

$\Omega.cm^2$ at 1 hour and $840 \Omega.cm^2$ at 10 hour). The Rp values of pure aloe vera reduced consistently after 10 hours and reached to very low values ($454 \Omega.cm^2$ at 48 hour) that were comparable to the reference sample without inhibitor ($435 \Omega.cm^2$ at 48 hour). Whereas, the Rp values for the combination of aloe vera and MEG increased up to 21 hours ($1025 \Omega.cm^2$) and remained relatively similar until 48 hours ($983 \Omega.cm^2$). The Rp values for MEG alone gradually increased from $347 \Omega.cm^2$ at 1 hour to $643 \Omega.cm^2$ at 31 hours and remained relatively similar until 48 hours ($613 \Omega.cm^2$).

At 200 ppm H_2S , the Rp values of the reference remained lower than all inhibitors and ranged from $228 \Omega.cm^2$ at 1 hour to $483 \Omega.cm^2$ at 42 hour with values remaining similar till 48 hour ($474 \Omega.cm^2$). The highest Rp values in the presence of different inhibitors at 200 ppm H_2S were $1562 \Omega.cm^2$ (at 18 hour), $604 \Omega.cm^2$ (at 46 hour), and $1371 \Omega.cm^2$ (at 24 hour) for pure aloe vera, pure MEG, and combination of aloe vera and MEG, respectively (Fig. 4c). The trend of change in Rp values over time at 200 ppm concentration of H_2S were similar to those seen at 100 ppm concentration of H_2S with three key differences (Fig. 4c). Firstly, the observed Rp values at 200 ppm were higher than 100 ppm with and without inhibitors. Secondly, the initial Rp values for pure aloe vera were the highest and did not start to reduce until 20 hours (ranged from $1022 \Omega.cm^2$ at 1 hour to $1562 \Omega.cm^2$ at 18 hour). Lastly, the Rp values for pure aloe vera remained substantially higher than the reference values even at the later hours ($1343 \Omega.cm^2$ at 20 hour to $1075 \Omega.cm^2$ at 48 hour).

At 400 ppm H_2S , the Rp values of the reference were higher than the Rp value of reference at 100 ppm H_2S and 200 ppm H_2S , but remained lower than all inhibitors at 400 ppm concentration H_2S . The Rp values of the reference ranged from $244 \Omega.cm^2$ at 1 hour to $593 \Omega.cm^2$ at 44 hour with values remaining similar till 48 hour ($524 \Omega.cm^2$). The highest Rp values for pure aloe vera, pure MEG, and combination of aloe vera and MEG, were $908 \Omega.cm^2$ (at 11 hour), $1154 \Omega.cm^2$ (at 40 hour), and $1152 \Omega.cm^2$ (at 40 hour), respectively (Fig. 4d). The trend of change in Rp values for 400 ppm of H_2S (Fig. 4d) was similar to 100 ppm values, except the MEG had exceptionally high values ranging between $577 \Omega.cm^2$ at 1 hour and $1154 \Omega.cm^2$ at 40 hour, which remained similar until 48 hours ($897 \Omega.cm^2$).

Fig. 4d shows the highest Rp values observed in the presence of H_2S (all concentrations) were higher than that observed in our previous study in the CO_2 environment [6] (reference $140 \Omega.cm^2$ (at 44 hour), aloe vera $115 \Omega.cm^2$ (at 15 hour), MEG $197 \Omega.cm^2$ (at 11 hour), and combined aloe vera and MEG $314 \Omega.cm^2$ (at 13 hour).

Table 3 shows the extracted inhibitor efficiency values under various conditions from the Rp values. For pure aloe vera, the inhibition efficiency initially increased from 41% to 70% with an increase in H_2S concentration from 100 ppm to 200 ppm. Upon further increase in H_2S concentration to 400 ppm, the efficiency for pure aloe vera reduced to 35%. Opposite trends were observed for the MEG, where the inhibition efficiency reduced (from 26% to 20%) with initial increase in H_2S concentration from 100 ppm to 200 ppm, and then increased to 49% at 400 ppm. The mixture of aloe vera and MEG followed the same trend as pure aloe vera with initial increase in efficiency from 56% (at 100 ppm) to 65% (at 200 ppm), and then a reduction to 49% (at 400 ppm). Overall, the highest efficiency was observed for aloe vera at 200 ppm H_2S concentration.

Table 3 also shows compares the inhibition efficiency values under similar conditions when the condition is pure CO_2 without H_2S (0 ppm H_2S). The corrosion inhibition efficiency values for pure aloe vera were higher in the CO_2 - H_2S environment as compared to pure CO_2 environment (10%). Whereas, in general for pure MEG and in combination with aloe vera, the

corrosion inhibition values were higher (47% and 76%, respectively) in pure CO₂ environment as compared to CO₂-H₂S environment .

Table 3. Inhibitor efficiency values for green inhibitor at 40 °C.

Inhibitor type	H ₂ S concentration			
	0 ppm*	100 ppm	200 ppm	400 ppm
Aloe vera	10	41	70	35
MEG	47	26	20	49
Aloe vera + MEG	76	56	65	49

*Note: Results shown at 0 ppm H₂S are taken from previous study conducted using same methods in pure CO₂ environment [6].

3.1.2. Potentiodynamic polarization

Fig. 5 shows the potentiodynamic polarization curves of L80-1Cr steel in NaCl solution with and without inhibitors at 40 °C and 200 ppm of H₂S concentration. The cathodic polarization results from the reaction: $2H^+ + 2e^- = H_2$, which takes place in the CO₂-H₂S saturated solutions. The anodic polarization results from dissolving of iron and formation of iron sulphide on the steel surface in the CO₂-H₂S solution. The displacement in potential values of >85 mV are indicative of anodic or cathodic type inhibitors, whereas displacement values of <85 mV suggest mixed type inhibitors[26,27]. The displacement in corrosion potential upon addition of inhibitors in the current study was less than 0.0850 V, suggesting inhibitors used in this study were of mixed-type rather than pure anodic or cathodic type. Interestingly, the current densities for L80-1Cr in the anodic branch of the curve decreases upon addition of inhibitors (pure MEG and mixture of MEG and aloe vera); however, in the cathodic branch of the curve, the changes in the current density values were marginal when using inhibitors. The corrosion potential clearly became slightly positive with addition of aloe vera alone or in combination with MEG compared to the reference.

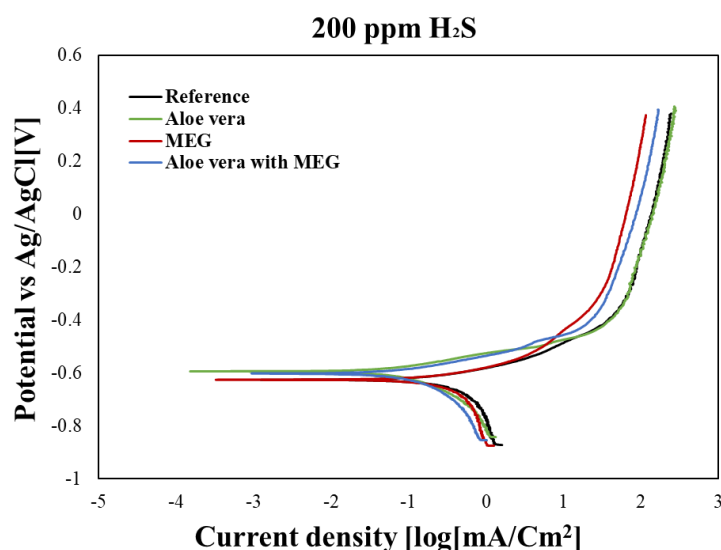
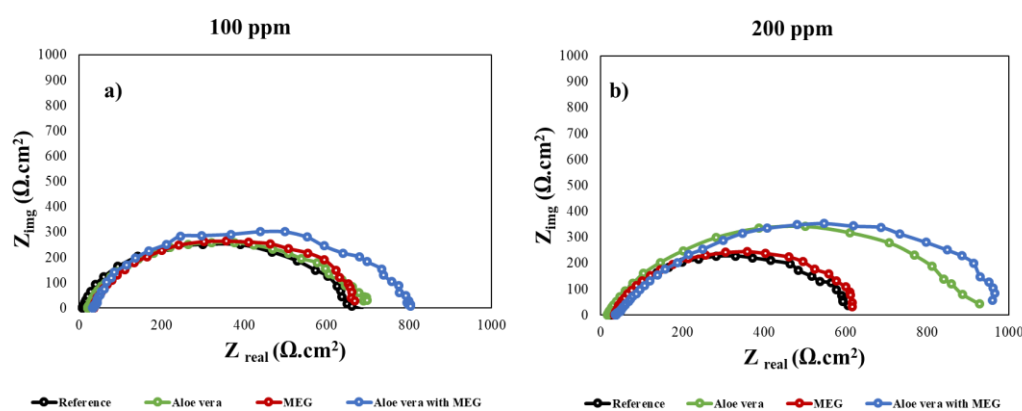


Figure 5. Potentiodynamic polarization curves for L80-1Cr steel exposed to 1 wt % NaCl solution with and without inhibitor at 40 °C, for 48 hrs at 200 ppm H₂S concentration.

3.1.3. Electrochemical impedance spectroscopy investigation

Figure 6 shows the impedance results in the form of Nyquist plots of L80-1Cr steel at 40 °C in the NaCl solution without and with inhibitors after 48 h in different H₂S concentrations in CO₂-H₂S environment. An increase in the capacitance loop diameter indicates an increase in corrosion resistance. With increase in H₂S concentration, without inhibitor, the diameter of the capacitance loop for the reference sample decreased from 251 Ω.cm² to 196 Ω.cm² (see Figs. 6 a, b and c). At all H₂S concentrations, the diameter of the capacitance loop increased upon addition of aloe vera in pure form or in combination with MEG. With increase in H₂S concentration from 100 ppm to 200 ppm, there was an increase in the capacitance loop diameter for aloe vera in its pure form (258 Ω.cm² and 341 Ω.cm², respectively see Figs. 6 a and b) and in combination with MEG (301 Ω.cm² and 354 Ω.cm², respectively see Fig. 6 a and b). Upon further increase in H₂S concentration to 400 ppm (see Fig. 6c), the capacitance loop diameter decreased to 228 Ω.cm² and 302 Ω.cm² for pure aloe vera and for combination of aloe vera and MEG respectively. The capacitance loop diameter for MEG alone (291 Ω.cm²) was higher than the reference sample (196 Ω.cm²) only at 400 ppm H₂S concentration. Whereas at 100 ppm and 200 ppm H₂S concentration, the capacitance loop diameter for MEG alone (264 Ω.cm² and 245 Ω.cm²) was comparable to the reference sample (251 Ω.cm² and 227 Ω.cm²). At all concentrations of H₂S, there was a shift in the high frequency impedance value for MEG alone and in combination with aloe vera.

Fig. 7 shows the equivalent electrical circuit model of the impedance behavior of the L80-1Cr steel without and with the inhibitors in the NaCl solution. The Randle's electrochemical system (Fig. 7) with its double time constant signifies either inhibitor film or the layer of corrosion products on the steel sample. The equivalent circuit consists of a solution resistance (R_s), which is connected to a double layer capacitance (C_{dl}) and is in parallel with a charge transfer resistance (R_{ct}). In the presence of aloe vera extract, however, an additional circuit consisting of a film capacitance (C_{fc}) and film pore resistance (R_{pr}) was added to account for an adsorbed inhibitor layer–solution interface, as applied elsewhere [15]. The R_{ct} represents a measure of the polarization resistance of the corroding L80-1Cr steel. The adsorbed species on the steel surface modifies the capacitance of charges present in the electric double layer at the steel/solution interface. Thus, the double layer capacitance (C_{dl}) provides a better validation of an equivalent circuit model. Table 4 represents fitting of impedance data at the last cycle of impedance measure (at 48 hrs).



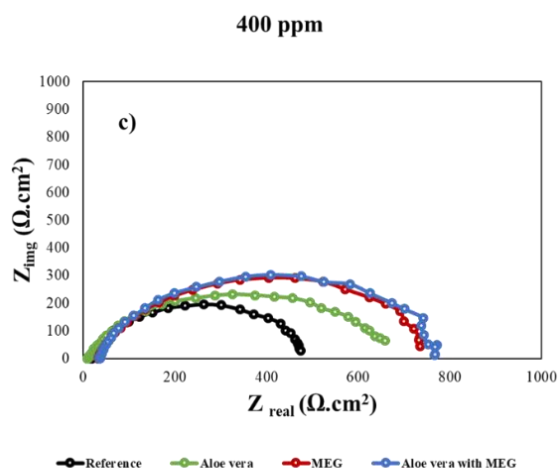


Figure 6. Results of Electrochemical impedance measurements: Nyquist plot for L80-1Cr steel exposed to 1 wt % NaCl solution without and with 4000 ppm aloe vera extract and MEG inhibitor at 40 °C (a): 100 ppm H₂S, (b): 200 ppm H₂S and (c): 400 ppm H₂S at 48 hr.

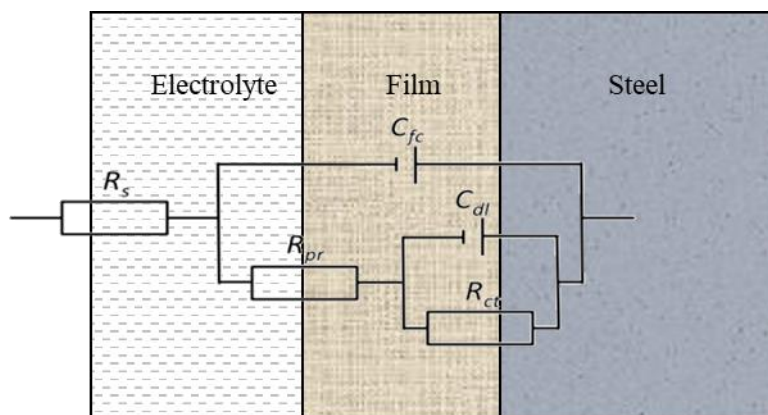


Fig. 7. A double-time constant circuit showing a perforated film interface or perforations filled with corrosion product.

Table 4. Circuit fitting elements: EIS parameters obtained based on the fitted curves on experimental data according to equivalent circuit presented in Fig. 5 for L80-1Cr steel exposed to 1 wt % NaCl solution at 40 °C, with and without the inhibitors at different concentrations of H₂S at 48 hr.

Sample	R_s $\Omega.cm^2$	C_{fc} $\mu\Omega^{-1}.cm^{-2}.s^n$	n1	R_{pr} $\Omega.cm^2$	C_{dl} $\mu\Omega^{-1}.cm^{-2}.s^n$	n2	R_{ct} $\Omega.cm^2$
100 ppm							
Reference	6	230	0.86	102	49	0.07	457
Aloe vera	21	376	0.90	350	375	0.38	364
MEG	35	362	0.95	392	305	0.93	226
Aloe vera with MEG	33	356	0.86	763	468	1.00	61
200 ppm							
Reference	11	1543	0.95	366	420	0.97	563
Aloe vera	18	412	0.87	1150	874	0.99	3891

MEG	35	2515	0.93	593	924	0.93	834
Aloe vera with MEG	39	583	0.85	961	362	0.85	3571
400 ppm							
Reference	18	1911	0.92	463	639	0.94	668
Aloe vera	23	768	0.79	759	2287	0.96	3556
MEG	35	1250	0.93	710	414	1.00	1268
Aloe vera with MEG	38	920	0.94	905	262	1.00	2026

3.1.4. Surface characterization of the corrosion product layer

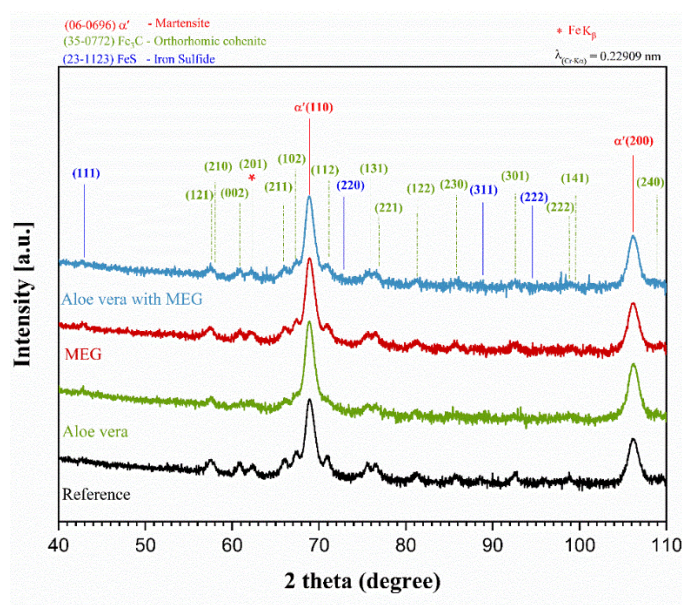


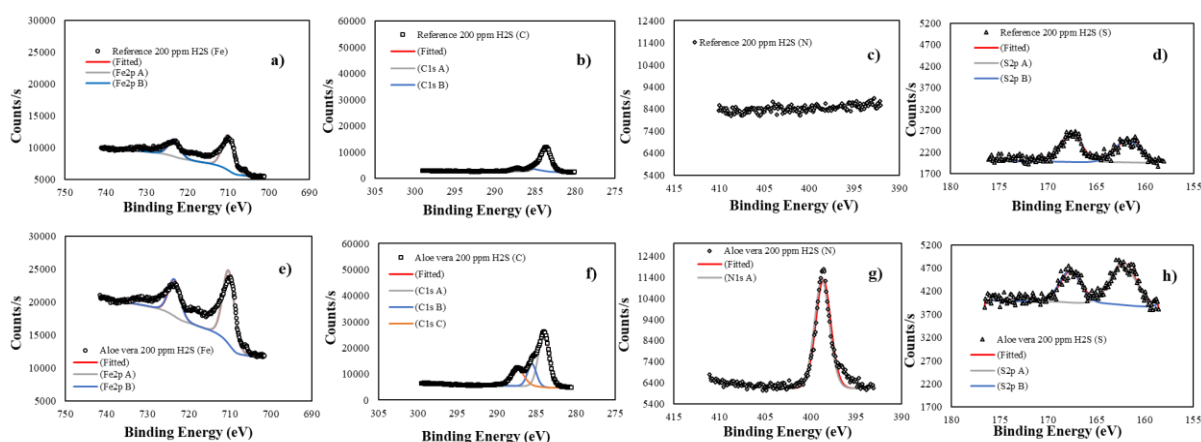
Fig. 8. Results of X-ray diffraction of L80-1Cr steel corroded in 1 wt% NaCl with and without inhibitors at 200 ppm H₂S concentration, 40 °C.

Fig. 8 shows the XRD patterns of the corrosion product scales that were formed on the steel samples during the electrochemical experiments in the NaCl solution with and without inhibitors at 40 °C at 200 ppm concentration of H₂S. The XRD results (Fig. 7) showed the presence of Fe₃C residual product and FeS corrosion product. The amount of Fe₃C was much higher than that of FeS in all samples. The low reflection peaks of FeS were observed (reflections 42.9, 73.4, and 88.9). Further, with the addition of aloe vera and MEG, the intensity of the Fe₃C diffracted peak were decreased. For example, the peaks as seen in reflections (121), (210), (002), (211), (102), (112), (131), (221) and (122) were almost relatively decreased in the presence of aloe vera alone and in combination with MEG indicating lower iron dissolution. In XRD analysis, the FeS formed lesser number of peaks with smaller intensity reflections (shown in Fig.8) suggesting a limited thickness (~ nm) of FeS layer on the steel surface.

3.1.2. Binding energy calculation using XPS

The XPS analyses were performed on the samples corroded without and with inhibitor in 1% NaCl solution saturated with CO₂-H₂S solution at 40 °C. The XPS results confirm the presence of FeS layer and for cases with inhibitor on the adsorption of green inhibitor (aloe vera) over the steel sample surfaces. The XPS results also confirm the formation of thin-layer (organic film) of inhibitor on the steel surface. Fig. 9 shows the wide-scan spectra of Fe2p, C1s, N1s and S2p of the corroded samples at 200 ppm H₂S concentration without inhibitor (Figs. 9a-9d) and with inhibitor (Aloe vera alone (Figs. 9e-9h) and in combination with MEG (Figs. 9i-9l)). All XPS spectra were found to have complex forms, which were assigned to the corresponding species through a deconvolution fitting procedure. The peaks in individual spectra confirmed the presence of Fe, C, N, and S. The signals of C1s and N1s were mainly attributed to the inhibitors adsorbed on the steel surface; the signals of S2p came from the corrosive products; and the signal of Fe2p could be assigned to the iron matrix and its corrosion products.

The XPS spectra of Fe2p peak was composed of two peaks for all samples. The Fe2p_{3/2} peaks at 709.28 eV, 709.68 eV and 709.78 eV in Figs 9a, 9e and 9i corresponds to Fe (III)-S peak respectively [28]. The high-resolution spectra of C1s are shown in Fig. 9b, 9f and 9j. The spectra in Fig. 9b splits into two peaks, one at 283.3 eV which corresponds to carbon in cementite (Fe₃C) [29] and other non-intensive peak at 285.8 eV which corresponds to binding energies of C-C bond [30]. However, in Figs. 9g and 9j spectra was decomposed into three peaks, where peaks at 283.8 eV and 285.8 eV were attributed to the Fe-C bond and C-C bond respectively [29,30], and -C=N at 287.4 eV [31,32]. Fig. 9g and 9k shows the high-resolution spectra of N1s. High intensive peak at 398.7 eV and 399.4 eV corresponds to the C=N-C in aloe vera [29,33] in Figs. 9g and 9k respectively. Again two peaks can be observed in the high-resolution spectra of S2p (Fig. 9d, 9h and 9l), Peaks at (161.88 eV, 162.48 eV and 161.88 eV) could be attributed to the ferrous sulfide on steel surface in Figs. 9a, 9h and 9l respectively [34,35], and peaks at (167.18 eV, 167.88 eV and 167.68 eV) in Figs. 9a, 9h and 9l corresponds to the oxidation of sulfur [36,37]. Similar to 200 ppm concentration of H₂S, the presence of varying extent of Fe, C, N and S was also confirmed at 100 and 400 pm H₂S concentration. The area for S2p peaks at different concentrations of H₂S with and without inhibitors is shown in Table 5.



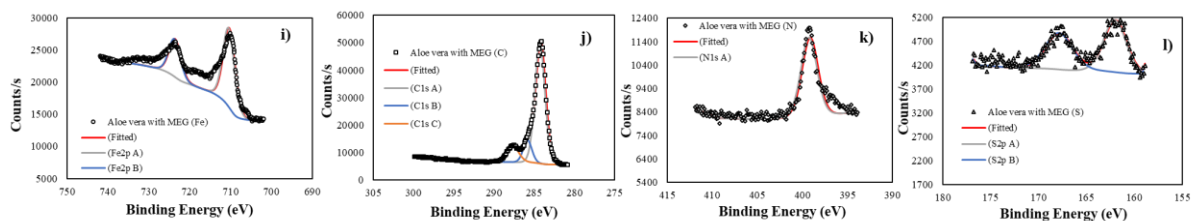


Figure 9: XPS spectrum of (a, b, c and d): Fe2p, C 1s, N 1s and S2p without inhibitor (e, f, g and h): Fe2p, C 1s, N 1s and S2p with aloe vera with corrosion products of NaCl-contaminated L-80 1 Cr steel specimens after 48 h exposure to 40 °C in CO₂-H₂S environment.

Table 5. Area under S2p peaks using XPS analysis on L80-1Cr steel exposed with and without aloe vera in 1% NaCl solution after 48 h exposure at different concentrations of H₂S at 40 °C.

H ₂ S Concentration	Area (CPS.eV)	Reference	Aloe vera
100 ppm	S2p Scan A	1089	1642
	S2p Scan B	912	1772
200 ppm	S2p Scan A	1807	3056
	S2p Scan B	1697	1895
400 ppm	S2p Scan A	4988	3215
	S2p Scan B	3785	3273

The morphology of L80-1Cr steel surface after 48 hrs immersion with and without inhibitors in different concentrations of H₂S solution at 40 °C are shown in Fig. 10. On the top surface view, the reference sample had minute pores at 100 ppm H₂S concentration (Fig. 10a). At 200 and 400 ppm H₂S (Fig 10c and 10e), the reference sample had more porous layer of corrosion products with some localized pits of larger size that may have resulted from combination of numerous micro pits. The top surface of the sample at 200 ppm and 400 ppm H₂S shows FeS film uniformly formed all over the sample surface (the content of Fe and S are high in the corrosion product as detected by energy-dispersive X-ray spectroscopy (EDS)). The cross-sectional view showed thicker corrosion product layer at 200 and 400 ppm (Figs. 10d and 10f). FeS layer as compared to 100 ppm H₂S concentration (Fig. 10b).

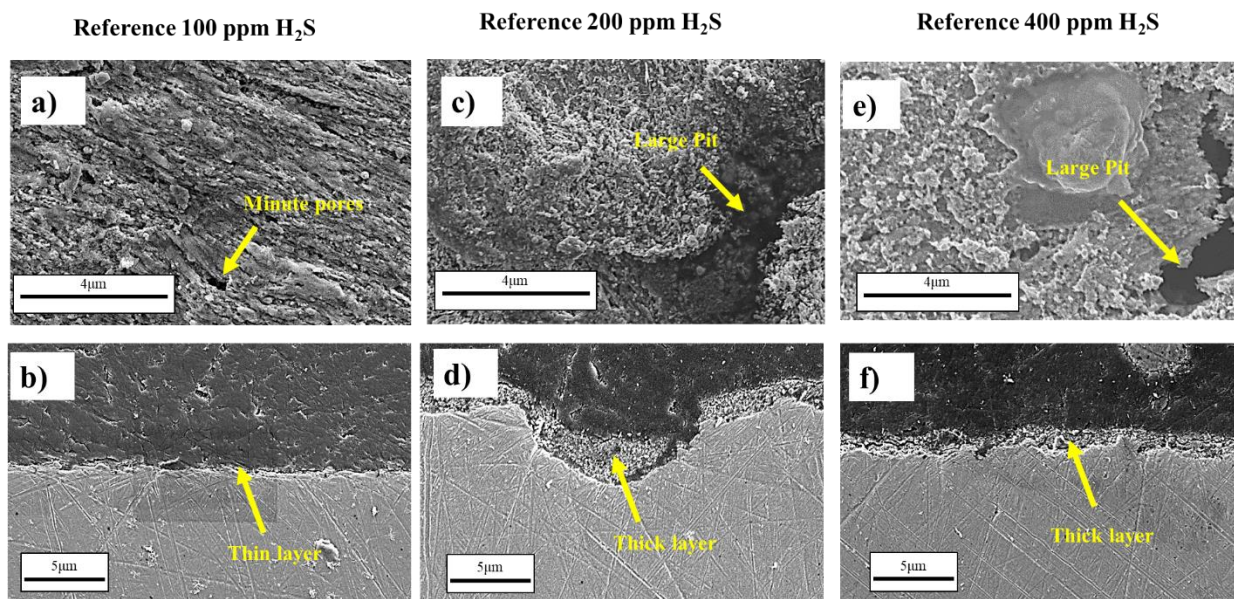


Figure 10. SEM images (top view and cross-sectional view) for L80-1Cr steel exposed to 1 wt% NaCl solution, with out inhibitor (Reference) at 40 °C (a-b): 100 ppm H₂S, (c-d): 200 ppm H₂S and (e-f): 400 ppm H₂S.

In the presence of aloe vera alone, the corrosion product layer was less thick as compared to the reference samples (Figs. 11b, 11d and 11f). In the presence of aloe vera, the top view showed minute pores at 100 ppm (Fig. 11a) and 200 ppm (Fig. 11c) H₂S concentrations. At 400 ppm, the FeS layer was highly porous and had cracks leading to maximal surface disruption as shown in Fig. 11e. In the cross-sectional view, the thickness of the corrosion product layer was very thin (< 1 micron) at 200 ppm (Fig. 11d) and 400 ppm (Fig. 11f) H₂S concentration as compared to that (~ 2 micron) at 100 ppm (Fig. 11b).

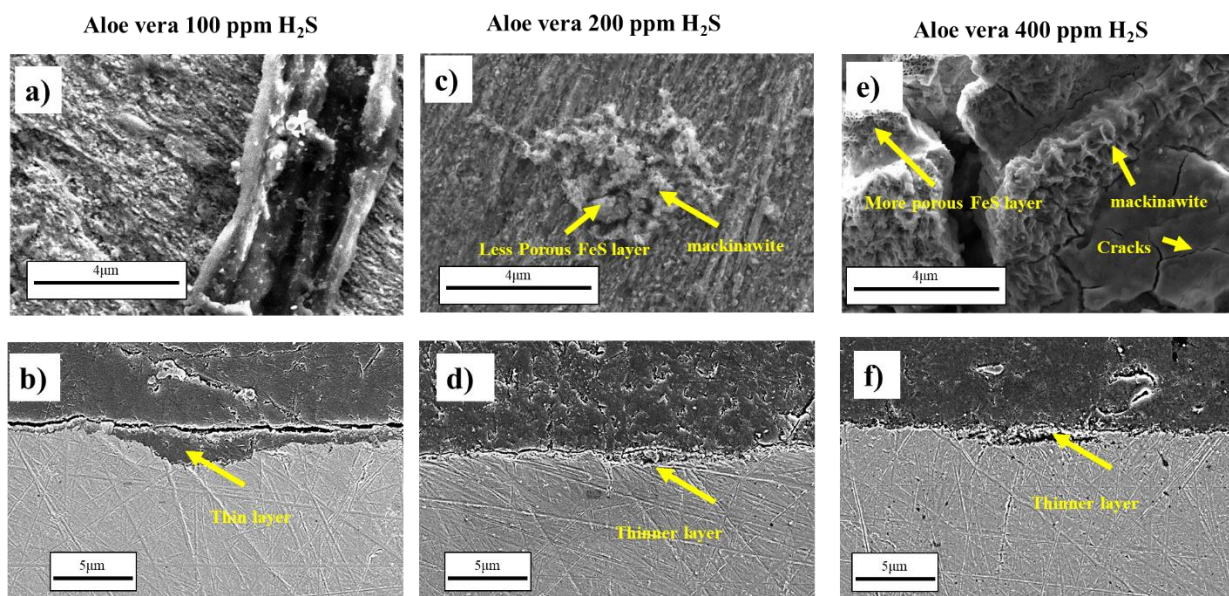


Figure 11. SEM images (top view and cross-sectional view) for L80-1Cr steel exposed to 1 wt% NaCl solution, with 4000 ppm aloe vera at 40 °C (a-b): 100 ppm H₂S, (c-d): 200 ppm H₂S and (e-f): 400 ppm H₂S.

4. Discussion

This paper extends the findings of our previous work on corrosion inhibition behavior of aloe vera on steel samples in pure CO₂ environment [6] and reports their corrosion inhibition behavior in CO₂-H₂S environment at different concentrations of H₂S. Overall the results show that there are significant differences between the inhibition behavior of aloe vera when H₂S is present, which is also due to the formation of FeS in comparison with the situation under pure CO₂ condition.

4.1. Effect of different concentration of H₂S without inhibitor

The presence of different concentrations of H₂S had an effect on the corrosion of L80-1Cr steel samples in the CO₂ environment. The partial pressure of CO₂: partial pressure of H₂S ratio influences the dominant type of corrosion such that: (i) ratio < 20: leads to H₂S dominant corrosion, (ii) 20 < ratio < 500: leads to mixed corrosion, and (iii) ratio > 500: leads to CO₂ corrosion [38,39]. In this study, the partial pressure of CO₂: partial pressure of H₂S ratio was > 500 suggesting a CO₂ dominant corrosion. Despite of CO₂ dominant corrosion, the effect of different concentrations of H₂S on the corrosion of L80-1Cr steel sample with and without inhibitors was evident in this study. In the absence of inhibitors, the reference sample had higher Rp values at higher H₂S concentrations (see Figs. 4a-c). In the presence of H₂S, the Rp values (Fig. 4) were higher as compared to the pure CO₂ environment in the absence of inhibitors (Fig. 3d and 4d) [6], which could be likely due to the formation of FeS in the presence of H₂S [40–42]. The area under S2p peaks that correspond to FeS increases with the concentration of H₂S (Table 5). Upon EDS analysis, the presence of sulphur was confirmed on the corroded sample surface, which further supports the role of involvement of H₂S in the corrosion process. Previous literature has also confirmed the detection of sulphur in the corrosion product layer in the presence of H₂S, which can increase the propensity for localized corrosion, especially at higher concentrations of H₂S [43,44].

Differences in the extent of corrosion at different concentrations of H₂S were seen in the top surface morphology of the reference samples. At 100 ppm H₂S concentration, least corrosion was observed with minute pores (Fig. 10a). The presence of H₂S in trace amount leads to FeS formation that offers corrosion resistance properties. Increasing the concentration further led to an increase in the thickness of the corrosion product layer (Figs. 10b, 10d and 10f). Overall density of the FeS layer increased with the concentration of H₂S as confirmed by an increase in corresponding impedance values (high R_{pr} and R_{ct} values) (Table 4). However, localized corrosion (pits) was observed likely due to higher H₂S concentration (Figs. Top view 10c and 10e). Localized corrosion observed with increasing H₂S concentration can occur due to the falling off of some loser part of the layer that can lead to pitting in the corrosion product layer. Localized pitting was also supported by higher C_{fc} and C_{dl} values at higher concentrations of H₂S. Localized pitting at higher concentrations of H₂S has also been reported by previous literature [43,44].

4.2. Effects of inhibitors on corrosion inhibition at different concentration of H₂S

Interestingly, aloe vera in its pure form had higher corrosion inhibition efficiency in the presence of H₂S (at 100 ppm H₂S = 41%, 200 ppm = 70%, and 400 ppm = 35%) as compared to the pure CO₂ environment (10%) see Table 3. The OCP (Fig. 3) and Rp (Fig. 4) values observed for pure aloe vera in the presence of H₂S were also more favorable for corrosion inhibition as compared to the pure CO₂ environment [6]. In the pure CO₂ environment, inhibitors can have higher affinity for adsorption on the residual or corrosion products (Fe₃C and FeCO₃) leading

to lesser adsorption on the Fe surface and lesser efficiency [45]. Whereas in the H₂S, it is possible that aloe vera had lesser affinity for FeS causing higher adsorption on the anodic Fe sites leading to better corrosion prevention. In combination with MEG, aloe vera had higher efficiency (76%) in the pure CO₂ environment as compared to CO₂-H₂S environment (at 100 ppm H₂S = 56%, 200 ppm = 65%, and 400 ppm = 49%). The addition of MEG may have favored the adsorption of inhibitor on the Fe surface by lowering the threshold of energy needed for its adsorption, leading to higher corrosion efficiency in the presence of CO₂ environment.

The aloe vera improved the corrosion inhibition properties in the CO₂-H₂S environment. In the previous study, aloe vera was shown to be effective in corrosion inhibition in pure CO₂ environment by adsorbing on the Fe surface [6]. Aloe vera consists of organic compounds have π centered electrons and functional groups of O, S or N/ or combination, which allows it to bind to the metal surface [7,8,17]. In contrast to the previous study in pure CO₂ environment [6], some interesting observations were made in corrosion inhibition behavior of pure aloe vera in the presence of H₂S. Firstly, there was an increase in corrosion inhibition (increase R_p value) for the first few hours (10-20 hours) followed by a reduction in the values. The initial increase in R_p values were likely due to the adsorption of aloe vera on the active anodic sites of the steel sample as supported by the positive shift in the potential values (Figs. 3 and 5) [46–49]. However, the R_p values of aloe vera reduced after few hours (< 20) in the CO₂-H₂S environment. Aloe vera may have caused the existing FeS layer to become loose and porous, which may have contributed to reduced inhibition properties over the time. Similarly, the corrosion inhibition effects in presence of aloe vera increased from 100 ppm to 200 ppm H₂S. However the effects diminished significantly at 400 ppm H₂S, likely due to more unstable and porous layer of FeS at higher concentrations of H₂S, which was also supported by the decrease in R_{pr} and R_{ct} and an increase in C_{fc} and C_{dl} values (Table 4). The changes in impedance values (C_{fc} and C_{dl}) suggest more anodic sites were available for corrosion at 400 ppm H₂S concentration [50]. Overall, the FeS had a larger area for 400 ppm (3215 CPS.eV), followed by 200ppm (3056 CPS.eV) and 100ppm (1642 CPS.eV) H₂S concentrations (Table 5). However, the protectiveness of the layer was poor at 400 ppm H₂S concentration as indicated by the impedance results as discussed above. Previous studies have also shown at higher concentrations of H₂S, the protective film can become porous, loose and detach from the metal surface [43]. The formation of FeS layer appeared to be very similar to aggregates of curved platelets that are much smaller and thinner [51–53]. Based on these results, the precipitated FeS can be identified as nanocrystalline mackinawite shown in Figs. 11c and 11e. In literature also FeS layer (mackinawite type) formation has shown to result from the reaction of wet elemental iron with sulfur at room temperature, which is very similar to mackinawite particles obtained by precipitation [54].

For pure MEG, the corrosion inhibition behavior was different from pure aloe vera in H₂S environment. Unlike aloe vera, the MEG had more gradual and sustained increase in R_p values over 48 hours at all H₂S concentrations. In addition, MEG had similar corrosion inhibition behavior at lower concentrations of H₂S (highest R_p = 643 Ω .cm² and 604 Ω .cm² at 100 ppm and 200 ppm, respectively) whereas substantially higher R_p values (highest R_p = 1154 Ω .cm²) were observed at 400 ppm H₂S concentration. These findings suggest the mechanisms underlying corrosion inhibition effects of pure MEG operated were different than pure aloe vera. It is known that MEG operates by two different mechanisms – adsorption of its molecules on the sample surface [6], and alteration of the properties of the solution, e.g., increased solubility of H₂S [55]. In terms of solution properties, MEG facilitates solubility of H₂S in the solution [56–58]. The presence of MEG contributed to higher solubility of H₂S in the solution, especially at high concentration (400 ppm) of H₂S. Greater amount of dissolved H₂S leads to a

denser FeS formation, which was evident from higher R_{pr} and R_{ct} values at 400 ppm than 200 ppm and 100 ppm H_2S (Table 4).

The effects of combined aloe vera and MEG in the H_2S environment were different from the previous study in pure CO_2 environment [6]. In pure CO_2 environment, the addition of MEG to aloe vera led to an eight-fold increase in corrosion inhibition efficiency values. However, in the CO_2 - H_2S environment, the combination of MEG and aloe vera led to a smaller (~1.5 fold at 400 ppm H_2S) increase in the inhibition efficiency. The addition of MEG to aloe vera obliterated the reduction in R_p values that were otherwise observed in the presence of pure aloe vera during later hours (> 20 hours) at all concentrations of H_2S (blue vs green lines in Fig. 4 a-c). These synergistic effects of aloe vera and MEG likely result from the different mechanisms underlying the action of these inhibitors. As shown in the previous study in CO_2 environment [6], the aloe vera acts through adsorption on the sample surface, whereas MEG changes in the properties of the solution in addition to getting adsorbed on the surface.

5. Conclusion

This study investigated the corrosion inhibition properties of aloe vera and MEG at different concentrations of H_2S in the CO_2 environment. Overall the results shows that the presence of H_2S has significant effect on inhibition due to aloe vera.

- In the absence of inhibitors, there was more porous corrosion product layer and pitting on the steel surface as compared to that in the presence of inhibitors. An increase in concentration of H_2S led to higher R_p values and impedance parameters, that were associated with a denser layer of FeS. Increase in H_2S concentration also led to localized pitting. The XPS results confirmed increase in area of S2p A peaks corresponding to FeS with an increase in H_2S concentration.
- Aloe vera is effective in corrosion inhibition in H_2S environment as indicated by improved inhibition efficiencies, LPR, and EIS values likely due to its adsorption on the anodic dissolution sites. Corrosion inhibition ability of pure aloe vera is reduced at 400 ppm of H_2S as compared to lower concentrations of H_2S .
- Adding MEG to pure aloe vera shows synergistic effects and can negate the reduction in R_p values that were otherwise observed in the presence of pure aloe vera.
- Impedance values confirm that formation of inhibitor film on the steel surface (higher R_{pr} and R_{ct}) and the changes in solution properties (R_s) contributed to corrosion prevention in the presence of inhibitors in the CO_2 - H_2S environment.

References

- [1] G.A. Zhang, Y. Zeng, X.P. Guo, F. Jiang, D.Y. Shi, Z.Y. Chen, Electrochemical corrosion behavior of carbon steel under dynamic high pressure H₂S/CO₂ environment, *Corros. Sci.* 65 (2012) 37–47.
- [2] P. Rajeev, A.O. Surendranathan, C.S.N. Murthy, Corrosion mitigation of the oil well steels using organic inhibitors—a review, *J. Mater. Environ. Sci.* 3 (2012) 856–869.
- [3] G. Fierro, G.M. Ingo, F. Mancia, XPS investigation on the corrosion behavior of 13Cr-Martensitic stainless steel in CO₂-H₂S-Cl⁻ environments, *Corrosion.* 45 (1989) 814–823.
- [4] K. Masamura, S. Hashizume, J. Sakai, I. Matsushima, Polarization behavior of high-alloy OCTG in CO₂ environment as affected by chlorides and sulfides, *Corrosion.* 43 (1987) 359–365.
- [5] Y.-S. Choi, S. Nesic, S. Ling, Effect of H₂S on the CO₂ corrosion of carbon steel in acidic solutions, *Electrochim. Acta.* 56 (2011) 1752–1760.
- [6] S. Gupta, R. Yazdi, M. Andersson, R. Ambat, CO₂ corrosion inhibition capability of an eco-friendly inhibitor containing green aloe vera plant extract on 1Cr steel: experimental and molecular modelling studies, *Unpubl. Results.* (2021).
- [7] M. Mehdipour, B. Ramezanzadeh, S.Y. Arman, Electrochemical noise investigation of Aloe plant extract as green inhibitor on the corrosion of stainless steel in 1 M H₂SO₄, *J. Ind. Eng. Chem.* 21 (2015) 318–327.
- [8] A.A. Ayoola, O.S.I. Fayomi, I.G. Akande, O.A. Ayeni, O. Agboola, O.R. Obanla, O.G. Abatan, C.J. Chukwuka, Inhibitive corrosion performance of the eco-friendly aloe vera in acidic media of mild and stainless steels, *J Bio Tribo Corros.* 6 (2020) 1–13.
- [9] O.A. Omotosho, Inhibition evaluation of chemical and plant extracts on the corrosion of metallic alloys in acidic environment, (2016).
- [10] H. Kuzuya, I. Tamai, H. Beppu, K. Shimpo, T. Chihara, Determination of aloenin, barbaloin and isobarbaloin in Aloe species by micellar electrokinetic chromatography, *J. Chromatogr. B Biomed. Sci. Appl.* 752 (2001) 91–97.
- [11] N.O. Eddy, S.A. Odoemelam, Inhibition of corrosion of mild steel in acidic medium using ethanol extract of Aloe vera, *Pigment Resin Technol.* (2009).
- [12] A.O. James, A.O. Atela, Aloe vera: an inhibitor of aluminium corrosion in hydrochloric acid solution, *Int. J. Pure Appl. Chem.* 3 (2008) 159–163.
- [13] O.K. Abiola, A.O. James, The effects of Aloe vera extract on corrosion and kinetics of corrosion process of zinc in HCl solution, *Corros. Sci.* 52 (2010) 661–664.
- [14] T. Derbe, B. Yilma, Investigation of the anti-corrosion activities of aloe vera extract on iron metal sheets, *J. Nat. Sci. Res.* 5 (2015) 18–24.
- [15] B. Benzidia, H. Hammouch, A. Dermaj, H. Benassaoui, S. About, N. Hajjaji,

- Investigation of green corrosion inhibitor based on aloe vera (L.) burm. F. for the protection of bronze B66 in 3% NaCl, *Anal. Bioanal. Electrochem.* 11 (2019) 165–177.
- [16] O.M. Ajayi, N.M. Everitt, K.T. Voisey, Evaluation of inulin and aloe vera as green corrosion inhibitors for mild steel in 15% HCl, (2016).
- [17] A.K. Singh, S. Mohapatra, B. Pani, Corrosion inhibition effect of Aloe Vera gel: gravimetric and electrochemical study, *J. Ind. Eng. Chem.* 33 (2016) 288–297.
- [18] S. Dahiya, S. Lata, P. Kumar, R. Kumar, A descriptive study for corrosion control of low-alloy steel by Aloe vera extract in acidic medium, *Corros. Rev.* 34 (2016) 241–248.
- [19] R.T. Vashi, H.G. Chaudhari, The study of aloe-vera gel extract as green corrosion inhibitor for mild steel in acetic acid, *Int J Innov Res Sci Eng Tech.* 6 (2017) 22081–22091.
- [20] P. Shah, S. Agarwal, Aloe-Vera: A Green Corrosion Inhibitor, *Int. J. Res. Appl. Sci. Eng. Technol.* 2 (2014) 12–16.
- [21] M. Singer, B. Brown, A. Camacho, S. Nesic, Combined effect of CO₂, H₂S and acetic acid on bottom of the line corrosion, in: *Corros. 2007*, OnePetro, 2007.
- [22] S.A. Umoren, M.M. Solomon, V.S. Saji, Corrosion Inhibitors for Sour Oilfield Environment (H₂S Corrosion), *Corros. Inhib. Oil Gas Ind.* (2020) 229–254.
- [23] M.A. Lucio-Garcia, J.G. Gonzalez-Rodriguez, M. Casales, L. Martinez, J.G. Chacon-Nava, M.A. Neri-Flores, A. Martinez-Villafañe, Effect of heat treatment on H₂S corrosion of a micro-alloyed C–Mn steel, *Corros. Sci.* 51 (2009) 2380–2386.
- [24] X.L. Cheng, H.Y. Ma, J.P. Zhang, X. Chen, S.H. Chen, H.Q. Yang, Corrosion of iron in acid solutions with hydrogen sulfide, *Corrosion.* 54 (1998) 369–376.
- [25] A. Traidia, M. Alfano, G. Lubineau, S. Duval, A. Sherik, An effective finite element model for the prediction of hydrogen induced cracking in steel pipelines, *Int. J. Hydrogen Energy.* 37 (2012) 16214–16230.
- [26] A. Singh, Y. Lin, I.B. Obot, E.E. Ebenso, Macrocyclic inhibitor for corrosion of N80 steel in 3.5% NaCl solution saturated with CO₂, *J. Mol. Liq.* 219 (2016) 865–874.
- [27] A. Khamis, M.M. Saleh, M.I. Awad, Synergistic inhibitor effect of cetylpyridinium chloride and other halides on the corrosion of mild steel in 0.5 M H₂SO₄, *Corros. Sci.* 66 (2013) 343–349.
- [28] M. Mullet, S. Boursiquot, M. Abdelmoula, J.-M. Génin, J.-J. Ehrhardt, Surface chemistry and structural properties of mackinawite prepared by reaction of sulfide ions with metallic iron, *Geochim. Cosmochim. Acta.* 66 (2002) 829–836.
- [29] S. Delpoux, F. Beguin, R. Benoit, R. Erre, N. Manolova, I. Rashkov, Fullerene core star-like polymers—1. Preparation from fullerenes and monoazidopolyethers, *Eur. Polym. J.* 34 (1998) 905–915.
- [30] N. Ochoa, C. Vega, N. Pébère, J. Lacaze, J.L. Brito, CO₂ corrosion resistance of carbon

- steel in relation with microstructure changes, *Mater. Chem. Phys.* 156 (2015) 198–205.
- [31] La Surface Database, (n.d.). <http://www.lasurface.com/accueil/index.php?lang=fr> (accessed November 30, 2021).
- [32] NIST X-ray Photoelectron Spectroscopy Database, (n.d.). <http://dx.doi.org/10.18434/T4T88K> (accessed November 30, 2021).
- [33] O. Olivares-Xometl, N. V. Likhanova, M.A. Domínguez-Aguilar, J.M. Hallen, L.S. Zamudio, E. Arce, Surface analysis of inhibitor films formed by imidazolines and amides on mild steel in an acidic environment, *Appl. Surf. Sci.* 252 (2006) 2139–2152.
- [34] J.M. Bonello, R.M. Lambert, The structure and reactivity of quinoline overlayers and the adsorption geometry of lepidine on Pt {1 1 1}: model molecules for chiral modifiers in enantioselective hydrogenation, *Surf. Sci.* 498 (2002) 212–228.
- [35] S. Nakamura, A. Yamamoto, Electrodeposition of pyrite (FeS₂) thin films for photovoltaic cells, *Sol. Energy Mater. Sol. Cells.* 65 (2001) 79–85.
- [36] B.C. Bostick, S. Fendorf, Arsenite sorption on troilite (FeS) and pyrite (FeS₂), *Geochim. Cosmochim. Acta.* 67 (2003) 909–921.
- [37] R. V. Kashkovskiy, Y.I. Kuznetsov, L.P. Kazansky, Inhibition of hydrogen sulfide corrosion of steel in gas phase by tributylamine, *Corros. Sci.* 64 (2012) 126–136.
- [38] I.B. Obot, M.M. Solomon, S.A. Umoren, R. Suleiman, M. Elanany, N.M. Alanazi, A.A. Sorour, Progress in the development of sour corrosion inhibitors: Past, present, and future perspectives, *J. Ind. Eng. Chem.* 79 (2019) 1–18.
- [39] D.E. Milliams, D. Cottage, R.N. Tuttle, ISO 15156/NACE MR0175-A new international Standard for metallic materials for use in oil and gas production in sour environments, in: *Corros. 2003, OnePetro*, 2003.
- [40] P. Bai, S. Zheng, C. Chen, Electrochemical characteristics of the early corrosion stages of API X52 steel exposed to H₂S environments, *Mater. Chem. Phys.* 149 (2015) 295–301.
- [41] S. Zheng, C. Zhou, P. Wang, C. Chen, L. Chen, Effects of the Temperature on the Hydrogen Permeation Behaviours of L360NCS Pipeline Steel in 1MPa H₂S Environments, (2013).
- [42] E. Wallaert, T. Depover, I. De Graeve, K. Verbeken, FeS corrosion products formation and hydrogen uptake in a sour environment for quenched & tempered steel, *Metals (Basel)*. 8 (2018) 62.
- [43] D. Li, L. Zhang, J. Yang, M. Lu, J. Ding, M. Liu, Effect of H₂S concentration on the corrosion behavior of pipeline steel under the coexistence of H₂S and CO₂, *Int. J. Miner. Metall. Mater.* 21 (2014) 388–394.
- [44] J. Tang, Y. Shao, J. Guo, T. Zhang, G. Meng, F. Wang, The effect of H₂S concentration on the corrosion behavior of carbon steel at 90 C, *Corros. Sci.* 52 (2010) 2050–2058.

- [45] S. Gupta, K.K. Gupta, M. Andersson, R. Yazdi, R. Ambat, Electrochemical and molecular modelling studies of CO₂ corrosion inhibition characteristics of alkanolamine molecules for the protection of 1Cr steel, *Corros. Sci.* (2021).
- [46] C. Zhang, J. Zhao, Effects of pre-corrosion on the corrosion inhibition performance of three inhibitors on Q235 steel in CO₂/H₂S saturated brine solution, *Int. J. Electrochem. Sci.* 12 (2017) 9161–9179.
- [47] C. Zhang, V. Zahedi Asl, Y. Lu, J. Zhao, Investigation of the corrosion inhibition performances of various inhibitors for carbon steel in CO₂ and CO₂/H₂S environments, *Corros. Eng. Sci. Technol.* 55 (2020) 531–538.
- [48] B. Hamrahi, A. Fattah-alhosseini, S.O. Gashti, A. Khanlarkhani, S.M. Madani, Green Corrosion Inhibitor of the *Matricaria Chamomilla* Oil to Protect Steel in the Acidic H₂S-Containing Solution, *J. Bio-and Tribo-Corrosion.* 7 (2021) 1–13.
- [49] J. Aslam, R. Aslam, S. Zehra, M. Rizvi, Corrosion inhibitors for sweet (CO₂ corrosion) and sour (H₂S corrosion) oilfield environments, in: *Environ. Sustain. Corros. Inhib.*, Elsevier, 2022: pp. 165–181.
- [50] A. Munis, T. Zhao, M. Zheng, A.U. Rehman, F. Wang, A newly synthesized green corrosion inhibitor imidazoline derivative for carbon steel in 7.5% NH₄Cl solution, *Sustain. Chem. Pharm.* 16 (2020) 100258.
- [51] R. Bolney, M. Grosch, M. Winkler, J. van Slageren, W. Weigand, C. Robl, Mackinawite formation from elemental iron and sulfur, *RSC Adv.* 11 (2021) 32464–32475.
- [52] D. Csákerényi-Malasics, J.D. Rodriguez-Blanco, V.K. Kis, A. Rečnik, L.G. Benning, M. Pósfai, Structural properties and transformations of precipitated FeS, *Chem. Geol.* 294 (2012) 249–258.
- [53] Y. Chen, W. Liang, Y. Li, Y. Wu, Y. Chen, W. Xiao, L. Zhao, J. Zhang, H. Li, Modification, application and reaction mechanisms of nano-sized iron sulfide particles for pollutant removal from soil and water: A review, *Chem. Eng. J.* 362 (2019) 144–159.
- [54] H. Ohfuji, D. Rickard, High resolution transmission electron microscopic study of synthetic nanocrystalline mackinawite, *Earth Planet. Sci. Lett.* 241 (2006) 227–233.
- [55] E. Gulbrandsen, J.H. Morard, Why does glycol inhibit CO₂ corrosion?, in: *Corros.* 98, OnePetro, 1998.
- [56] P.D. Mantor, The solubility of methane, carbon dioxide, and hydrogen sulfide in oxygenated compounds at elevated pressures, (1960).
- [57] N. Dawass, R.R. Wanderley, M. Ramdin, O.A. Moulton, H.K. Knuutila, T.J.H. Vlught, Solubility of carbon dioxide, hydrogen sulfide, methane, and nitrogen in monoethylene glycol; Experiments and molecular simulation, *J. Chem. Eng. Data.* 66 (2020) 524–534.
- [58] F.-Y. Jou, R.D. Deshmukh, F.D. Otto, A.E. Mather, Vapor-Liquid Equilibria of H₂S and CO₂ and Ethylene Glycol At Elevated Pressures, *Chem. Eng. Commun.* 87 (1990) 223–231.

9. Paper IV: Corrosion inhibition properties of eco-friendly green inhibitors containing aloe vera plant extract on 1 Cr steel under H₂S conditions with CO₂

Shivangi Gupta, Martin Andersson, Rouhollah Yazdi, Rajan Ambat, Corrosion inhibition properties of eco-friendly green inhibitors containing aloe vera plant extract on 1 Cr steel under H₂S conditions with CO₂, manuscript form to be submitted.



10. Overall Discussion

Corrosion in oil and gas industry is a cause of major economic losses. Amongst corrosion mitigation techniques, the use of inhibitors is an attractive option due to its low cost and easy application. This thesis has investigated the corrosion inhibition properties of different inhibitors including alkanolamines, imidazoline, aloe vera, and mono-ethylene glycol (MEG) on low carbon steel. Different electrochemical and characterization techniques are used such as LPR, EIS, Potentiodynamic sweep, SEM, XRD and XPS, etc. The thesis builds on the previous literature on corrosion inhibition properties of different types of inhibitors in three distinct ways.

10.1. Molecular modelling for screening inhibitor molecules

This thesis investigated the mechanism of action for the inhibitors at molecular levels using modelling techniques. Molecular modelling results confirm that adsorption of these inhibitors on the metal surface contributes to their corrosion inhibition properties, therefore the method can be used for screening of inhibitor molecules. Higher adsorption energy of the inhibitor molecules as compared to water molecules support adsorption of the inhibitor molecules from an aqueous phase. The molecular modeling results of this thesis support the experimental findings such that the inhibitors with higher inhibition efficiencies were found to have higher adsorption energies on the Fe surface.

10.2. Inhibition studies using organic amines and imidazoline

This thesis established the corrosion inhibition properties of organic amines and imidazolines in harsh environments typically seen in oil and gas industry i.e., in the presence of CO₂ (sweet environment) and H₂S (sour environment). Ethanol amine was found to have the best corrosion inhibition efficiency amongst all alkanolamines. The corrosion efficiency of amines decreased with increase in temperature of the solution due to higher corrosion kinetics and desorption of the inhibitors from the surface. This is a relevant finding as higher temperatures are common in oil wells. When amines were injected at the beginning of the experiment, the protectiveness of the FeCO₃ layer was delayed due to a longer immersion time. Whereas, when the amines were injected later (after the formation of FeCO₃), there was no major change in inhibitor efficiency. Molecular modeling confirmed that the amine molecules get adsorbed on the Fe surface due to their higher adsorption energy than water molecules. Also, amines had stronger affinity to bind to FeCO₃ and Fe₃C as compared to the Fe surface.

Among imidazoline used in this thesis, larger structures with the phenyl group (2-PI) led to better corrosion inhibition than the smaller structures (2-MI) in pure CO₂ environment. Molecular modeling confirmed higher adsorption energy values for 2-PI as the phenyl group provides additional site for bonding with the Fe surface. The corrosion inhibition efficiency of 2-PI inhibitor was higher (2.6 times) in the presence of H₂S as compared to pure CO₂. The addition of MEG improved the corrosion inhibition properties of both types of imidazolines. This opens avenues for the oil and gas industry to experiment with combination of inhibitors that may offer synergistic effects on corrosion prevention. This thesis also confirmed that re-injections of imidazoline later (after 48 hours) can help in attenuating the lowering of corrosion inhibition properties over the time.

10.3. Eco-friendly green inhibitor

The last unique aspect of this thesis addresses the environmental aspect of inhibitor-based corrosion inhibition to the largest extent. The commercially available inhibitors can lead to environmental degradation warranting a need of alternative plant-based inhibitors that are cleaner and do not lead to environmental toxicity. This thesis established the corrosion inhibition properties of aloe vera (a green inhibitor) on steel surface in CO₂ and CO₂-H₂S environments. At higher concentrations of H₂S (400 ppm) the corrosion inhibition effects of aloe vera are lowered. The corrosion inhibition properties of aloe vera were increased substantially when used in higher concentrations (8000 ppm) or when used in combination with MEG (4000 ppm + MEG) in CO₂ environment. In CO₂-H₂S environment, addition of MEG to aloe vera assists in prevention of lowering of corrosion inhibition effects of aloe vera. Molecular modeling confirms that the corrosion inhibition effect of aloe vera are due to adsorption of its constituent molecules (e.g. aloin) on the metal surface. Establishing the corrosion inhibition properties of aloe vera in this thesis is a step towards addressing the issue of environmental degradation that is associated with use of commercial inhibitors and devising environment friendly strategies for corrosion inhibition. Molecular modeling can help in screening the adsorption properties of green inhibitors and finding the inhibitors that can potentially offer good corrosion inhibition in oil and gas industry.





11. Overall Conclusions

Conclusions covering the work reported in various chapters are summarized below.

- 1) Amines were effective in corrosion inhibition of steel surface in CO₂ environment due to adsorption of its molecules on the steel surface. The formation of the corrosion products (FeCO₃) is delayed with addition of amines when injected before FeCO₃ formation. Ethanolamine had the best corrosion inhibition efficiency when compared to other tested amines.
- 2) Imidazolines (2-MI and 2-PI) were found to be effective in corrosion inhibition of steel surface in CO₂ and H₂S (only 2-PI tested) environment. Addition of MEG to imidazolines improve their corrosion inhibition properties due to increase surface coverage arising from ion-pair interactions. Re-injection of another dose of 2-PI partially improves the corrosion inhibition by preventing degradation of the initially formed inhibitor film.
- 3) Aloe vera, which is a form of green inhibitor, was effective in corrosion inhibition of steel samples in pure CO₂ environment. The corrosion inhibition efficiency of aloe vera improved to ~8 times upon addition of MEG. Higher concentration of aloe vera led to better corrosion inhibition efficiencies. The corrosion inhibition effects were likely due to the adsorption of its constituent molecules (e.g. aloin) on the steel surface.
- 4) In the presence of H₂S in the CO₂ environment, aloe vera was found to be effective in corrosion inhibition of steel samples. Corrosion inhibition ability of pure aloe vera is reduced at 400 ppm of H₂S. Adding MEG to pure aloe vera shows synergistic effects and can negate the reduction in Rp values that were otherwise observed in the presence of pure aloe vera.



12. Future Work

- 1) Molecular modelling work in this thesis is focused only on calculating the adsorption energy, and found it is very useful for screening molecules. However, more detailed molecular studies can be carried out including atmospheric conditions such as CO₂, H₂S environment, temperature and pressure, etc. This will be very much useful for finding suitable green inhibitor molecules.
- 2) Aloe vera was found to be a good green extract providing high inhibition efficiency together with MEG. However, this is based on the lab scale investigation, which does not include all realistic conditions in the well. Therefore, additional flow loop experiments are needed in order to understand the effects of temperature, pressure, flow conditions and inhibitors injection frequencies.
- 3) Aloe vera inhibition effect is not fully explained from the mechanistic point of view. Additional investigations focusing on spectroscopic methods. Also, other detailed investigations are required for understanding the molecular chemistry of aloe vera extract and its constituent molecules that offers corrosion inhibition.
- 4) Highest efficiency was found when aloe vera was mixed with MEG. However, MEG is categorized as “yellow” chemical. Therefore, more research in the direction of finding a green alternative for MEG is important.
- 5) Many other natural extracts can be potentially used as corrosion inhibitors. Finding suitable extracts using a combination of molecular modelling and experimental work will be good to increase the matrix of green inhibitor chemistry.





DTU Mechanical Engineering
Section of Materials and Surface Engineering
Technical University of Denmark

Produktionstorvet, Bld. 425
DK-2800 Kgs. Lyngby
Denmark
Tlf.: +45 4525 2205
Fax: +45 4525 1961

www.mek.dtu.dk

January 2022

ISBN: 978-87-7475-676-7